Universiteit
Leiden
The Netherlands

Temperature and pressure effects on the electrochemical CO2 reduction

Vos, R.E.

Citation
Vos, R. E. (2025, February 5). *Temperature and pressure effects on the electrochemical CO2 reduction*. Retrieved from https://hdl.handle.net/1887/4179004

Version:	Publisher's Version
License:	Licence agreement concerning inclusion of doctoral thesis in the Institutional Repository of the University of Leiden
Downloaded from:	https://hdl.handle.net/1887/4179004

Note: To cite this publication please use the final published version (if applicable).

Temperature and pressure effects on the electrochemical CO_2 reduction

Rafaël E. Vos

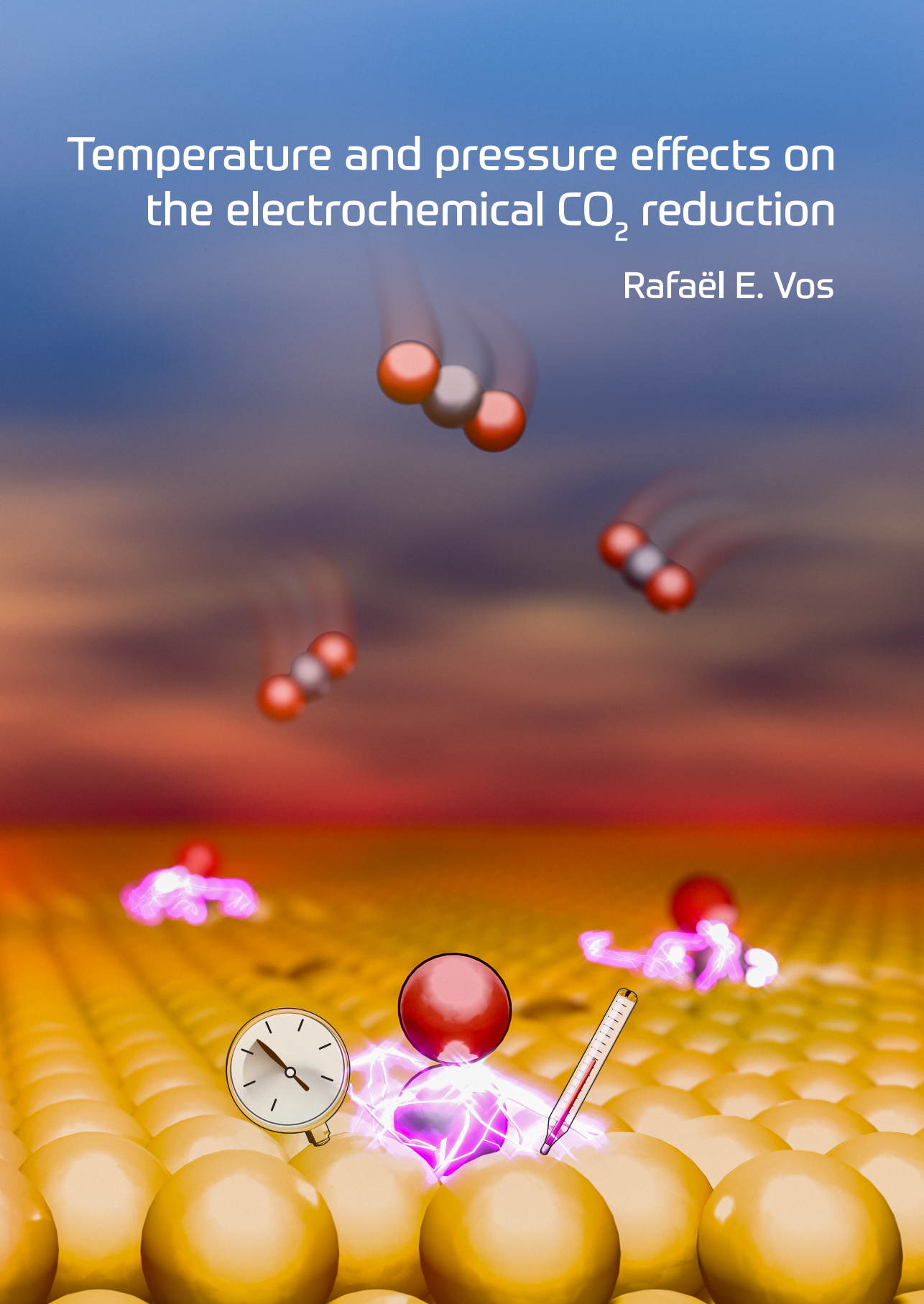

Temperature and pressure effects on the electrochemical CO_2 reduction

Proefschrift

ter verkrijging van

de graad van doctor aan de Universiteit Leiden

op gezag van rector magnificus prof.dr.ir. H. Bijl,

volgens besluit van het college voor promoties

te verdediging op woensdag 5 februari 2025

klokke 14:30

door

Rafaël Enro Vos

geboren te Almere, Nederland

in 1995

Promotores:
Prof. dr. M.T.M. Koper
Prof. dr. ir. B.M. Weckhuysen (Universiteit Utrecht)

Promotiecommissie:
Prof. dr. M. Ubbink
Prof. dr. E. Bouwman
Prof. dr. I.M.N. Groot
dr. W. van der Stam (Universiteit Utrecht)
dr. R. Buonsanti (EPFL, Zwitserland)

This research was carried out under project number ENPPS.IPP.019.002 in the framework of the Research Program of the Materials innovation institute (M2i) (www.m2i.nl) and received funding from Tata Steel Nederland Technology BV and the Dutch Research Council (NWO) in the framework of the ENW PPP Fund for the top sectors and from the Ministry of Economic Affairs in the framework of the "PPS-Toeslagregeling".

ISBN: 978-94-6510-408-9

Cover art by Thomas Hartman (THIS Illustrations)

Printed by proefschriftmaken.nl

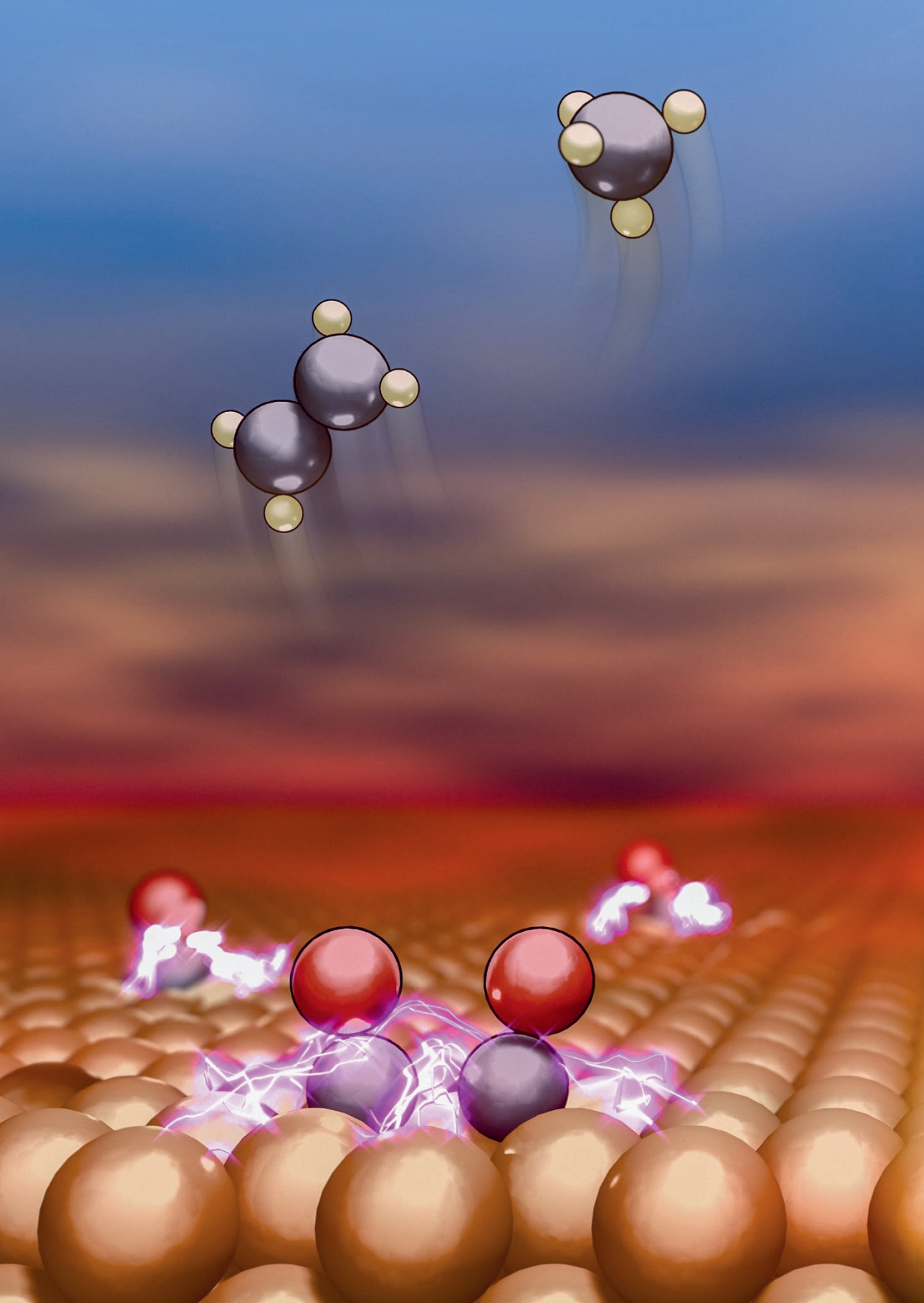

Table of Contents

1 Introduction **4**

2 The effect of temperature on the cation-promoted electrochemical CO_2 reduction on gold **18**

3 How temperature affects the selectivity of the electrochemical CO_2 reduction on copper **44**

4 The temperature dependence of electrochemical CO_2 reduction on Ag and CuAg alloys **72**

5 Nickel as electrocatalyst for $CO_{(2)}$ reduction: effect of temperature, potential, partial pressure and electrolyte composition **94**

6 Design of a Rotating Disk Electrode setup operating under high pressure and temperature: application to CO_2 reduction on gold **114**

7 Change in the C-C coupling mechanism during CO_2 electroreduction on Cu at elevated temperature and pressure **136**

8 Screening of various metals for electrochemical CO_2 reduction at elevated temperatures and pressures **158**

Appendices

A. Supporting information to Chapter 2 . . . . . **181**

B. Supporting information to Chapter 3 . . . . . **195**

C. Supporting information to Chapter 4 . . . . . **225**

D. Supporting information to Chapter 5 . . . . . **243**

E. Supporting information to Chapter 6 . . . . . **253**

F. Supporting information to Chapter 7 . . . . . **263**

G. Supporting information to Chapter 8 . . . . . **282**

I. Summary, Outlook and Samenvatting **298**

II. List of publications, Curriculum Vitae & Acknowledgements. **314**

1

Introduction

1.1 General context

One of the largest and most pressing issues of this time is the changing climate due to manmade emissions of greenhouse gasses, most importantly CO_2. Since the industrial revolution in 18th century, atmospheric CO_2 concentrations have risen with 50 percent to over 420 ppm currently[1]. In fact, more than 40 percent of the historic CO_2 emissions has been emitted since the turn of the last century[2]. Increasing atmospheric CO_2 concentrations leads to global warming, increased extreme weather events such as storms, droughts and floods, ocean acidification, melting of glaciers and pole ice and sea level rise[3]. This decreases the livability of earth for many humans around the world and harms nature and its ecosystems severely[3].

To limit the effects of climate change, the world should stay below 1.5 °C global warming compared to the pre-industrial era, as agreed upon in the Paris agreement. To reach this ambitious goal, or at least limit global warming as much as possible, a rigorous change is needed in the way modern society uses energy and materials. A transition is needed from a world based on fossil fuels to a world based on renewable resources. For the energy transition, a shift takes place from gas and coal based energy supply to an energy system build on solar and wind energy. Mobility is shifting from petroleum-based to electric cars and buses. However, for some forms of transportation, such as aviation and freight ships, liquid based fuels might still be necessary, due to the advantages of their high energy density [4–7].

Fossil resources are not only used to produce energy, but also as feedstock for many materials society uses, as the entire chemical industry[8] and also the steel industry are based on them. Therefore, not only an energy transition is needed, but also a material or chemical feedstock transition is necessary. Due to the scale of this transition, many solutions are needed simultaneously, especially as climate change is only one of the parameters to stay within the planetary boundaries[9]. Besides improving plastic recycling and the use of biomass as feedstock, using CO_2 as feedstock [10,11] can give a vital contribution to make both the energy and material transition possible. More research is necessary [9] to improve technologies that use CO_2 as a feedstock to make these transitions possible and to turn CO_2 from a pollutant into a valuable resource.

1.2 Electrocatalysis

With the acceptance that climate change is one of the major issues of this time and that an energy transition is needed to stop climate change, electrocatalysis has gained more attention recently. While in thermocatalysis reactions are driven by temperature and pressure, in electrocatalysis the energy to drive a chemical

reaction is provided by electricity. This is interesting as the new renewable energy sources as wind and solar energy produce primarily electrical energy in contrast to the old fossil fuel energy sources which typically produce heat. Electrocatalysis is part of the broader field of electrochemistry, which is defined as the study of the transformation of electrical energy in chemical bonds and vice versa [12]. Electrochemistry is an old field as the first experiments generating hydrogen from electricity where conducted at the end of the 18th century, shortly afterward followed by the production of the first battery [13]. Besides electrocatalysis and batteries, the field also includes sensors such as glucose sensors, corrosion processes and electroplating techniques, for example to produce cans [12].

Catalysts are materials that enable or enhance a chemical reaction, by lowering the reaction barrier. Electrocatalysts use electricity to convert molecules as H_2O, CO_2 and N_2 into energy carriers or chemical building blocks such as hydrogen, CO, ethylene and ammonia. In general, electrocatalysts can be divided into homogeneous and heterogeneous catalysts. Homogeneous catalysts facilitate a redox reaction in the liquid phase[14]. This thesis only discusses heterogeneous catalysts, for which the electrochemical reaction takes place at the surface of the electrode, which is often a metal[14].

The electrochemical conversion is performed in a device known as an electrolyser. On the cathode material a reduction reaction takes place in which the electrode provides electrons to the reactants. On the anode material an oxidation reaction takes place in which electrons are transferred from the reactants to the electrode material. The oxidation and reduction reaction are performed simultaneously to complete the electrical circuit. For example, in a water electrolyser, H_2O is split into hydrogen on the cathode and oxygen on the anode according to the following half reactions:

$$2\,H_2O + 2e^- \rightarrow H_2 + 2\,OH^- \qquad (1.1)$$

$$2\,H_2O \rightarrow O_2 + 4\,H^+ + 4\,e^- \qquad (1.2)$$

$$2\,H_2O \rightarrow 2\,H_2 + O_2 \qquad (1.3)$$

The two half reactions in equation 1.1. and 1.2 are required to complete the total reaction given by equation 1.3. In an industrial electrolyser, the cathode and anode are the only two electrodes. However, our experiments in the lab are performed with a three electrode system to gain more fundamental understanding by studying one specific half reaction. In this configuration, the working electrode is the electrode that carries out the reaction of interest. The counter electrode completes the circuit and the reference electrode is used to determine the potential applied to the working electrode[15], as illustrated in Figure 1.1. In this thesis, the

cathode is always the working electrode, making the anode the counter electrode. We will discuss the reference electrode in more detail below. All electrodes are placed in the electrolyte. This is an electrically conducting medium and for electrocatalysis often consists of water with certain concentrations of salt. Throughout this thesis, common electrolytes are 0.1 M sodium bicarbonate or potassium bicarbonate. During electrolysis, the cathode and anode are often separated with a membrane, which prevents products to cross over to the other electrode and react there. The electrolyte at the cathode side is called the catholyte and the electrolyte on the anode side the anolyte.

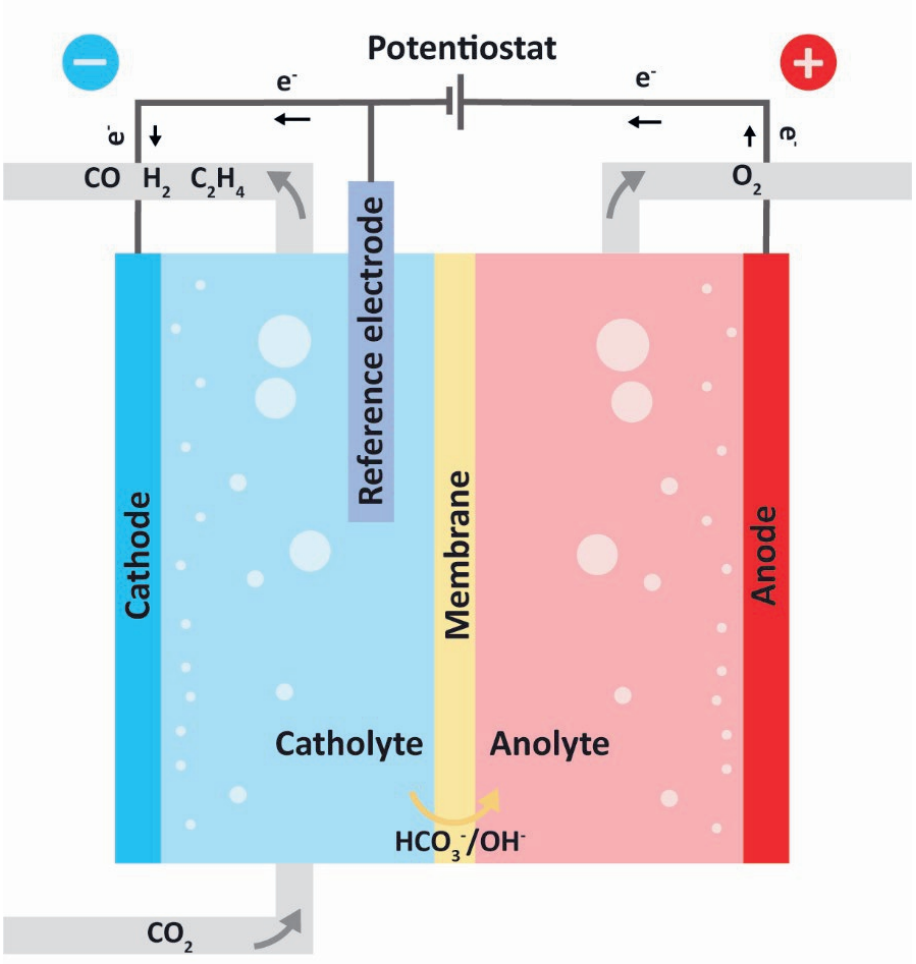

Figure 1.1 Pictorial representation of a three-electrode H-cell configuration for electrochemical CO_2 reduction where the cathode and anode are separated by an anion-exchange membrane

The potential at which a half reaction such as equation 1.1 is at thermodynamic equilibrium, is given by the Nernst equation:

$$E = E^0 - \frac{RT}{nF}\ln(Q) \qquad (1.4)$$

in which E is the potential, E^0 the standard equilibrium potential, R the gas constant, T the temperature, n the number of electrons transferred, F Faraday constant and Q the reaction quotient, which is derived from the activities of all electroactive species. Since the Nernst potential describes equilibrium, an additional potential needs to be applied to overcome several barriers and resistances, which is called the overpotential. Some of these barriers are due to the reaction and a good catalyst minimizes the overpotential needed to drive the reaction. Other resistances can come from the electrolyser design, such as the ohmic drop due to the resistance of the electrolyte. These losses can be minimized by design of the electrolyser and electrolyte, and by optimizing process parameters such as temperature. Fundamental electrocatalysis research focuses on understanding and optimizing the catalyst and its environment to minimize the overpotential needed, while electrochemical engineering focuses more on optimizing the process parameters and cell design.

1.3 Electrochemical CO_2 reduction

Since the seminal reports of the electrochemical CO_2 reduction reaction (CO2RR) by Hori et al. in the 80s of the last century [16–18], the interest for this reaction accelerated around the beginning of this century due to the urgency of climate change. Heterogeneous CO2RR catalysts are generally classified in four groups [19,20]. Au, Ag and Zn produce mainly CO from CO_2, while Pb, Sn, In, Cd, Hg and Tl produce mainly HCOOH via reaction 1.5 and 1.6, respectively. CO can be used in syngas as an important chemical precursor for numerous reactions such as to produce hydrocarbons via the Fischer-Tropsch reaction[21] or to produce methanol in the methanol synthesis process[22]. HCOOH can be used as fuel[23] or hydrogen carrier[24] although it is nowadays mostly used as intermediate or additive in industrial applications[25]. Cu is a unique catalyst for electrochemical CO_2 reduction as it can go beyond these simple C1 products and make C2+ products in which a C-C bond is generated. Products can be ethylene and ethanol, as given in equations 1.7 and 1.8, but Cu can form a scala of other products such as methanol, 1-propanol and acetate [26]. Some of these products are of particular interest within the material and energy transition as they can be used as fuel (methanol/ethanol) or as feedstock for the chemical industry (ethylene). The last group of CO2RR catalysts, such as Pt, Fe and Ni, is not very active in CO_2 reduction but rather produces H_2 via the competing hydrogen evolution reaction (HER) in equation 1.1. HER is active in a comparable

potential region to CO2RR, so for active and selective CO2RR catalysts, HER always needs to be minimized.

$$CO_2 + H_2O + 2\,e^- \rightarrow CO + 2\,OH^- \quad (1.5)$$

$$CO_2 + 2\,H_2O + 2\,e^- \rightarrow HCOOH + 2\,OH^- \quad (1.6)$$

$$2\,CO_2 + 8\,H_2O + 12\,e^- \rightarrow C_2H_4 + 12\,OH^- \quad (1.7)$$

$$2CO_2 + 9\,H_2O + 12\,e^- \rightarrow C_2H_5OH + 12\,OH^- \quad (1.8)$$

A good CO2RR catalysts needs to be active, meaning the current density that goes towards CO2RR products such as CO and HCOOH is high and the overpotential is minimized. Moreover, the catalyst needs to be selective. This means that the competing HER should be minimized, which is difficult on many catalyst materials. As Cu can produce many different products, selectivity in this case also means that the Cu catalyst produces primarily one of the possible CO2RR products, which has shown especially challenging due to the complex reaction network. Lastly, for commercialization, a good catalyst should be stable and be able to operate for thousands of hours [27–30]. Many parameters have been studied in recent years to improve the CO2RR catalysts on all these aspects. Some parameters are related to the catalysts itself, such as the facet dependence [31–34], morphology [35–39], alloying [40–44] and surface modifications [45–50], while others are related to the environment of the catalyst, primarily the electrolyte, such as cations [51–54], anions [55–58], pH [59–63] and electrolyte concentration [64–66]. These studies are often performed on small scales, but when moving towards industrialization, other parameters become important as well, such as cell configuration, temperature and pressure.

Electrochemical CO_2 reduction is typically performed in neutral aqueous media. Acidic electrolytes are avoided as they enhance hydrogen evolution, although recently more studies have been performed at low pH with promising results [67–70]. Alkaline electrolytes are avoided in studies using a H-type cell as the OH^- would react with the CO_2 forming bicarbonate. With the use of gas diffusion electrodes, the CO_2 gas is not bubbled through the electrolyte, and alkaline electrolytes are commonly used [71–74]. In this thesis, all experiments are performed using a H-type cell and thus neutral bicarbonate electrolytes are used. Moreover, as we are interested in the performance of the catalyst and not the entire electrolyser, a three electrode system is used in combination with IR correction to overcome the Ohmic losses of the electrolyte. Furthermore, simple metal foils and wires are typically used as working electrodes to limit the complexity of the system studied. Electrochemistry in general and CO2RR specifically are typically performed at ambient conditions, as this is often seen as one of the advantages of electrocatalysis over thermocatalysis. However, for industrialization [75–77], this might not be the most

suitable condition as electrolytes are expected to heat up due to thermal losses [78–80] and warm feedstocks, and higher temperatures can lower the overall cell potential [76,77]. Therefore, it is important to fundamentally investigate the effect of temperature and pressure on the electrochemical CO_2 reaction.

1.4 Temperature as parameter in electrochemistry

Thermoelectrochemistry is "the branch of electrochemistry which is devoted to the influence of temperature as an independent variable on the charge transfer reaction at condensed interfaces" as defined by Gründler et al.[81]. Within electrocatalysis, there are some studies on the effect of temperature and pressure on several reactions, such as the hydrogen evolution reaction [76,82–84], oxygen evolution reaction [85–88], oxygen reduction reaction [89–91] and CO_2 reduction reaction [17,92–95]. However, temperature and also pressure are still very understudied parameters in electrocatalysis and systematic studies are scarce.

When pressure and especially temperature are changed in electrochemical systems, several factors have to be considered. As seen in equation 1.4, the potential of a reaction is dependent on the temperature, especially as besides the explicit T in the Nernst equation also the standard potential and activities are dependent on temperature. This is important to consider when measuring a potential as also the reference electrode potential depends on temperature [81,96]. In thermo-electrochemistry, an external reference electrode can be used , where the reference electrode operates at room temperature and is connected to the electrolyser with an electrolyte bridge [96]. However, due to the difference in temperature, the external references experience a thermal liquid junction potential [81], for which an empirical correction has to be made to determine the potential precisely [96,97]. Therefore, we use internal reference electrodes in this thesis. Internal reference electrodes are used at the same temperature and pressure as the rest of the electrochemical system and the effect of temperature can be calculated with the Nernst equation (1.4). As SHE is defined 0 at all temperatures,[81,97] the RHE is the most easy internal reference electrode to use. At ambient pressures we therefore us this reference electrode in this thesis. However, at elevated pressures, a Ag/AgCl reference had to be used and more corrections have to be made to compare results on an SHE scale.

Temperature and pressure influence many other parameters of the electrochemical system. During CO_2 reduction, an important one is the CO_2 solubility, which decreases with increasing temperature. This can significantly influence the catalytic reaction as many CO2RR catalysts are sensitive to the bulk concentration of CO_2. As the CO_2 pressure also influences its solubility, it is possible to gain more insights with partial pressure experiments, by deconvoluting the direct effect of temperature with the indirect effect via the CO_2 solubility. Other

parameters that are influenced by the temperature are the pH, diffusion coefficients and viscosity [81] which can influence the reaction itself, the reference potential and the mass transport during the reaction. Most importantly for catalysis, temperature influences the kinetics of the reaction via the Arrhenius equation, where k is the rate constant, A the pre-exponential factor, E_a the activation energy, R the gas constant and T the temperature:

$$k = A\, e^{-\frac{E_a}{RT}} \qquad (1.9)$$

1.5 Outline of this thesis

The main goal of this thesis is to study the effect of temperature on the electrochemical CO_2 reduction. We start this study at ambient pressures on several different heterogeneous electrocatalysts. Simultaneously, we have developed a high-pressure, high-temperature electrochemical setup which allows us to study the effect of temperature at elevated pressures, which is discussed in the second part of this thesis.

Chapter 2 discusses the effect of temperature on the CO2RR on Au using a rotating-ring disk electrode (RRDE) system. Au was chosen as first electrocatalyst to study as it is a relatively simple system which produces only CO and H_2. We show that temperature can enhance both the activity and selectivity for the CO2RR although an optimum is observed at intermediate temperature (ca. 50 °C) and at high temperatures the selectivity decreases again. In **Chapter 3**, we move on to a more complex catalyst namely Cu. Cu produces a great variety of CO2RR products, the formation of which behave differently with temperature. Methane and formate selectivity decrease with temperature, while ethylene and ethanol show an optimum around 48 °C. This optimum divides the temperature effect in two regimes. In the first regime up to 48 °C, C2+ activity and selectivity increases with temperature and HER selectivity remains stable. We contribute this to a combination of kinetics, local pH and CO coverage. In the second regime after 48 °C, C2+ selectivity decreases and HER starts to dominate. This is contributed to a too high local pH in combination with a changing Cu surface. In **Chapter 4** we try to improve the Cu catalyst at high temperatures and inhibit HER by alloying Cu with Ag. We show that HER can indeed be inhibited at high temperatures, although the optimum in C2+ products is still observed. Moreover, we study the effect of temperature on Ag itself and compare this to results of Au from Chapter 2. We observe that mass transport and the applied potential are important other parameters influencing the temperature effect, which is also convoluted with the effect of CO_2 solubility.

Chapter 5 studies the electrochemical CO2 reduction on Ni. Even though Ni is not a very active CO2RR catalyst, it is interesting to study as it makes C-C bonds via a chain-growth mechanism, in contrast to the CO dimerization mechanism on Cu. We show the effect of temperature, partial pressure, potential and electrolyte composition on the activity and chain-growth probability.

Chapter 6 discusses the development of the high-pressure, high-temperature setup. As a proof of concept, we show the effect of temperature and pressure on the CO2RR on Au. At ambient pressures similar results are obtained as in Chapter 2, but at higher pressures the optimum in FE towards CO with temperature vanishes. Temperature and pressure then have no significant effect on the selectivity anymore, but still enhance the activity significantly. **Chapter 7** follows the sequence of the beginning of the thesis where a study using Au electrodes is followed by a study using Cu electrodes. We show that temperature influences the selectivity more significantly than pressure. Most interestingly, at very high temperatures, above 100 °C, the C-C coupling mechanism changes from the CO dimerization mechanism to the chain-growth mechanism observed for Ni in Chapter 5. Moreover, we show that elevated CO_2 pressures can stabilize the Cu and increase the temperature range in which high C2+ selectivity can be reached in the dimerization mechanism.

The electrode categorization discussed in section 1.3 is based on experiments at ambient temperatures. To see if this categorization is still valid and to observe the effect of pressure and temperature on the CO2RR on various electrodes, we performed a catalyst screening study in **Chapter 8**, where we study 20 metals at elevated temperatures and pressures. We show that elevated pressures inhibit HER significantly and turn reasonable CO2RR catalysts into excellent catalysts with more than 90% FE for CO2RR, which can be maintained even at 100 °C. However, when a catalyst produces mostly H_2 at ambient conditions, it does not become a good catalyst at elevated pressures, although some metals can produce interesting products such as methanol and long chain hydrocarbons, but in (very) low quantities.

References

1. Carbon Dioxide. *https://climate.nasa.gov/vital-signs/carbon-dioxide/?intent=121* (2024).
2. Ritchie, H., Rosado, P. & Roser, M. Cumulative CO_2 emissions. *https://ourworldindata.org/grapher/cumulative-co-emissions* (2023).
3. Intergovernmental Panel on Climate Change. *Climate Change 2022 – Impacts, Adaptation and Vulnerability: Working Group II Contribution to the Sixth Assessment Report of the Intergovernmental Panel on Climate Change*. (2023)
4. Gray, N., McDonagh, S., O'Shea, R., Smyth, B. & Murphy, J. D. *Advances in Applied Energy* 1 (2021).
5. Su-ungkavatin, P., Tiruta-Barna, L. & Hamelin, L. *Progress in Energy and Combustion Science* 96 (2023).
6. Rojas-Michaga, M. F. *et al. Energy Convers Manag* **292**, (2023).
7. Xing, H., Stuart, C., Spence, S. & Chen, H. *J Clean Prod* **297**, (2021).
8. Kätelhön, A., Meys, R., Deutz, S., Suh, S. & Bardow, *Proc Natl Acad Sci U S A* **166**, 11187–11194 (2019).
9. Bachmann, M. *et al. Nat Sustain* **6**, 599–610 (2023).
10. Meys, R. *et al. Science (1979)* **374**, 71–76 (2021).
11. Bachmann, M. *et al. Faraday Discuss* **230**, 227–246 (2021).
12. Bard, A. J. & Faulkner, L. R. *Electronchemical Methods*. (John Wiley & Sons, 2001).
13. Smolinka, T., Bergmann, H., Garche, J. & Kusnezoff, M. Chapter 4 - The history of water electrolysis from its beginnings to the present. in *Electrochemical Power Sources: Fundamentals, Systems, and Applications* (eds. Smolinka, T. & Garche, J.) 83–164 (Elsevier, 2022).
14. Hanefeld, U. & Lefferts, L. *Catalysis*. (Wiley-VCH, 2018).
15. Elgrishi, N. *et al. Chem Educ* **95**, 197–206 (2018).
16. Hori, Y., Kikuchi, K. & Suzuki, S. *Chem Lett* **14**, 1695–1698 (1985).
17. Hori, Y., Kikuchi, K., Murata, A. & Suzuki, S. *Chem Lett* **15**, 897–898 (1986).
18. Hori, Y., Murata, A., Kikuchi, K. & Suzuki, S. *J. CHEM. SOC., CHEM. COMMUN* 728–729 (1987).
19. Hori, Y., Wakebe, H., Tsukamoto, T. & Koga, O. *Electrochim Acta* **39**, 1833–1839 (1994).
20. Bagger, A., Ju, W., Varela, A. S., Strasser, P. & Rossmeisl, J. *ChemPhysChem* **18**, 3266–3273 (2017).
21. Chae, H. J. *et al Catalysts* 10 (2020).
22. Bozzano, G. & Manenti, F. *Prog Energy Combust Sci* **56**, 71–105 (2016).
23. Zhang, C. *et al. Angewandte Chemie - International Edition* **63**, (2024).
24. Eppinger, J. & Huang, K. W. *ACS Energy Letters* 2 188–195 (2017).
25. Agarwal, A. S., Zhai, Y., Hill, D. & Sridhar, N. *ChemSusChem* **4**, 1301–1310 (2011).
26. Kuhl, K. P., Cave, E. R., Abram, D. N. & Jaramillo, T. F. *Energy Environ Sci* **5**, 7050–7059 (2012).
27. Martín, A. J., Larrazábal, G. O. & Pérez-Ramírez, J. *Green Chemistry* 17 5114–5130 (2015).

28. Schmidt, O. *et al. Int J Hydrogen Energy* **42**, 30470–30492 (2017).
29. Xu, D. *et al.*. *Carbon Energy* 5 (2023).
30. Rumayor, M., Dominguez-Ramos, A., Perez, P. & Irabien, A.. *Journal of CO2 Utilization* **34**, 490–499 (2019).
31. Schouten, K. J. P., Pérez Gallent, E. & Koper, M. T. M. *ACS Catal* **3**, 1292–1295 (2013).
32. Todoroki, N. *et al. ACS Catal* **9**, 1383–1388 (2019).
33. Clark, E. L. *et al. ACS Catal* **9**, 4006–4014 (2019).
34. Zhu, C. *et al. Chem* **7**, 406–420 (2021).
35. da Silva, A. H. M. *et al. Journal of Electroanalytical Chemistry* **880**, (2021).
36. Jiang, K. *et al. ACS Energy Lett* **5**, 1206–1214 (2020).
37. Lum, Y., Yue, B., Lobaccaro, P., Bell, A. T. & Ager, J. W. *Journal of Physical Chemistry C* **121**, 14191–14203 (2017).
38. Kim, H., Park, H. S., Hwang, Y. J. & Min, B. K. *Journal of Physical Chemistry C* **121**, 22637–22643 (2017).
39. Dutta, A., Rahaman, M., Luedi, N. C., Mohos, M. & Broekmann, P. *ACS Catal* **6**, 3804–3814 (2016).
40. Jia, Y., Li, F., Fan, K. & Sun, L. *Advanced Powder Materials* 1 (2022).
41. Li, J., Halldin Stenlid, J., Tang, M. T., Peng, H. J. & Abild-Pedersen, F. *J Mater Chem A Mater* **10**, 16171–16181 (2022).
42. Zhi, X., Jiao, Y., Zheng, Y., Vasileff, A. & Qiao, S. Z. *Nano Energy* **71**, (2020).
43. Zhu, C. *et al*. *Small Struct* **4**, (2023).
44. Ren, W. *et al. Nat Commun* **12**, (2021).
45. Wagner, A., Sahm, C. D. & Reisner, E. *Nature Catalysis* 3 775–786 (2020).
46. Li, C. *et al. ACS Catal* **13**, 16114–16125 (2023).
47. Fan, L. *et al. Joule* **6**, 205–220 (2022).
48. Wang, M. *et al*. *ACS Nano* (2024)
49. Cheng, B. *et al. ACS Appl Mater Interfaces* **14**, 27823–27832 (2022).
50. Wang, J. *et al. J Am Chem Soc* **143**, 2857–2865 (2021).
51. Ringe, S. *et al. Energy Environ Sci* 17–25 (2019) doi:10.1039/c9ee01341e.
52. Resasco, J. *et al. J Am Chem Soc* **139**, 11277–11287 (2017).
53. Monteiro, M. C. O., Dattila, F., López, N. & Koper, M. T. M. *J Am Chem Soc* **144**, 1589–1602 (2022).
54. Monteiro, M. C. O. *et al. Nat Catal* **4**, 654–662 (2021).
55. Huang, Y., Ong, C. W. & Yeo, B. S. *ChemSusChem* **11**, 3299–3306 (2018).
56. Resasco, J., Lum, Y., Clark, E., Zeledon, J. Z. & Bell, A. T. *ChemElectroChem* **5**, 1064–1072 (2018).
57. Ovalle, V. J. & Waegele, M. M. *Journal of Physical Chemistry C* **124**, 14713–14721 (2020).
58. Casebolt, R. *et al*. *ChemElectroChem* **8**, 681–688 (2021).
59. Varela, A. S. *Curr Opin Green Sustain Chem* **26**, 100371 (2020).
60. Narayanaru, S., Chinnaiah, J., Phani, K. L. & Scholz, F. *Electrochim Acta* **264**, 269–274 (2018).
61. Liu, X. *et al. Nat Commun* **10**, 32 (2019).
62. Jiang, X., Li, H., Yang, Y. & Gao, D. *J Mater Sci* **55**, 13916–13926 (2020).

63. Schouten, K. J. P., Pérez Gallent, E. & Koper, M. T. M. *Journal of Electroanalytical Chemistry* **716**, 53–57 (2014).
64. Varela, A. S., Kroschel, M., Reier, T. & Strasser, P. *Catal Today* **260**, 8–13 (2016).
65. Kas, R., Kortlever, R., Yılmaz, H., Koper, M. T. M. & Mul, G. *ChemElectroChem* **2**, 354–358 (2015).
66. Singh, M. R., Clark, E. L. & Bell, A. T. *Physical Chemistry Chemical Physics* **17**, 18924–18936 (2015).
67. Bondue, C. J., Graf, M., Goyal, A. & Koper, M. T. M. *J Am Chem Soc* **143**, 279–285 (2021).
68. Erick Huang, J. *et al. Science* **273**, 1074–1078 (2021).
69. Gu, J. *et al*. *Nat Catal* **5**, 268–276 (2022).
70. Xie, Y. *et al. Nat Catal* **5**, 564–570 (2022).
71. Chen, C., Li, Y. & Yang, P. *Joule* **5**, 737–742 (2021).
72. Dolmanan, S. Bin *et al. J Mater Chem A Mater* **11**, 13493–13501 (2023).
73. Chen, L. *et al. ACS Catal* **13**, 11934–11944 (2023).
74. Chen, X. *et al. ACS Catal* **10**, 672–682 (2020).
75. Krause, R. *et al. Chemie Ingenieur Technik* **92**, 53–61 (2020).
76. Lei, H., Wan, Q., Tan, S., Wang, Z. & Mai, W. *Advanced Materials* **35**, (2023).
77. Liu, X. *et al.*. *Advanced Materials* **32**, (2020).
78. Lobaccaro, P. *et al. Physical Chemistry Chemical Physics* **18**, 26777–26785 (2016).
79. Corral, D. *et al. Energy Environ Sci* **14**, 3064–3074 (2021).
80. Iglesias Van Montfort, H. P. & Burdyny, T. *ACS Energy Lett* **7**, 2410–2419 (2022).
81. Gründler, P., Kirbs, A. & Dunsch, L. *ChemPhysChem* **10**, 1722–1746 (2009).
82. Tang, Z. Q., Liao, L. W., Zheng, Y. L., Kang, J. & Chen, Y. X. *Chinese Journal of Chemical Physics* **25**, 469–474 (2012).
83. Stühmeier, B. M., Pietsch, M. R., Schwämmlein, J. N. & Gasteiger, H. A. *J Electrochem Soc* **168**, 064516 (2021).
84. Zeradjanin, A. R., Narangoda, P., Masa, J. & Schlögl, R. *ACS Catal* **12**, 11597–11605 (2022).
85. Shi, G. *et al. ACS Catal* **12**, 14209–14219 (2022).
86. Govind Rajan, A., Martirez, J. M. P. & Carter, E. A. *ACS Catal* **11**, 11305–11319 (2021).
87. Liu, X. *et al. Advanced Materials* **32**, (2020).
88. Abdelghafar, F., Xu, X., Jiang, S. P. & Shao, Z. *ChemSusChem* (2024).
89. Liu, B. Y., Chen, W., Ye, X. X., Cai, J. & Chen, Y. X. *Journal of Chemical Physics* **158**, (2023).
90. Đukić, T. *et al.*. *ACS Catal* **12**, 101–115 (2022).
91. Zhu, Z., Liu, Q., Liu, X. & Shui, J. *Journal of Physical Chemistry C* **124**, 3069–3079 (2020).
92. Mizuno, T. *et al. Energy Sources* **17**, 503–508 (1995).
93. Löwe, A. *et al*. *ChemElectroChem* **6**, 4497–4506 (2019).
94. Ahn, S. T., Abu-baker, I. & Palmore, G. T. R. *Catal Today* **288**, 24–29 (2017).
95. Dufek, E. J., Lister, T. E., Stone, S. G. & McIlwain, M. E. *J Electrochem Soc* **159**, F514–F517 (2012).

96. Wildgoose, G. G., Giovanelli, D., Lawrence, N. S. & Compton, R. G. *Electroanalysis* 16 421–433 (2004).
97. Bosch, R. W., Bogaerts, W. F. & Zheng, J. H. *CORROSION SCIENCE SECTION* 162 (2003).

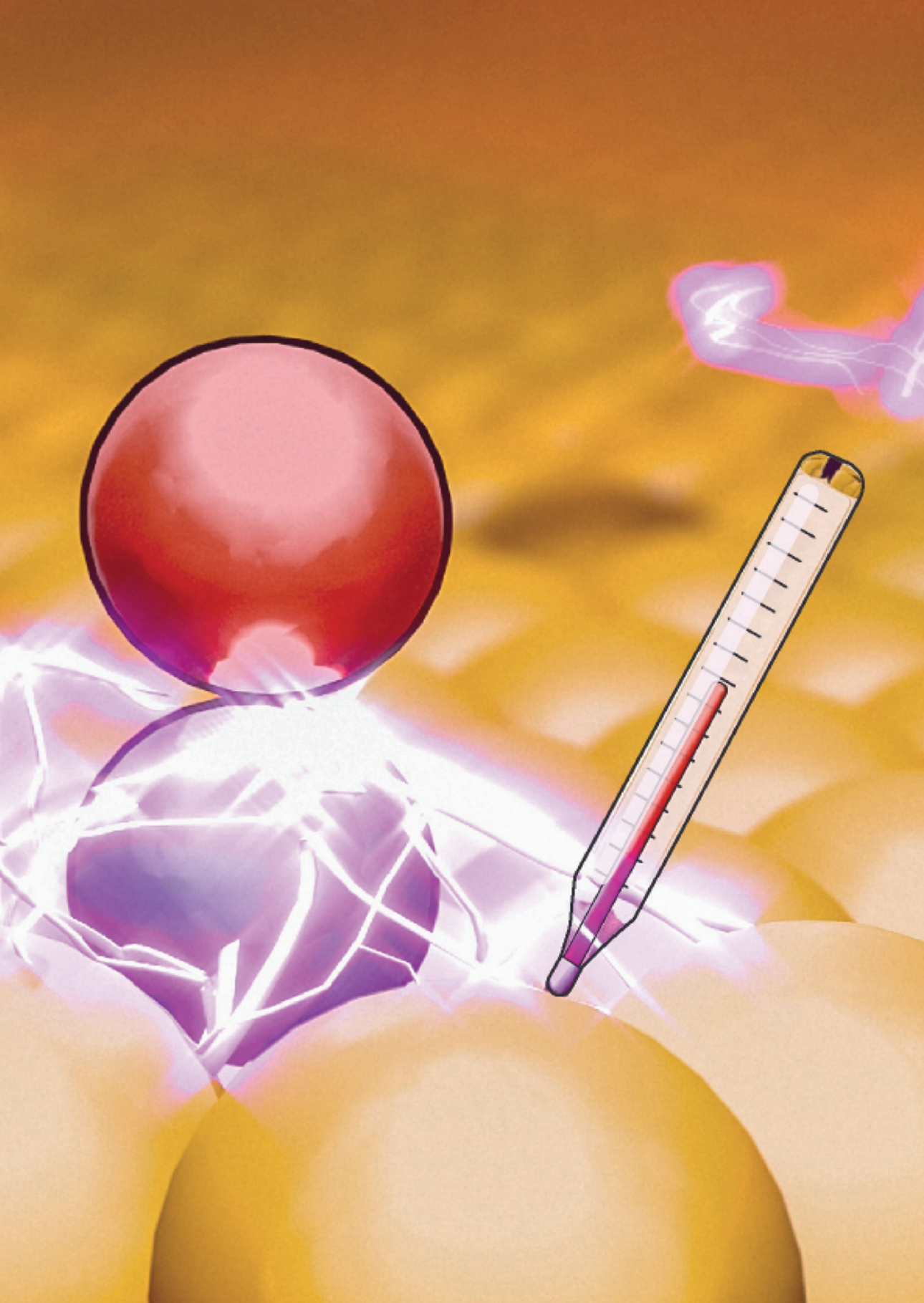

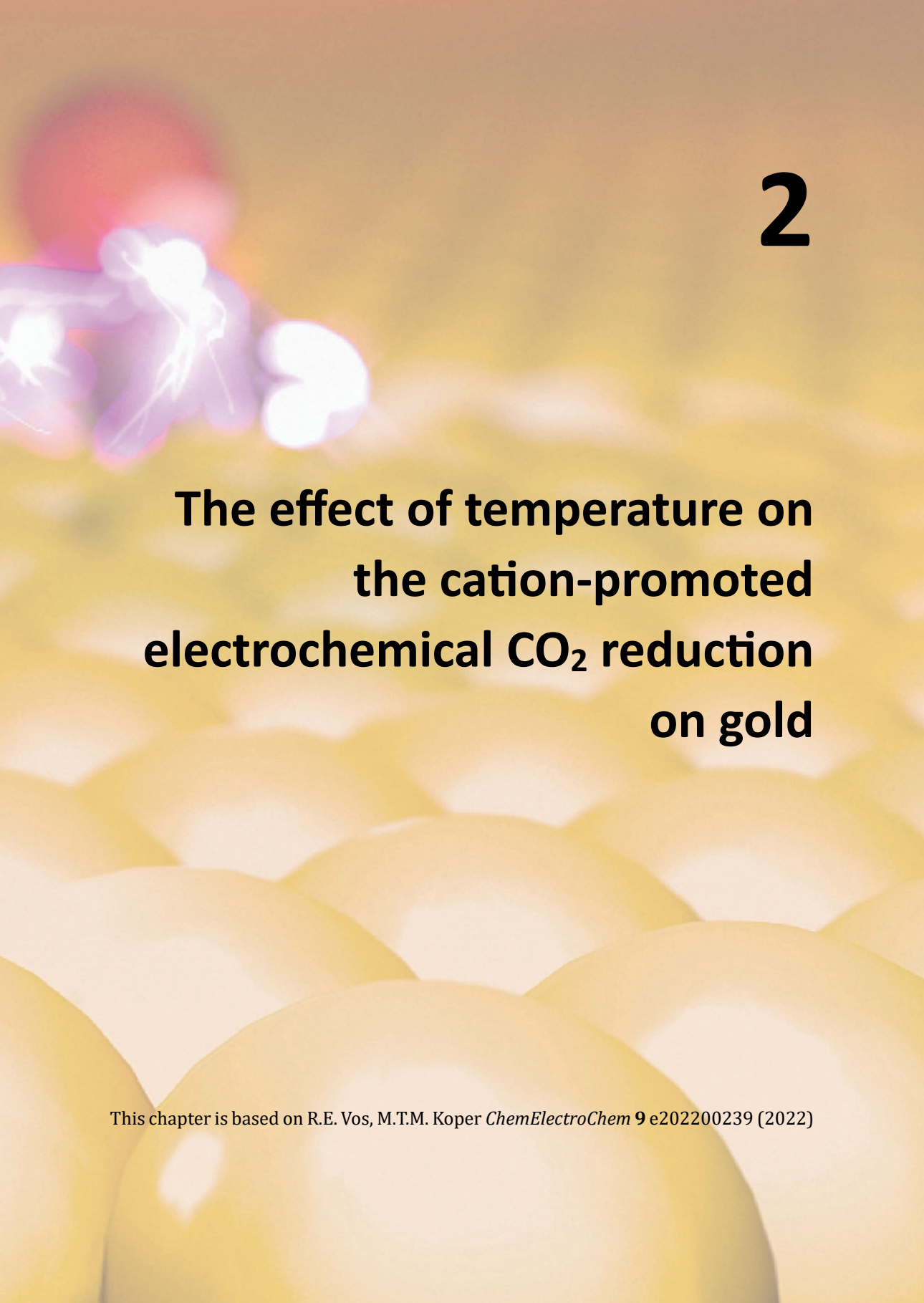

2

The effect of temperature on the cation-promoted electrochemical CO_2 reduction on gold

This chapter is based on R.E. Vos, M.T.M. Koper *ChemElectroChem* **9** e202200239 (2022)

Abstract:

Electrochemical reactions in general, and the CO_2 reduction reaction (CO2RR) in particular, are commonly studied at room temperature. However, practical electrolysers may use elevated temperatures. There is currently a lack of fundamental understanding of the effect of temperature on the CO2RR. Here, we have performed temperature-dependent studies on the CO2RR on a relatively simple electrode material, namely gold, to obtain insights into how temperature influences this reaction and the competing hydrogen evolution reaction. A rotating ring disk electrode setup has been used to show that the CO2RR activity and selectivity increases with temperature, and to obtain kinetic parameters such as the apparent activation energy and transfer coefficient. The magnitude of the temperature effect and the activation energy is affected by both the cation identity and concentration in the electrolyte. Moreover, the positive effect of temperature on the kinetics of the CO2RR is counteracted by the lower CO_2 solubility, making efficient mass transport even more important at higher temperatures.

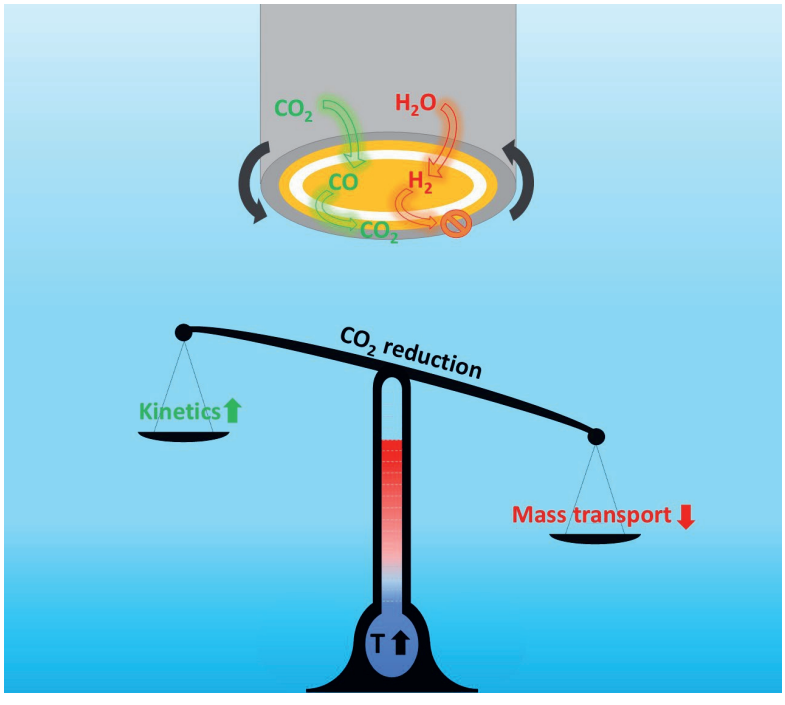

2.1 Introduction

Electrochemical CO_2 reduction (CO2RR) has the potential to generate clean fuels and building blocks for the chemical industry with CO_2, water and renewable energy, thereby creating a closed carbon cycle without the use of fossil fuels. This reaction has gained substantial attention and many aspects of CO_2 reduction have been studied,[1,2] such as catalyst material and the effect of the electrolyte. Electrolyte properties ranging from pH,[3–7] buffer capacity,[8–10] cations,[11–14] and anions,[15,16] to catalyst properties such as the facet,[17–20] defects,[21,22] morphology[23–25] and roughness, [4,26,27] have all been shown to influence the activity and selectivity for the CO2RR and the competing hydrogen evolution reaction (HER).

An aspect which has been studied less is the effect of temperature on CO_2 reduction. Most electrochemical experiments have been performed at room temperature and ambient pressure, even though most industrial (water) electrolyzers work at slightly elevated temperatures.[28–32] Some degree of heating is intrinsic to these industrial systems as they are the consequence of overpotentials and resistive losses.[32,33] Moreover, the sources of concentrated CO_2, for example from electricity production or steel manufacturing, often emit hot CO_2. The temperature during the electrochemical CO2RR could also be deliberately increased to increase activity and selectivity or to open up new mechanisms and generate other products.

Although some studies do include a section with temperature dependent experiments,[34–37] there are not many systematic studies on the effect of temperature on the CO2RR.[1,38] Systematic studies are important to elucidate how temperature exactly influences the reaction, as various aspects of the system may change with changing temperature. One of the most important changes is the solubility of CO_2, which decreases with increasing temperature. This results in a change in pH, which will also change due to the difference in acid-base equilibria such as the water disproportionation at different temperatures. Furthermore, reaction rates, diffusion coefficients, equilibrium potentials, and the conductivity of solution and membranes all change with temperature.

One of the few systematic studies on the effect of temperature on CO_2 reduction has been done by Ahn et al.[39] They studied a Cu electrode at -1.60 V vs Ag/AgCl at temperatures from 2 to 42 ^{0}C in a 0.1M $KHCO_3$ electrolyte. They showed that methane is the dominant product at low temperatures, but the faradaic efficiency (FE) decreases with increasing temperature. For ethylene, there seems to be an optimum in the FE at medium temperatures. At the highest temperature, 42 ^{0}C in the mentioned study, the system is dominated by the parasitic hydrogen evolution.

They attributed these observations to the combined effect of CO_2 solubility and local pH. These results are mostly in agreement with experiments by Hori et al., [40] although they did not see an optimum in ethylene production in this temperature range.

Most studies on the effect of temperature on the CO2RR are not performed in a H-cell, but in a GDE (Gas Diffusion Electrode) setup. Dufek et al.[31] studied an Ag GDE at 18, 35 and 70 ^{0}C in a 0.5 M K_2SO_4 electrolyte. They observed a decrease in both cell and cathodic potential with increasing temperature. This decrease is not surprising as the conductivity of both the electrolyte and the membrane will increase with increasing temperature, lowering the ohmic drop. Moreover, they observed that the FE for CO increases at higher current densities when the temperature goes from 18 to 35 ^{0}C, but decreases again at 70 ^{0}C. In terms of activity, a plateau is observed for CO formation. The activity first increases from 18 to 35 ^{0}C and remains the same for 35 and 70 ^{0}C. This plateau was associated with mass transport limitations of CO_2.

Löwe et al.[41] used a Sn GDE and observed a decrease in the required potential at higher temperatures, similar to Dufek et al. [31] This resulted in a small shift in product distribution from HCOOH to CO. When CO_2 becomes mass transport limited, they noticed an increase in HER. With increasing the temperature from 25 ^{0}C to 50 ^{0}C, they observed an increase in the potential at which this happens, but a further increase of the temperature to 70 ^{0}C resulted in the reverse trend. This optimum was attributed to the interplay of the diffusion rate which increases with temperature and the CO_2 solubility which decreases with temperature. In summary, all mentioned studies observed effects at elevated temperatures which are assumed to be an indirect effect of temperature on the mass transport limitation. The intrinsic effect of temperature on the CO_2 reduction reaction rate is concealed by these indirect effects.

An aspect of CO_2 reduction that has recently been studied in some detail is the cation effect. It has been shown that the activity of the CO2RR is significantly influenced by the nature of the cation. An activity trend $Cs^+ > K^+ > Na^+ > Li^+$ has been observed at several electrode materials,[12,42–44] whereas on Cu the

selectivity towards C2+ products also increases in this order.[12,13] There are three main theories proposed to explain this cation effect.[45] Some studies attribute the cation effect to differences in the local pH,[13,46,47] where Cs^+ buffers better than Li^+. Other explanations focus on the effect of the electric field, which changes with the size of the cation. This electric field then either stabilizes intermediates [12,14,48] or changes the local potential in the outer Helmholtz layer.[11] Besides the electric field,

also short-range electrostatic interactions can help stabilize the intermediates. [48] However, the cation effect has not been studied yet in combination with varying temperature.

In this study, we systematically studied the effect of temperature on CO_2 reduction. We used Au as a catalyst to simplify the system as only CO and H_2 are produced in significant amounts.[49–51] We performed partial pressure experiments to study the effect of temperature and CO_2 solubility independently. A rotating ring disk electrode (RRDE) setup was used to deconvolute the current to the CO2RR and the HER,[52] and to control and improve mass transport. With a diffusion layer thickness in the range of 1µm,[53] the RRDE allows for a better study of the intrinsic catalytic activity of the electrochemical reduction processes. We show that both activity and selectivity of CO_2 reduction are increased with temperature, although there is a complex balance between the effect of increased kinetics and decreasing CO_2 concentration. Furthermore, we extract kinetic data such as the transfer coefficient and the apparent activation energy. We show that the latter is influenced by the cation and that therefore the magnitude of the temperature effect depends on the electrolyte used.

2.2 Experimental Section

2.2.1 Chemicals

The electrolytes were prepared from H_2SO_4 (98%, EMSURE, Merck), $NaHCO_3$ (≥99.7%, Sigma Aldrich), Li_2CO_3 (99.997%, Sigma Aldrich), $KHCO_3$ (99.95%, Sigma Aldrich), $CsHCO_3$ (99.99%, Alfa Aesar), $NaClO_4$ *H_2O (Emsure, Merck) and Milli-Q water (≥18.2 MΩcm, TOC < 5 ppb). Ar (6.0 purity, Linde), CO_2 (4.5 purity, Linde), and H_2 (5.0 purity, Linde) were used for purging the electrolytes. For the dopamine modification, the RRDE tip was coated using dopamine hydrochloride (≥98.5%, Sigma-Aldrich). To determine the collection efficiency, $K_3Fe(CN)_6$ (>99%, Sigma-Aldrich) was used.

2.2.2 General Electrochemical Methods

All experiments were performed using homemade borosilicate glass cells, which were cleaned prior to experiments by storing the cells in an acidified (0.5 M H_2SO_4) $KMnO_4$ solution (1 g/L) overnight. Before experiments, the glassware was submerged in diluted piranha to remove any traces of MnO_4 and MnO_2. Then the cells were boiled at least three times with MilliQ water. Experiments were performed in a three-electrode configuration where the reference electrode was separated from the working compartment with a Luggin capillary. The reference electrode was either a home-made RHE or, for the temperature-dependent

measurements, a commercial RHE from Gaskatel, which was placed in the cell to be at the same temperature as the working electrode. The counter electrode was a gold wire (99.99% purity). The working electrode was a gold disk in a PEEK shroud with gold ring (E6/E5 ChangeDisk tips, Pine research) and the RRDE measurements were performed with a Modular Speed Rotator (Pine research). All the electrochemical measurements were carried out using an IviumStat bipotentiostat (Ivium Technologies). For the activity measurements, 85% ohmic drop compensation was performed. The ohmic drop was determined by electrochemical impedance spectroscopy (EIS) at 0.05 V vs RHE. Before experiments, the electrolytes were purged with either Ar or CO_2 for at least 15 minutes and purging continued during measurements. To control the temperature a water bath was used (Ecoline e100, Lauda). For the partial pressure experiments, the flow of CO_2 and Ar was set accordingly using two mass flow controllers (SLA5850, Brooks Instrument).

2.2.3 Working Electrode Preparation and Dopamine Modification

The RRDE method used in this study has been developed in our group and described in detail in a previous publication.[52] In this study, we slightly modified some steps. Before each experiment, the gold disk (diameter = 5 mm, Pine Instruments) was mounted in the RRDE tip which contained a gold ring. The tip was mechanically polished with decreasing diamond polishing suspension (3.0, 1.0 and 0.25 μm) on Buehler micropolishing cloths (8 in.). After polishing, the tip was successively sonicated in ethanol and water for 3 min to remove any impurities. Next, the Au disk and ring were short-circuited and electrochemically polished in 0.1 M H_2SO_4 by cycling into the Au oxide formation and reduction region (0.05 – 1.7 V vs RHE, 200 cycles at 1 V/s). A characterization cyclic voltammogram (CV) of the ring and disk was obtained in this same potential window at a scan rate of 50 mV/s. Next, the RRDE tip was modified by coating with dopamine to prevent bubble attachment on the Teflon spacer between the disk and the ring of the RRDE tip.[54] This bubble attachment leads to noise in the CO oxidation current on the ring. The dopamine modification was performed by immersing the RRDE tip in a 2 g/L solution of dopamine hydrochloride (prepared with 20 mL of bicarbonate electrolyte). This was done for 1 hour at about 55 ^{0}C, while the RRDE was rotated at 450 rotations per minute (rpm). After the coating, any dopamine on the ring and the disk had to be removed. This was done by electrochemical polishing in 0.1M H_2SO_4 once again for 200 cycles. Next, 75 cycles were performed in the same potential range but in the measurement cell with CO_2 saturated bicarbonate solution. This was followed by a reduction going to -1.0 V vs RHE at 50 mV/s for 3 cycles in the measurement cell and a polishing step in H_2SO_4 for 100 cycles. Then, a characterization CV was obtained for the ring and disk, which was compared with the CV of the unmodified surface. A good agreement between these CVs indicated

that the surface morphology had not changed significantly during the coating procedure and that any dopamine was removed from the ring and disk.

2.2.4 RRDE CO_2 reduction measurements

After the working electrode was prepared as described above, the CO2RR measurements were performed in the measurement cell with a CO_2 saturated 0.1 M bicarbonate electrolyte. This measurement cell was placed in a water bath to control the temperature in the cell. For the measurements, the disk was cycled from 0.05 to -1.0 V vs RHE in a bicarbonate electrolyte with a scan rate of 20 mV/s. The ring current was measured simultaneously, while the ring potential was set to 1.0 V vs RHE. The measurements were performed with two different rotation speeds, namely 1200 and 2500 rpm. At each temperature, both rotation rates were measured three times in an alternating way. These three measurements were averaged afterwards. In order to make sure that the surface did not change during measurements, the disk and ring were short-circuited after every individual measurement and cycled 8 times in the Au oxide formation/reduction potential window (0.05 – 1.75 V vs RHE at 1 V/s) in the measurement cell.

Between every set of measurements at a given temperature, the RRDE tip was electrochemically polished in 0.1 M H_2SO_4 and a characterization CV was obtained for the disk. The electrochemically active surface area (ECSA) of the disk was determined by calculating the charge of the reduction peak in this characterization CV and dividing this by the specific charge of one monolayer of Au (390 μC/cm^2).[55] Then, the tip was transferred to the measurement cell and cycled from 0.05 – 1.75 V vs RHE at 1 V/s for 75 cycles to stabilize the temperature of the cell and the tip. Thereafter, the resistance was determined using electrochemical impedance spectroscopy (EIS) and compensated for 85% in the measurement CVs. Next, the measurements could start as described above.

2.2.5 Collection Efficiency Determination

The apparent collection efficiency of the ring was determined at the end of a day of experiments to account for the changes in tip geometry that incur with the assembling of the tip. The apparent collection efficiency was determined in a separate cell containing 0.1 M Ar saturated $NaHCO_3$ with 5 mM $K_3Fe(CN)_6$. The disk was cycled between 0.27 and 1.27 V vs RHE and the ring potential was set to 0.96 V vs RHE. The collection efficiency was determined for each rotation rate and was calculated according to equation 2.1:

$$N = \left|\frac{i_{ring}}{i_{disk}}\right| \qquad (2.1)$$

2.2.6 The CO2RR and HER Current Deconvolution

The selective oxidation of CO on the gold ring, under diffusion limited conditions, makes it possible to deconvolute the CO2RR and the HER current under the assumption that H_2 and CO are the only products on the Au polycrystalline disk in the potential window used in this study. This assumption is reasonable as studies have determined CO as the only appreciable product of CO2RR on gold.[49–51] The partial current density for CO formation can be calculated from the experimental ring current (i_{ring}) and the apparent collection efficiency N:

$$J_{CO} = \frac{-i_{ring}}{N * ECSA_{disk}} \qquad (2.2)$$

The Faradaic efficiency for CO formation can be calculated as

$$FE_{CO} = \frac{i_{ring}}{|i_{disk}| * N} * 100\% \qquad (2.3)$$

The partial current density and faradaic efficiency for the HER can be calculated from

$$J_{H_2} = J_{tot} - J_{CO} \qquad (2.4a)$$

$$FE_{H_2} = 100 - FE_{CO} \qquad (2.4b)$$

2.2.7 Temperature dependence of the reference electrode

It is important to choose a proper reference electrode to conduct temperature dependent electrochemical experiments. The reference potential depends explicitly on the temperature via the entropy term, but also implicitly via the standard potential and the activity of ions. Specifically, for the Ag/AgCl and the RHE electrode:

$$E^{Ag|AgCl} = E^{0,\,Ag|Ag^+} + \frac{RT}{F}\ln(K_s) - \frac{RT}{F}\ln(a_{Cl^-}) \qquad (2.5a)$$

$$E^{RHE} = E^{SHE} - \frac{RT\lambda}{F}\mathrm{pH} \qquad (2.5b)$$

In many high-temperature corrosion studies, Ag/AgCl has been used as reference electrode.[56] To determine the potential of the Ag/AgCl electrode, empirical formulas have been used both to correct for the temperature dependence of the standard potential, the solubility product, and the activity of chloride ions.[57–59] However, it would be easier if one could employ a RHE reference. The SHE is namely defined zero at all temperatures and the only implicit temperature

dependent term left is the pH, which can be measured experimentally. Furthermore, it is important that the reference electrode is at the same temperature as the working electrode, otherwise other unknown potential drops can occur due to the temperature gradient.[56] This is why we have chosen to work with an RHE reference from Hydroflex, as this can easily be kept at the same temperature as the working electrode and no extra correction is needed as with an Ag/AgCl electrode.

2.2.8 Determination of apparent activation energy

The exchange current density was used to calculate the apparent activation energy. The exchange current density of CO formation was determined from a Tafel plot (Figure A.1). The current density between -0.575 and -0.775 V vs RHE was extrapolated to the standard equilibrium potential of CO_2 reduction towards CO. This potential range was chosen due to practical considerations: between -0.3 and -0.4 V the currents are too low for an accurate extrapolation, whereas between -0.4 and -0.5 the Tafel plot is too strongly curved for a reliable extrapolation (see Figure A.1). The standard equilibrium potential was calculated for each individual temperature (Table A.2).

2.3 Results and Discussion

2.3.1 Temperature effect on activity and selectivity of the CO2RR and HER

Figure 2.1 shows the effect of temperature on the activity of CO_2 reduction and hydrogen evolution on a gold electrode at 2500 rpm. The partial current density for CO increases with increasing temperature up to 50-55 ^{0}C. For T > 50-55 ^{0}C, there is a plateau in the activity of the CO2RR, which can more clearly be seen in Figure A.2. No qualitative differences are observed when the SHE scale (Figure A.3) is used instead of the RHE scale. With increasing temperature, several aspects of this system change which can cause this behavior (see Figure A.4). The CO_2 solubility decreases with temperature,[60–62] while the diffusion coefficients increase. [63–65] Reaction equilibria shift with temperature and reaction rate constants will increase increasing temperature.[66] The thermodynamic equilibrium potential also shifts with temperature, meaning that the same absolute potential does not give the same overpotential. However, calculations show this shift is less than 16 mV in the temperature range studied (Table A.2) and that it shifts negatively with increasing temperature, so most of the changes in activity will be governed by kinetics and diffusion and not the thermodynamics of the CO2RR. The conductivity of the electrolyte increases with temperature, at least for aqueous electrolytes up to 90 ^{0}C.[66] Although this is not relevant for this study as we perform IR correction, it can

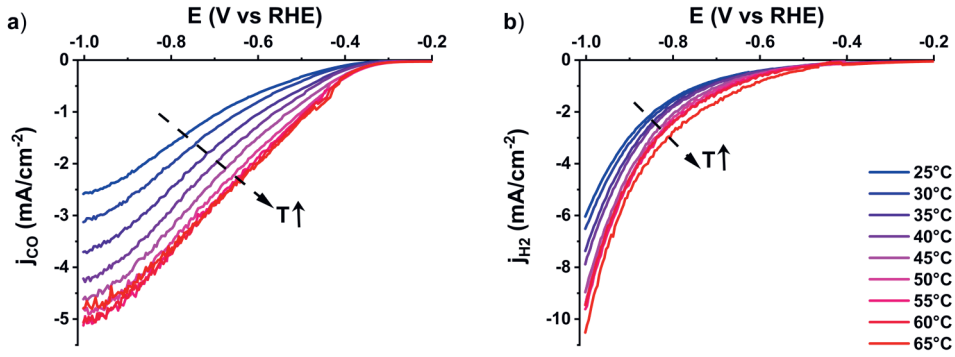

Figure 2.1 The partial current density towards CO formation (a) and H_2 (b) at different temperatures in 0.1M $NaHCO_3$ on a gold RRDE at 2500 rpm and 20 mV/s

be an important consideration for practical applications of electrolyzers, as this will decrease the cell potential and could increase the cell efficiency. [32]

In general, the pH tends to decrease with temperature due to increased ionization of water.[66] However, in our system, the CO_2 concentration decreases with temperature and due to the complex equilibria with bicarbonate, carbonate, hydroxide and water, the net change in pH is an increase of about half a pH unit from 25 to 70 ^{0}C (Figure A.4). Moreover, the buffer capacity decreases as both the CO_2 and HCO_3^- concentrations decrease with temperature.[67] This means that the local pH can increase even more with temperature than the bulk pH, also because the currents increase with temperature. As we are using the rotating disc electrode, minor differences between the bulk and local pH could be expected. Zhang et al.[46] have shown that for low current densities (<4.33 mA/cm^2 at 1600 rpm) no significant local pH changes are observed. On the other hand, recent experiments in our group have shown that even at relatively low current densities, the local pH at rotating electrodes can be significantly different from the bulk pH.[68] However, as the change in bulk pH and buffer capacity are minor, we do not expect the pH to dominate the temperature effect observed in Figure 2.1. The local pH can change because the current densities are higher, but this is then the result of the increased activity, instead of the cause. Moreover, the local pH tends to influence the FE by influencing the activity of the HER rather than the activity of the CO2RR.[69,70]

The solubility of CO_2 is an important factor which depends on the temperature according to the van 't Hoff equation. The solubility can be estimated with Henry's law:

$$C = KP \qquad (2.6)$$

where C is the concentration, K is the Henry's constant and P is the partial pressure. The Henry's constant depends on temperature and we used the empirical equation 2.7 to calculate this dependence.[62]

$$\log(K) = 108.3865 + 0.01985076 * T - \frac{6919.53}{T} - 40.4515 * \log(T) + \frac{669365}{T^2} \qquad (2.7)$$

With the use of Henry's law, we can deconvolute the effect of CO_2 concentration from the overall effect of temperature. By changing the partial pressure at constant temperature, the effect of CO2 concentration can be studied independently of the effect of temperature. It is expected that if the concentration of CO_2 in the bulk is altered, a corresponding change in the CO_2 concentration at the surface of the electrode will occur.[67] Figure A.5 shows that the activity for the CO2RR decreases with decreasing dissolved CO_2 concentration. This trend is as expected and has been observed in literature before.[71–73] The corresponding reaction order of CO_2 is 0.9 (Figure A.6), which is comparable with literature.[73–75]

We have studied the effect of temperature independent of the CO_2 concentration by adjusting the partial pressure at different temperatures. As the "standard" concentration we take the CO_2 concentration at 1 atm of CO_2 at 70 ^{0}C.

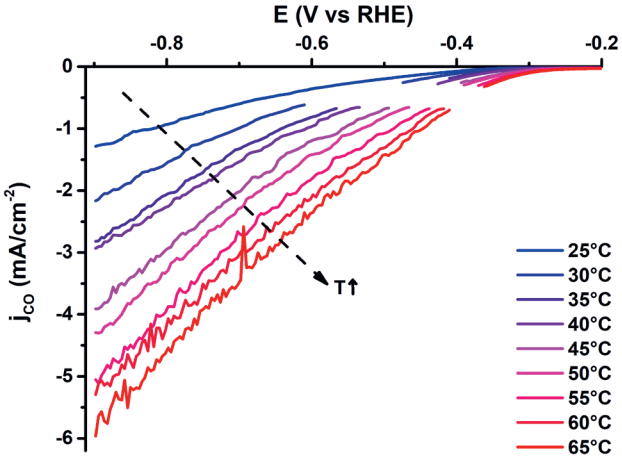

Figure 2.2 The partial current density for CO formation at different temperatures at constant CO_2 concentrations in 0.1M $NaHCO_3$ on a gold RRDE at 2500 rpm and 20 mV/s.

For all the other temperatures, we determined the required partial pressure of CO_2 to obtain this same CO_2 concentration. Figure 2.2 shows the partial current density of CO formation with increasing temperature at the same CO_2 concentration at each temperature. The activity for the CO2RR increases with temperature and the increase in activity is larger in Figure 2.2 than in Figure 2.1a. Based on Figure A.5, this result is to be expected as Figure 2.1 is a convolution of the effect of temperature and the decreasing activity due to lower CO2 concentrations. This also shows that the enhancing effect of temperature on the activity is larger than the suppressing effect of CO_2 concentration, resulting in a net increase in activity in Figure 2.1a. Furthermore, no plateau in activity as a function of temperature is observed in Figure 2.2. This suggests that the plateau observed in Figure 2.1 is related to a decreasing concentration of CO_2 in solution. From 55 ^{0}C onwards, the effect of temperature is not strong enough anymore to compensate for the decrease in activity due to the lower CO_2 concentration.

As the CO_2 concentration is lower at higher temperatures, we need to consider mass transport. Similar to our result, Löwe et al.[41] observed an optimum in the CO2RR selectivity at 50 ^{0}C. They explained this optimum as a compromise between decreasing solubility and the increasing diffusion coefficient. With our RRDE setup, we can control mass transport by varying the rotation rate and we do not observe this optimum in mass transport. Figure 2.3 shows the CO_2 activity at different rotation rates at different temperatures. At 25 ^{0}C, it can be seen that there is no rotation rate dependence up to high overpotentials. This suggests that there are no mass transport limitations at this temperature. At 40 ^{0}C, we see some rotation rate dependence, with higher partial current densities at higher rotation rates. The potential at which this rotation dependence sets in shifts to lower values at 55 ^{0}C; the "critical" current density appears around -1.0 mA/cm^2 for all three temperatures. Below this current, there seems to be no positive effect of faster mass transport at any temperature, so an increase in diffusivity should not lead to an increase in activity. Moreover, when the Levich equation is used to calculate the limiting current densities (Table A.3), we observe that the limiting current densities decrease with temperature (104, 95 and 90 mA/cm^2 respectively for 25 ^{0}C, 40 ^{0}C and 55 ^{0}C at 2500 rpm) but they are still considerably higher than the measured current densities, indicating that the increase in activity is mainly caused by an increase in kinetics and not due to the increasing diffusion coefficient. Furthermore, Koutecky-Levich analysis (Figure A.7, Table A.4) at the different temperatures also shows that the kinetic current increases and the Levich constant decreases with temperature.

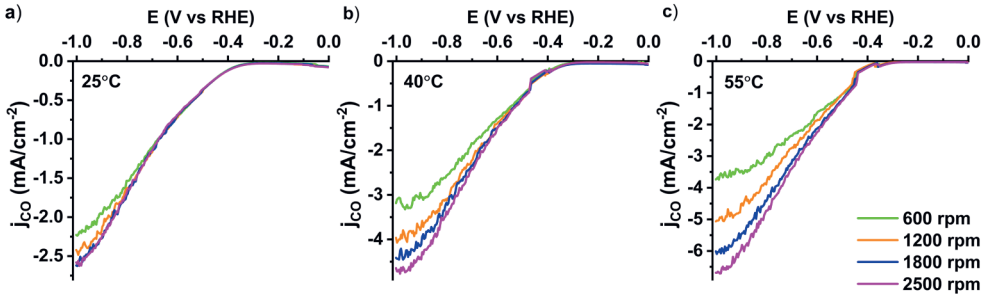

Figure 2.3 Partial current densities for CO formation at different rotation rates at 25 (a) 40 (b) and 55 ^{0}C (c) in 0.1M $NaHCO_3$ at 20 mV/s

Interestingly, even below -1.0 mA/cm^2, where no mass transport limitations are present, we observe the plateau in the CO2RR activity for higher temperatures than 55 ^{0}C. As mentioned, the calculated limiting current densities are much larger than observed in Figure 2.3. This has been observed before and has been attributed to the homogenous reaction 2.8 which consumes CO_2 and lowers its concentration at the surface.[73,76]

$$CO_2 + OH^- \rightarrow HCO_3^- \qquad (2.8)$$

At the higher current densities not only more CO_2 is consumed in the electrochemical reaction but also more OH^- is generated which consumes more CO_2 in the homogenous reaction, increasing the effect of the rotation rate. Moreover, at higher temperatures, the reaction rate of the homogeneous reaction of CO_2 increases, so even at the same local pH, more CO_2 will be consumed due to reaction 3.[77]

Figure 2.1b shows that also hydrogen evolution activity increases with temperature. It can be observed that the activity for the HER does not show a plateau as a function of temperature. Although it has been shown recently that the HER can show an unexpected mass transport dependence,[78] this is not expected to limit the HER at higher temperatures as the near-surface cation concentration is not decreasing with increasing temperatures. As a control experiment, we also studied the effect of temperature on the HER without CO_2 in solution. Figure A.8 shows that also in this case, the HER increases with temperature and no plateau is observed.

Figure 2.4a shows the FE towards CO as a function of both temperature and applied potential. An optimal potential around -0.55 V vs RHE is observed, in agreement with previous experiments.[52] The trend as a function of temperature is

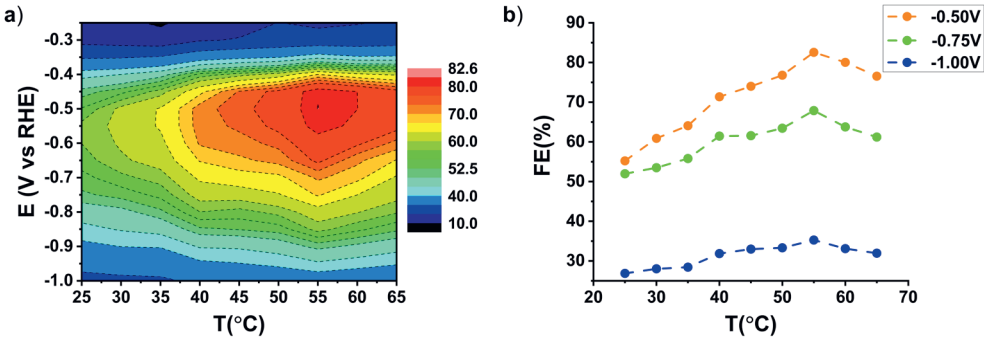

Figure 2.4 Faradaic efficiency for CO formation plotted as (a) a function of both potential and temperature and (b) as a function of temperature at distinct potentials for a gold RRDE at 2500 rpm in 0.1M $NaHCO_3$

less clear and depends on potential. Figure 2.4b shows that at medium overpotentials, the FE towards CO has a maximum at 55 ^{0}C. This optimum is logical as from this temperature onwards the CO2RR activity starts plateauing, while the HER rate keeps increasing with temperature. When the CO_2 concentration is kept constant, as in Figure 2.2, the FE does not decrease at these temperatures but plateaus. At higher overpotentials, the optimum remains at 55 ^{0}C, however the differences in FE between different temperatures become smaller.

Up to now, we have looked at the effect of temperature on CO_2 reduction mostly in a qualitative way. To have a more quantitative evaluation, we define ratios of partial current densities according to equation 2.9:

$$r_T = \frac{j_T}{j_{25°C}} \qquad (2.9)$$

where *r* is the ratio, and *j* is the partial current density. Table A.5 plots these ratios as a function of temperature and applied potential. Not surprisingly, these ratios increase with temperature. However, it can also be observed that with increasing overpotential, the effect of temperature becomes smaller. Whereas at -0.4 V the activity at 55 ^{0}C is almost 4 times higher than at 25 ^{0}C, the ratio has decreased to a factor 2 at -1.0V. This explains why the effect of temperature on the FE decreases at more negative potentials. In most studies for CO_2 reduction, these higher overpotentials are used and it is thus important to realize that the effect of temperature will be smaller (though still significant) at these potentials. We will go into more detail later why it is to be expected from theory that the temperature effect depends on potential.

2.3.2 Activation energies

From the temperature dependent experiments we can obtain the apparent activation energy for the CO_2 reduction on gold using the Arrhenius equation:

$$k = Ae^{\frac{-E_a}{RT}} \qquad (2.10)$$

where k is the reaction rate constant, A is the pre-exponential factor, E_a is the activation energy, R is the gas constant and T the absolute temperature. Since the exchange current density depends on the reaction rate constant, the j_0 will also follow an Arrhenius relation and equation 2.11a can be used. In order to obtain the "real" activation energy, we need to correct for the T-dependence of the CO2 concentration and equation 2.11b is derived from equation 2.11a (see SI).

$$\ln(j_0) = \ln(A') - \frac{E_a}{R} * \frac{1}{T} \qquad (2.11a)$$

$$\ln(j_0) + \ln\left(\frac{C_{25^\circ C}}{C_T}\right) = \ln(A') - \frac{E_a}{R} * \frac{1}{T} \qquad (2.11b)$$

where j_0 is the exchange current density, A' the pre-exponential factor, E_a the activation energy, R the gas constant, T the absolute temperature, $C_{25^\circ C}$ and C_T the concentration of CO_2, at 25 ^{0}C and a given temperature, respectively.

Figure 2.5 shows the corrected Arrhenius plot for CO_2 reduction in 0.1M $NaHCO_3$ on gold using the standard exchange current densities. From the slope of the Arrhenius plot, the apparent activation energy is determined to be 61 ±2 kJ/mol, according to equation 2.11b. This value applies (as extrapolated to) to the standard equilibrium potential; values for the activation energy at different overpotentials will be discussed below. As mentioned in the experimental section, the standard potential of the CO2RR also changes with temperature and in the above calculations this has been taken into account. If we would calculate all exchange current densities at -0.1 V, the standard potential at 25 ^{0}C, there is only about 1 kJ/mol difference.

The corrected apparent activation energy takes the variable CO_2 concentration into account and is close to the apparent activation energy determined from the activities at constant CO_2 concentration of Figure 2.2, supporting our correction method. With constant CO_2 concentration the apparent activation energy is 60 kJ/mol (Figure A.10). Moreover, our apparent activation energy is comparable to barriers calculated with DFT in the literature [79] (though such comparisons have certain pitfalls regarding the exact assumptions made in the computations).

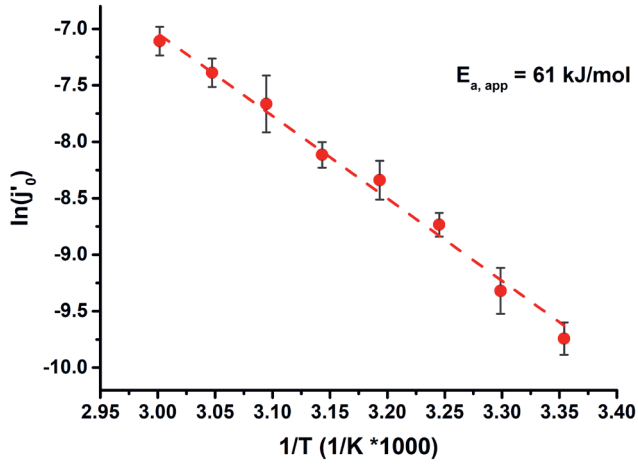

Figure 2.5 Arrhenius plot of CO_2 standard reduction current in 0.1M NaHCO3 in the temperature range of 25-60 ^{0}C

The apparent activation energy of the HER is expected to be lower than for the CO2RR as the activity of the HER is less temperature dependent than that of the CO2RR. For an accurate independent measurement of the activation energy for HER, we have performed experiments without CO_2 in solution, from which we determined the apparent activation energy for the HER to be 25 ± 3 kJ/mol (Figure A.11). In the literature, the apparent activation energy for the HER on Pt has been reported to be between 9.5 and 18 kJ/mol, depending on the facet,[79] although other studies found considerable higher activation energies.[80] On Ag an activation energy between 20 and 30 kJ/mol has been found.[81,82] Thus, it seems that the activation energy of the HER is indeed lower than that for the CO2RR, explaining the larger increase in activity with temperature for the latter.

The activation energy is expected to be dependent on the potential. This is an underlying assumption of the Butler-Volmer equation (equation 2.12[83]), describing the relationship between the applied potential and Faradaic current. Equations 2.13a and b[84] are used to derive the Butler-Volmer equation from the Arrhenius equation, linking activation energy to potential.

$$j = j_0 \left\{ exp\left[\frac{\alpha_c F\eta}{RT}\right] - exp\left[-\frac{\alpha_a F\eta}{RT}\right]\right\} \qquad (2.12)$$

$$\Delta G_c^{\ddagger} = \Delta G_{0c}^{\ddagger} + a_c F\eta \qquad (2.13a)$$

$$\Delta G_a^{\ddagger} = \Delta G_{0a}^{\ddagger} + a_a F\eta \qquad (2.13b)$$

$$\Delta H_c^{\ddagger} = \Delta H_{0c}^{\ddagger} + \alpha_{c,H} F\eta \qquad (2.13c)$$

where $\Delta G_{Oc}^{\ddagger}$ is the free energy of activation at the standard equilibrium potential, $\Delta H_{Oc}^{\ddagger}$ the enthalpy of activation at the standard equilibrium potential, α_c and α_a the cathodic and anodic transfer coefficient respectively, j_0 the standard exchange current density and η the overpotential.

Equation 2.13c is similar to equation 2.13a, but is used instead because the activation enthalpy is more directly related to the apparent activation energy determined using the Arrhenius equation.[85] Both equations state that the activation energy depends linearly on the applied potential.[86,87] At zero overpotential, the same apparent activation energy is obtained as determined from the standard exchange current density. Figure 2.6 and A.12 show the experimental relation between activation enthalpy and potential, which is indeed linear. The apparent activation enthalpy at zero overpotential in $NaHCO_3$ is 59 ± 4 kJ/mol, which is similar to the 61 kJ/mol determined with the exchange current densities. Moreover, from the slope we can determine the enthalpic transfer coefficient α_H to be 0.3, independent of cation identity and concentration (Figure A.12/13). Commonly the Butler-Volmer transfer coefficient α_c is assumed to be 0.5 as the first electron transfer is considered the rate limiting step for CO_2 reduction on gold,[75,88–90]

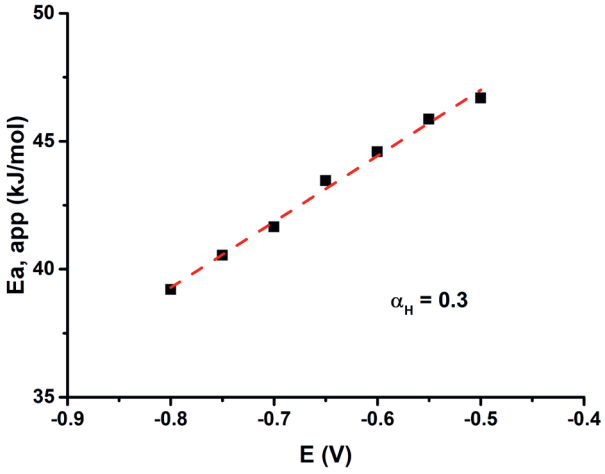

Figure 2.6 The apparent activation energy of CO_2 reduction towards CO in 0.1M $NaHCO_3$ plotted against the applied potential

although there is still some debate around this.[70,91] Conway et al. have discussed in detail this difference between the enthalpic part of the transfer coefficient and the Butler-Volmer transfer coefficient:[86,87,92–94]

$$\alpha_c = \alpha_H + T\alpha_s \qquad (2.14)$$

The entropic part of the transfer coefficient can be obtained by plotting the natural logarithm of the pre-exponential factor against the potential[87] (Figure A.14) and from the slope, α_s has been calculated to be 5 * 10^{-4} K^{-1} for CO_2 reduction on gold. At room temperature, this is roughly 0.15 meaning that the enthalpic part dominates the transfer coefficient. This implies that in this catalytic process most of the potential dependence of the rate is due to changes in the height of the potential energy barrier, but the entropy of activation is not negligible. This is in contrast to a process such as oxygen reduction, where the opposite has been found.[92,95]

2.3.3 Cation effect

It is well known that cations affect the CO_2 reduction rate,[11–14] but this effect has not yet been studied in combination with the temperature effect. Figure 2.7 shows that there is an increase in activity in the order Li^+ < Na^+ < K^+ < Cs^+. This order is observed at both 25 ^{0}C and 50 ^{0}C. The apparent activation energy decreases gradually from 65 ±2 kJ/mol (Li^+) to 54 ±2 kJ/mol (Cs^+) (see Table 2.1). A lower activation energy results in a weaker temperature effect, therefore the differences in activity are expected to become smaller with increasing temperature. This effect is difficult to observe in Figure 2.7 as the temperature

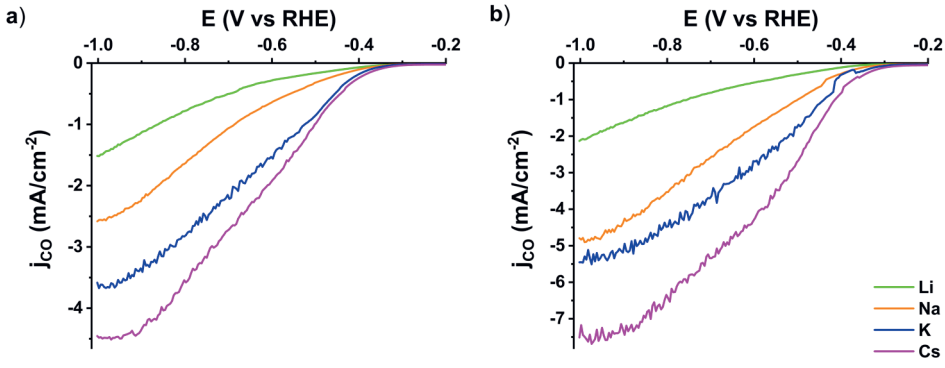

Figure 2.7 The partial current densities for the CO2RR for different cations at 25^{0}C (a) and 50^{0}C (b) on a gold RRDE at 2500 rpm at 20 mV/s

interval seems to be too small to observe major differences. For the pre- exponential factor a comparable (albeit reversed) tendency is observed, with Cs^+ having the lowest value. If extrapolated to high temperatures, the cation effect would reverse and Cs^+ would become the least active, but most likely these trends cannot be extrapolated in this way.

Similar trends can be observed if the concentration of cations is increased by adding $NaClO_4$ to 0.1M $NaHCO_3$ as seen in Table 2.2. The apparent activation energy decreases from 61 ±2 kJ/mol in 0.1M Na^+ to 51 ±3 kJ/mol in 0.5M Na^+ and the pre-exponential factor decreases in the same sequence. The decreasing activation energy going from Li^+ to Cs^+ agrees with all of the most proposed mechanisms for the cation effect and can therefore not be used to differentiate between them. The theory which states that the local potential in the outer Helmholtz layer changes with cation predicts this decrease in activation energy. Furthermore, the explanation of stabilizing intermediates due to the electric field, or as recently proposed by a short-range electrostatic interaction,[48] would also lead to lower activation energies for Cs^+ compared to Li^+. According to the buffering theory, cations influence the local pH and consequently the local CO_2 concentration differently as Cs^+ is a better buffer than Li^+.[13] This leads to differences in coverage and thus a difference in apparent activation energy. However, it is unlikely that the cation buffering is the cause of the cation effect observed in this study as we have efficient mass transport and the cation effect is already observed at very low current densities. Most likely the decrease in activation energy is either due the change in local potential or to the stabilization of intermediates by to the cations.

A smaller pre-exponential factor going from Li^+ to Cs^+ is likely a limitation of the extrapolation of the data to infinite temperature. This so-called compensation effect has been observed in literature before and arises because the pre-exponential factor and the activation energy are determined from the same Arrhenius plot.[80] However, this observation could in principle also fit in the picture where the concentration of Cs^+ near the surface is higher than that of Li^+. This might make it more difficult for the CO_2 to reach the surface if the concentration is high. It has been shown that the concentration of cations can be considerably higher at the interface than the bulk concentration: a recent computational study has suggested that the concentration of cations at the surface could reach up to 1.5 M with a bulk concentration of only 0.1 M.[96] 1.5 M of K^+ would fill up to 34 percent of the space (see calculation in the SI), making it reasonable to argue this could hinder the CO_2 to reach the surface. This hindrance would decrease the pre-exponential factor as this can be seen as the likelihood of the reactant reaching the electrode surface.[97] This likelihood would decrease if more cations screened the surface. This interpretation is supported by the rapid decrease of the pre-exponential factor with

increasing cation concentration. Although this is certainly an oversimplification of the interpretation of the pre-exponential factor, it could carry an element of truth and helps visualizing how cations can influence this parameter. Nevertheless, for the time being, we interpret the observations as a compensation effect, the nature of which is still very much debated.[98]

Table 2.1 Apparent activation energies both uncorrected and corrected, and the pre-exponential factor for the CO2RR in different 0.1M bicarbonate electrolytes

	$E_{a,app}$ (kJ/mol)	$E_{a,app}^{corrected}$ (kJ/mol)	ln(A) (A in cm/s)
Li^+	48	65	7.1
Na^+	44	61	6.8
K^+	39	57	6.1
Cs^+	36	54	5.7

Table 2.2 Apparent activation energies both uncorrected and corrected, and the pre-exponential factor for the CO2RR in NaHCO3 electrolytes with different concentrations of Na

	$E_{a,app}$ (kJ/mol)	$E_{a,app}^{corrected}$ (kJ/mol)	ln(A) (A in cm/s)
0.1 M	44	61	6.8
0.2 M	39	56	5.4
0.3 M	36	53	4.0
0.5 M	33	51	3.0

2.4 Conclusion

In this paper we have shown that both the activity and selectivity of electrochemical CO_2 reduction can benefit from elevating the temperature of the electrochemical system. However, there is a complex balance between the increase in kinetics and the decreasing solubility of CO_2. This balance results in a limiting temperature of 55 ^{0}C, after which the CO2RR activity plateaus and the selectivity decreases. Moreover, because of the limiting amount of CO_2 in solution, mass transfer becomes more important at higher temperatures, though we emphasize that at all temperatures the system is still rather far from the theoretical mass transport limited CO_2 reduction current. If the CO_2 solubility can be increased, for

example by increasing the pressure of CO_2, it is to be expected that the optimum temperature for CO_2 reduction can be further increased. The effect of temperature is largest at lower overpotentials and decreases with increasing overpotential as the activation energy is influenced by the potential. The apparent activation energy for the CO2RR is 61 kJ/mol in 0.1M $NaHCO_3$. This activation energy depends on the electrolyte and decreases both with cation concentration and identity. This is in agreement with the cation effect known in literature and shows that this effect becomes less significant at elevated temperatures. Moreover, we show that the enthalpic part of the transfer coefficient for the CO2RR on gold is 0.3. This indicates that the enthalpy plays a dominant role in this process, although the entropy contribution cannot be neglected. This study has focused on Au as a model catalyst for CO_2 reduction as it provides a simple system with only CO as the product of the CO2RR. This relative simplicity made it possible to study the basic effects of temperature. Future work will study this effect on other catalysts such as Cu and investigate how the product distribution of the CO2RR changes with temperature. Furthermore, pressurized experiments should be performed to broaden the temperature range that can be studied.

References

1. Nitopi, S. *et al. Chemical Reviews* vol. 119 7610–7672 Preprint at (2019).
2. Birdja, Y. Y. *et al. Nat Energy* **4**, 732–745 (2019).
3. Varela, A. S. *Curr Opin Green Sustain Chem* **26**, 100371 (2020).
4. Narayanaru, S., Chinnaiah, J., Phani, K. L. & Scholz, F. *Electrochim Acta* **264**, 269–274 (2018).
5. Liu, X. *et al. Nat Commun* **10**, 32 (2019).
6. Jiang, X., Li, H., Yang, Y. & Gao, D. *J Mater Sci* **55**, 13916–13926 (2020).
7. Schouten, K. J. P., Pérez Gallent, E. & Koper, M. T. M. *Journal of Electroanalytical Chemistry* **716**, 53–57 (2014).
8. Varela, A. S., Kroschel, M., Reier, T. & Strasser, P. *Catal Today* **260**, 8–13 (2016).
9. Kas, R., Kortlever, R., Yılmaz, H., Koper, M. T. M. & Mul, G. *ChemElectroChem* **2**, 354–358 (2015).
10. Singh, M. R., Clark, E. L. & Bell, A. T. *Physical Chemistry Chemical Physics* **17**, 18924–18936 (2015).
11. Murata, A. & Hori, Y. *Bulletin of the Chemical Society of Japan* vol. 64 123–127 (1991).
12. Resasco, J. *et al. J Am Chem Soc* **139**, 11277–11287 (2017).
13. Singh, M. R., Kwon, Y., Lum, Y., Ager, J. W. & Bell, A. T. *J Am Chem Soc* **138**, 13006–13012 (2016).
14. Ringe, S. *et al. Energy Environ Sci* 17–25 (2019) doi:10.1039/c9ee01341e.
15. Resasco, J., Lum, Y., Clark, E., Zeledon, J. Z. & Bell, A. T. *ChemElectroChem* **5**, 1064–1072 (2018).
16. Huang, Y., Ong, C. W. & Yeo, B. S. *ChemSusChem* **11**, 3299–3306 (2018).
17. Schouten, K. J. P., Qin, Z., Gallent, E. P. & Koper, M. T. M. *J Am Chem Soc* **134**, 9864–9867 (2012).
18. Schouten, K. J. P., Pérez Gallent, E. & Koper, M. T. M. *ACS Catal* **3**, 1292–1295 (2013).
19. Pérez-Gallent, E., Marcandalli, G., Figueiredo, M. C., Calle-Vallejo, F. & Koper, M. T. M. *J Am Chem Soc* **139**, 16412–16419 (2017).
20. Todoroki, N. *et al. ACS Catal* **9**, 1383–1388 (2019).
21. Jia, Y., Jiang, K., Wang, H. & Yao, X. *Chem* **5**, 1371–1397 (2019).
22. Mariano, R. G., McKelvey, K., White, H. S. & Kanan, M. W. *Science* **358**, 1187–1192 (2017).
23. Vickers, J. W., Alfonso, D. & Kauffman, D. R. *Energy Technology* **5**, 775–795 (2017).
24. Chen, C., Zhang, B., Zhong, J. & Cheng, Z. *J Mater Chem A Mater* **5**, 21955–21964 (2017).
25. da Silva, A. H. M. *et al. Journal of Electroanalytical Chemistry* **880**, (2021).
26. Jiang, K. *et al. ACS Energy Lett* **5**, 1206–1214 (2020).
27. Lum, Y., Yue, B., Lobaccaro, P., Bell, A. T. & Ager, J. W. *Journal of Physical Chemistry C* **121**, 14191–14203 (2017).
28. Scheepers, F. *et al. Appl Energy* **283**, 1–11 (2021).
29. Chandrasekar, A., Flynn, D. & Syron, E. *Int J Hydrogen Energy* (2021)

30. Carmo, M., Fritz, D. L., Mergel, J. & Stolten, D. *Int J Hydrogen Energy* **38**, 4901–4934 (2013).
31. Babic, U., Suermann, M., Büchi, F. N., Gubler, L. & Schmidt, T. J. *J Electrochem Soc* **164**, F387–F399 (2017).
32. Dufek, E. J., Lister, T. E. & McIlwain, M. E. *J Appl Electrochem* **41**, 623–631 (2011).
33. Pino, F. J., Valverde, L. & Rosa, F. *J Power Sources* **196**, 4418–4426 (2011).
34. Lee, W., Kim, Y. E., Youn, M. H., Jeong, S. K. & Park, K. T. *Angewandte Chemie - International Edition* **57**, 6883–6887 (2018).
35. Kim, H. Y. *et al. Int J Hydrogen Energy* **39**, 16506–16512 (2014).
36. Han, L., Zhou, W. & Xiang, C. *ACS Energy Lett* **3**, 855–860 (2018).
37. Gabardo, C. M. *et al. Joule* **3**, 2777–2791 (2019).
38. Endrődi, B. *et al. Prog Energy Combust Sci* **62**, 133–154 (2017).
39. Ahn, S. T., Abu-baker, I. & Palmore, G. T. R. *Catal Today* **288**, 24–29 (2017).
40. Hori, Y., Kikuchi, K., Murata, A. & Suzuki, S. *Chem Lett* **15**, 897–898 (1986).
41. Löwe, A. *et al. ChemElectroChem* **6**, 4497–4506 (2019).
42. Thorson, M. R., Siil, K. I. & Kenis, P. J. A. *J Electrochem Soc* **160**, F69–F74 (2012).
43. Kim, H., Park, H. S., Hwang, Y. J. & Min, B. K. *The Journal of Physical Chemistry C* **121**, 22637–22643 (2017).
44. Malkani, A. S., Anibal, J. & Xu, B. *ACS Catal* **10**, 14871–14876 (2020).
45. Waegele, M. M., Gunathunge, C. M., Li, J. & Li, X. *Journal of Chemical Physics* **151**, 1DUMMT (2019).
46. Zhang, F. & Co, A. C. *Angewandte Chemie - International Edition* **59**, 1674–1681 (2020).
47. Ayemoba, O. & Cuesta, A. *ACS Appl Mater Interfaces* **9**, 27377–27382 (2017).
48. Monteiro, M. C. O. *et al. Nat Catal* **4**, (2021).
49. Kauffman, D. R. *et al. ACS Appl Mater Interfaces* **7**, 15626–15632 (2015).
50. Kim, D., Resasco, J., Yu, Y., Asiri, A. M. & Yang, P. *Nat Commun* **5**, 4948 (2014).
51. Cave, E. R. *et al. Physical Chemistry Chemical Physics* **19**, 15856–15863 (2017).
52. Goyal, A., Marcandalli, G., Mints, V. A. & Koper, M. T. M. *J Am Chem Soc* **142**, 4154–4161 (2020).
53. Marcandalli, G., Goyal, A. & Koper, M. T. M. *ACS Catal* 4936–4945 (2021)
54. Vos, J. G. & Koper, M. T. M. *Journal of Electroanalytical Chemistry* **850**, 113363 (2019).
55. Łukaszewski, M., Soszko, M. & Czerwiński, A. *Int. J. Electrochem. Sci* **11**, 4442–4469 (2016).
56. Wildgoose, G. G., Giovanelli, D., Lawrence, N. S. & Compton, R. G. *Electroanalysis* 16 421–433 (2004).
57. Greeley, R. S., Smith Jr, W. T., Stoughton, R. W. & Lietzke, M. H. *J Phys Chem* **64**, 652–657 (1960).
58. Macdonald, D. D., Scott, A. C. & Wentrcek, P. *J Electrochem Soc* **126**, 908–911 (1979).
59. Öijerholm, J., Forsberg, S., Hermansson, H.-P. & Ullberg, M. *J Electrochem Soc* **156**, P56 (2009).
60. Harned, H. S. & Davis Jr, R. *J Am Chem Soc* **65**, 2030–2037 (1943).
61. Duan, Z. & Sun, R. *Chem Geol* **193**, 257–271 (2003).

62. Plummer, L. N. & Busenberg, E. *Geochim Cosmochim Acta* **46**, 1011–1040 (1982).
63. Lu, W., Guo, H., Chou, I. M., Burruss, R. C. & Li, L. *Geochim Cosmochim Acta* **115**, 183–204 (2013).
64. Tamimi, A., Rinker, E. B. & Sandall, O. C. *J Chem Eng Data* **39**, 330–332 (1994).
65. Unver, A. A. & Himmelblau, D. M. *J Chem Eng Data* **9**, 428–431 (1964).
66. Gründler, P., Kirbs, A. & Dunsch, L. *ChemPhysChem* **10**, 1722–1746 (2009).
67. Lobaccaro, P. *et al. Physical Chemistry Chemical Physics* **18**, 26777–26785 (2016).
68. Monteiro, M. C. O., Liu, X., Hagedoorn, B. J. L., Snabilié, D. D. & Koper, M. T. M. *ChemElectroChem* 1–8 (2021).
69. Hall, A. S., Yoon, Y., Wuttig, A. & Surendranath, Y. *J Am Chem Soc* **137**, 14834–14837 (2015).
70. Ringe, S. *et al. Nat Commun* **11**, (2020).
71. Noda, H., Ikeda, S., Yamamoto, A., Einaga, H. & Ito, K. *Bull Chem Soc Jpn* **68**, 1889–1895 (1995).
72. Kyriacou, G. Z. & Anagnostopoulos, A. K. *J Appl Electrochem* **23**, 483–486 (1993).
73. Marcandalli, G., Villalba, M. & Koper, M. T. M. (2021)
74. Dunwell, M. *et al. J Am Chem Soc* **139**, 3774–3783 (2017).
75. Wuttig, A., Yaguchi, M., Motobayashi, K., Osawa, M. & Surendranath, Y. *Proc Natl Acad Sci U S A* **113**, E4585–E4593 (2016).
76. Rebouillat, S., Lyons, M. E. G. & Bannon, T. *Journal of Solid State Electrochemistry* **3**, 215–230 (1999).
77. Schulz, K. G., Riebesell, U., Rost, B., Thoms, S. & Zeebe, R. E. *Mar Chem* **100**, 53–65 (2006).
78. Goyal, A. & Koper, M. T. M. *Angewandte Chemie - International Edition* **60**, 13452–13462 (2021).
79. Liu, M. *et al. Nature* **537**, 382–386 (2016).
80. Marković, N. M., Grgur, B. N. & Ross, P. N. *Journal of Physical Chemistry B* **101**, 5405–5413 (1997).
81. He, Z. Da, Wei, J., Chen, Y. X., Santos, E. & Schmickler, W. *Electrochim Acta* **255**, 391–395 (2017).
82. Eberhardt, D., Santos, E. & Schmickler, W. *Journal of Electroanalytical Chemistry* **461**, 76–79 (1999).
83. Kang, J., Lin, C. H., Yao, Y. & Chen, Y. X. *Chinese Journal of Chemical Physics* **27**, 63–68 (2014).
84. Bockris, J. O. & Nagy, Z. *J. Chern. Ed.* **50**, 839–843 (1973).
85. Protsenko, V. S. & Danilov, F. I. *Journal of Electroanalytical Chemistry* **651**, 105–110 (2011).
86. Berry, R. S., Rice, S. A. & Ross, J. (Oxford University Press, 2000).
87. Conway, B. E. & Wilkinson, D. P. *Electrochim Acta* **38**, 997–1013 (1993).
88. Gojković, S. L., Zečević, S. K. & Dražić, D. M. *Journal of Electroanalytical Chemistry* **399**, 127–133 (1995).
89. Wuttig, A., Yoon, Y., Ryu, J. & Surendranath, Y. *J Am Chem Soc* **139**, 17109–17113 (2017).

90. Zhang, B. A., Ozel, T., Elias, J. S., Costentin, C. & Nocera, D. G. *ACS Cent Sci* **5**, 1097–1105 (2019).
91. Dunwell, M., Luc, W., Yan, Y., Jiao, F. & Xu, B. *ACS Catal* **8**, 8121–8129 (2018).
92. Solorza-Feria, O. & Durón, S. *Int J Hydrogen Energy* **27**, 451–455 (2002).
93. Conway, B. E. & Wilkinson, D. F. *Journal of Electroanalytical Chemistry* **214**, 633–653 (1986).
94. Conway, B. E., Tessier, D. F. & Wilkinson, D. P. *Journal of Electroanalytical Chemistry* **199**, 249–269 (1986).
95. Clouser, S. J., Huang, J. C. & Yeager, E. *J Appl Electrochem* **23**, 597–605 (1993).
96. Weitzner, S. E. *et al. Journal of Physical Chemistry Letters* **11**, 4113–4118 (2020).
97. Costentin, C., Louault, C., Robert, M., Rogé, V. & Savéant, J. M. *Physical Chemistry Chemical Physics* **14**, 1581–1584 (2012).
98. Bligaard, T. *et al. J Phys Chem B* **107**, 9325–9331 (2003).

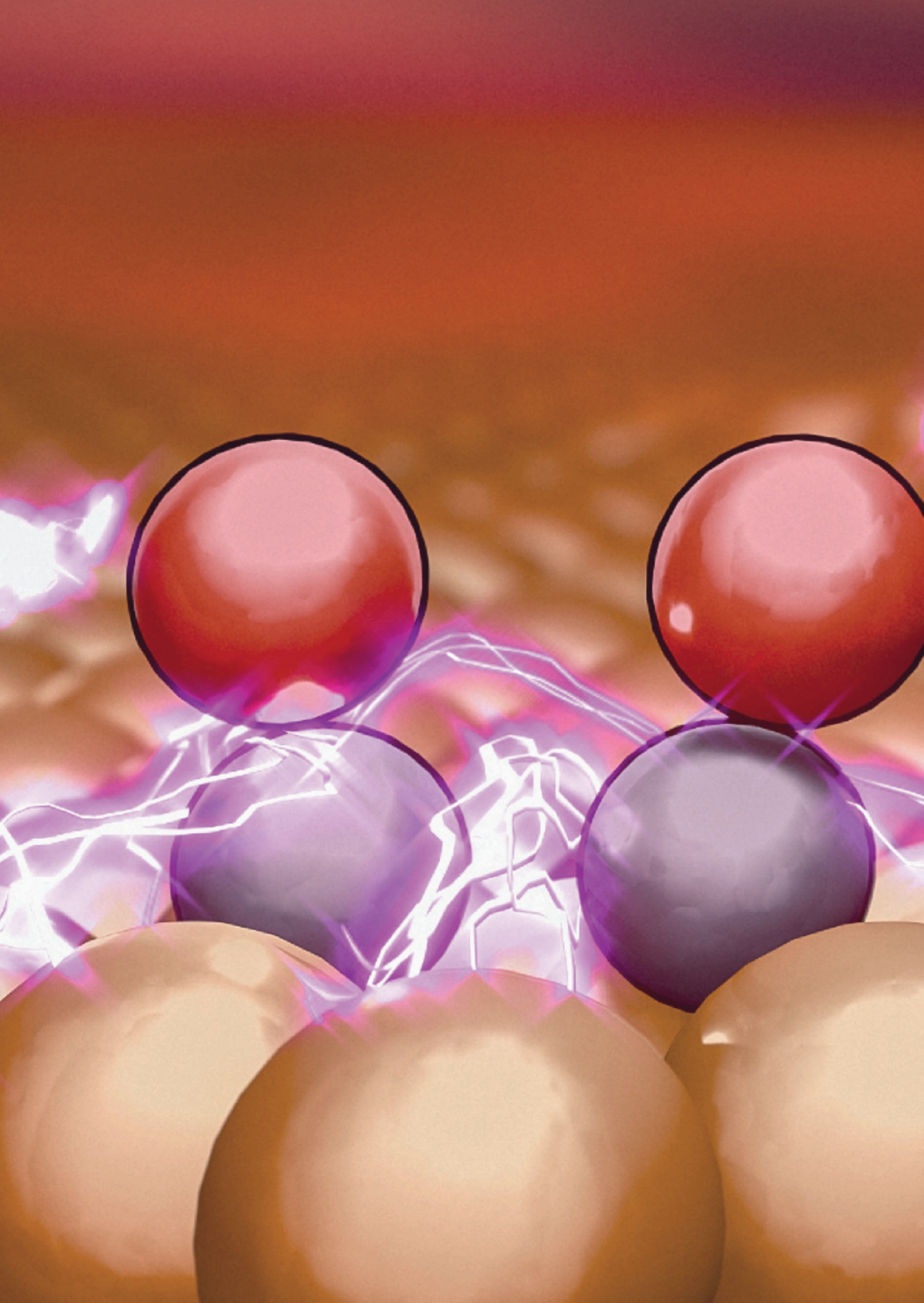

3

How temperature affects the selectivity of the electrochemical CO_2 reduction on copper

This chapter is based on R.E. Vos, K.E. Kolmeijer, T.S. Jacobs, W van der Stam, B.M. Weckhuysen, M.T.M. Koper, *ACS Catalysis* **13** 8080-8091 (2023)

Abstract

Copper is a unique catalyst for the electrochemical CO_2 reduction reaction (CO2RR) as it can produce multi-carbon products, such as ethylene and propanol. As practical electrolyzers will likely operate at elevated temperatures, the effect of reaction temperature on the product distribution and activity of CO2RR on copper is important to elucidate. In this study, we have performed electrolysis experiments at different reaction temperatures and potentials. We show that there are two distinct temperature regimes. From 18 up to ∼ 48 °C, C2+ products are produced with higher Faradaic Efficiency, while methane and formic acid selectivity decreases, and hydrogen selectivity stays approximately constant. From 48 to 70 °C, it was found that HER dominates and the activity of CO2RR decreases. Moreover, the CO2RR products produced in this higher temperature range are mainly the C1 products, namely CO and HCOOH. We argue that CO surface coverage, local pH and kinetics play an important role in the lower-temperature regime, while the second regime appears most likely to be related to structural changes in the copper surface.

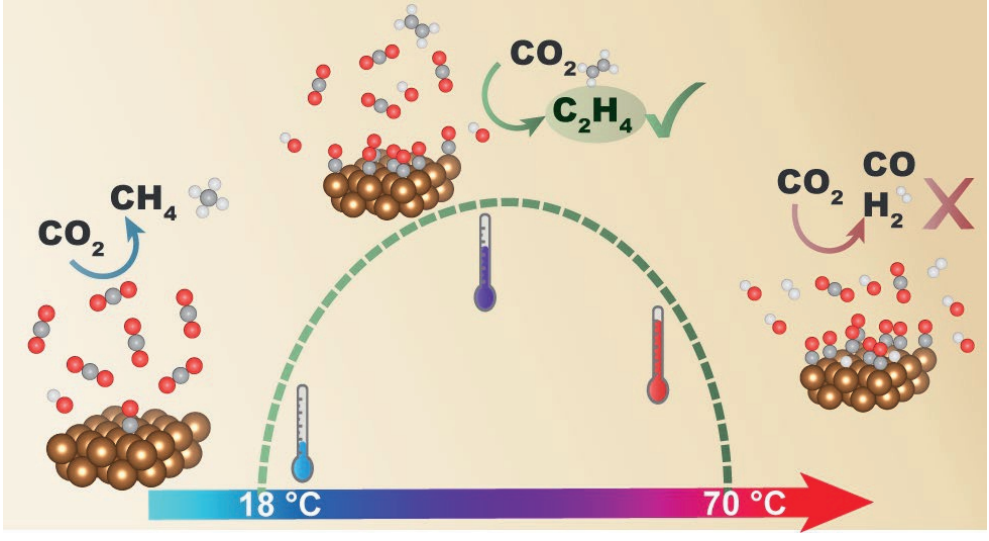

3.1 Introduction

Electrochemical CO_2 reduction (CO2RR) is an interesting process as it exhibits the unique ability to use CO_2 as a resource to produce renewable feedstocks for the chemical industry or so-called solar fuels, which can be used within a future renewable energy system. [1,2] Many different catalysts can be used, of which copper is remarkable as it is practically the only catalyst able to make multi-carbon products such as ethylene, ethanol and propanol. Although other metals such as Ag have shown to be able to produce these products, [3] copper is the only monometallic metal that can produce them at significant Faradaic Efficiencies (FE). [4–6] However, copper is not very selective and produces a complex mixture of both gaseous and liquid reaction products. [7] To be able to employ CO2RR on an industrial level, a FE towards a single product of over 90% is needed. [8,9] Therefore, it is crucial that both the selectivity and activity of the catalysts are further improved, for example by tuning the reaction conditions. [8–11]

Reaction temperature is an important, but often neglected parameter in the field of electrochemistry in general and for CO_2 reduction in particular. Often a perceived benefit of electrocatalysis over thermal catalysis is that the former can be performed at room temperature and ambient pressures. However, in practice, [12] electrolyzers will always operate at elevated temperatures, for example due to thermal losses [13–15] and/or hot feedstocks. In a previous paper, [16] we have investigated the effect of temperature on a simple CO2RR system using gold as catalyst. We found that on gold it is beneficial to perform CO2RR at increased temperature as both the selectivity and the activity towards CO increases. However, mass transport becomes more important at elevated temperatures and at a certain point, CO_2 availability becomes the limiting factor. From 55 °C onwards, we observed a plateau in the activity of CO_2 reduction, even under highly efficient mass transport conditions.

Several other studies have shown the effect of temperature on CO2RR on other simple electrode systems, such as Ag [17] and Sn [18–20]. However, for copper, still not all selectivity trends with temperature have been well identified. Ahn et al. [21] have shown that the selectivity towards methane decreases with reaction temperature, whereas hydrogen dominates at higher temperatures at -1.6 V vs. Ag/AgCl. They also observed an optimum in ethylene selectivity around 22 °C. The trends in CO and HCOOH selectivity with temperature are unclear, although in a recent study a decreasing trend with temperature was observed for the HCOOH selectivity on a copper foam.[22] Hori [23] showed similar results using galvanostatic electrolysis, as he found that hydrogen selectivity is increasing and methane selectivity decreasing with temperature. However, Hori observed different trends for the selectivity of

ethylene and CO compared to Ahn et al. as they did not observe an optimum in ethylene production, whereas CO selectivity seemed to increase with temperature. Although Zong et al. [24] mainly focused on obtaining apparent activation energies of the different products of CO2RR on Cu at different potentials, they did show that the Faradaic Efficiency for hydrogen increases with temperature, while methane selectivity decreases, in agreement with the works of Ahn and Hori. However, again the trends in CO and C_2H_4 selectivity with temperature are less well defined.

Even though there exists some literature about the temperature effect on CO2RR over copper, there remains a significant gap in our understanding. All studies discussed above were limited in their temperature range to a maximum of 45 °C, while industrial electrolyzers will not be limited to these temperatures. [12] Moreover, optima in selectivity for CO2RR at other electrode materials were found at higher temperatures. [16,18] Additionally, although clear trends can be observed for methane and hydrogen selectivity, for the other products the exact trends with temperature remain unresolved. Lastly, previous work has not provided detailed explanations of the trends observed; most ascribe the trends simply to the balance of kinetics and CO_2 solubility, without testing alternatives.

In this chapter, we investigate how reaction temperature affects the electrochemical CO_2 reduction on copper in the temperature range from 18-70 °C. We show that different products display different trends with temperature. CO selectivity remains relatively stable, while the CH_4 and HCOOH selectivities decrease with temperature. The selectivity towards C2+ products shows an optimum around 48 °C, whereas hydrogen formation dominates at higher temperatures. We identify two regimes in this temperature range, the first up to ∼ 48 °C, in which CO2RR activity increases, and the second above 48 °C, in which CO_2 reactivity declines. The observations in the first regime can be explained by an increase in the CO coverage on the surface as evidenced by in situ Raman spectroscopy, in combination with increased local pH and faster kinetics with temperature. The second regime seems not to be related to any limited CO_2 concentration, but rather due to changes in the copper surface as shown with lead underpotential deposition and double layer capacitance measurements, although a too high local pH could also be a factor.

3.2 Experimental

3.2.1 Chemicals

The electrolytes were prepared from $KHCO_3$ (99.95%, Sigma-Aldrich), KOH (99.99%, Sigma-Aldrich), K_2SO_4 (99.999% Suprapur, Sigma-Aldrich), $NaClO_4$ (Emsure, Sigma-Aldrich), NaCl (99.99% Suprapur, Merck), $Pb(ClO_4)_2$ (99.995%, Sigma-Aldrich) and Milli-Q water (≥18.2 MΩcm, TOC < 5 ppb). H_2SO_4 (95-98%, Sigma-Aldrich), H_2O_2 (35%, Merck) and $KMnO_4$ (99%, Sigma-Aldrich) were used to clean the cells. The $KHCO_3$ and KOH + K_2SO_4 electrolytes were stored with Chelex (100 sodium form, Sigma-Aldrich) to clean the electrolyte from any metal impurities.[25] The KOH + K_2SO_4 electrolyte was stored in a plastic container to prevent contamination by leaching of metals from glass. Ar (5.0 purity, Linde), He (5.0 purity, Linde), CO (4.7 purity, Linde) and CO_2 (4.5 purity, Linde) were used for purging the electrolytes.

3.2.2 General Electrochemical Methods

The experiments were performed in a home-made PEEK H-cell or a borosilicate glass cell, which were cleaned prior to experiments by storing in permanganate solution overnight (0.5 M H_2SO_4, 1g/L $KMnO_4$). Before use, the cell was rinsed, submerged in diluted piranha acid solution to remove any traces of MnO_4 and MnO_2, rinsed again and boiled three times with Milli-Q water. The polycrystalline Cu working electrode (99.99%, Mateck) was first mechanically polished with a diamond polishing suspension of decreasing particle size (3.0, 1.0 and 0.25 μm, Buehler) on micropolishing cloths (8 in.). After polishing, the electrode was successively sonicated in ethanol and Milli-Q water for 3 min to remove any impurities and dried with pressurized air. The Cu disk was then electrochemically polished in a solution of H_3PO_4 (85%, Suprapure, Merck) by applying +3 V versus a graphite counter electrode for 20 s and subsequently rinsed with Milli-Q water. All the electrochemical measurements were carried out using an IviumStat potentiostat (Ivium Technologies).

3.2.3 Electrolysis experiments

The electrolysis experiments were performed in the home-made PEEK H-cell containing 7.5 mL 0.1 M $KHCO_3$ electrolyte in each compartment, see Figures B.1 and B.2 for details of the cell employed. For the CO reduction experiments 0.1 M KOH + 0.2 M K_2SO_4 was used as electrolyte instead of $KHCO_3$. The PEEK H-cell was embedded in a jacket which was connected to the water bath (Ecoline e100, Lauda) to control the temperature in the cell. The temperature of the electrolyte in the cell was calibrated to the temperature of the jacket using a thermocouple in the cell

before the actual CO2RR experiments. Low partial current densities have been used to prevent heating of the electrode. [14,15] Experiments were performed in a three-electrode configuration with the reference electrode in the same compartment as the working electrode, which had a geometric surface area of 0.785 cm^2. The reference electrode was a commercial RHE (mini Hydroflex, Gaskatel). The counter electrode was a dimensionally stable anode (DSA, Magneto) and was separated from the working electrode by an anion exchange membrane (AMVN Selemion, AGC). Before electrolysis, CO_2 was purged through the electrolyte for 15 min while controlling the potential at -0.1 V vs. RHE to saturate the electrolyte and heat the electrolyte to the proper temperature. The flow of CO_2 or CO (and He for the partial pressure experiments) was controlled using a mass flow controller (SLA5850, Brooks Instrument). Next, the ohmic resistance was determined by electrochemical impedance spectroscopy (EIS) at -0.1 V vs. RHE and 85% ohmic drop compensation was performed for all chronoamperometry measurements. Chronoamperometry was performed for 60 min while CO_2 was constantly purged through a PEEK-frit (0.2 um pore size, IDEX) at 40 mL/min to increase mass transport in the cell. [13,26] At 5, 19, 32, 46 and 60 min a gas sample was analyzed online using a Shimadzu 2014 gas chromatograph with two detectors (one TCD with a Shincarbon column and one FID with a RTX-1 column). At the end of the electrolysis, a liquid sample was taken and analyzed using high performance liquid chromatography (HPLC, Shimadzu) with an Aminex HPX-87H column (Bio-rad). The 5 gas samples were averaged and combined with the HPLC data to obtain the selectivities and activities of the different products for a single experiment. The values reported are averages of at least three repetitions with twice the standard deviation as the reported error bars.[27–30] The sum of the FEs for the major products (hydrogen, CO, methane, ethylene, ethanol, formic acid and propanol) for every individual measurements is between 85 and 102%.

3.2.4 Efficiency calculations

Because the Faradaic Efficiencies (FE) become dominated by hydrogen at higher temperatures, we have defined a Carbon Efficiency (CE) to obtain better insights into how CO2RR activity itself changes at higher temperature. The CE is defined equivalently to the FE:

$$CE = \frac{c_i * a_i}{\sum_i c_i * a_i} = \frac{c_i * \frac{j_i}{n_i}}{\sum_i c_i * \frac{j_i}{n_i}} \qquad (3.1)$$

where c_i is the number of carbon atoms in product *i*, a_i is the production rate of *i* in mol/min, j_i is the corresponding partial current density and n_i is the number of electrons transferred during CO2RR for product *i*.

3.2.5 Partial pressure experiments

With the use of flow controllers, the partial pressure of CO_2 can be changed by mixing the inlet flow with He gas. He was chosen instead of Ar as He is the carrier gas used in the GC so it would not lead to broad extra peaks in the chromatogram. Controlling the partial pressure allows us to change the CO_2 concentration in the bulk electrolyte independently of temperature. We estimate the CO_2 concentration at different temperatures by using Henry's law in combination with an empirical equation to estimate Henry's constant. [31]

$$C = KP \qquad (3.2)$$

$$\log(K) = 108.3865 + 0.01985076 * T - \frac{6919.53}{T} - 40.4515 * \log(T) + \frac{669365}{T^2} \qquad (3.3)$$

where *C* is the concentration, *K* is the Henry's constant, *P* is the partial pressure and *T* is temperature.

3.2.6 Reversibility experiment

To assess whether observed changes in selectivity with temperature are reversible, 'reversibility experiments' were carried out. For the reversibility experiments, the measurement was started at -1.1 V vs. RHE at 70 °C (or 48 °C for the control experiments) in a similar way as the other electrolysis experiment. However, after 20 min, the water bath was changed with water at 35 °C to cool the cell down for 8 min. Then the temperature was increased to 48 °C and was maintained for the rest of the experiment. During this cooling and reheating of the electrolyte for 15 min in total, the potential was maintained at -0.1 V vs. RHE. Then the resistance was measured again and chronoamperometry was performed at -1.1 V vs. RHE for another 32 min.

3.2.7 Surface area determination

The electrochemical surface area was determined from the double layer capacitance. These were measured following the protocol of Morales et al. [32] The potential was scanned in a broad potential range, namely -0.2 to 0.3 V vs. RHE at sufficiently high scan rates (200 – 1400 mV/s). The capacitance was determined from the current width between the anodic and cathodic scan at 0.0 V vs. RHE

plotted against the scan rate. The slope of this graph gives the double layer capacitance. These measurements were performed before CO2RR, and after 15 min and 30 min of CO2RR at the different temperatures.

3.2.8 Raman experiments

In situ Surface Enhanced Raman Spectroscopy (SERS) was performed using an inverted confocal Raman microscope (LabRam HR, Horiba Jobin Yvon with a 50x objective and grating of 1800 lines/mm). A He/Ne laser (633 nm) was used as excitation source, which has an intensity of 8.5 mW at the sample without density filter. The acquisition time of all the Raman spectra was 10 s. An edge filter at 633 nm was used to filter the backscattered light, which was subsequently directed to the spectrograph and to the CCD detector; further details of the setup can be found in ref. 29 and 30. [33,34] The experiments were performed in a homemade jacketed three-electrode cell made of borosilicate glass, with a quartz window at the bottom. The jacket was connected to the water bath to heat the electrolyte. A platinum mesh was used as counter electrode, a Hydroflex RHE as reference electrode, and a roughened copper disk as working electrode. The copper was first polished as described above and consequently roughened by applying -1.8 V vs. a copper counter electrode for 25 s in 0.1M H_2SO_4 + 0.1 M $CuSO_4$. The same roughened copper electrode was used at all measured temperatures (i.e. 20, 30, 40, 50 and 60°C) and at each temperature 10 different, randomly picked spots on the electrode were measured. The obtained spectra were baseline corrected using the SNIP algorithm for background elimination.[35] After the background correction, a Gaussian fit was performed on the individual spectra to calculate the area of the 280 and 360 cm^{-1} peaks. The Raman shift window between 250 and 400 cm^{-1} was used for the fits, with a set boundary between the two peaks at 310 cm^{-1}. An example of the background correction and the fit can be found in Figure B.11. The ratio of the 360 and 280 cm^{-1} peaks areas was used to determine the CO coverage, following the methodology used by Zhan et al. [36] The ratio of the different spots was averaged, and only spectra where the peak intensity of the 360 cm^{-1} peak is above 500 counts were taken into account. The coverage was determined at -0.7 and -0.95 V vs. RHE. At -1.1 V too many bubbles were produced to obtain sufficient spectra with a decent signal-to-noise ratio, so we decided not to take this potential into account.

3.2.9 Lead (Pb) under-potential deposition experiments.

Lead under-potential deposition (UPD) experiments were performed to examine the copper surface for changes after electrolysis. For the Pb UPD experiments the procedure of Sebastián-Pascual et al. [37] was followed. First, electrolysis was performed for 20 min at the desired temperature in 0.1 M $KHCO_3$. Then the electrode was rinsed, dried with air and transferred to an Ar-purged glass

cell containing 0.1 M $NaClO_4$ + 1 mM NaCl + 2 mM $PbClO_4$ electrolyte. A homemade RHE was used as reference electrode and a gold wire as counter electrode. The working electrode was introduced into the electrolyte while holding the potential at 0.3 V vs. RHE and subsequently a cyclic voltammetry (CV) measurement was performed from 0.3 to 0.0 V vs. RHE at 5 mV/s, of which the second scan was used.

3.2.10 Characterization of morphology and chemical composition.

To examine the copper surface further and to inspect the surface for any deposits, scanning electron microscopy (SEM) combined with energy dispersive X-Ray spectroscopy (EDX) was performed. Micrographs of Cu after CO2RR at different temperatures (i.e., 25, 48 and 70 °C) were obtained in an Apreo SEM (ThermoFisher Scientific) with an acceleration voltage of 15 kV and an electron beam current of 0.4 nA. The chemical composition of the electrode was investigated by EDX using an Oxford Instruments X-MaxN 150 Silicon Drift detector coupled to the Apreo SEM. EDX data was processed with the Pathfinder™ X-ray Microanalysis software v1.3. The quantification of chemical elements was performed in automatic mode and the chemical composition of the electrodes was determined by averaging the chemical compositions of at least 5 different sections of the electrode surface.

3.3 Results and Discussion

3.3.1 Trends in selectivity with temperature.

Figure 3.1 shows the effect of reaction temperature on the product distribution of CO2RR on copper. This Figure shows the Faradaic Efficiencies (FEs) towards the most important products between 18 and 70 °C at -1.1 V vs. RHE in dark circles. Several trends can be observed, which can be divided into two regimes. The first regime transitions into the second regime at around 48 °C. This exact transition temperature can be debated, but 48 °C has been chosen as ethylene shows an optimum in FE and CE (Carbon Efficiency) here and the CE of CO starts to increase from this temperature onwards. In the first regime, the hydrogen evolution reaction (HER) selectivity remains constant, while in the second regime it increases significantly with temperature up to 84% FE at 70 °C. Of the CO_2 reduction products, methane and formic acid show a strong decreasing trend with temperature in both regimes. The selectivity towards CO stays reasonably stable, except for the highest temperature at 70 °C. The C2+ products increase in the first regime, while they decrease in the second regime resulting in an optimum in FE around 40-48 °C.

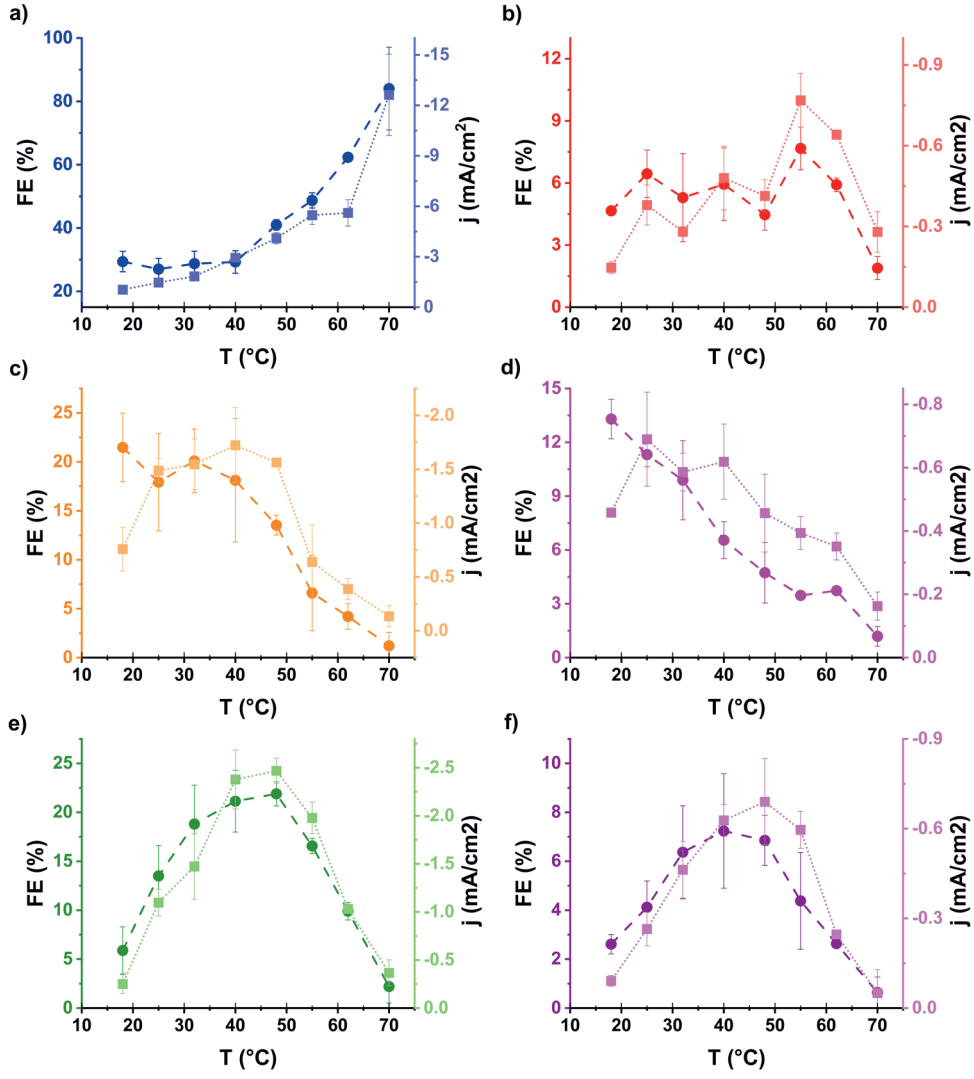

Figure 3.1 Faradaic Efficiency (in dark circles) and partial current density (in light squares) during CO2RR at different reaction temperatures in 0.1 M $KHCO_3$ at -1.1 V vs. RHE for a) hydrogen b) formic acid c) CO d) ethylene e) methane and f) ethanol. The error bars are determined from at least 3 separate experiments. The gray background indicates the second regime and the dotted lines are a guide to the eye.

Figure 3.1 shows the corresponding activity trends of all these products in the same temperature range in light squares. Initially, the activity towards all products increases with temperature, although the increase for the C2+ products is more significant than for the other carbon products. The activity towards the C2+ products shows an optimum at ~ 40-48 °C, similar to the FE trend. The activity towards methane and formic acid clearly decreases from 40 °C onwards and CO shows an optimum around 55 °C. Liquid products, especially ethanol, might evaporate at elevated temperatures. However, we do not think this significantly affects the results as we have not observed ethanol in the GC, and ethanol follows a similar trend as ethylene. The HER rate increases steadily with temperature and shows a large increase at around 70 °C, for which temperature there is also a sudden increase in overall current as can be seen in Figure 3.2a. This Figure shows that the total current density increases with increasing temperature, although the current density decreases slightly from 48 °C to 62 °C due to the fast decrease in CO_2 reduction activity, after which HER takes over and the total current density increases rapidly at higher temperatures.

Figure 3.2a and b show that the total activity for CO_2 reduction increases in the first regime and decreases in the second at -1.1V vs RHE, regardless if we look at CO_2 consumption or current density for CO2RR. The CO_2 consumption has been back calculated from the partial current densities of the CO2RR products. To clearly identify the temperature effect on the CO2RR pathways, we define a carbon efficiency (CE), which is essentially the FE but excluding H_2. The optimum found in CO_2 consumption around 40-48 °C is also observed in CE for the C2+ products, as can be seen in Figure B.3. The trends in CE are mostly similar to the trends in the FEs, although the two regimes are more pronounced in de CE graphs. Methane shows similar trends in FE and CE, although in the CE a rapid decrease is visible when switching between regimes. On the other hand, CO and HCOOH show significantly different trends in the CE compared to the FE, because the FE for H_2 changes strongly with temperature. The CE towards CO (Figure 3.2c) remains stable in the first regime but increases significantly at high temperatures in the second regime. Formic acid shows decreasing CE in the first regime (just as for the FE), but in the second regime it increases slightly. Therefore, at the higher temperatures, CO2RR mostly (>70% at 70 °C) produces the most simple C1 products, namely HCOOH and CO.

Experiments at different potentials (-0.95 and -0.7 V) were performed to assess if these trends hold at other potentials as well. Figure 3.2b shows that the optimum in CO_2 consumption is most pronounced at the highest overpotential. Figures B.2 and B.4 show the FE and CE at -0.95 V vs. RHE, which was chosen as it is near the onset of C2+ formation. This results in the same products as at -1.1 V, but generated

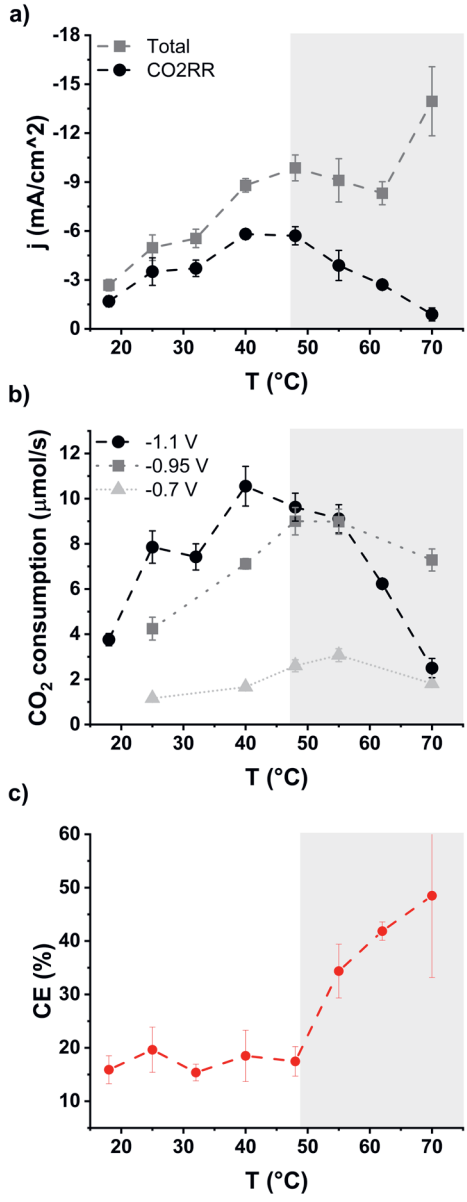

Figure 3.2 a) Total current density and current density towards CO2RR at -1.1 V vs. RHE b) Total consumption of CO_2 during CO2RR at different reaction temperatures in 0.1 M $KHCO_3$ at -1.1 V, -0.9 V and -0.7 V vs. RHE c) Carbon efficiency towards CO at -1.1 V vs RHE, CEs for other products can be found in Figure B.3. The error bars are determined from at least 3 separate experiments. The gray background indicates the second regime and the dotted lines are a guide to the eye.

at lower currents so that probably there is lower local pH and there are less pronounced mass transport limitations. Most of the trends are quite similar to -1.1 V vs. RHE, although the FEs for the multi-carbon products are much lower than at -1.1 V vs. RHE. There is an optimum in both CE and FE for C2+ products at 48 °C, whereas the hydrogen selectivity increases in the second regime. Main differences are that the CE towards HCOOH does not increase at high temperatures, instead mainly CO is the favored carbon product. Moreover, the FE towards CO decreases with temperature, although the CE increases in the second regime similarly to the situation at -1.1 V. The decrease of FE for CO might be linked to the lack of CH_4 formation. As there is already hardly any methane at 25 °C, its selectivity cannot decrease with temperature. However, ethylene, ethanol and hydrogen still show an increased FE with temperature, so that the FE for some other product(s), i.e., CO and HCOOH, should be decreasing.

Figures B.6 and B.7 show the FE and CE at -0.7 V vs. RHE, which was chosen as only HCOOH, CO and H_2 are produced. At this potential, similar trends in FE are observed; HCOOH decreases and CO remains reasonably stable except at 70 °C, at which temperature it drops rapidly. Hydrogen mostly increases with temperature although the first point at 25 °C does not fit this trend. We attribute this to the very small amounts of hydrogen produced at this temperature. This is close to the detection limit of our GC, which makes these measurements less accurate, thus overestimating the amount of hydrogen. Higher temperatures lead to an increasing carbon efficiency for CO, which is also observed at -0.95 V vs. RHE. At -1.1 V vs. RHE, not only the carbon efficiency towards CO but also towards HCOOH is increased at high temperatures. This increase seems mainly due to the fast decrease in CE of the C2+ products, which results in a relative increase in CE towards CO and HCOOH.

3.3.2 CO_2 concentration and mass transport

In all the results discussed above, the temperature change is convoluted with a change in CO_2 concentration in the electrolyte. This effect can be corrected for by performing partial pressure experiments in which the concentration of CO_2 can be adjusted independently of the temperature. Figure B.8 shows the effect of the bulk CO_2 concentration on the FE at 25 °C. The chosen concentrations are equivalent to the maximum CO_2 concentrations at 25, 40, 55, 70 and 85 °C in equilibrium with 1 atm of CO_2. A lower CO_2 bulk concentration leads to an increase in hydrogen evolution, however not nearly as much as in Figure 3.1. With decreasing partial pressure, the FE towards methane increases, while the FEs for HCOOH and CO decrease. The FE towards C2+ products is not significantly affected by the changing CO_2 concentration. These results mostly agree with literature, in which either the partial pressure was changed,[38,39] or the local CO_2 availability was determined.[40]

Other studies found that the ethylene activity can increase with slightly lowered partial pressures of CO_2,[41] in agreement with our observations.

In Figure B.9, the concentration of CO_2 was kept constant at different temperatures by changing the partial pressure accordingly. All measurements were performed with 14 mM of CO_2 in the bulk. This concentration is equivalent to the concentration at 70 °C at 1 atm of CO_2 as calculated with equations 3.2 and 3.3. The trends observed here are very similar to the trends observed in Figure 3.1: there is an increase in selectivity towards hydrogen, a decrease towards methane formation, and an optimum in C2+ product formation. However, the FE for CO is slightly different as it now also seems to show an optimum at 55 °C. Furthermore, the HCOOH selectivity seems to be stable, except at the highest temperature. From these results we conclude that most trends in Figure 3.1 are caused directly by the increase in temperature and not indirectly by the decrease in CO_2 solubility with increasing temperature. However, formic acid is an exception to this observation as the change in selectivity seems mostly governed by the changes in the CO_2 bulk concentration, suggesting that formic acid is made in a different pathway from the other products. Moreover, the steadiness in CO selectivity appears to be due to the convolution of the enhancing effect of temperature and decreasing effect of the CO_2 concentration.

The large drop in FE towards CO at 70 °C at -1.1V vs. RHE and the sharp increase in activity for HER at this temperature might indicate that there are some mass transport limitations at this temperature. We have shown before that efficient mass transport becomes more important at higher temperatures, [16] due to higher current densities and higher rates of the homogeneous reaction with OH^- generated at the surface.[42,43] In our experiments, CO_2 was bubbled through the cell at 40 sccm, which is the limit of our setup. This high flow rate, in combination with a PEEK frit, is to facilitate mass transport and prevent CO_2 depletion, [13,26] but it might not be sufficient. When the mass transport boundary layer is not optimized, this can influence the selectivities significantly. [26] To check whether an unoptimized mass transport boundary layer is involved in the observed trends, we have performed some experiments with enhanced mass transport by stirring the electrolyte with a small stirring bar in the cathode chamber. Figure B.10 shows that all trends observed in Figure 3.1 do not significantly change when mass transport is improved. This indicates that the trends observed in this study are not caused by insufficient mass transport due to un unoptimized boundary layer. Local pH on the other hand is not influenced significantly by better convection [44] and could still cause the changes in selectivity as will be discussed later.

Comparing our trends to the trends observed by Ahn et al., [21] their study shows a similar decrease in the selectivity towards methane and an increase towards hydrogen with increasing temperature, although in our case hydrogen selectivity only increases at the highest temperatures (from 48 °C onwards, which was not included in their work, which was limited to 42 °C). They also observe an optimum in ethylene selectivity but at lower temperature (22 °C). Their trends in FE towards CO and HCOOH are not very distinct, although the activity of CO formation clearly increases with temperature. We suspect that some of these differences are due to mass transport limitations as in their experiments the HER already dominates at 42 °C. Ahn et al. attributed some of their trends to the temperature dependence of the solubility of CO_2, but our experiments show that this effect cannot explain most of the trends observed.

3.3.3 First regime; CO coverage

To assess whether the observed trends in the first temperature regime (i.e., below 48 °C) could be related to a temperature dependent CO coverage on the copper electrode surface, we have performed in situ Surface-Enhanced Raman Spectroscopy (SERS) experiments. SERS is ideally suited to study CO2RR on Cu electrodes, due to the ability to probe reaction intermediates, electrolyte species and the electrode surface simultaneously.[45] It is inferred that with increasing CO coverage, the rate of CO dimerization should be favored [46–49] and therefore one expects the production of ethylene or ethanol to be related to the CO coverage. Zhan et al. [36] suggested a qualitative SERS-based measure of (the potential-dependence of) surface CO coverage, namely the peak ratio between the Raman peaks at 360 cm^{-1} (assigned to the Cu-C vibration of *CO on Cu) and 280 cm^{-1} (assigned to the Cu-CO twisted rotation or bending vibration). They postulated that a decrease in the 280 cm^{-1} band intensity compared to the 360 cm^{-1} band is indicative of high *CO coverage, because multiple *CO close together will frustrate the Cu-CO bending vibration.[29]

Figure 3.3a shows an example of an unprocessed Raman spectrum with these two peaks. Figure B.11 gives more details how this data was processed to obtain the peak area ratios. Figure 3.3b shows that the coverage of *CO is not only affected by the potential, but also by the temperature. With increasing temperature, the peak ratio, and the coverage of CO, increases both at -0.7 and -0.95 V vs. RHE, which could explain the increase in C2+ products in the first regime. Literature suggests that the coverage at -0.95 is higher than at -0.7 V, which we also observe at all temperatures.[36] In the SI and Figures B.12-B.16, the Raman data and analysis are discussed in more detail. From this analysis of the Raman spectra, we conclude an increasing trend in CO coverage with temperature, independently of the exact

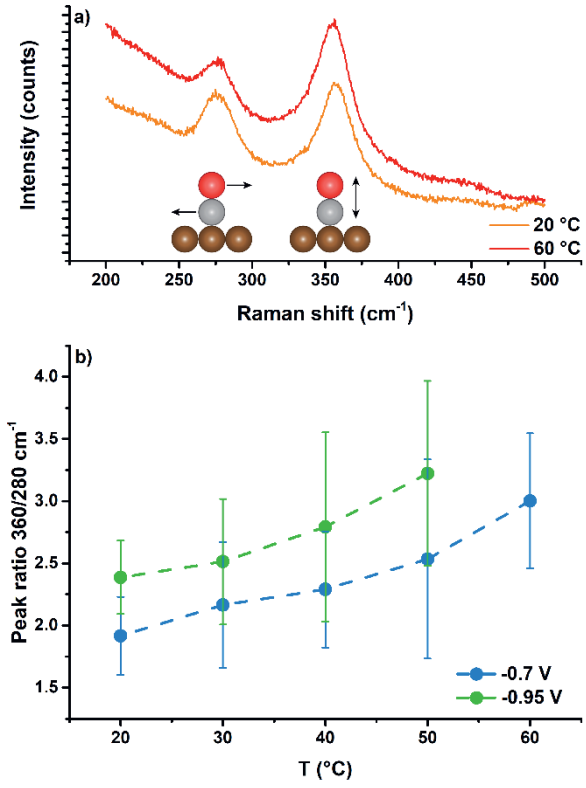

Figure 3.3 a) Unprocessed Raman spectrum at 20 and 60 °C and -0.7 V vs RHE, representative for the other Raman spectra b) The ratio between the 360 cm^{-1} and 280 cm^{-1} Raman peak areas on Cu in 0.1 M $KHCO_3$ as a function of reaction temperature, at -0.7 V and -0.95 V vs. RHE. The error bars are composed of at least 4 spectra and the dotted lines are a guide to the eye.

methods used to analyze the data. With our dataset, it is only possible to make a qualitative statement, but we consider this sufficient for the purpose of this research.

As adsorption is an exothermic process, we would expect the coverage to decrease with temperature based on a simple Langmuir isotherm (equation 3.4) as the equilibrium constant *K* should decrease with temperature according to the van 't Hoff equation. However, the local CO pressure can increase with increasing temperature because the rate of the CO_2 reduction to CO production becomes higher at higher temperature. This would lead to a higher local CO concentration near the Cu surface [50] and consequently the CO coverage.

$$\theta = \frac{Kp_a}{1+Kp_a} \qquad (3.4)$$

with θ the coverage, K the equilibrium constant, and p_a the (local) pressure or concentration.

Additionally, it has been proposed that significant amounts of CO_2 are absorbed on the surface, thereby blocking part of the surface. [41,51] It could be that due to the lower CO_2 concentration, in combination with more active reduction, less adsorbed CO_2 ($*CO_2$) is blocking part of the Cu surface at elevated temperatures. Therefore, more CO can adsorb at the catalyst surface and thereby C-C coupling is facilitated when the temperature increases in the first regime. [41]

From equation 3.4, one would expect the CO coverage should decrease during CO reduction as both K and p_a would decrease with temperature, because CO is not generated in situ and its solubility decreases with temperature. Thus, the temperature trend for CO reduction is expected to be different than for CO_2 reduction, if the CO coverage is an important factor. Figures B.17 and B.18 show that for CO reduction indeed there is no optimum between 20 and 70 °C for both the C2+ products selectivity and activity. The FE towards ethylene decreases slowly up to 50 °C and then more rapidly from 50 to 70 °C. This is accompanied by a stable activity towards ethylene up to 50 °C, which starts to decrease at higher temperatures. These results confirm that the CO coverage is an important parameter affecting the C2+ formation rate. The increasing CO coverage with temperature during CO2RR thus provides a plausible explanation for the increase in C2+ products with increasing temperature during CO2RR.

3.3.4. Kinetics and local pH

Although the coverage of CO can be linked to the selectivity trends observed in the first regime, the temperature dependence of CO_2 reduction is a complicated interplay of direct and indirect effects.[16] Temperature has a direct effect on the kinetics of the reactions via the Arrhenius equation. As the reaction pathways towards different products have different activation energies (E_a), the changes in kinetics for each product should result in different selectivities. We have shown previously that on a gold electrode, the (apparent) E_a for the CO2RR towards CO is higher than for the HER, which results in an increase in CO selectivity with increasing temperature. [16] With our dataset it is difficult to determine reliable apparent activation energies of the different products on copper (see SI and Figure B.19-20 for a further discussion). Only for HER a relatively accurate value could be determined, although this value is significantly lower than the value determined by

Zong et al. (38 ± 2 kJ/mol vs. ~ 60 kJ/mol, respectively). [24] They also show that methane has a significant lower apparent activation energy compared to both CO and ethylene. These results indicate that kinetics could give an explanation for the trends observed as methane selectivity decreases, while hydrogen selectivity increases with temperature. However, it is difficult to obtain accurate experimental data on the activation energies for CO2RR on copper, due to the large variety of products, and presumably even more difficult to interpret them.

An indirect effect of the temperature rise is an increase in local pH, as a result of the higher current densities related to a higher OH^- production. This local pH increase will certainly influence the reaction rates and the corresponding product distribution. Higher local pH is beneficial for ethylene selectivity, while it inhibits both HER and methane formation. [40,52,53] However, there is an optimum in the influence of the local pH and when increased too much the selectivity towards ethylene decreases again. [53,54] When the local pH is too high, the OH^- near the surface reacts with CO_2 to form bicarbonate via the homogeneous reaction, [42,43] lowering the CO_2 concentration near the surface, which causes the FE for hydrogen to increase. [54]

In this perspective, the trend in total CO_2 consumption at different potentials is interesting (Figure 3.2b). At lower potentials, the current densities are lower and the optimum in CO_2 consumption shifts to higher temperatures. This suggests that at a certain point the local CO_2 availability will be limited due to a high local pH. Moreover, the total CO_2 consumption at 70 °C is higher at -0.95 V than at -1.1 V, indicating that a too high local pH can be a factor in the second regime. However, at -0.95 V the HER dominates the FE at 70 °C, even though significant amounts of CO_2 are still being consumed. Furthermore, the total current density at -1.1 V slightly decreases at the start of the second regime (Figure 3.2a), so it is unlikely that the local pH increases in this region. However, a similar local pH might have a larger effect as there is a lower bulk concentration of CO_2. Moreover, even at -0.7 V vs. RHE, the activity of CO2RR decreases with increasing temperature, although the total current density is significantly lower than at -1.1V vs. RHE. This indicates that the increase in FE for HER under these conditions is not solely related to a lack of CO_2 due to a too high local pH. Furthermore, the trends in product distribution are similar at both potentials, as also at -0.95 V CO_2 is mostly converted towards CO and less C_2H_4 is produced at the highest temperatures (Figure B.4). This indicates that the decrease in C2+ products in the second regime is likely not exclusively due to the changes in the local pH.

Summarizing, the trends observed in the first regime between 18 and 48 °C can probably be explained by a combination of CO coverage, differences in kinetics and

local pH. With higher temperatures, the rate of CO2RR to CO increases, and hence the CO coverage increases, boosting the C2+ formation. The local pH also increases, which is less favorable for methane formation and better for ethylene. Moreover, the activation energy for methane seems to be smaller than for the other CO2RR products, although activation energies are difficult to determine and interpret. The lower CO_2 bulk concentration with increasing temperature cannot be linked to most observed selectivity trends. However, it is probably the main reason for the decrease in formic acid selectivity. On the other hand, this decrease might also indicate a lower coverage of the OCHO* intermediate, which has been suggested as a key intermediate for HCOOH formation. [55]

3.3.5. Second regime; surface change

In the second regime, the CO2RR activity decreases significantly at higher temperatures and HER dominates. This seems not due to the lower bulk CO_2 concentration as shown with partial pressure experiments; however, a too high local pH probably does have some contribution here. To check if this apparent deactivation might also be related to a change in the copper surface at elevated temperatures, we have performed electrochemical surface characterization experiments. Figures 4, S21 and S22 show cyclic voltammograms (CV) of Pb underpotential deposition (UPD) on the Cu electrode after CO_2 reduction at different temperatures. Pb UPD is known to be sensitive to the structure of the Cu surface. [37] The blank CV (Figure B.21a) was measured before CO2RR but after the polishing procedure and shows two major peaks in the reduction scan. The peak at 0.07 V vs. RHE is attributed to Cu(100) sites and the peak at 0.10 V vs. RHE to Cu(111) sites. [37] In the oxidation scan, the peaks are more convoluted as the Cu(100) peak is less reversible compared to the Cu(111) peak. The shape of the CV stays similar to the blank up to 48 °C, although the peaks shift slightly positively and become gradually smaller. The smaller peak areas indicate that the surface smoothens at higher temperatures, as the Pb UPD can also be used qualitatively to measure the electrochemical surface area (ECSA). [37] However, as the shape of the CVs stays the same, no major surface changes are likely to take place up to 48 °C. On the other hand, when the temperature is increased beyond 48 °C, the Pb UPD CV changes drastically. At 55 °C, the Cu(100) peak seems to disappear and the Cu(111) broadens. However, the exact change in the CV is not reproducible, whereas it was very reproducible at the lower temperatures (Figure B.21e). At 70 °C, the changes are even more pronounced as the Pb UPD peaks almost completely disappear.

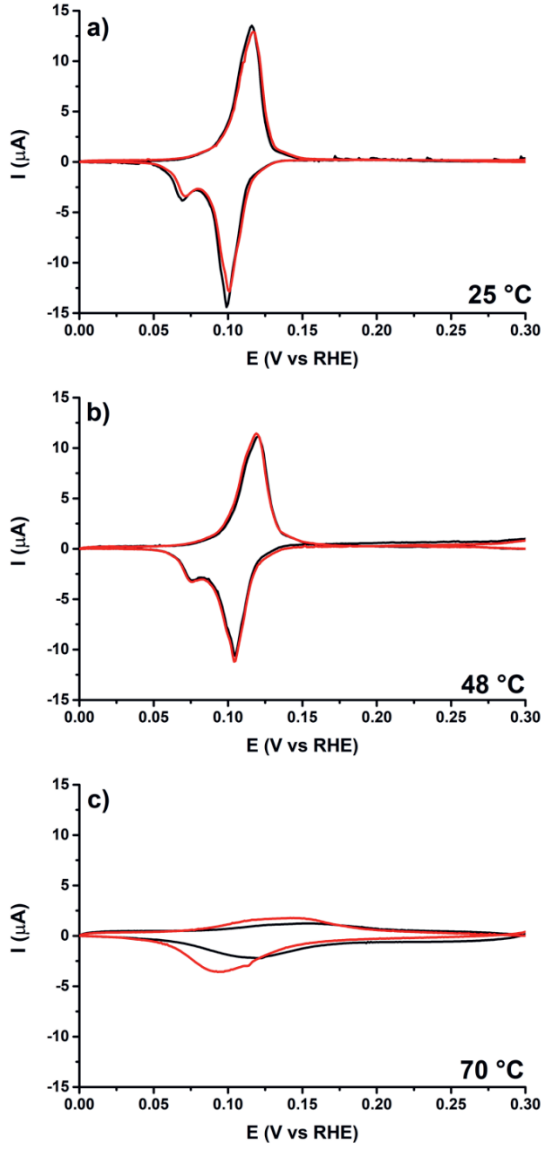

Figure 3.4: Pb UPD CVs from 0.0 to 0.3 V vs. RHE at 5 mV/s in 0.1 M $NaClO_4$ + 1mM NaCl + 2 mM $PbClO_4$ after CO2RR for 20 min at -1.1 V vs. RHE in 0.1 M $KHCO_3$ at a) 25 °C b) 48 °C c) 70 °C. The red and black line represent two different measurements to illustrate reproducibility.

From these observations, it is clear that the copper surface undergoes substantial changes at high temperature, but it is unclear what these changes entail exactly as the Pb UPD peaks are not observed anymore. Carbon might deposit on the copper surface at higher temperatures, comparable to surface chemistry reactions taking place in thermocatalytic processes, although for CO_2 reduction to methanol on Cu coking is normally not a significant cause of deactivation. [56] On the other hand, it has been claimed that coking can occur during electrochemical CO_2 reduction as well. [57,58] This could explain the broadening and eventually disappearance of the Pb UPD peaks. However, EDX measurements (see Figure B.24) show that although some carbon can be detected at the copper surface, the composition of the Cu electrode does not change after CO2RR at different temperatures. The carbon can be due to the SEM beam itself [59] and as the amount of carbon does not change with different samples, we assume that no deposit is formed during CO2RR. The observed oxygen is most likely due to the oxidation of the copper surface during the transfer through air from the electrochemical cell to the SEM-EDX. However, a recent theoretical study suggests that oxygen diffuses faster from the bulk to the surface at higher temperatures causing the residual Cu_2O to be reduced quicker, [60] which might change the nature of the copper catalyst and its selectivity. Similar to the Pb UPD measurements, the SEM images indicated that the surface becomes smoother at higher temperatures (Figure B.25).

Double layer capacitance studies have been performed to confirm this smoothening in a quantitative manner. This technique gives an indication of the roughness factor and these measurements confirm that at higher temperatures the surface becomes less rough (Figure B.26 and S27). Interestingly, it seems that this difference is mainly due to a roughening of the surface after CO2RR at 25 °C, while at 40 and 55 °C the surface roughness does not significantly change after CO2RR. At 70 °C, the surface actually seems to become smoother during electrolysis.

Recently, the group of Buonsanti [61,62] showed that Cu dissolves under negative applied potentials, with subsequent redeposition on the electrode roughening the electrocatalyst surface. Based on their results, we hypothesize that this dissolution can be promoted by small amounts of oxygen in the system as they show the dissolution is enhanced in air.[62] Even though CO_2 is being purged throughout the experiment, we cannot guarantee that the cell is completely oxygen free. At higher temperatures, surface diffusion of the copper atoms is expected to be enhanced. This process might be facilitated by CO produced on the surface, equivalent to the increased Cu surface mobility with CO in gas phase. [63] Since the CO coverage increases with increasing temperature, more CO is available to smoothen the surface. A combination of these processes could explain why smoother copper surfaces are observed at higher temperatures. A more flat surface indicates that

there are fewer defects and the surface is more ordered. Such surfaces tend to mainly produce hydrogen, whereas hydrocarbons tend to be formed at the defect sites. [64] A smoother surface at high temperature could thus be one of the reasons for the increase in hydrogen evolution.

Thus, the copper surface changes with temperature, both gradually over the entire temperature range and rapidly at temperatures higher than 48 °C. However, it is unknown what these changes are exactly and how they are related to the trends in selectivity observed.

3.3.6. Reversibility of temperature effect

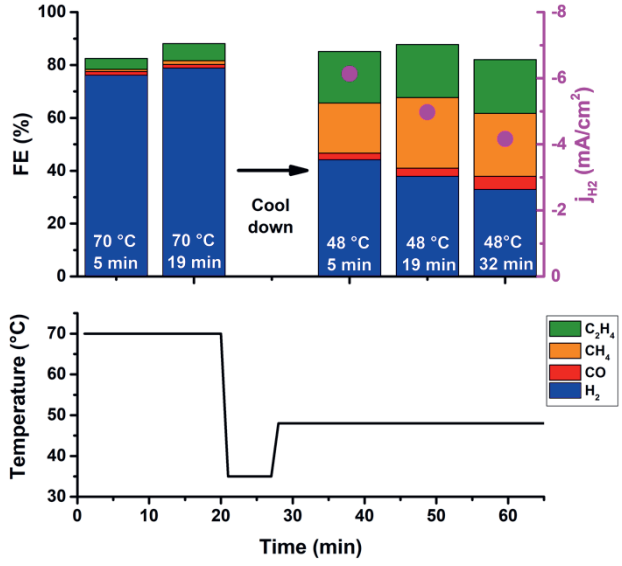

Figure 3.5 Reversibility experiments; the Faradaic Efficiency (FE) of the gaseous products of CO2RR at -1.1V vs. RHE at 70 °C after 5 and 19 min, and after cooling down at 5, 19 and 32 min at 48 °C. The current density of HER is shown with the magenta dots (at 70 °C, these are too large and fall of the scale). The lower panel shows the temperature profile of the water bath.

At high temperature, copper mainly produces hydrogen, whereas the optimum in the ethylene production is at 48 °C. However, this change in selectivity can be reverted when the same Cu electrode is cooled down again from 70 °C to 48 °C, as shown in Figure 3.5. This can be compared to the control experiment at 48 °C in Figure B.28. Even when the catalyst has experienced CO2RR at high temperature and its surface has changed, it can still produce comparable amounts of ethylene

and methane as when the catalyst remains at maximum 48 °C (see Figure B.28). Interestingly, the selectivity keeps changing with time after the electrode is cooled down from 70 °C to 48 °C, especially the hydrogen activity decreases with time. The changes in selectivity are thus reversible, although not instantaneous. Remarkably, the changes seen in the Pb UPD are not reversible. If the Cu electrode is first used at 70 °C and then CO2RR is performed at 48 °C, the Pb UPD is still comparable to the Pb UPD of the electrode which was only used at 70 °C (Figure B.23). This observation complicates the interpretation: even though the change in the copper surface and the optimum in activity coincide, this might be just a coincidence and the changes on the surface of the copper might not be the cause of the deactivation of the CO2RR in the second regime.

3.4 Conclusion

In this work, we have investigated the effect of the reaction temperature between 18 and 70 °C on the CO_2 reduction on copper. We observe that it is beneficial to work at elevated temperatures and the optimal temperature for CO2RR electrolysis would be ~ 48 °C. Different products respond differently to the reaction temperature. The selectivity of methane and formic acid decreases with increasing reaction temperature, while the C2+ products show an optimum in both selectivity and activity around 48 °C. At high temperature (e.g., 70 °C), the Faradaic Efficiency for hydrogen evolution dominates, while CO_2 is mostly reduced to CO. The temperature range can thus be divided in two regimes: a first regime from 18 up to ~ 48 °C, in which C2+ production increases and hydrogen evolution selectivity stays fairly constant, and then a second, high temperature, regime from 48 to 70 °C, in which hydrogen starts to dominate and the activity of CO2RR decreases. Our results show that for industrial applications at elevated reaction temperatures, it will be crucial to find strategies to limit HER and that temperature is a crucial parameter to consider for CO2RR, also in GDE setups. Furthermore, we show that CO reduction does not experience an optimum in C2+ products, which can have implications if one would use a cascade reaction to produce C2+ products at elevated temperatures.

The observed trends are not simply due to the balance of reaction kinetics and CO_2 solubility. Although kinetics will certainly play a role in the first regime, also an increase in both the CO coverage (as determined with Raman spectroscopy) and the local pH will result in a change in the selectivities For the second regime it is more difficult to determine the exact causes of the decrease in CO2RR activity, although with partial pressure experiments we showed that this is not due to the decreasing CO_2 bulk concentration. Pb UPD and double layer capacitance studies show substantial structural changes in the copper surface at these high temperatures,

which may be related to the changing selectivities. Moreover, this decrease could be partially due to a too high local pH. Future experiments will have to consider using a GDE setup to improve mass transport and see if the onset of the second regime is intrinsic to copper or due to the system used. Moreover, elevated pressures could be used to increase the solubility of CO_2, which allows to study the effect of pressure and temperature, especially from the second, high temperature, regime onwards, more deeply.

References

1. Van Der Giesen, C., Kleijn, R. & Kramer, G. J. *Environ Sci Technol* **48**, 7111–7121 (2014).
2. Seh, Z. W. *et al. Science (1979)* **355**, eaad4998 (2017).
3. Hatsukade, T., Kuhl, K. P., Cave, E. R., Abram, D. N. & Jaramillo, T. F. *Physical Chemistry Chemical Physics* **16**, 13814–13819 (2014).
4. Hori, Y., Wakebe, H., Tsukamoto, T. & Koga, O. *Electrochim Acta* **39**, 1833–1839 (1994).
5. Raciti, D. & Wang, C. *ACS Energy Lett* **3**, 1545–1556 (2018).
6. Bagger, A., Ju, W., Varela, A. S., Strasser, P. & Rossmeisl, J. *ChemPhysChem* **18**, 3266–3273 (2017).
7. Kuhl, K. P., Cave, E. R., Abram, D. N. & Jaramillo, T. F. *Energy Environ Sci* **5**, 7050–7059 (2012).
8. De Luna, P. *et al. Science (1979)* **364**, eaav3506 (2019).
9. Sisler, J. *et al. ACS Energy Lett* **6**, 997–1002 (2021).
10. Lee, M. Y. *et al. Crit Rev Environ Sci Technol* **50**, 769–815 (2020).
11. Jhong, H. R. M., Ma, S. & Kenis, P. J. *Curr Opin Chem Eng* **2**, 191–199 (2013).
12. Krause, R. *et al. Chemie Ingenieur Technik* **92**, 53–61 (2020).
13. Lobaccaro, P. *et al. Physical Chemistry Chemical Physics* **18**, 26777–26785 (2016).
14. Iglesias Van Montfort, H. P. & Burdyny, T. *ACS Energy Lett* **7**, 2410–2419 (2022).
15. Corral, D. *et al. Energy Environ Sci* **14**, 3064–3074 (2021).
16. Vos, R. E. & Koper, M. T. M. *ChemElectroChem* **9**, e20220023 (2022).
17. Dufek, E. J., Lister, T. E. & McIlwain, M. E. *J Appl Electrochem* **41**, 623–631 (2011).
18. Löwe, A. *et al. ChemElectroChem* **6**, 4497–4506 (2019).
19. Mizuno, T. *et al. Energy Sources* **17**, 503–508 (1995).
20. Kim, H. Y. *et al. Int J Hydrogen Energy* **39**, 16506–16512 (2014).
21. Ahn, S. T., Abu-baker, I. & Palmore, G. T. R. *Catal Today* **288**, 24–29 (2017).
22. Ahn, S. T., Sen, S. & Palmore, G. T. R. *Nanoscale* **14**, 13132–13140 (2022).
23. Hori, Y., Kikuchi, K., Murata, A. & Suzuki, S. *Chem Lett* **15**, 897–898 (1986).
24. Zong, Y., Chakthranont, P. & Suntivich, J. *Journal of Electrochemical Energy Conversion and Storage* **17**, 1–7 (2020).
25. Wuttig, A. & Surendranath, Y. *ACS Catal* **5**, 4479–4484 (2015).
26. Clark, E. L. *et al. ACS Catal* **8**, 6560–6570 (2018).
27. Arán-Ais, R. M., Scholten, F., Kunze, S., Rizo, R. & Roldan Cuenya, B. *Nat Energy* **5**, 317–325 (2020).
28. Li, F. *et al. Nature* **577**, 509–513 (2020).
29. Kim, C. *et al. Nat Energy* **6**, 1026–1034 (2021).
30. Wang, M. *et al. Chem Sci* **13**, 12673–12680 (2022).
31. Plummer, L. N. & Busenberg, E. *Geochim Cosmochim Acta* **46**, 1011–1040 (1982).
32. Morales, D. M. & Risch, M. *Journal of Physics: Energy* **3**, 34013 (2021).
33. Diaz-Morales, O., Calle-Vallejo, F., De Munck, C. & Koper, M. T. M. *Chem Sci* **4**, 2334–2343 (2013).

34. Lai, S. C. S., Kleyn, S. E. F., Rosca, V. & Koper, M. T. M. *Journal of Physical Chemistry C* **112**, 19080–19087 (2008).
35. Caccia, M. *et al. Educational Note* **2**, ED3163 (2013).
36. Zhan, C. *et al. ACS Catal* **11**, 7694–7701 (2021).
37. Sebastián-Pascual, P. & Escudero-Escribano, M. *Journal of Electroanalytical Chemistry* **896**, 115446 (2021).
38. Schreier, M., Yoon, Y., Jackson, M. N. & Surendranath, Y. *Angewandte Chemie - International Edition* **57**, 10221–10225 (2018).
39. Moradzaman, M., Martínez, C. S. & Mul, G. *Sustain Energy Fuels* **4**, 5195–5202 (2020).
40. Veenstra, F. L. P., Ackerl, N., Martín, A. J. & Pérez-Ramírez, J. *Chem* **6**, 1707–1722 (2020).
41. Song, H., Song, J. T., Kim, B., Tan, Y. C. & Oh, J. *Appl Catal B* **272**, 119049 (2020).
42. Marcandalli, G., Villalba, M. & Koper, M. T. M. *Langmuir* **37**, 5707–5716 (2021).
43. Zhang, B. A., Ozel, T., Elias, J. S., Costentin, C. & Nocera, D. G. *ACS Cent Sci* **5**, 1097–1105 (2019).
44. Liu, X., Monteiro, M. C. O. & Koper, M. T. M. *Physical Chemistry Chemical Physics* **25**, 2897–2906 (2023).
45. de Ruiter, J. *et al. J Am Chem Soc* **144**, 15047–15058 (2022).
46. Sandberg, R. B., Montoya, J. H., Chan, K. & Nørskov, J. K. *Surf Sci* **654**, 56–62 (2016).
47. Huang, Y., Handoko, A. D., Hirunsit, P. & Yeo, B. S. *ACS Catal* **7**, 1749–1756 (2017).
48. Kong, X. *et al. Nano Lett* **22**, 3801–3808 (2022).
49. Wang, C. *et al. Mater Adv* 4964–4972 (2022).
50. Louisia, S. *et al. Proc Natl Acad Sci U S A* **119**, 1–9 (2022).
51. Singh, M. R., Goodpaster, J. D., Weber, A. Z., Head-Gordon, M. & Bell, A. T. *Proceedings of the National Academy of Sciences* **114**, E8812 LP-E8821 (2017).
52. Varela, A. S., Kroschel, M., Reier, T. & Strasser, P. *Catal Today* **260**, 8–13 (2016).
53. Raciti, D., Mao, M., Park, J. H. & Wang, C. *J Electrochem Soc* **165**, F799–F804 (2018).
54. Lum, Y., Yue, B., Lobaccaro, P., Bell, A. T. & Ager, J. W. *Journal of Physical Chemistry C* **121**, 14191–14203 (2017).
55. Feaster, J. T. *et al. ACS Catal* **7**, 4822–4827 (2017).
56. Twigg, M. V. & Spencer, M. S. *Top Catal* **22**, 191–203 (2003).
57. Lim, C. F. C., Harrington, D. A. & Marshall, A. T. *Electrochim Acta* **238**, 56–63 (2017).
58. Xie, J. F. *et al. Electrochim Acta* **139**, 137–144 (2014).
59. Was, G. S. *et al. Nucl Instrum Methods Phys Res B* **412**, 58–65 (2017).
60. Lian Z, Dattila F & López N. *ChemRxiv. Cambridge: Cambridge Open Engage;* (2023).
61. Vavra, J., Shen, T., Stoian, D., Tileli, V. & Buonsanti, R. *Angewandte Chemie International Edition* **60**, 1347–1354 (2021).
62. Vavra, J. *et al.* (2022).
63. Eren, B. *et al. Science (1979)* **351**, 475–478 (2016).
64. Scholten, F., Nguyen, K. C., Bruce, J. P., Heyde, M. & Roldan Cuenya, B. *Angewandte Chemie* **133**, 19318–19324 (2021).

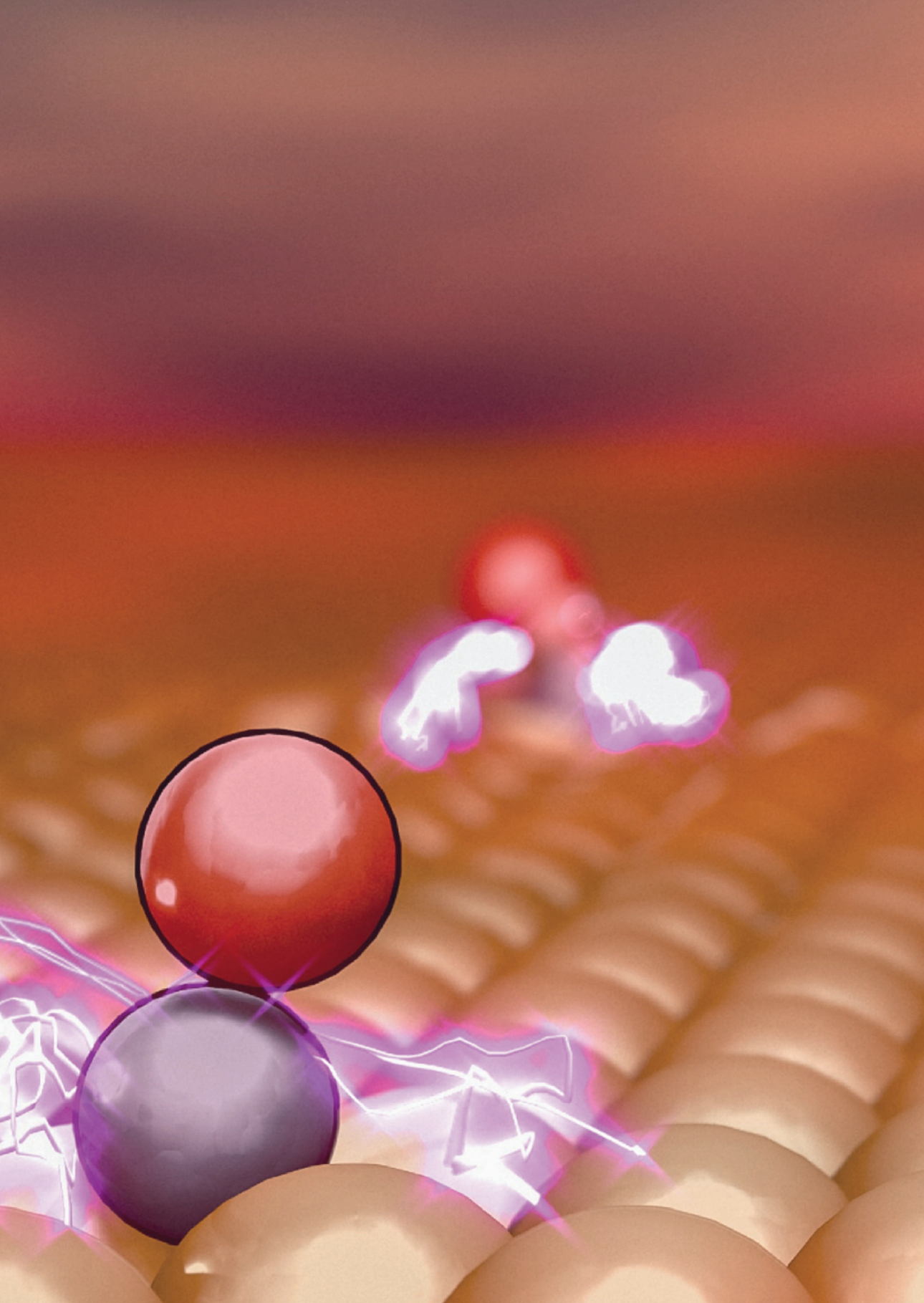

4

The temperature dependence of electrochemical CO_2 reduction on Ag and CuAg alloys

This chapter is based on R.E. Vos, J.S. Smaak, M.T.M. Koper *Journal of Catalysis* 115613 (2024)

Abstract:
Ag is often studied as catalyst for electrochemical CO_2 reduction as it shows high selectivity towards CO and is easily alloyed with Cu to enhance performance using CuAg catalysts. In this study, we investigated the effect of temperature on Ag and CuAg catalysts and compare these with previous results on Au and Cu catalysts. We show that the temperature effect is complicated as it shows an interplay with CO_2 concentration, potential and mass transport. It is therefore crucial to deconvolute these parameters and study the effect of temperature under different conditions. Moreover, we show that alloying Ag with Cu can inhibit some of the deactivation effects observed at high temperatures on pure Cu. CuAg alloys can prevent the dominance of hydrogen evolution at elevated temperatures, although an optimum of C2+ products with temperature is still observed.

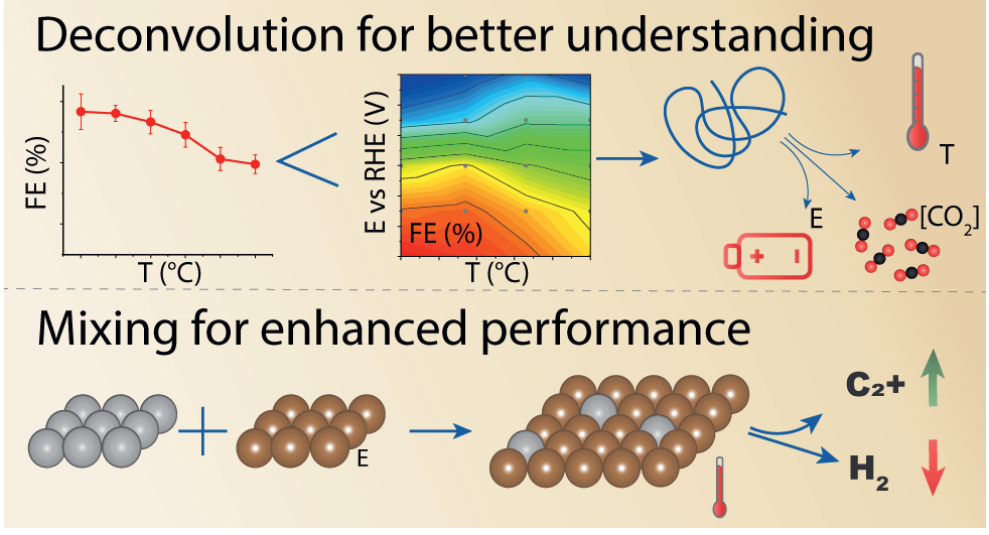

4.1 Introduction

Electrochemical CO_2 reduction has the potential to recycle CO_2 and be used in a sustainable and clean economy.[1,2] Copper is often studied as a catalyst for CO2RR as it can produce multicarbon products such as ethylene and ethanol. Au and Ag are also frequently studied catalysts as they are (model) catalysts producing mainly CO and H_2. They are known to be among the most active and selective catalysts towards CO.[3–8] This high selectivity is due to the weak hydrogen and CO binding strength on these metals, which avoids further reduction of CO or CO poisoning, while also suppressing the hydrogen evolution reaction (HER).[9,10]

Ag produces mostly CO or H_2 depending on the potential. The optimum selectivity towards CO is reached around -1.1 V vs RHE.[3] With increasing overpotential, Ag can also produce quite some HCOOH. Moreover, at very high overpotentials it has been shown to produce methane, methanol and ethanol.[3] At ambient pressure this was maximum -0.01 mA/cm^2,[3] but at elevated pressures these activities are increased considerably.[11] Moreover, at elevated pressures, other multicarbon products such as acetic acid, ethylene glycol and n-propanol can also be produced, showing that Ag is capable of making C-C bonds, provided that the experimental conditions promote higher CO coverages.[11]

Recently, more studies have looked at the effect of temperature on the electrochemical CO_2 reduction, as temperature is an understudied but relevant parameter. Au, as a simple model catalyst, shows a beneficial effect with regard to the Faradaic efficiency (FE) towards CO with increasing temperature up to 55 °C.[12] On Ag in a gas-diffusion electrode (GDE) system, an optimum in FE with temperature has been observed as well, although only 3 temperatures were studied.[13] It is interesting to study in more detail if the temperature effect on Ag is similar to that found before on Au and if Ag is able to make C-C bonds at elevated temperatures. On copper, increasing temperature also results in an optimum, both in CO2RR activity and in C2+ selectivity.[14] The decrease in both activity and selectivity at high temperatures is due to the dominance of HER under these conditions. This behaviour was tentatively related to a change in the copper surface, combined with a too high local pH. Alloying of Cu might be a strategy to prevent the change in the Cu surface and inhibit HER at higher temperatures.

Ag is one of the metals used to alloy with Cu to obtain higher efficiencies towards C2+ products,[15–20] and might be interesting to inhibit HER at elevated temperatures as it has shown this capability at ambient temperature. [20–22] The underlying idea of combining Cu with Ag is that in this catalyst, Ag will produce the CO, which can spill over to the Cu to give higher CO coverages and higher C2+ efficiencies. [21–26] However, some studies show that the effect of alloying is more a

strain effect than a spillover effect.[17,21] Moreover, the composition of the surface alters the d-band center which could tune the *CO binding strength, thus controlling the product selectivity.[16] The exact composition of the (surface) alloy has been shown to alter the selectivity significantly.[16,20] There are reports of CuAg alloys with a FE of above 60% towards CH_4,[18,27] although most studies indeed report increased selectivity towards C2+ products, specifically oxygenates.[15,19,21] For example, FEs towards acetaldehyde of 70%,[15] or ethanol with more than 35% FE, have been reported.[28]

In this chapter, we show that temperature has an important effect on the electrochemical CO_2 reduction on Ag, but this effect is not similar at all applied potentials. This is due to the significant dependence of CO2RR on Ag on the bulk CO_2 concentration and mass transport. This interdependence illustrates that other parameters have to be taken into account to make proper conclusions about the effect of a single parameter such as temperature. We also show that the exact nature of the CuAg electrode can result in very different product distributions. Nonetheless, in all cases there is an optimum in C2+ products at a temperature around 40 °C, just as on bare Cu. However, with the right alloy we observe that it is possible to reduce the dominance of HER at higher temperature and maintain significant FE for CO_2 reduction.

4.2 Experimental

4.2.1 Chemicals

$AgNO_3$ (Acros Organics) was used for the galvanic exchange. The electrolytes for electrolysis was prepared from $KHCO_3$ (99.95%, Sigma-Aldrich), $CsHCO_3$ (99.99%, Alfa Aesar) and Milli-Q water (≥18.2 MΩcm, TOC < 5 ppb). The electrolytes were stored with Chelex (100 sodium form, Sigma-Aldrich) to clean the electrolyte from any metal impurities.[29] Ar (5.0 purity, Linde) and CO_2 (4.5 purity, Linde) were used for purging the electrolytes.

4.2.2 General Electrochemical Methods

The experiments were performed in a home-made PEEK H-cell. To clean the cell prior to experiment, all parts were stored overnight in permanganate solution (0.2 M H_2SO_4, 1g/L $KMnO_4$). Before use, the cell was rinsed, washed in diluted piranha to remove any traces of MnO_4 and MnO_2, rinsed again and boiled three times with Milli-Q water. A three-electrode configuration was used during experiments. The reference electrode was a commercial RHE (mini Hydroflex, Gaskatel) and was placed in the same compartment as the working electrode. The counter electrode was a dimensionally stable anode (DSA, Magneto) and was

separated from the working electrode by an anion exchange membrane (AMVN Selemion, AGC). All the electrochemical measurements were carried out using an IviumStat potentiostat (Ivium Technologies). The flow of CO_2 (and Ar for the partial pressure experiments) was controlled using a mass flow controller (SLA5850, Brooks Instrument).

4.2.3 Electrode preparations

The polycrystalline Ag working electrode (99.99%, Mateck) was mechanically polished with decreasing diamond polishing suspension (3.0, 1.0 and 0.25 um, Buehler) on micropolishing cloths (8 in.) until the surface was mirror polished. Then, the electrode was successively sonicated in ethanol and Milli-Q water for 3 min to remove any impurities and dried with pressurised air, after which the electrode was ready to use.

A polycrystalline Cu working electrode (99.99%, Mateck) was used for the CuAg experiments. First, the electrode was mechanically polished similar as described above for the Ag electrode. After mechanical polishing, the Cu disk was electrochemically polished in a solution of H_3PO_4 (85%, Suprapure, Merck) by applying +3 V versus a graphite counter electrode for 20 seconds and subsequently rinsed with Milli-Q water. A galvanic exchange method based on the work of Clark et al.[21] was used to synthesize the CuAg surface alloy. Using a meniscus configuration, the electrode surface was put in contact with a $AgNO_3$ solution, which was heated to 50 °C. Different concentrations of $AgNO_3$ were used and either Ar was bubbled through the galvanic exchange solution or the solution was open to air. These different conditions were used as it was found they influence the product distribution after galvanic exchange. After 5 min the electrode was rinsed, dried with pressurized air and ready to use for the electrolysis experiments.

4.2.4 Electrolysis experiments

The electrolysis experiments were performed in a home-made PEEK H-cell containing 6.8 mL 0.1 M bicarbonate electrolyte in each compartment. Pictures and schematics of the jacketed cell can be found in Figures C.1 and C.2. For the experiments with Ag, $KHCO_3$ was used as electrolyte as this is common electrolyte for CO_2 reduction to CO. For the experiments with CuAg, $CsHCO_3$ was used to enhance the formation of multicarbon products and to increase the chances of gaining insights into the effect of temperature on minor CO2RR products such as acetate and propionaldehyde. The PEEK H-cell was embedded in a home-made jacket which was connected to the water bath (Ecoline e100, Lauda) to control the temperature in the cell.[14] Before electrolysis, CO_2 was purged through the electrolyte for 15 min while controlling the potential at -0.1 V vs RHE to saturate

the electrolyte and heat the electrolyte to the proper temperature. Then the ohmic drop was determined by electrochemical impedance spectroscopy (EIS) at -0.1 V vs RHE and 85% ohmic drop compensation was performed for all chronoamperometry measurements. Chronoamperometry was performed for either 60 min for the CuAg electrodes and for 32 min for the Ag electrodes. CO_2 was constantly purged at 20 mL/min during the experiments. At 5, 19, 32, 46 and 60 min a gas sample was online analyzed using a Shimadzu 2014 gas chromatograph containing two detectors (one TCD with a Shincarbon column and one FID with a RTX-1 column). A liquid sample was taken at the end of the electrolysis. The liquid products were analyzed using high performance liquid chromatography (HPLC, Shimadzu) with a Aminex HPX-87H column (Bio-rad).

4.2.5 Efficiency calculations

To be able to better compare the results on pure Cu with the results obtained with the CuAg alloys we have defined a Carbon efficiency as in a previous study.[14] The Carbon efficiency is defined equivalently to the Faradaic efficiency:

$$CE = \frac{c_i * a_i}{\sum_i c_i * a_i} = \frac{c_i * \frac{j_i}{n_i}}{\sum_i c_i * \frac{j_i}{n_i}} \qquad (4.1)$$

where *c* number of carbons in product *I*, *a* is the production rate in mol/min, *j* is the partial current density and *n* is the number of electrons transferred during CO2RR, all for product *i*.

4.2.6 Partial pressure experiments

With the use of flow controllers the partial pressure of CO_2 can be altered by mixing the inlet flow with Ar gas. This allows us to change the CO_2 concentration in the bulk electrolyte independently of temperature. We estimate the CO_2 concentration using Henry's law in combination with an empirical equation to estimate Henry's constant.[30]

$$c = KP \qquad (4.2)$$

$$\log(K) = 108.3865 + 0.01985076 * T - \frac{6919.53}{T} - 40.4515 * \log(T) + \frac{669365}{T^2} \qquad (4.3)$$

where *c* is the concentration, *K* is the Henry's constant, *P* is the partial pressure and T is temperature. Only for the partial pressure experiments, the CO_2

concentration is actively controlled. In other experiments it follows the temperature dependence of equation 4.3. So unless otherwise stated, the partial pressure of CO_2 is 1 bar.

4.2.7 Characterization of morphology and chemical composition

The electrochemical surface area (ECSA) was determined from the double layer capacitance measurements following the protocol of Morales et al.[31] The potential was scanned in a broad potential range, namely -0.15 to 0.25 V vs. RHE at sufficiently high scan rates (200 – 1000 mV/s). The capacitance was determined from the current difference between the anodic and cathodic scan at 0.05 V vs. RHE plotted against the scan rate. The slope of this graph gives the double layer capacitance.

Micrographs of the CuAg electrodes were obtained by scanning electron microscopy (SEM) in an Apreo SEM (ThermoFisher Scientific) with an acceleration voltage of 10 kV and an electron beam current of 1.6 nA.

The XPS measurements were performed in a SPECS Phoibos system equipped with an XRM50 X-ray source set to the Al K-alpha line used along with a monochromator to excite the sample with a beam spot of 0.4 mm diameter at 55° incidence. The acceleration voltage was set to 12 kV and a power of 400 W was used for all the measurements. The HAS7500 hemispherical analyser with a pass energy of 20 eV was employed to analyse the photoemission. All peaks have been calibrated according to the Cu2p peak.[32] All the atomic percentages were calculated according to the cross sections at the Al K-alpha energy.[33]

To analyze the XPS data, CASA-XPS software was employed. For the peak fitting a Shirley background and a linear background were subtracted for the Ag3d and the Cu2p respectively. Gaussian-Lorentzian (50 curves) were used for peak fitting after using the respective background subtraction.

4.3 Results and discussion

4.3.1 Temperature effect on Ag

Figure 4.1 shows that the selectivity towards CO2RR on Ag decreases with temperature. Interestingly, apart from a small increase at low temperatures, the partial current density towards CO is hardly effected by the temperature change and it is mostly the increase in HER which changes the selectivities. This is striking as this apparent independence of the CO2RR activity on temperature is different from that observed on Au, Cu and Ni catalysts.[12,14,34] Temperature not only

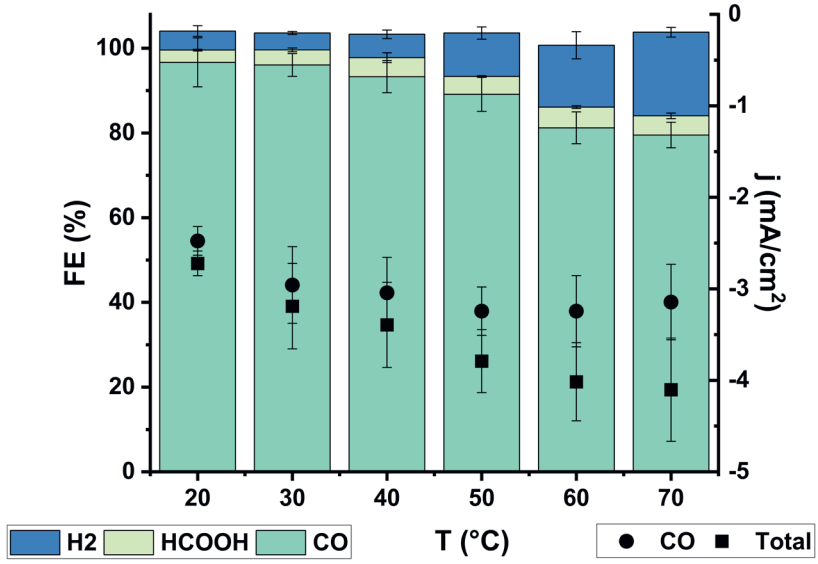

Figure 4.1 Temperature dependence of the Faradaic efficiency of CO2RR on Ag at -1.1 V vs RHE in 0.1 M $KHCO_3$

influences the intrinsic kinetics of the reaction, but also influences many other parameters such as CO_2 solubility, pH and diffusion coefficients. Figure 4.1 shows the overall effect of temperature taking all these effects into account. The effect of the CO_2 concentration is convoluted with the intrinsic effect of temperature as the bulk concentration of CO_2 decreases with increasing temperature according to equation 4.3 as illustrated in Figure C.3. The different temperature dependences of the activity of Ag compared to the catalysts previously studied might be related to the strong dependence of the CO2RR on Ag on the bulk concentration of CO_2.[35,36] By changing the partial pressure of CO_2, the bulk concentration of CO_2 can be altered. From these partial pressure experiments we indeed observe a strong effect of the CO_2 concentration on the CO2RR activity on Ag, as can be seen in Figure C.4.

To better understand the temperature dependence of Ag as observed in Figure 4.1, different potentials were studied as this might influence the temperature effect. Figure 4.2a shows that at a lower overpotential of -0.8 V vs RHE there is a strong dependence of the partial current density towards CO. The FE towards CO is only slightly affected by the temperature at this potential as also the current density for HER and for CO2RR towards HCOOH increase with temperature. Additionally, for a

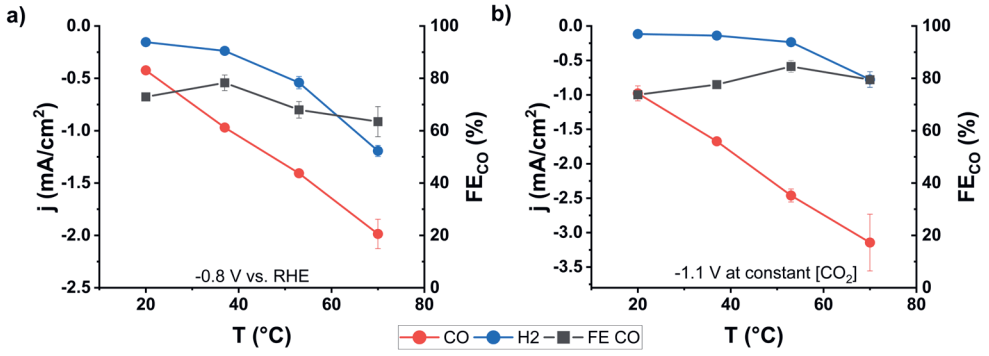

Figure 4.2 Temperature effect of the partial current densities for CO and H_2 and the FE for CO on Ag in 0.1 M $KHCO_3$ a) at -0.8 V vs RHE, and b) at constant CO_2 concentration by adjusting the partial pressure accordingly at -1.1 V vs RHE

better understanding of the overall effect of temperature on the CO2RR on Ag, we try to deconvolute some of the effects of temperature. Some parameters change only slightly with temperature, such as pH,[12] or are difficult to deconvolute, such as the diffusion coefficient of CO_2. However, the parameter which is the most pronounced and easiest to deconvolute is the effect of temperature on the CO_2 bulk concentration. With increasing temperature the CO_2 solubility decreases as can be seen in Figure C.3. By adjusting the partial pressure accordingly, the bulk concentration can be maintained constant at different temperatures. This is primarily done to gain better understanding, and not for practical applications, as this means lowering the CO_2 concentration at the lower temperatures measured, which results in worse CO2RR than at 1 bar of CO_2 partial pressure as illustrated in Figure C.4.

Figure 4.2b and C.5b show the effect of temperature at higher overpotential (-1.1V vs RHE) at a constant CO_2 concentration of 14 mM. This concentration is chosen as it is the concentration at the highest temperature of 70 °C at 1 bar of CO_2 partial pressure. Unlike in Figure 4.1, a strong dependence of CO2RR activity with temperature can now be observed. Initially, the FE towards CO increases, but above 55 °C the efficiency slightly decreases. This indicates that the lack of temperature dependence in Figure 4.1 is due to the strong dependence of the CO2RR on Ag on the bulk concentration. Figure C.5a shows that this also holds at a lower overpotential of -0.8 V vs RHE, where at constant CO_2 bulk concentration the partial current density towards CO as well as the corresponding FE increase even more strongly with temperature when the bulk CO_2 concentration is kept constant.

These results illustrate that even though understanding the overall temperature effect is imperative to link to (industrial) applications, it is important to deconvolute this overall effect in its single components to gain more insight into the exact nature of the temperature effect. Besides the direct effect of temperature on the kinetics, the effect on the bulk concentration of CO_2 is the most important factor to study. Moreover, to fully grasp the effect of a single parameter it is important to study this parameter at different conditions. For example, the effect of temperature depends heavily on the potential as well which has been observed in the differences between Figure 4.1 and 4.2a. To obtain a complete picture of the temperature effect, we have made a 2D map of the FE for CO as a function of potential and temperature, as we have done before for an Au rotating ring disk electrode (RRDE).[12] This is easily feasible if several potentials can be studied within a single experiment such as in a RRDE system, but requires significantly more experiments when electrolysis experiments are required such as when GC and HPLC are being used as product detection methods.

Figure 4.3a shows the effect of temperature and potential on the FE towards CO on Ag in a 2D plot. The gray dots indicate the measured datapoints and the map was constructed by interpolation between these points. It can be seen that the temperature effect is very potential dependent. At high overpotentials the temperature has a negative effect on the FE, while at low overpotentials it has a positive effect on the FE.

The difference in temperature dependence with potential might be caused by a change in reaction order of CO_2 with potential. Singh et al.[35] suggested that the effect of CO_2 bulk concentration is stronger at higher overpotentials because of an increase of the adsorption free energy of CO_2 with higher overpotentials, which increases the reaction order. Zhu et al.[36] also indicate a dependence of the reaction order in CO_2 with potential. They attribute this to differences in adsorbates on the surface. However, we measured the reaction order at different potentials and do not observe the same trend (Figure C.6). At high overpotentials, as used in both references, the reaction order might increase.

However, at lower overpotentials we observe a reaction order which is even higher than at these high overpotentials. Moreover, the reaction orders at high overpotentials in our experiments are significantly lower than observed by both references.[35,36] We have observed before that on Au the effect of temperature is stronger at lower overpotentials. As a stronger dependence on the CO_2 concentration with increasing overpotential has not been observed, this is most likely due to the activation barrier becoming smaller with larger overpotentials as expressed in equation 4.4, where $\Delta H^{\ddagger}$ is the activation enthalpy, $\Delta H_0^{\ddagger}$ is the

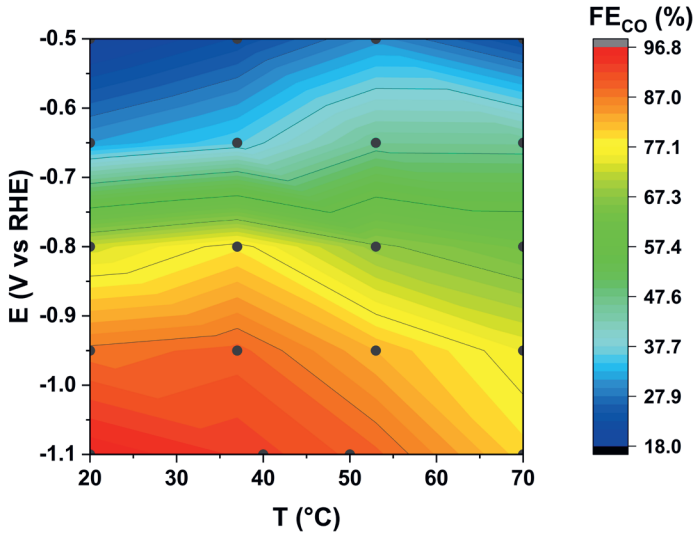

Figure 4.3 FE towards CO vs temperature and potential on Ag in 0.1 M $KHCO_3$

activation enthalpy at the standard equilibrium potential, α_H is the enthalpic transfer coefficient, F is the Faraday constant and η the overpotential:[37–39]

$$\Delta H^{\ddagger} = \Delta H_0^{\ddagger} + \alpha_H F\eta \qquad (4.4)$$

The FE map with potential and temperature of Ag differs significantly from the map of Au observed before.[12] In that study, the magnitude of the temperature effect differed with potential, but it always showed a positive effect of temperature on the FE up to 55 °C, independently of potential. However, in the case of Au, the measurements were performed with an RRDE setup, while in this study on Ag, the measurements were performed in an H-cell configuration. To check if this difference in setup and measuring method causes the differences in the temperature-potential map or if this is caused by the differences in catalyst material, we have performed experiments with Au in the H-cell setup as well. Figure C.7 shows similar results as on Ag, namely a decreasing efficiency with temperature.

This indicates that the temperature effect will differ between different setups. In the RRDE setup used before, rotation rates of 2500 rpm where used to create a controlled convection in the cell, which results in higher mass transport than in the H-cell.[40] So in the H-cell, mass transport might be limiting, as observed before in literature.[3] However, we observe that the current for CO2RR stays stable at -0.80 V vs RHE on the Au with increasing temperature, but with increasing potential the

current can still increase, which would not be possible if the system is mass transport limited. However, the local environment has shown to be important for the activity of CO2RR and this environment can be different due to differences in mass transport.[36,41–43] Mass transport is likely to already show an effect before mass transport limited currents are reached,[43,44] for example by influencing the local CO_2 concentration, which influences the rate as seen by the reaction order measurements, or by influencing the local pH.[45]

To check if the observed differences are due to differences in mass transport and to observe the effect of mass transport on the Ag electrode, we have increased the CO_2 flow through the H-cell. Experiments in the RRDE setup as discussed above for Au are much less straightforward for Ag, also because the latter electrode material produces significant amounts of formate. Figure C.8 illustrates that higher flow rates lead to a higher limiting current for the ferricyanide couple, showing an improved mass transport at higher flows.[44] Figure C.9 shows that mass transport does influence the Faradaic efficiencies for CO_2 reduction on Ag, but not as expected. At high overpotential of -1.1 V vs RHE, the CO_2 current density increases with increased flow rate, but the H_2 current density increases as well, leading to a similar Faradaic efficiencies. At a lower overpotential of -0.8 V vs RHE, the FE increases with temperature at the higher flow rates. Interestingly, it is not that CO_2 is mass transport limited at these potentials as enhanced mass transport actually decreased the FE towards CO at low temperatures. This is because better mass transport enhances HER instead of CO_2RR and this effect seems larger at lower temperatures. Lower HER with lower mass transport has been observed previously on Au,[46] although in an RRDE system the opposite has also been observed.[47] Clark et al.[48,49] show that at high overpotentials increased flow rates decrease HER, but for the currents at low overpotentials this trend seems opposite.[49] How the HER during CO2RR exactly depends on mass transport is an interesting matter on its own, but outside the scope of this paper. These results show that with increased mass transport conditions, similar results as previously for Au[12] can be obtained, where increasing temperature increases the FE towards CO up to about 50 °C. This illustrates that mass transport is important in determining the temperature dependance, but also that the effect of temperature with mass transport might not be intuitive and depends on potential as well. To fully understand the interdependence between mass transport and temperature and its effect on HER and CO2RR, more study is required into this complex issue.

The local environment might not only be different due to the differences in mass transport between the RRDE and H-cell experiments, but also due to the electrochemical measurement technique. For this study chronoamperometry (CA) has been used, while for the previous study a linear sweep voltammogram (LSV)

was taken. During a LSV the system might not be in steady state,[49–51] especially the local pH and CO_2 concentration might be very different than during an CA. As we see a clear dependence of the CO2RR on both Ag and Au[12] on the CO_2 concentration, this might partially explain the differences observed.

4.3.2 Temperature effect on CuAg alloys

We have shown previously that on Cu, HER starts to dominate at elevated temperatures. Moreover, we have shown that the effect of temperature leads to an optimum in CO2RR activity and C2+ selectivity around 48 °C. At higher temperatures only little CO2RR takes place, of which most results in CO.[14] Alloying Ag with Cu has been shown before to result in more C2+ products, and specifically more oxygenates such as ethanol and acetate. [15,19,21] Studying the effect of CuAg surface alloys can be interesting to probe the effect of temperature on these minor products, which are difficult to detect on a Cu catalyst. To enhance the production of minor products even more, $CsHCO_3$ is used as electrolyte as it has shown to enhance the production of multicarbon products on Cu.[52,53] Moreover, we have

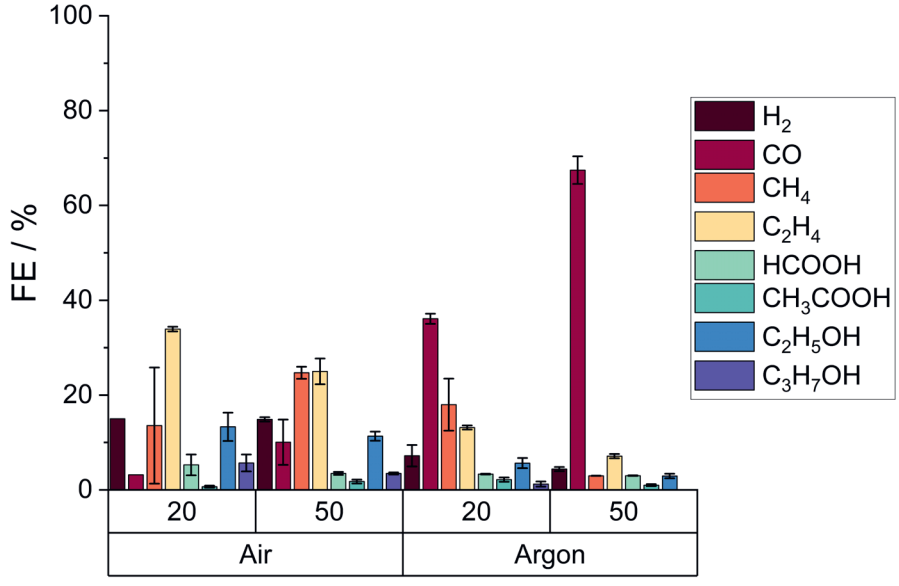

Figure 4.4 The effect of the galvanic exchange procedure on the Faradaic efficiencies of the CuAg alloys at room temperature at -1.1 V vs RHE in 0.1 M $CsHCO_3$. Both the concentration of $AgNO_3$ and the nature of the gas atmosphere influences the galvanic exchange leading to differences in FE.

shown above that Ag generates less H_2 at high temperatures and it might be able to prevent the dominance of HER on Cu at 70 °C, for example by stabilizing the copper structure via strain effects.[21]The CuAg surface alloys have been synthesized via a galvanic exchange procedure. Figure 4.4 shows that both the $AgNO_3$ concentration and the gas composition during galvanic exchange have effect on the product distribution of the formed CuAg surface alloy. These differences in product distribution might be related to differences in morphology and Ag content caused by the different conditions during galvanic exchange. We determined the electrochemical surface area (ECSA) by measuring the double layer capacitance as a measure of the morphology. Figure C.10 shows that the ECSAs are very similar between the different samples and do not explain the trends observed. With XPS, the Ag content near the surface was determined, as shown in Figure C.11 and Table C.1. The XPS results relate very well to the activity trends observed in Figure 4.4, where more Ag leads to more CO and less ethylene selectivity. As expected, samples contain more Ag with more $AgNO_3$ in the galvanic exchange solution, but surprisingly also the gas atmosphere significantly influences the amount of Ag present, with an Ar atmosphere leading to more Ag in the catalyst than an air atmosphere.

We decided to continue the temperature dependence experiments with the CuAg synthesized in 20 μM $AgNO_3$ in air (hereafter called CuAg20) as this produces the most C2+ products and oxygenates, and the CuAg produced in 50 μM $AgNO_3$ in argon (hereafter called CuAg50) as this catalyst produces the least amount of H_2. Figure C.12 shows the SEM images of these two catalysts. These images show that the overall structure of the catalyst is not that different. Both electrodes do not show the very flat surface which was observed for Cu,[14] but seem more flaky. This could be caused by the galvanic exchange at open circuit potential, which will probably oxidize the copper surface and change its morphology. The ECSA measurements in Figure C.10 show indeed that the CuAg alloys are slightly rougher than pristine Cu, although the differences are not very large. EDX analysis has been performed as well to observe where the Ag is located on these CuAg surface alloys. Figure C.13 shows that in both cases the Ag is spread over the entire surface as would be expected from galvanic exchange.

Figure C.14 shows the effect of temperature on both CuAg surface alloys. The CuAg20 has a broader range of products similar to Cu whereas CuAg50 is dominated by CO. Moreover, the product distribution on the CuAg20 is more effected by temperature than on the CuAg50. The latter is hardly influenced by the temperature, while the first has a similar behaviour as bare Cu. To compare the different catalysts better with each other and with bare Cu, we have plotted

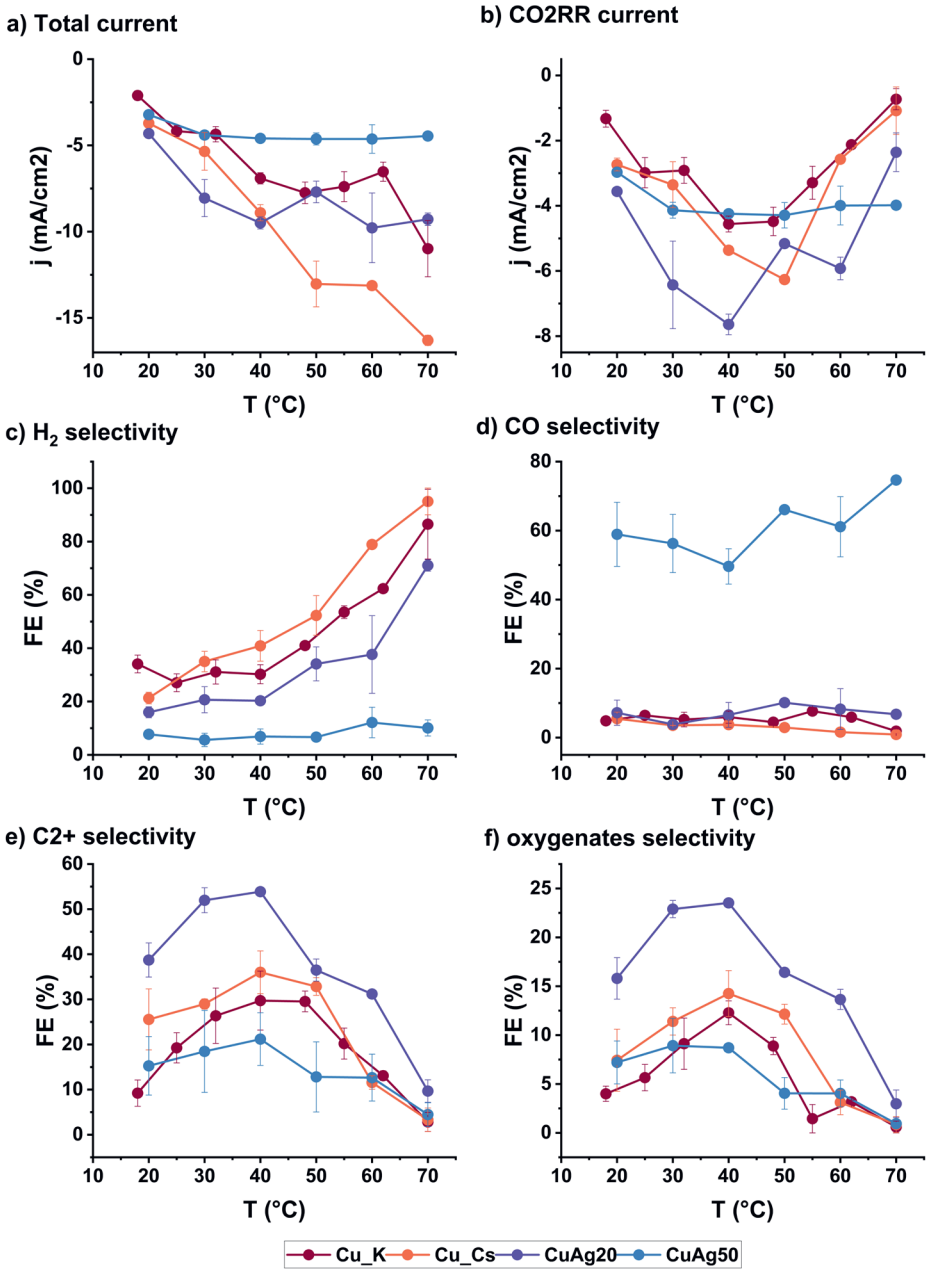

Figure 4.5 a) Total current density and b) current density towards CO2RR and faradaic efficiency for c) hydrogen d) CO e) C2+ products f) oxygenates for Cu, CuAg20 and CuAg50 at -1.1V vs RHE in 0.1 M CsHCO3 and also in 0.1 M $KHCO_3$ for Cu.[14]

them together in Figures 4.5, C.16 and C.17. Here we also compare the data of pure Cu in $CsHCO_3$ with the data obtained previously in $KHCO_3$.[14] At room temperatures, the Cs^+ containing electrolyte results in less hydrogen and more C2+ products than the K^+ electrolytes, as expected from literature.[52,53] However, with increasing temperature the difference between the two electrolytes becomes less pronounced and at the higher temperatures the K^+ containing electrolytes produce less hydrogen, as shown in Figure 4.5b and C.12f. This indicates that the cation identity might be an important parameter for the stability of Cu at elevated temperatures and to inhibit HER at elevated temperatures. For the CuAg alloys, the cation does not have a significant effect on the HER selectivity, but it changes the CO2RR product distribution from more CH_4 in K^+ containing electrolytes to more C2+ products in Cs^+ containing electrolytes, as shown in Figure C.15.

It can be seen in Figure 4.5 that although the selectivities are different among the catalysts, most trends on the CuAg alloys resemble the trends with temperature on the bare Cu electrode, especially for the CuAg20. Interestingly, the total current density and in particular the CO2RR current density of the CuAg50 is very stable with temperature, whereas the Cu and CuAg20 show an increase in total current density and an optimum in CO2RR current density. The CuAg50 resembles more the Ag catalyst shown in Figure 4.1, as it also produces significantly higher amounts of CO than the other catalysts. Remarkably, it shows a very stable HER selectivity with temperature, while the CuAg20 follows the trend of Cu, although both the activity and selectivity towards H_2 are significantly lower than on pure Cu, even compared to the pure Cu in $KHCO_3$ electrolyte. This indicates that the dominance of HER at elevated temperatures can be suppressed by alloying the Cu with Ag. Alloying might stabilize Cu, which would also explain why we observe almost no cation effect on the HER on the CuAg electrode, whereas there is a clear cation effect on Cu. The increased HER in Cs^+ containing electrolytes on Cu could be due to the instability of the Cu at elevated temperatures; by stabilizing the Cu with Ag this effect appears to be eliminated.

Both CuAg alloys show an optimum in C2+ products. Interestingly, on the CuAg50, where the CO coverage on Cu sites is likely to be high due to the large amount of CO produced, the optimum is the least pronounced. The increase in C2+ products with temperature up to 40 °C is the least for this catalyst, indicating that CO coverage is probably important for the increasing C2+ selectivity in the first regime. However, even when CO is produced significantly on the CuAg50, at high temperature C2+ activity still decreases. Moreover, Figure C.16 shows that the effect of temperature on most carbon efficiencies is relatively stable for the CuAg20 compared to the pure Cu. This seems mostly due to the higher C2+ and lower formic

acid production at lower temperatures for the CuAg20 compared to the pure Cu catalyst.

CuAg20 also produces relatively large amounts of minor liquid products, which makes it possible to observe the temperature effect on acetate, 1-propanol, propionaldehyde and acetaldehyde in more detail (Figure 4.6). Interestingly, the CE of acetate increases with temperature. From all other products, this is only the case for CO. This might indicate that acetate follows a different mechanism than the other C2+ products.[54] It has recently been suggested that a ketene intermediate has to desorb from the catalyst surface which then forms acetate in solution by reacting with OH^-.[55] Similarly to CO, desorption would be important to form this product and can be facilitated by increasing temperatures, leading to increased CE for both CO and acetate. Acetaldehyde is another stable intermediate for which we can expect desorption to be important to obtain higher efficiencies. However, we do not observe a continuous increase in CE with temperature for acetaldehyde. Similar to

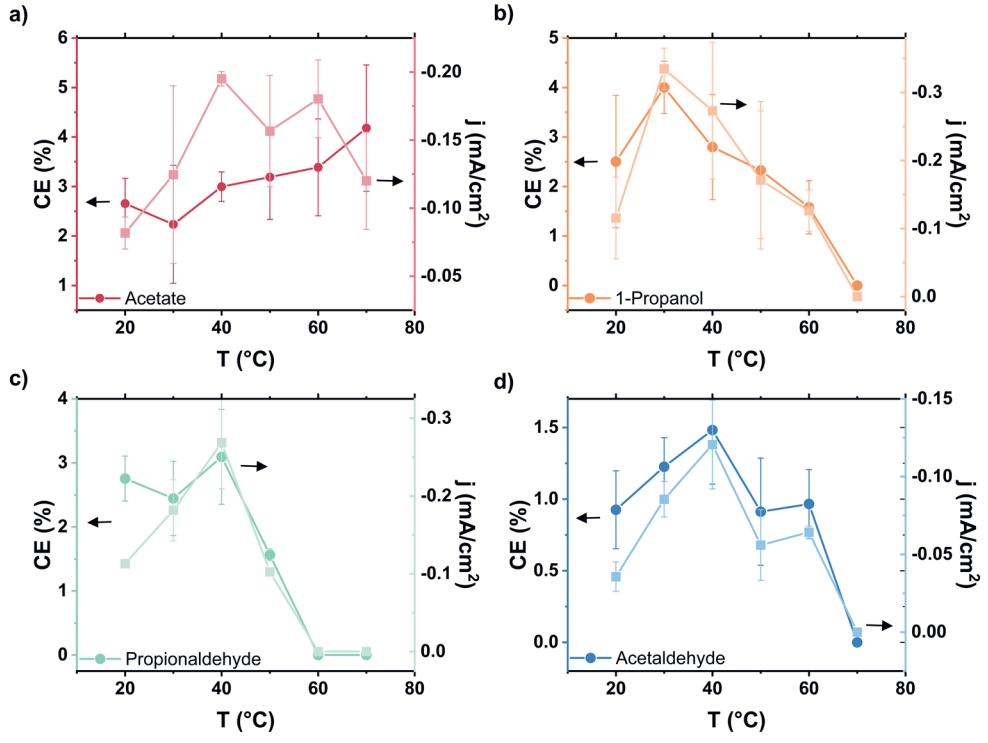

Figure 4.6 Carbon efficiency and partial current density for minor liquid products on CuAg20 at -1.1 V vs RHE in $CsHCO_3$ a) acetate b) 1- propanol c) propionaldehyde and d) acetaldehyde. All data has been corrected for the evaporation of the liquid products as described in the SI

the other minor products 1-propanol and propionaldehyde, it shows an optimum in CE and partial current density with temperature and an optimal production is obtained around 30-40 °C.

These results show that alloying Cu, in this case with Ag, can be an effective strategy to counteract the negative impact of temperature at temperatures above 50 °C, where hydrogen starts to dominate at Cu. With the proper alloy, it seems possible to inhibit the HER, even at temperatures up to 70 °C. However, the decrease in C2+ products at elevated temperatures seems more intrinsic and has been observed not only for pure Cu, but also for the different CuAg alloys studied. Thus, depending on the desired product, the proper temperature and alloy should be chosen carefully. For C2+ products, often desired when Cu is used as catalyst, the optimum temperature remains around 40-50 °C.

4.4 Conclusion

In this chapter we have shown that the activity of Ag for CO_2 reduction to CO is almost temperature independent at -1.1 V vs RHE. We show that this is due to the interplay of potential, CO_2 concentration and mass transport on the temperature effect on CO2RR. It is important to deconvolute these effects to obtain better insight in the intrinsic effect of temperature. The intrinsic kinetics of CO2RR on Ag seems to favour higher temperatures, also compared to HER. However, the strong dependence on the bulk concentration counteracts this effect and results in a very moderate overall temperature effect. Increased mass transport can lower CO2RR selectivity by increasing HER activity. However, the exact effect of (temperature on) mass transport on the CO2RR and the competing HER is not fully understood and would require more detailed study. Therefore, it would be interesting to complement studies in H-cell configurations with other setups such as rotating ring disk setups and gas diffusion electrode configurations. Moreover, the effect of temperature can be potential dependent, so to fully understand this effect, one can not suffice with measuring the temperature effect at a single potential. Instead, the interplay between potential and temperature should be investigated by studying at least two different parameters, as illustrated by the 2D map of the effect of potential and temperature on selectivity.

Surface alloying of Ag on Cu can alter the effect of temperature on the CO_2 reduction of Cu. However, it does not alter the temperature dependence of C2+ products at high temperatures. In all cases an optimum at 40-50 °C has been observed and at higher temperatures both activity and selectivity towards C2+ products such as ethylene and ethanol decreases. Acetate seems to be an exception as its carbon efficiency keeps increasing with increasing temperature. More importantly, the dominance of HER seems to be cation dependent on pure Cu and

could be reduced with the CuAg20 catalysts and even be removed completely with the CuAg50 catalyst. This indicates that alloying might be able to give more robust Cu based catalysts at higher temperature, although significant development is still required to attain the Cu alloy with the desired properties and selectivities at elevated temperatures.

References

1. De Luna, P. *et al. Science* **364**, eaav3506 (2019).
2. Mikkelsen, M., Jørgensen, M. & Krebs, F. C. *Energy and Environmental Science* vol. 3 43–81 (2010).
3. Hatsukade, T., Kuhl, K. P., Cave, E. R., Abram, D. N. & Jaramillo, T. F. *Physical Chemistry Chemical Physics* **16**, 13814–13819 (2014).
4. Hansen, H. A., Varley, J. B., Peterson, A. A. & Nørskov, J. K. *Journal of Physical Chemistry Letters* **4**, 388–392 (2013).
5. Lu, Q. *et al. Nat Commun* **5**, (2014).
6. Kibria, M. G. *et al. Advanced Materials* 31 (2019).
7. Feaster, J. T. *et al. ACS Catal* **7**, 4822–4827 (2017).
8. Sun, D., Xu, X., Qin, Y., Jiang, S. P. & Shao, Z. *ChemSusChem* vol. 13 39–58 (2020).
9. Bagger, A., Ju, W., Varela, A. S., Strasser, P. & Rossmeisl, J. *ChemPhysChem* **18**, 3266–3273 (2017).
10. Rosen, J. *et al. ACS Catal* **5**, 4293–4299 (2015).
11. Raaijman, S. J., Schellekens, M. P., Corbett, P. J. & Koper, M. T. M. *Angewandte Chemie - International Edition* **60**, 21732–21736 (2021).
12. Vos, R. E. & Koper, M. T. M. *ChemElectroChem* **9**, e20220023 (2022).
13. Dufek, E. J., Lister, T. E. & McIlwain, M. E. *J Appl Electrochem* **41**, 623–631 (2011).
14. Vos, R. E. *et al. ACS Catal* **13**, 8080–8091 (2023).
15. Wang, L. *et al.* **117**, (2020).
16. Wei, D. *et al. Angewandte Chemie - International Edition* **62**, (2023).
17. Hailu, A. & Shaw, S. K. *J Electrochem Soc* **167**, 126509 (2020).
18. Choi, C. *et al. Nano Res* **14**, 3497–3501 (2021).
19. Robens, E., Hecker, B., Kungl, H., Tempel, H. & Eichel, R. A. *ACS Appl Energy Mater* **6**, 7571–7577 (2023).
20. Xu, Y. *et al. ACS Appl Mater Interfaces* **14**, 11567–11574 (2022).
21. Clark, E. L., Hahn, C., Jaramillo, T. F. & Bell, A. T. *J Am Chem Soc* **139**, 15848–15857 (2017).
22. Lee, S., Park, G. & Lee, J. *ACS Catal* **7**, 8594–8604 (2017).
23. Iyengar, P., Kolb, M. J., Pankhurst, J. R., Calle-Vallejo, F. & Buonsanti, R. *ACS Catal* **11**, 4456–4463 (2021).
24. Gao, J. *et al. J Am Chem Soc* **141**, 18704–18714 (2019).
25. Ting, L. R. L. *et al. ACS Catal* **10**, 4059–4069 (2020).
26. Jeon, Y. E. *et al. Journal of Industrial and Engineering Chemistry* **116**, 191–198 (2022).
27. Chang, C.-J. *et al. J Am Chem Soc* **142**, 12119–12132 (2020).
28. Li, Y. C. *et al. J Am Chem Soc* **141**, 8584–8591 (2019).
29. Wuttig, A. & Surendranath, Y. *ACS Catal* **5**, 4479–4484 (2015).
30. Plummer, L. N. & Busenberg, E. *Geochim Cosmochim Acta* **46**, 1011–1040 (1982).
31. Morales, D. M. & Risch, M. *Journal of Physics: Energy* **3**, 34013 (2021).
32. Strohmeier, B. R. *Journal of Vacuum Science & Technology A* **14**, 481–484 (1996).
33. Shard, A. G. *Journal of Vacuum Science & Technology A* **38**, 041201 (2020).

34. Vos, R. E. & Koper, M. T. M. *ACS Catal* 4432–4440 (2024) doi:10.1021/acscatal.4c00009.
35. Singh, M. R., Goodpaster, J. D., Weber, A. Z., Head-Gordon, M. & Bell, A. T. *Proc Natl Acad Sci U S A* **114**, E8812–E8821 (2017).
36. Zhu, X., Huang, J. & Eikerling, M. *ACS Catal* **11**, 14521–14532 (2021).
37. GojkoviC, Sl., ZeCeviC, S. & Dra, D. *Journal of Electroanalytical Chemistry* vol. 399 (1995).
38. Conway, B. E. & Wilkinsont, D. P. *J. Chem. SOC., Faraday Trans. I* vol. 85 (1989).
39. Protsenko, V. S. & Danilov, F. I. *Journal of Electroanalytical Chemistry* **651**, 105–110 (2011).
40. Marcandalli, G., Goyal, A. & Koper, M. T. M. *ACS Catal* 4936–4945 (2021) doi:10.1021/acscatal.1c00272.
41. Bui, J. C. *et al. Acc Chem Res* **55**, 484–494 (2022).
42. Zhang, Q. *et al. Adv Funct Mater* **31**, (2021).
43. Dolmanan, S. Bin *et al. J Mater Chem A Mater* **11**, 13493–13501 (2023).
44. Qi, Z., Hawks, S. A., Horwood, C., Biener, J. & Biener, M. M. *Mater Adv* **3**, 381–388 (2022).
45. Marcandalli, G., Monteiro, M. C. O., Goyal, A. & Koper, M. T. M. *Acc Chem Res* **55**, 1900–1911 (2022).
46. Zhang, B. A., Ozel, T., Elias, J. S., Costentin, C. & Nocera, D. G. *ACS Cent Sci* **5**, 1097–1105 (2019).
47. Goyal, A., Marcandalli, G., Mints, V. A. & Koper, M. T. M. *J Am Chem Soc* **142**, 4154–4161 (2020).
48. Clark, E. L. *et al. ACS Catal* **8**, 6560–6570 (2018).
49. Clark, E. L. & Bell, A. T. *J Am Chem Soc* **140**, 7012–7020 (2018).
50. Anantharaj, S., Kundu, S. & Noda, S. *J Electrochem Soc* **169**, 014508 (2022).
51. Marcandalli, G., Villalba, M. & Koper, M. T. M. *Langmuir* **37**, 5707–5716 (2021).
52. Ringe, S. *et al. Energy Environ Sci* **12**, 3001–3014 (2019).
53. Resasco, J. *et al. J Am Chem Soc* **139**, 11277–11287 (2017).
54. Wang, H. *et al. Curr Opin Electrochem* **39**, (2023).
55. Heenen, H. H. *et al. Energy Environ Sci* **15**, 3978–3990 (2022).

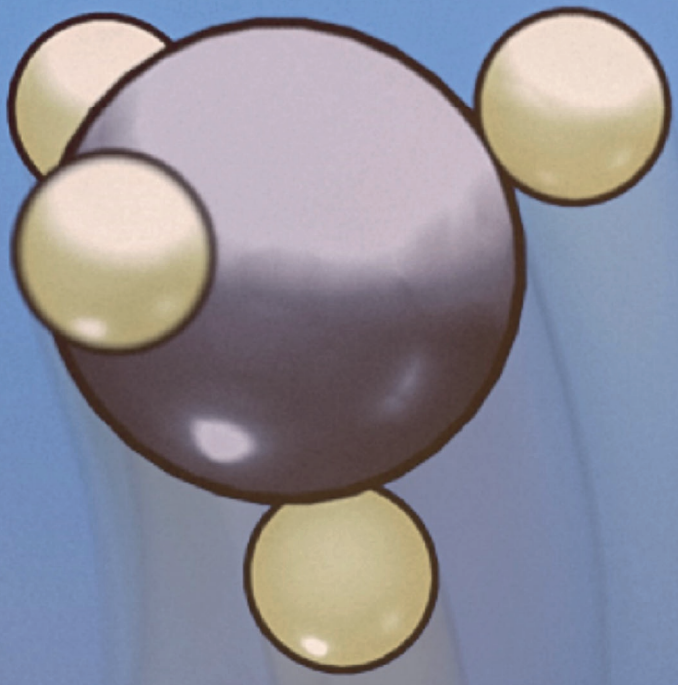

5

Nickel as electrocatalyst for $CO_{(2)}$ reduction: effect of temperature, potential, partial pressure and electrolyte composition

This chapter is based on R.E. Vos, M.T.M. Koper, *ACS Catalysis* **14** 4432-4440 (2024)

Abstract

Electrochemical CO_2 reduction on Ni has recently been shown to have the unique ability to produce longer hydrocarbon chains in low but measurable amounts. However, the effect of the many parameters of this reaction remain to be studied in more detail. Here, we have investigated the effect of temperature, bulk CO_2 concentration, potential, the reactant, cations and anions on the formation of hydrocarbons via a chain growth mechanism on Ni. We show that temperature increases the activity but also the formation of coke, which deactivates the catalyst. The selectivity and thus the chain growth probability is mainly affected by the potential and the electrolyte composition. Remarkably, CO reduction shows lower activity, but higher chain growth probability than CO_2 reduction. We conclude that hydrogenation is likely to be the rate determining step and hypothesize this could happen either by *CO hydrogenation or by termination of the hydrocarbon chain. These insights open the way to further development and optimization of Ni for electrochemical CO_2 reduction.

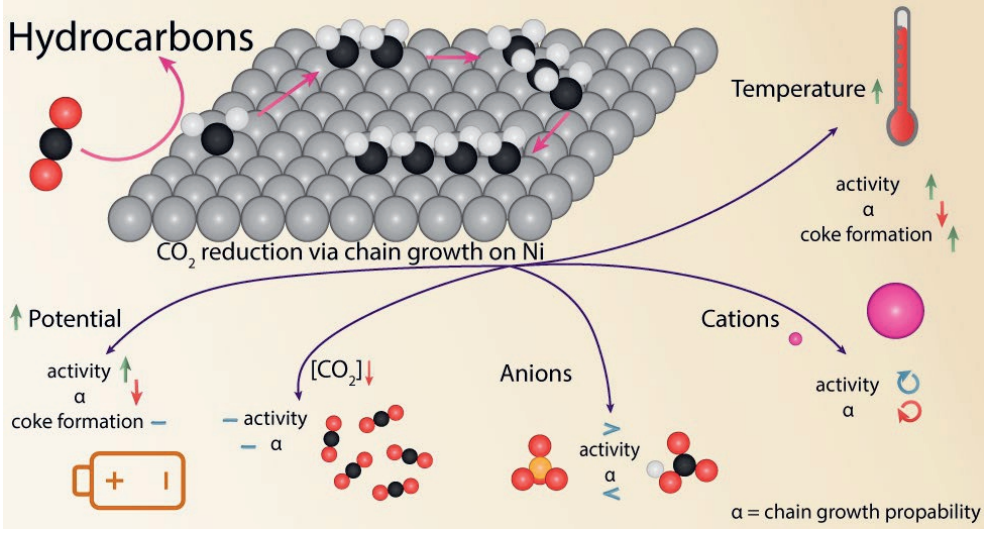

5.1 Introduction

Electrochemical CO_2 reduction (CO2RR) using renewable electricity is an interesting process to produce sustainable hydrocarbons in the future. Multicarbon products are of particular relevance as they are required in chemicals and fuels. Although several metal catalysts are able to reduce CO_2 to useful products, Cu is the only metal able to produce C2+ products in significant amounts.[1–3] However, the largest molecule that Cu is able to form electrochemically from CO_2 is propanol, a C3 molecule.[4] Efforts to produce longer hydrocarbons using Cu derived catalysts have not been very successful up to now.[5–7]

Already in the 1990s, Kudo et al.[8] showed that at elevated temperatures and pressures, nickel electrodes are able to reduce CO_2 and to form longer hydrocarbons, following the Anderson-Schultz-Flory distribution known from thermochemical Fischer-Tropsch synthesis.[9] However, the selectivities were extremely small. Recently, Zhou et al.[5] showed that higher hydrocarbon selectivities, of up to 15 percent, are possible on nickel oxygenate-derived catalysts. They found linear and branched hydrocarbons with chains of up to six carbon atoms and indicate that Ni follows a Fischer-Tropsch like mechanism where CH_x intermediates are inserted into the growing hydrocarbon chain.

In the literature, it has been suggested that elevated temperatures could be beneficial for the formation of longer hydrocarbon chains.[8,10] However, these results are convoluted with a pressure effect as both are increased simultaneously. We have shown in previous work that temperature can play a major role in CO_2 reduction and can influence both the selectivity and the activity. On copper, higher temperatures lead to more C2+ products, although there is an optimum around 48 °C.[11] Ni binds the intermediate CO too strong to obtain high conversion rates of CO2RR,[3,12] however an increase in temperature could help to overcome this barrier and facilitate CO2RR. Moreover, the thermocatalytic Fischer-Tropsch reaction is influenced by temperature as well, with higher temperatures leading to shorter hydrocarbons and higher conversions.[13] It is interesting to compare the effect of temperature on Ni to what is known on Cu, as Ni presumably follows an entirely different mechanism. Moreover, more insights are needed to understand why some catalysts like Ni, but also PdAu, [14] Au/Ti,[15] and Fe phthalocyanine catalysts[16] follow a kind of chain growth mechanism, while the most commonly studied catalysts as Cu, Ag, Au and Sn do not. Additionally, studying this electrochemical Fischer-Tropsch mechanism could give us more insight in other CO2RR mechanisms that might open up at elevated pressures and temperatures.

In this chapter, we investigate a nickel-derived catalyst for the electrochemical CO_2 reduction. Specifically, we investigate the effect of temperature on the

performance of nickel for CO2RR, but also the effects of partial pressure, electrode potential and electrolyte composition are investigated. We show that the chain growth probability does not depend intrinsically on the temperature and partial pressure, although temperature does influence the degradation rate. Electrode potential and especially electrolyte cations influence the chain growth probability. Moreover, CO and CO_2 as reactant show interesting differences in activity and selectivity. Furthermore, we discuss that the rate determining step is most likely a hydrogenation step and offer several possibilities.

5.2 Experimental

5.2.1 Chemicals

The electrolytes for electrolysis were prepared from Li_2CO_3 (99.999%, Acros Organics), $NaHCO_3$ (99.7%, Sigma-Aldrich), $KHCO_3$ (99.95%, Sigma-Aldrich), $CsHCO_3$ (99.99%, Alfa Aesar), KH_2PO_4 (99.9%, Sigma Aldrich), K_2HPO_4 (TraceSELECT, 99.999%, Sigma Aldrich) and Milli-Q water (≥18.2 MΩcm, TOC < 5 ppb). The HCO_3^- electrolytes were stored with Chelex (100 sodium form, Sigma-Aldrich) to clean the electrolyte from any metal impurities.[17] $Ni(NO_3)_2$ *6 H_2O (99.999%, Sigma-Aldrich), Na_2HPO_4 *2 H_2O (99.5%, Merck), ethanol (puriss, Honeywell) and Milli-Q water were used to prepare the deposition electrolyte. H_2SO_4 (95-98%, Sigma-Aldrich), H_2O_2 (35%, Merck) and $KMnO_4$ (99%, Sigma-Aldrich) were used to clean the cells. Ar (5.0 purity, Linde), CO (4.7 purity, Linde) and CO_2 (4.5 purity, Linde) were used for purging the electrolytes.

5.2.2 General Electrochemical Methods.

The experiments were performed in a home-made PEEK H-cell or a borosilicate glass cell. The cells were cleaned prior to experiment by storing them overnight in a permanganate solution (0.2 M H_2SO_4, 1g/L $KMnO_4$). Before use, the cells were rinsed and submerged in diluted piranha to remove any traces of MnO_4 and MnO_2. Thereafter, they were rinsed again and boiled three times with Milli-Q water. A three-electrode configuration was used during experiments. The reference electrode was a commercial RHE (mini Hydroflex, Gaskatel) and was placed in the same compartment as the working electrode. An anion exchange membrane (AMVN Selemion, AGC) was used to separate the counter electrode (DSA, Magneto) from the working electrode. All the electrochemical measurements were carried out using an IviumStat potentiostat (Ivium Technologies). The flow of CO_2 or CO (and Ar for the partial pressure experiments) was controlled using a mass flow controller (SLA5850, Brooks Instrument).

5.2.3 Electrode preparation.

The polycrystalline Ni working electrode (99.99%, Mateck) was mechanically polished with decreasing diamond polishing suspension (3.0, 1.0 and 0.25 um, Buehler) on micropolishing cloths (8 in.) until the surface was mirror polished. Then, the electrode was successively sonicated in ethanol and Milli-Q water for 3 min to remove any impurities and dried with pressurised air. Thereafter, the electrode was electrochemically polished in a 50/50 solution of H_2SO_4 and H_3PO_4 (85%, Suprapure, Merck) by applying +2 V versus a graphite counter electrode for 20 seconds. Subsequently, the electrode was rinsed with Milli-Q water, dried with pressurized air and used for deposition. The Ni electrode was put in contact with the deposition solution (63 mM $Ni(NO_3)_2$ + 8 mM Na_2HPO_4 in MilliQ-water with 25% ethanol) using a meniscus. Deposition was performed by cyclic voltammetry from -0.75 to 0.65 V vs RHE for 5 cycles at 15 mV/s. Next, the electrode was thoroughly rinsed with Milli-Q water and dried with pressurized air, after which it was ready to use for the electrolysis experiments. For control experiments, the electrode was used after the electropolishing step without deposition.

2.4. Electrolysis experiments.

The electrolysis experiments were performed in the home-made PEEK H-cell containing 6.8 mL 0.1 M HCO_3^- electrolyte in each compartment. The PEEK H-cell was embedded in a home-made jacket which was connected to a water bath (Ecoline e100, Lauda) to control the temperature in the cell. Before electrolysis, CO_2 (or CO) was purged through the electrolyte for 15 min while controlling the potential at -0.1 V vs RHE to saturate the electrolyte and get the electrolyte to the proper temperature. Then the ohmic drop was determined by electrochemical impedance spectroscopy (EIS) at -0.1 V vs RHE and 85% ohmic drop compensation was performed for all chronoamperometry measurements. Chronoamperometry was performed for 32 min and CO_2 was constantly purged at 20 mL/min. At 5, 19 and 32 min a gas sample was analyzed online using a Shimadzu 2014 gas chromatograph containing two detectors (one TCD with a Shincarbon column and one FID with a RTX-1 column). These time intervals were chosen based on the limitations of the GC. A liquid sample was taken at the end of the electrolysis. The liquid products were analyzed using high performance liquid chromatography (HPLC, Shimadzu) with a Aminex HPX-87H column (Bio-rad).

5.2.5 Chain growth probability calculation

If the formation of hydrocarbons occurs though the polymerization of C1 intermediates, this mechanism resembles the Fischer-Tropsch synthesis mechanism.[9,18] This mechanism follows the Anderson-Schultz-Flory model:[19]

$$W_n = n(1-\alpha)^2\alpha^{n-1} \qquad (5.1)$$

where W_n is the weight percent of a product containing n carbon atoms and α is the chain growth probability. Equation 5.1 can be used to calculated the chain growth probability by plotting $\ln(W_n/n)$ vs. n:

$$\ln\left(\frac{W_n}{n}\right) = n\ln(\alpha) - \ln(\alpha) + 2\ln(1-\alpha) \qquad (5.2)$$

5.2.6 Deactivation ratio

To get better insight in the deactivation of the catalyst over time we compare the chain growth probability at the last and first measurement and have defined a deactivation ratio with the following expression:

$$DR = \frac{\alpha_{32\ min}}{\alpha_{5\ min}} \qquad (5.3)$$

where DR is the deactivation ratio and α is the chain growth probability. 32 min has been used due to the sampling time of the GC.

5.2.7 Partial pressure experiments

With the use of flow controllers the partial pressure of CO_2 can be altered by mixing the inlet flow with Ar gas. This allows us to change the CO_2 concentration in the bulk electrolyte independently of temperature. We estimate the CO_2 concentration using Henry's law in combination with an empirical equation to estimate Henry's constant.[20]

$$C = KP \qquad (5.4)$$

$$\log(K) = 108.3865 + 0.01985076 * T - \frac{6919.53}{T} - 40.4515 * \log(T) + \frac{669365}{T^2} \qquad (5.5)$$

where C is the concentration, K is the Henry's constant, P is the partial pressure and T is temperature

5.2.8 Characterization of morphology and chemical composition

Micrographs of the deposited Ni electrodes were obtained by scanning electron microscopy (SEM) in an Apreo SEM (ThermoFisher Scientific) with an acceleration voltage of 15 kV and an electron beam current of 1.6 nA. The chemical composition of the electrode was investigated by energy dispersive X-Ray spectroscopy (EDX) using an Oxford Instruments X-MaxN 150 Silicon Drift detector coupled to the

Apreo SEM. EDX data was processed with the Pathfinder™ X-rayMicroanalysis software v1.3. The quantification of chemical elements was performed in automatic mode.

5.2.9 Raman Spectroscopy

Raman spectroscopy measurements were carried out to determine the formation of coke during electrochemical CO_2 reduction on Ni. The measurements were carried out ex-situ both before and after the reaction. A confocal spectrometer (Witec Alpha300 R) was used with a 457 nm excitation wavelength laser. A 100 times magnification objective was used for spectra collection. The laser power was kept below 2 mW to prevent sample damaging. All measurements were performed under ambient conditions at room temperature. Optical images of the electrode were recorded using the optical camera equipped to the Raman microscope setup.

5.3 Results and Discussion

5.3.1 Temperature effect and deactivation.

Inspired by Zhou et al.[5] we have used a phosphate derived Ni catalyst in this study as it is more active than metallic Ni. The phosphate derived Ni was prepared by electrodeposition with a Ni foil as substrate to avoid any influence of other metals in the catalyst. Figure D.1 shows an SEM picture and a EDX map of the Ni electrode before electrolysis, from which it can be seen that the deposit forms a layer on top of the Ni foil. This layer does not cover the Ni foil completely but consists of small patches with cracks in between where the underlaying Ni foil is still visible. The observation of cracks might be due to drying of the layer when transferring the electrode from the electrolyte to the SEM. The deposited layer consists of Ni with oxygen and phosphor atoms, possibly forming a nickel phosphate layer mixed with nickel oxide. The atomic ratio of the EDX analysis suggests the layer is not fully nickel phosphate as the oxygen phosphor ratio is 8:1 instead of 4:1. However, it could also be that the layer is nickel phosphate and the Ni underneath is oxidized, resulting in this ratio. During electrolysis the surface changes significantly as there is not a clear layer visible anymore but rather oxide particles on the surface are observed (Figure D.2). However, phosphor is still observed in the EDX spectrum and for the activity the formation of the deposited precatalyst is important. Zhou et al.[5] suggested that it is imperative that the nickel is not fully reduced during CO2RR to obtain moderate CO binding sites, and they reported that a nickel phosphate precatalyst works best. We also observe that the deposited Ni is a better catalyst towards CO2RR than the bare Ni foil (Figures D.3 and D.5), which is not due to

a roughness effect as shown in the capacitive measurements in Figure D.4, but probably due to similar effects as the catalysts of Zhou et al.[5] Throughout the remainder of this study the deposited Ni is used as the catalyst as it is a better catalyst and the production of hydrocarbons is sufficiently high to accurately determine parameters such as the Faradaic efficiency (FE) and chain growth probability (α) under all conditions used.

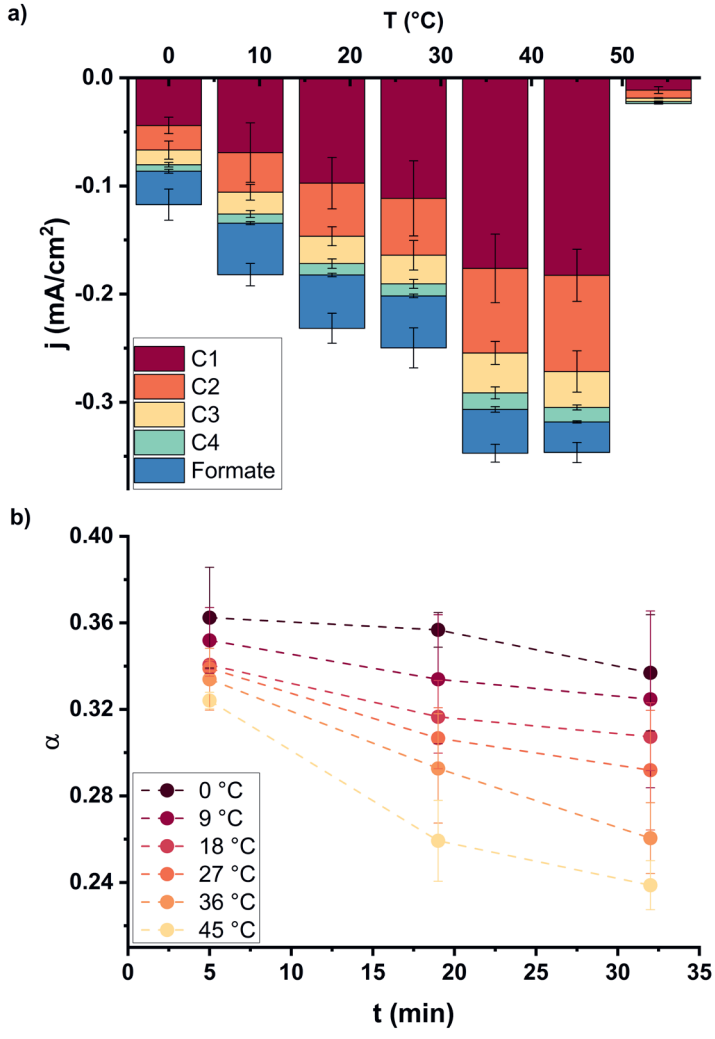

Figure 5.1 a) Activity and b) chain growth probability as function of temperature on Ni in 0.1 M $KHCO_3$ at -1.175 V vs RHE

Figure 5.1a shows the partial current densities for the CO_2 reduction to different products (up to C4) on the nickel catalyst as a function of temperature. The C1 product is methane, and ethylene and ethane are the C2 products observed. Interestingly we only detect propene as C3 product, while butene and butane are the observed C4 products. Some C5 products, namely pentene and pentane were also detected, although in such small quantities that accurate quantification was not possible, so these products are omitted from all figures shown. Figure 5.1 shows that by increasing temperature, the activity towards CO2RR increases up to 45 °C, after which it rapidly decreases. The mechanism of CO2RR on Ni must be different than on Cu, which does not show the formation of C3-C5 hydrocarbons. Nickel follows a chain growth mechanism comparable with the mechanism of the Fischer-Tropsch reaction in thermocatalysis. Just like for the Fischer-Tropsch reaction, an Anderson-Flury distribution is followed and a chain growth probability α can be determined (Figure D.6). However, an interesting observation is that besides the hydrocarbons also formate is produced, for which the activity is highest between 10 and 30 °C. Kudo et al.[8] also showed the formation of formate,

especially at elevated pressures, whereas Zhou et al.[5] did not report any formation of formate. Formate does not feature in the chain-growing Fischer-Tropsch mechanism and is likely to be formed via a different mechanism which occurs in parallel. Figure D.7 shows the FE for the chain growth products with temperature and time. Although the FE for CO2RR is low, a total FE around 100% is reached as the hydrogen evolution reaction (HER) clearly dominates the reaction. This is generally known in literature,[3,12] and to use Ni as an active catalyst for CO_2 reduction, significant progress to reduce HER is still required. However, to study the chain growth mechanism on Ni on a fundamental level, these activities and selectivities are sufficient. At lower temperatures, some time is necessary to activate the catalyst, as the selectivity increases in time. At higher temperatures the opposite occurs and the selectivity slightly decreases in time.

The effect of the temperature on the chain growth probability is shown in Figure 5.1b. The chain growth probability decreases with increasing temperature, especially at longer reaction times. The decrease in chain-growth probability is the most significant at the highest temperature, as is illustrated by the deactivation ratios in Figure D.7. When the graphs would be extrapolated to 0 minutes of reaction time, it seems that the chain growth probability could be similar between the different temperatures. This would indicate that temperature does not have an intrinsic effect on the mechanism of chain growth on Ni. However, higher

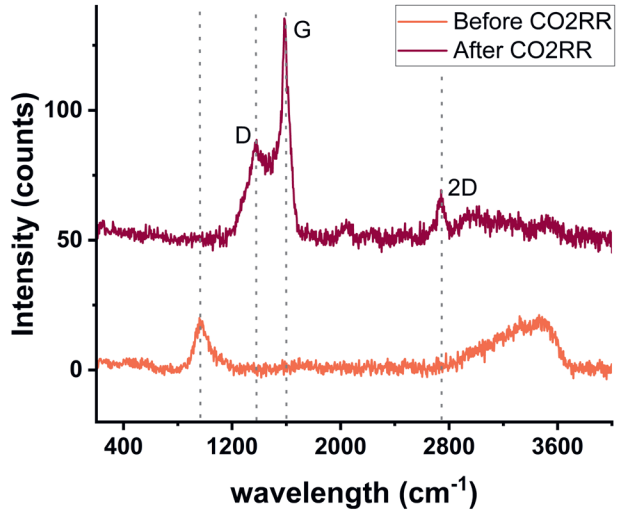

Figure 5.2 Raman spectrum before and after CO2RR on Ni in 0.1 M $KHCO_3$ at -1.175 V vs RHE showing the formation of coke on the electrode

temperatures lead to higher activities of CO_2 reduction, which is accompanied with a higher deactivation rate, affecting the chain growth probability.

Moreover, at elevated temperatures, the current increases over time, as can be observed in Figure D.9a. This increase in current is due to an increase in hydrogen activity and is not caused by the catalyst preparation as it is also observed on the plain Ni electrode (Figure D.9b). The formation of carbon deposits, hereafter called coking, on the electrode surface is the most probable cause of the deactivation of the catalyst, leading to a lower chain growth probability and an apparently higher HER activity. Coking is generally observed in the thermocatalytic Fischer-Tropsch reaction[21–25] and as CO2RR on Ni presumably follows a similar reaction mechanism, coke is expected to form here as well. Moreover, the electrode becomes visibly black after CO2RR, but not after HER (Figure D.10). A microscopic image shows black patterns all over the electrode after CO2RR (Figure D.11). To provide solid evidence for the formation of coke, Figure 5.2 shows Raman spectra before and after CO_2 reduction. The peak around 960 cm^{-1} in the spectrum before CO2RR is likely from PO_4.[26] After CO_2 reduction, intense bands are observed at 1370 and 1585 cm^{-1}, which are characteristic for coke formation. [21–23,25,27,28] The band at 1370 cm^{-1}, commonly called the D band, is assigned to a more disordered type of carbonaceous species and arises due to the breakdown of the selection rule due to defects and disorder in the crystal structure.[21,27,28] The band at 1585 cm^{-1} is called the G band

and is assigned to a more graphite-like carbon.[21,22] The 2D peak is typical for graphene,[29] but can also be observed in graphite, where it shifts to the higher wavelengths observed here.[30] Combined with the high intensity of the G band, this indicates that the coke formed on the Ni catalyst during electrochemical CO_2 reduction consists mostly of a graphite-like structure. This graphitic carbon is often considered to be responsible for catalyst deactivation by blocking the active sites for CO2RR.[21,22,25] The faster decrease of the chain growth probability with higher temperatures suggests the coke could inhibit the propagation of the hydrocarbon chain, possibly by occupying adsorption sites making it more difficult for carbon intermediates to reach the growing hydrocarbon chain. Quantification of the coke is difficult due the inhomogeneous coke formation as can be seen from Figure D.11.

5.3.2 Effect of electrode potential and bulk CO_2 concentration

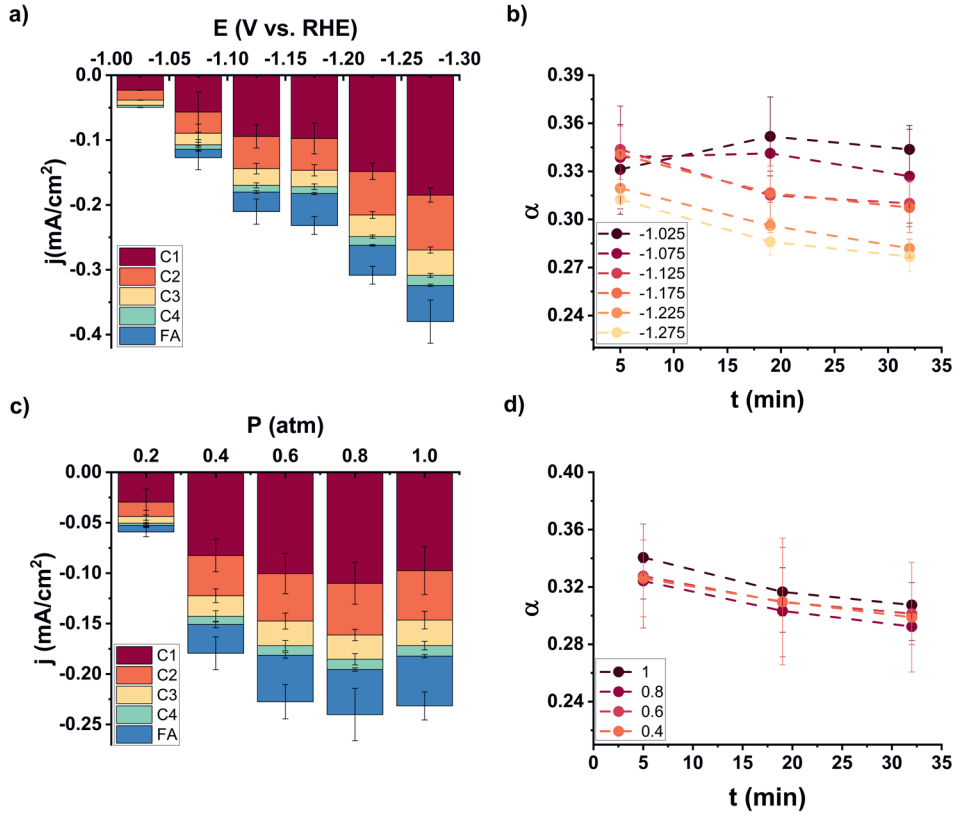

Figure 5.3 a) activity and b) chain growth probability as a function of electrode potential. c) activity and d) chain growth probability as function of CO_2 partial pressure on the Ni catalyst in 0.1 M $KHCO_3$ at -1.175 V vs RHE

To understand the effect of temperature on the CO2RR on the Ni catalyst and its deactivation in more detail, additional parameters have been studied. Figures 5.3a and b show the effect of electrode potential, while Figures 5.3c and d show the effect of the bulk concentration of CO_2 by adjusting the partial pressure. It can be seen that with increasing potential the activity of CO2RR increases. However, the FE shows an optimum around -1.125V vs RHE (Figure

D.12). Figure 5.3b shows that the chain growth probability is influenced by the potential, with lower overpotentials producing longer chains. Yet, at 5 min this dependency is less obvious. This time effect is not caused by deactivation as is the case with temperature. Instead, from 5 to 19 min the chain growth probability increases at -1.075 and especially at -1.025 V vs RHE. Therefore, at the lowest potentials, time is needed to activate the catalyst, which is also apparent from the FE in Figure D.11 and the deactivation ratio in Figure D.8. This indicates that the Ni phosphate deposited pre-catalyst requires negative potential to transform into the active catalyst. We hypothesize the Ni might need to be partially reduced or the phosphate needs to be partially removed to obtain the active phosphate derived catalyst. The deactivation between 19 and 32 minutes seems similar at all potentials. Figure D.13 shows indeed that not higher current densities but higher temperatures are causing the higher deactivation rate observed in Figure 5.1b. In this figure, the chain growth probability of two experiments with similar current densities are compared. The experiment at higher temperature and lower potential shows higher deactivation than the experiment at lower temperature and higher potential. This is even more apparent in the deactivation ratio plotted versus both temperature and potential in Figure D.7, which illustrates that there is a strong deactivation at higher temperatures. The deactivation at higher potentials stays constant, while at low potentials the beforementioned activation is evident by a deactivation ratio higher than 1.

The bulk concentration of CO_2 does not influence the chain growth probability or the deactivation as can be seen in Figure 5.3d. The chain growth probability at 0.2 atm has not been taken into account as the C4 production was too low to obtain an accurate value. The activity is also not impacted significantly with decreasing CO_2 concentration until a partial pressure of 0.2 atm. Below this concentration the activity decreases very rapidly. These results show that the effects in Figure 5.1 are mainly caused by the increase in temperature and not due to the changes in the bulk CO_2 concentration.

5.3.3 Effect of electrolyte cation and reactant

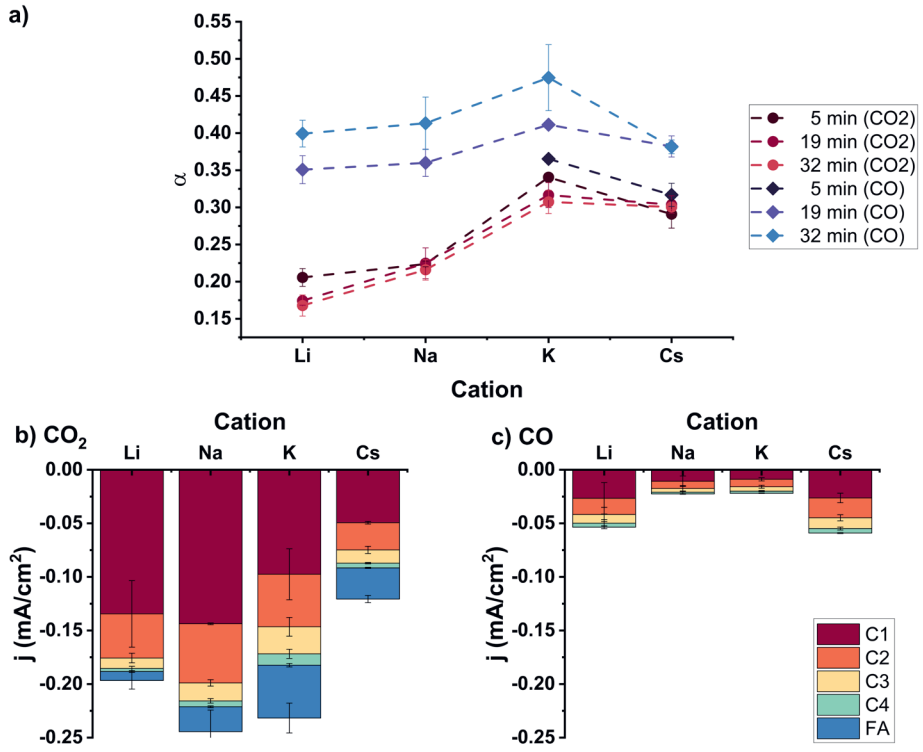

Figure 5.4 a) Chain growth probability for different cations for both CO2RR and CORR b) activity for CO2RR for different cations at -1.175 V vs RHE and c) activity for CORR for different cations at -1.075 V vs RHE on the Ni catalyst in 0.1 M $KHCO_3$

For CO_2 reduction, a cation effect is commonly observed.[31–34] Figure 5.4 shows that cations also influence the CO2RR and CO reduction (CORR) on the Ni catalyst. The chain growth probability of CO2RR depends significantly on the cation used and is the highest for K^+. However, the total current density of CO2RR does not depend significantly on the cation as seen in Figure 5.4b. Li^+ and Na^+ show almost similar activities as K^+, although the product distribution is significantly altered. Cs^+ however shows significantly lower activities, which is notable as on other metals Cs^+ electrolytes often results in the most active catalyst.[32,33] Figure D.14 shows that the deactivation rate also depends on the cation, where Cs is the most stable and Li the most unstable. However, this does not influences the activities significantly as both at 5 min and at 32 min the trend is similar to the time-averaged trend observed in Figure 5.4b.

In addition to CO_2 reduction, we also performed experiments with CO as the reactant, as CO is expected to be a likely intermediate to form CH_x intermediates to grow the hydrocarbon chain. Figures 5.4a and c show that CO reduction does indeed occur on the Ni catalyst, and that the chain growth probability is higher than for CO2RR, although the activity is significantly lower. The chain growth probability and activity for CORR depend significantly on time, whereas this was not the case for CO2RR. It seems that the catalyst requires an activation time as α increases with time. This might be due to the lower activities and could be comparable to the observations at lower overpotentials during CO2RR in Figure 5.3b. Moreover, the cation effect on CORR is significantly smaller than for CO_2 reduction.

To be able to compare the CO reduction vs. the CO_2 reduction in more depth we have compared them in different electrolytes and at different electrode potentials. Experiments in Figure 5.4 have been performed in bicarbonate electrolyte.

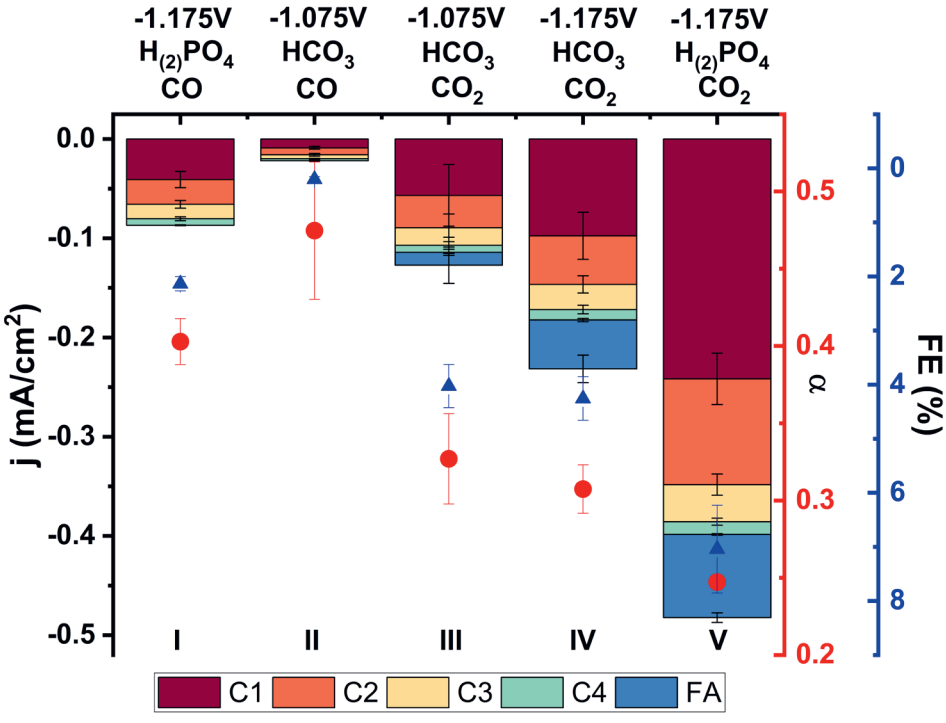

Figure 5.5 The activity, selectivity and chain growth probability on the Ni catalyst with different applied potential, reactant and anions. The potential given is on the RHE scale, bicarbonate and phosphate electrolytes were used at 0.1 M and either CO or CO_2 was saturated in the solution.

However, CO and CO_2 saturated bicarbonate electrolytes have different pH values. If the rate determining step (RDS) comprises of a proton transfer, this can be important because both reactions should then either be compared on an SHE or RHE scale. For Cu catalysts, methane and hydrogen formation have been compared on the RHE scale, while CO and the C2+ products have been compared on the SHE scale.[35,36] To check for these pH effects we have compared both reactions at similar potentials both at the RHE and SHE scale (Figure 5.5; II, III, IV). Moreover, both reactions have been performed in a pH 7 phosphate buffer, which does not change pH when saturated with either CO or CO_2 (Figure 5.5; I and V). Figure 5.5 shows that when CO2RR and CORR are compared at the same potential vs SHE instead of RHE, the differences only become larger, indicating pH is important for the RDS. Moreover, the differences in activity and chain growth probability also remain when the experiments are performed in phosphate buffer. However, an interesting observation is that the activities and selectivities of both CORR and CO2RR increase when phosphate is used as electrolyte instead of bicarbonate. At the same time the chain growth probabilities decrease in both cases. Phosphate is known to be a good proton donor[37] and it might be that this increases the activity of $CO_{(2)}$RR on Ni (also compared to HER). This would also suggest that these reactions might benefit from more acidic electrolyte conditions and that electrolyte engineering can play an important role in optimizing this reaction.

5.3.4. Discussion and open questions

For the thermocatalytic Fischer-Tropsch reaction, CO dissociation, oxygen removal, carbon hydrogenation and chain termination have all been suggested as the rate-determining step and it appears difficult to reach a consensus.[18] However, recent studies show that the hydrogenation step is the most important for the overall kinetics.[38] For the electrochemical Fischer-Tropsch like mechanism of CO2RR, the CO_2 activation is an additional step which could be rate-limiting. For CO_2 to CO, it is generally assumed that the first electron transfer to activate CO_2 is the RDS,[39–42] while for C2+ formation on copper the CO dimerization is generally considered the RDS.[43–45] Both steps are highly sensitive to catalyst structure[46–48] and local electrolyte composition, i.e. cation concentration and identity. [32–34] From the data in Figure 5.5, we suggest that the CO_2 dissociation is not the RDS for the formation of hydrocarbons on Ni as the activities for CO2RR are higher than for CORR. If CO_2 activation would be the RDS, we would expect higher activities when this step is bypassed by starting with CO as reactant. Similar activities are expected if the RDS is after the CO_2 activation, as has been observed on Cu electrocatalysts.[49,50] Moreover, CO_2 activation as RDS would result in a dependence on the bulk CO_2 concentration. However, Figure 5.3c shows this is not the case unless very low concentrations are used.

The apparent activation energy for the different products can be obtained by an Arrhenius plot (Figure D.15). This activation energy is ca. 60 kJ/mol and is similar for the different CO2RR products. This would suggest that the rate determining step is the same step for all products. Moreover, we observe an anion effect, with a better proton donor leading to higher activities. This indicates that a hydrogenation step is the RDS. Another indication for hydrogenation as the rate determining step is the effect of pH as seen in Figure 5.5. These results indicate that a proton transfer is involved in the rate determining step, as is the case for hydrogenation.

Equivalent to the thermocatalytic Fisher-Tropsch reaction, both the termination of the hydrocarbon chain by hydrogenation or hydrogenation of *CO could be the rate determining step. From our data, it is not possible to exclude CO reduction as the RDS as we have done for CO_2. If CO reduction is the RDS, we might expect that CO2RR and CORR give equal activities as the CO_2 activation to CO should not have any effect. However, we observe that CO reduction leads to lower activities than CO2RR. This might be explained if the local CO concentration is higher during CO_2 reduction than during CO reduction due to the low CO solubility. A dependence on the CO coverage could also explain why the activity decreases only at low CO_2 concentrations, where the CO coverage might be more limited. However, it could also be that CO adsorbs strongly to the surface, which blocks sites for hydrogenation of the hydrocarbon chain and thus lowers the activity. This could be another explanation why CO leads to lower activities, something that also has been observed in thermocatalytic Fischer-Tropsch synthesis, where CO has a negative reaction order.[38] Another possible explanation for the observation that CO2RR is more active than CORR is that they follow different pathways, as has been suggested by Zhou et al.[5] However, this is merely an hypothesis and could also be due to different reaction sites for CO and not to a difference in mechanism, as has been observed for co-feeding experiments on Cu electrodes.[51,52] An argument in favor of *CO hydrogenation as RDS is that for the formation of methane on Cu, the RDS is hydrogenation of *CO to form *CHO.[53]

When the chain growth probability is plotted vs activity, a negative trend is observed (Figure D.16). The chain growth probability can be defined as:[9]

$$\alpha = \frac{R_P}{R_P + R_T} \qquad (6)$$

where α is the chain growth probability, R_p the rate of propagation, and R_T the rate of termination. The negative trend between activity and chain probability could be related to the deactivation by coke formation. However, this trend is also seen for the experiments at different potentials, where no difference in deactivation due to

coking has been observed (Figure D.7). This negative trend might therefore indicate that the hydrogenation to terminate the chain is the rate determining step instead of *CO hydrogenation. This would namely mean that an increase in activity is related to an increase in R_T, which leads to an decrease in chain growth probability. This is similar to the thermocatalytic Fischer-Tropsch reaction, where at low pressures the termination step is also considered rate limiting.[38]

The only observation which is more difficult to align directly with hydrogenation as rate determining step is the cation effect observed in Figure 5.4. The cation effect on its own can still be explained as the hydrogenation can be cation mediated, similar to the hydrogen evolution reaction.[54] However, this would not explain why the cation effect is larger for CO2RR than for CORR. It might be that the cations only start to be important at higher coverage of intermediates and that when CO is absorbed these coverages cannot be reached. Moreover, the cations do not follow the same negative trend between activity and chain growth probability.

This might indicate that the cations interact in a different way with the chain growth on the Ni catalyst. These observations strongly suggests that hydrogenation is involved in the rate determining step. However, whether this is the hydrogenation of *CO or the hydrogenation that leads to termination of the hydrocarbon chain cannot be answered conclusively. A systematic mechanistic study including in situ spectroscopic experiments is required to determine the exact rate determining step and the precise role of the cations. This is outside the scope of the current study, but shows that many open questions remain to be answered about the electrochemical chain growth mechanism.

5.4 Conclusion

In this work, we have investigated the electrochemical reduction of CO_2 on Ni via an electrochemical Fischer-Tropsch-like mechanism. We observe that temperature enhances the activity, but also the formation of coke, which deactivates the catalyst. This results in a faster decrease of the chain growth probability with time at higher temperatures. The bulk concentration of CO_2 hardly influences the reaction. The chain growth probability is mainly influenced by potential and especially the electrolyte composition. Lower potentials lead to lower activities and higher chain growth probabilities. Moreover, K^+ containing electrolytes form the longest hydrocarbons, although the effect is smaller with CO as reactant instead of CO_2. Also the anions can influence the reaction, where better proton donating anions seem to increase the rate of reaction. The rate determining step is most likely a hydrogenation step and we hypothesize this could either be the hydrogenation of *CO or the hydrogenation of the hydrocarbon chain to terminate its growth. These results open the way to further development of Ni as a catalyst for electrochemical

CO_2 reduction. Furthermore, they give insight in the Fischer-Tropsch-like mechanism, which makes it possible to optimize this reaction, also on other catalysts. However, more research is needed to understand the mechanism in more detail and especially the influence of the electrolyte composition on the mechanism.

References

1. Raciti, D. & Wang, C. *ACS Energy Lett* **3**, 1545–1556 (2018).
2. Hori, Y., Wakebe, H., Tsukamoto, T. & Koga, O. *Electrochim Acta* **39**, 1833–1839 (1994).
3. Bagger, A., Ju, W., Varela, A. S., Strasser, P. & Rossmeisl, J. *ChemPhysChem* **18**, 3266–3273 (2017).
4. Kuhl, K. P., Cave, E. R., Abram, D. N. & Jaramillo, T. F. *Energy Environ Sci* **5**, 7050–7059 (2012).
5. Zhou, Y. *et al. Nat Catal* **5**, 545–554 (2022).
6. Nitopi, S. *et al. Chemical Reviews* 119 7610–7672 (2019).
7. Wang, X., Hu, Q., Li, G., Yang, H. & He, C. *Electrochemical Energy Reviews* 5 (2022).
8. Kudo, A., Nakagawa, S., Tsuneta, A. & Sakata, T. *J. Electrochem. Soc* **140**, 1541–1545 (1993).
9. Van Der Laan, G. P. & Beenackers, A. A. C. M. *Catal Rev Sci Eng* **41**, 255–318 (1999).
10. Ougitani, Y., Aizawa, T., Sonoyama, N. & Sakata, T. *Bull. Chem. Soc. Jpn* **74**, 2119–2122 (2001).
11. Vos, R. E. *et al. ACS Catal* **13**, 8080–8091 (2023).
12. Kuhl, K. P. *et al. J Am Chem Soc* **136**, 14107–14113 (2014).
13. Akbarzadeh, O. *et al. Catalysts* **11**, 846 (2021).
14. Kortlever, R. *et al. Chemical Communications* **52**, 10229–10232 (2016).
15. Kim, Y. J., Maeng, J. Y., Hwang, S. Y., Rhee, C. K. & Sohn, Y. *Appl Catal B* **338**, 123017 (2023).
16. Dong, S. T., Xu, C. & Lassalle-Kaiser, B. *Chem Sci* **14**, 550–556 (2022).
17. Wuttig, A. & Surendranath, Y. *ACS Catal* **5**, 4479–4484 (2015).
18. ten Have, I. C. & Weckhuysen, B. M. *Chem Catalysis* 1 339–363 (2021).
19. Gordan J. Kelly. in *Hydrogenation: Catalysts and Processes* 155–172 (De Gruyter, 2018).
20. Plummer, L. N. & Busenberg, E. *Geochim Cosmochim Acta* **46**, 1011–1040 (1982).
21. Cats, K. H. & Weckhuysen, B. M. *ChemCatChem* **8**, 1531–1542 (2016).
22. De Smit, E. *et al. J Am Chem Soc* **132**, 14928–14941 (2010).
23. Ahn, C. Il *et al. Microporous and Mesoporous Materials* **188**, 196–202 (2014).
24. Tsakoumis, N. E., Rønning, M., Borg, Ø., Rytter, E. & Holmen, A. in *Catalysis Today* vol. 154 162–182 (2010).

25. Carballo, J. M. G. *et al. Catal Today* **214**, 2–11 (2013).
26. Oliveira, E. M., Rogero, M., Ferreira, E. C. & Gomes Neto, J. A. *Spectrochim Acta A Mol Biomol Spectrosc* **246**, 1386–1425 (2021).
27. Sattler, J. J. H. B., Beale, A. M. & Weckhuysen, B. M. *Physical Chemistry Chemical Physics* **15**, 12095–12103 (2013).
28. Tuinstra F & Koenig JL. *Journal of Chemical Physics* **53**, 1126–1130 (1970).
29. Childres, I., Jauregui, L. A., Park, W., Cao, H. & Chen, Y. P. in *New developments in photon and materials research* vol. 1 1–20 (2013).
30. Ferrari, A. C. *Solid State Commun* **143**, 47–57 (2007).
31. Monteiro, M. C. O. *et al. Nat Catal* **4**, 654–662 (2021).
32. Ringe, S. *et al. Energy Environ Sci* **12**, 3001–3014 (2019).
33. Resasco, J. *et al. J Am Chem Soc* **139**, 11277–11287 (2017).
34. Monteiro, M. C. O., Dattila, F., López, N. & Koper, M. T. M. *J Am Chem Soc* **144**, 1589–1602 (2022).
35. Resasco, J., Lum, Y., Clark, E., Zeledon, J. Z. & Bell, A. T. *ChemElectroChem* **5**, 1064–1072 (2018).
36. Schouten, K. J. P., Pérez Gallent, E. & Koper, M. T. M. *Journal of Electroanalytical Chemistry* **716**, 53–57 (2014).
37. Jackson, M. N., Jung, O., Lamotte, H. C. & Surendranath, Y. *ACS Catal* **9**, 3737–3743 (2019).
38. Pestman, R., Chen, W. & Hensen, E. *ACS Catal* **9**, 4189–4195 (2019).
39. Deng, W., Zhang, P., Seger, B. & Gong, J. *Nat Commun* **13**, 803 (2022).
40. Ringe, S. *et al. Nat Commun* **11**, 33 (2020).
41. Dunwell, M., Luc, W., Yan, Y., Jiao, F. & Xu, B. *ACS Catal* **8**, 8121–8129 (2018).
42. Wuttig, A., Yaguchi, M., Motobayashi, K., Osawa, M. & Surendranath, Y. *Proc Natl Acad Sci U S A* **113**, E4585–E4593 (2016).
43. Kortlever, R., Shen, J., Schouten, K. J. P., Calle-Vallejo, F. & Koper, M. T. M. *Journal of Physical Chemistry Letters* **6**, 4073–4082 (2015).
44. Li, Z., Zhang, T., Raj, J., Roy, S. & Wu, J. *Energy and Fuels* **37**, 7904–7910 (2023).
45. Calle-Vallejo, F. & Koper, M. T. M. *Angewandte Chemie* **125**, 7423–7426 (2013).
46. Vickers, J. W., Alfonso, D. & Kauffman, D. R. *Energy Technology* 5 775–795 (2017).
47. Zhu, C. *et al. Chem* **7**, 406–420 (2021).
48. Kim, H., Park, H. S., Hwang, Y. J. & Min, B. K. *Journal of Physical Chemistry C* **121**, 22637–22643 (2017).
49. Wang, L. *et al. ACS Catal* **8**, 7445–7454 (2018).
50. Liu, X. *et al. Nat Commun* **10**, 32 (2019).
51. Wang, X. *et al. Nat Nanotechnol* **14**, 1063–1070 (2019).
52. Gao, W., Xu, Y., Fu, L., Chang, X. & Xu, B. *Nat Catal* **6**, 885–894 (2023).
53. Schreier, M., Yoon, Y., Jackson, M. N. & Surendranath, Y. *Angewandte Chemie - International Edition* **57**, 10221–10225 (2018).
54. Goyal, A. & Koper, M. T. M. *Angewandte Chemie - International Edition* **60**, 13452–13462 (2021).

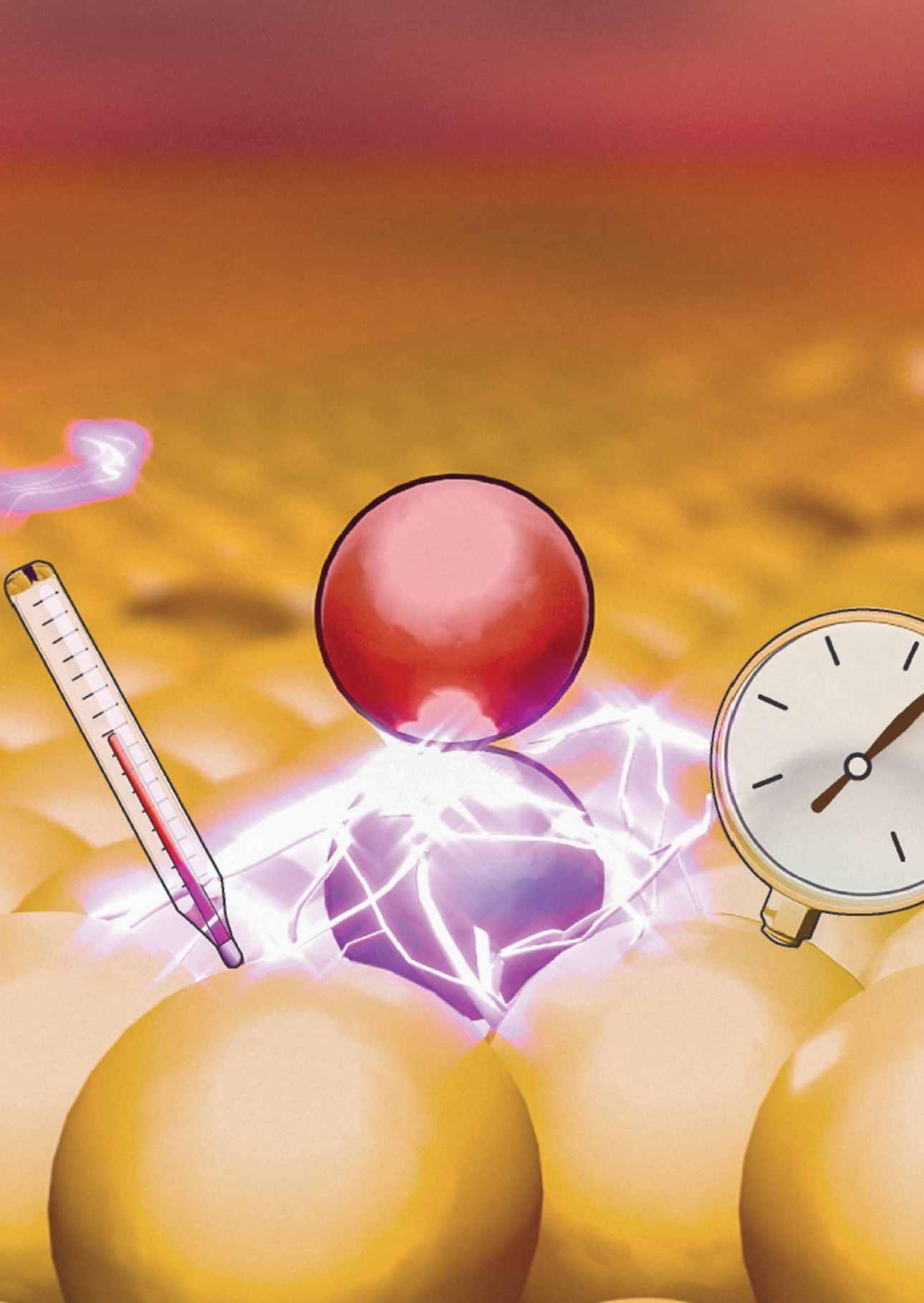

6

Design of a Rotating Disk Electrode setup operating under high pressure and temperature: application to CO_2 reduction on gold

This chapter is based on A.H.M. da Silva, R.E. Vos, R.J.C. Schrama, M.T.M. Koper *Electrochimica Acta* 144612 (2024)

Abstract

We describe the design and development of a rotating disk electrode (RDE) cell capable of operating at pressures up to 140 bar and temperatures up to 200°C. This setup enables electrochemical surface characterization through techniques such as voltammetry and impedance spectroscopy, under different mass transport regimes. Furthermore, evaluation of catalytic performance, including CO_2 reduction, is possible as the system works in a semi-continuous mode interfaced with online gas sample measurements. As a proof of concept of the high-pressure cell designed, we examined the temperature-dependent changes in the cyclic voltammograms (CVs) of polycrystalline gold up to 150°C and 50 bar. Additionally, online catalytic performance of CO_2 reduction to CO on a rotating polycrystalline gold disk electrode was investigated under different pressure and temperature. Our results indicate a positive impact of pressure on the faradaic efficiency (FE) towards CO up to 6 bar after which it plateaued around 90%. Further increase of pressure and temperature had a significant positive effect on the activity. This study opens up promising avenues for future investigations in electrocatalysis, ranging from fundamental explorations of surface modifications induced by variations in temperature and pressure to the development of high-performance catalysts.

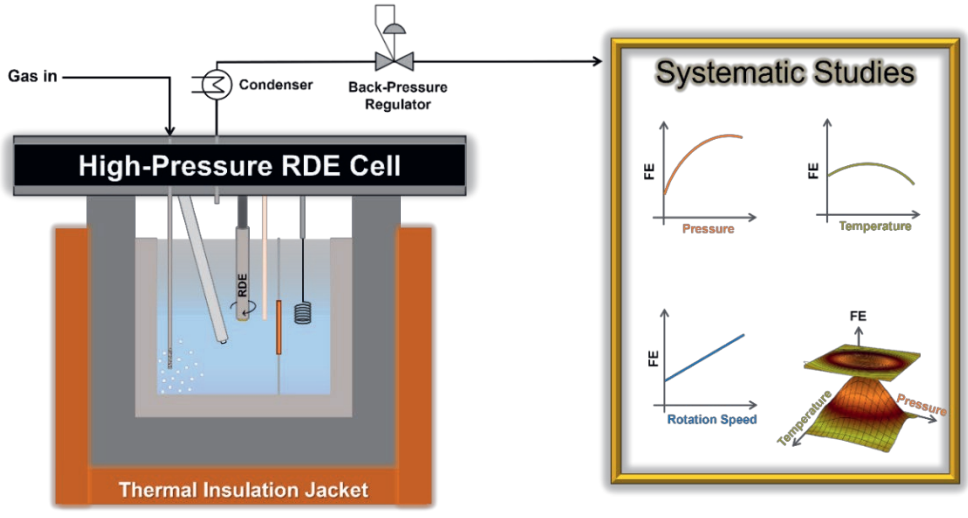

6.1 Introduction

The CO_2 electrochemical reduction reaction (CO_2RR) offers a promising strategy for CO_2 utilization when powered with renewable electricity. Through this approach, CO_2 can be converted using water as a proton donor, which provides an advantage compared to the use of H_2 in conventional thermal catalytic conversion. A wide range of products has already been reported from CO_2RR, including C_1 to C_3 compounds such as formic acid, CO, ethylene, ethanol, n-propanol, as well as other compounds like aldehydes and ketones [1,2]

To date, CO_2RR has primarily been studied under ambient conditions, where Cu is the sole metal capable of facilitating C-C coupling and thereby producing C_{2+} compounds with higher yields [3,4]. Conversely, in thermal catalysis, Cu-based catalysts predominantly yield C_1 compounds such as CO and methanol [5,6]. Fe and Co are well-established metals utilized in the Fischer-Tropsch reaction to generate olefins and high-density carbonaceous compounds at temperatures exceeding 200°C and pressures of 30 bar [7–9]. However, Fe exhibits limited electrochemical CO_2 conversion capability [10,11]. Some of these disparities between thermal and electrocatalysis may be related to variations in reaction conditions, wherein temperature and pressure significantly influence compound adsorption on the catalytic surface. For example, Zhang et al. [12] demonstrated that the selectivity for multicarbon products follows a volcano trend based on the ratio of the Cu–CO stretching band to the Cu–CO rotation band. This ratio increases with increasing temperature [13], which agrees with the enhanced formation of C_{2+} compounds at temperatures around 50°C compared to room temperature.

The temperature effect is typically not studied in CO_2RR studies and often avoided due to membrane instability and/or rapid catalyst deactivation at higher temperatures. However, in practical applications, electrolyzers will invariably operate at elevated temperatures [14–18]. Only a few studies delve into the temperature effect at the fundamental level. We have previously studied the temperature effect on the CO_2RR on Cu electrodes and its impact on product distribution [13], as well as the kinetic parameters of CO_2RR on Au electrodes at elevated temperatures [19]. Recently, a similar temperature dependence has been demonstrated for C_{2+} compounds in the CO reduction reaction using Cu gas diffusion electrodes (GDE) operating under more industrial conditions (current densities up to 500 mA/cm^2) [20]. These works show similar results: the catalytic

performance towards $CO_{(2)}RR$ decreases at temperatures over 50°C, favoring hydrogen evolution reaction (HER). The reasons for HER enhancement at the expense of $CO_{(2)}RR$ are attributed to a change in the hydrophobicity of the gas diffusion layer (GDL), leading to flooding of the GDE [20], reconfiguration of the catalyst particles at the atomic scale due to increased atom mobility at elevated temperatures [13,20], and CO_2 availability potentially becoming the limiting factor at higher temperatures [19]. However, if CO_2 availability would be the limiting factor, an increase in CO_2 concentration, such as by raising the pressure, should prevent the observed decrease in performance in the formation of carbon products at temperatures exceeding 50°C.

The impact of pressure on CO_2RR has been extensively studied in the literature [21–27]. At the end of the last century, Hara and coworkers made an important contribution identifying the pressure effect on CO_2 reduction [21,23,28,29]. They demonstrated that a 44% faradaic efficiency to CO could be achieved on glassy carbon at 30 bar and approximately 100 mA/cm^2 [23], despite glassy carbon being known as an inert substrate with minimal activity for CO_2 conversion at atmospheric pressure [30]. Hara et al [28]. also investigated the effect of pressure on several metal wires (Ti, Zr, Nb, Ta, Cr, Mo, W, Mn, Fe, Co, Rh, Ir, Ni, Pd, Pt, Cu, Ag, Au, Zn, Al, In, Sn, Pb, and Bi) at 167 mA/cm^2 and identified mainly CO and HCOOH as the primary carbon products at 30 bar for all metals, including Pt, where a 56% FE was found for CO + HCOOH, whereas >90% FE towards H_2 is expected at 1 bar. Additionally, Hara et al. [21] investigated the impact of pressure on the CO formation from CO_2 reduction using Co-, Cu-, Rh-, Ni-, Pd-, Ag-, and Ag-GDEs, with Ag showing the highest catalytic activity. Specifically, the FE to CO on Ag increased from around 40% to 86% by raising the pressure from 1 bar to 20 bar. Ramdin et al. [24,25] studied the effect of pressure on formic acid formation using a tin-based electrode. They explored different scenarios, including the use of cationic exchange membranes, bipolar membranes, and pH effects. In summary, they achieved an improvement in FE to formate from approximately 40% to 90% by increasing the pressure up to 50 bar. This enhancement was attributed to the higher concentration of CO_2 in solution. Recently, Zong et al. [26] have reviewed the influence of the pressure on CO_2RR. They concluded that pressure can influence catalytic performance through various mechanisms, such as the thermodynamics of the reaction, the acid/base buffer balance ($CO_2/HCO_3^-/CO_3^{2-}$), and the degree of coverage of CO_2 on the catalyst surface. Interestingly, metals such as Ni, Fe, and Pt exhibit low selectivity

to CO at ambient conditions but demonstrate significant improvements in CO and/or formic acid production at relatively high CO_2 pressures [29,31,32], which aligns with the hypothesis that the disparities between thermal and electrocatalysis may be bridged by variations in reaction conditions.

However, to date, there are no studies that investigate the combined effects of mass transport, temperature, and pressure simultaneously at a fundamental level. One reason for this gap may be the complexity involved in designing and constructing an electrochemical cell capable of altering parameters such as temperature and pressure, as well as the fluid dynamics within the cell (e.g., by varying the rotation speed of the disk electrode), while ensuring safety and proper electrical connections. Additionally, the compartment housing the electrochemical components must be predominantly metal-free to minimize metal contamination in the experiments.

Here, we present the design of a rotating disk electrochemical cell, which is based on a commercial (Parr) rotating cylinder electrode high-pressure reactor, with several modifications. The designed high-pressure and high-temperature electrochemical cell is capable of operating in a semi-continuous mode under pressures of up to 140 bar and temperatures of up to 200°C, with a maximum rotation speed of 2500 rpm for the disk electrode. In this system, several fundamental electrochemical surface investigations, such as cyclic and linear voltammetry, impedance spectroscopy, and electrochemical frequency modulation, can be conducted under different pressure, temperature, and mass transfer conditions. Additionally, catalytic performance investigations including $CO_{(2)}$RR, HER, oxygen evolution reaction (OER), electro-organic oxidation, nitrogen reduction, etc., can be explored, as the cell is also interfaced with online gas chromatography (GC) and mass spectrometry. As a proof of concept, we investigate here the influence of temperature, pressure, and rotation speed on CO_2RR on a gold electrode, while also providing surface characterization of polycrystalline Pt and Au via cyclic voltammetry, to demonstrate cleanliness and reproducibility of the electrochemical experiments. Our results show that the combination of high pressure and high temperature favorably impact current density and Faradaic efficiency towards CO.

6.2 Experimental

6.2.1 Chemicals

All solutions used in this work were made by dissolving appropriate amounts of chemicals in Milli-Q water (Millipore, resistivity ≥ 18.2 MΩ cm). All chemicals were used as received: $KHCO_3$ (>99.5%, Sigma-Aldrich), $KMnO_4$ (ACS reagent, Fluka), H_2SO_4 (ACS Reagent, Fluka), H_2O_2 (35%, Merck), CO_2 (Linde, 4.5), and Ar (Linde, 5.0).

6.2.2 General Procedures

Prior to each day of experiments, all glassware, the PEEK cup, and the PEEK membrane separator were soaked in a 0.5 M H_2SO_4 and 1 g/L $KMnO_4$ acid solution for at least 12 hours. The glassware and the PEEK compartments were then rinsed and submerged in a diluted solution of H_2O_2 and H_2SO_4 to remove any remaining manganese oxide. Next, the solution was drained, and the glassware and the PEEK compartments were rinsed and boiled three times in MilliQ water (≥18.2 MΩ cm).

In this work, a Au disk electrode embedded in a PEEK holder with dimensions of 8 mm diameter, Au wire (2 mm) or Pt wire (0.5 mm) exposing 5 cm^2 area were used as working electrodes. For the wires, a flame annealing procedure was used for surface cleaning and preparation. For the gold disk electrode, gold was mechanically polished on a microcloth (Buehler) with diamond suspensions (Buehler) of 3.0, 1.0, and 0.25 μm successively. Next, the electrode was rinsed and sonicated in ultrapure water for at least 10 min to remove remnant diamond suspension from the surface.

6.2.3 High-pressure and High-temperature Rotating Disk Electrode (RDE) electrochemical cell.

The electrochemical cell developed in this work is based on the Rotating Cylinder Electrode (RCE) high-pressure reactor developed by Parr Company, with several modifications. Figure 6.1 shows a schematic of the high-pressure Rotating Disk Electrode (RDE) cell developed for this study. Pictures of the actual cell and its components are provided in Figure E.1. A 120 mL PEEK insert was positioned in the stainless-steel vessel (Figure E.1b and E.1c). The electrolyte was placed within

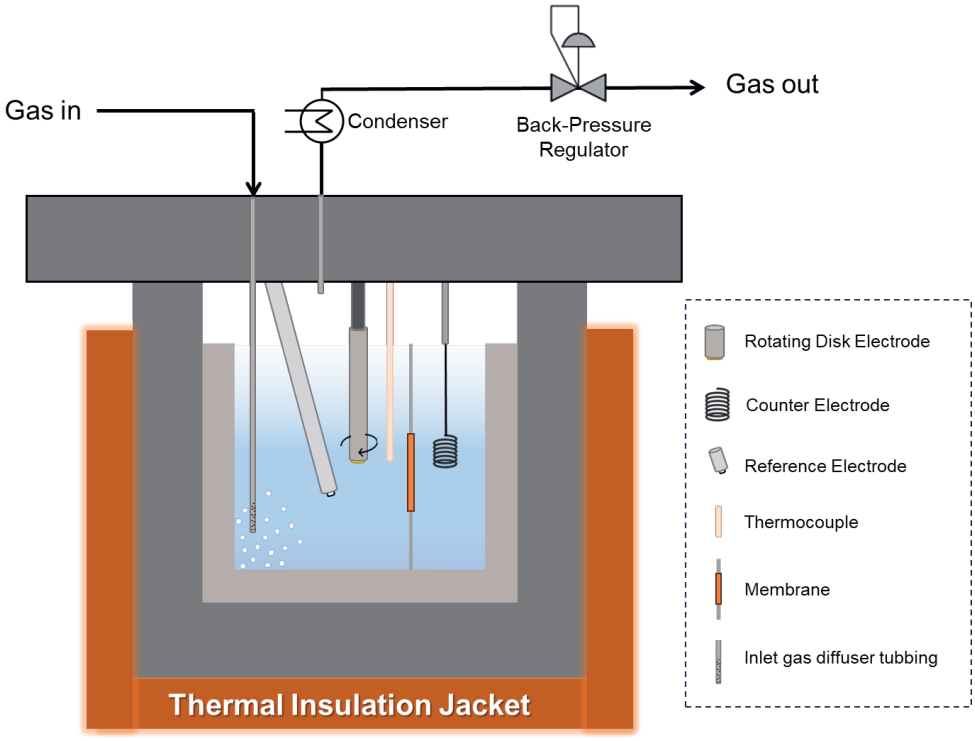

Figure 6.1 Schematic illustration of the high-pressure and high-temperature rotating disk electrode cell.

the PEEK insert, preventing contact with the metal wall of the vessel. Another PEEK compartment with a circular window of 25 mm diameter was positioned inside of the insert, creating an H-type cell configuration (Figures E.1d-f). This configuration allows for the incorporation of a membrane that separates the working electrode compartment from the counter electrode compartment. The working and counter electrode compartments can be filled with up to 90 mL and 10 mL of electrolyte, respectively.

The system can accommodate wire, cylinder or disk electrode configurations for the working electrode. In this work, both wires and disk electrodes were used. The disk electrode was made of an 8 mm x 2 mm (diameter x height) cylinder embedded in PEEK material (Figure E.1f), exposing only the electrode disk area and preventing contact between the electrode sides and any other metal with the electrolyte. Wires offer flexibility and can be easily modified to achieve a desired

exposed surface area. Furthermore, at high temperatures (>100°C), disk electrodes embedded with a plastic matrix are compromised as the metal and plastic exhibit different thermal expansion characteristics, allowing electrolyte to permeate from the junction, compromising the measurements. In contrast, wires offer more flexibility at high temperatures.

A coated DSA titanium mesh was used as the counter electrode for CO_2 electrolysis tests, while Au (or Pt) wire was used as the counter electrode for CV characterization measurements. An UltraDeg® High-Pressure Ag/AgCl (Corr instruments) and a PiperION-A anionic exchange membrane (A40 from Versogen) were used as the reference electrode and membrane, respectively, for all tests. The metal walls of the reference, thermocouple, and holders were meticulously wrapped with Teflon tape to prevent metal exposure (Figure E.1h and E1i). Wrapping the thermocouple with Teflon tape requires more time for temperature stabilization, but it prevents metal contact in the electrolyte. Even the lid and other cell parts that do not directly contact the electrolyte were meticulously coated with Teflon and Kapton tape before the tests start to prevent condensed steam droplets from the metal vessel walls and contaminating the electrolyte, especially during high-temperature tests. A Teflon cylinder was placed on the top of the PEEK cup to decrease the headspace volume of the vessel (Figure E.1c and E.1j).

An inlet PEEK gas diffuser tubing for continuously electrolyte saturation and a back-pressure regulator (BPR) are connected to the cell to operate the electrolysis reaction in a semi-continuous mode. A external thermal insulator jacked is placed around the vessel so that the temperature can be increased and isolated. A condenser is placed before the BPR to prevent steam and volatile compounds from being carried away. The system can operate at pressures up to 140 bar and temperatures up to 200°C, although we limited our tests up to 50 bar and 150°C. The pressure measured in the system is gauge pressure (barg) rather than absolute pressure (bar). At sea level, 0 barg corresponds to 1.01325 bar. Therefore, the pressures reported in this manuscript will be represented in barg rather than bar.

It is important to mention that for studies involving high current, the design of the cathode and anode chambers should be slightly modified to prevent the mixing of higher concentrations of O_2 and H_2 in the vessel at elevated temperatures. In such cases, the anode compartment should be a closed chamber with a small tubing leading to the outlet gas tube of the cell, passing through the condenser where O_2,

in case of reduction reactions are studied on the working electrode, is released. This configuration ensures that O_2 and H_2 are mixed after exiting the hot chamber but before reaching the backpressure valve, thereby maintaining both the cathode and anode compartments at the same pressure. This is crucial to prevent a pressure gradient across the membrane. In the experiments conducted in this study, relatively low currents were employed, and either high CO_2 flow or Ar flow was utilized, resulting in less than 1% of the total flow being a mixture of O_2 and H_2. As a result, the approach of mixing the gases after the condenser was deemed unnecessary.

6.2.4 Cyclic voltammograms of Au and Pt wires in different temperatures and pressures.

Cyclic voltammograms (CVs) of Au and Pt wires were recorded in a 0.1 M H_2SO_4 electrolyte. Au or Pt wire was used as the counter-electrode for the Au or Pt working-electrodes, respectively. An UltraDeg® High-Pressure Ag/AgCl (Corr Instruments) was used as the reference electrode. Before each measurement, the electrolyte was purged with argon at a flow rate of 100 mL/min for at least 30 minutes. The measurements were recorded with a scan rate of 100 mV/s using an Ivium potentiostat (Ivium Technologies) to control the potentials. For the CVs recorded while changing temperature and pressure, argon was continuously used as the purging gas.

6.2.5 Linear sweep voltammograms of rotating disk Au electrode

Linear sweep voltammograms (LSVs) of the rotating disk Au electrode were recorded following the procedure described for cyclic voltammograms, but in a 0.1 M $KHCO_3$ electrolyte and using a coated DSA titanium mesh as the counter electrode. For tests conducted in the presence of CO_2 (CO_2-saturated electrolyte), CO_2 was purged at a flow rate of 100 mL/min for at least 30 minutes before the measurements began. For tests conducted in the absence of CO_2, Ar-purging was carried out at the same flow rate and duration. The rotation speed was mechanically controlled by the high-pressure unit, ranging from 0 rpm to 2500 rpm. For LSVs measurements in different pressures, the cell was submerged in a water bath to maintain a constant temperature in order to mitigate the effects of temperature fluctuations resulting from increased pressure.

6.2.6 CO_2 reduction in the RDE high-pressure and high-temperature cell.

0.1 M CO_2-saturated $KHCO_3$ (pH = 6.8) was used as the electrolyte for CO_2RR. In all experiments, the electrolyte was continuously purged with the corresponding gas (CO_2 or Ar) at a rate of 100 mL/min using high-pressure mass flow controllers from Brooker. All potentials were controlled with an Ivium potentiostat (Ivium technologies). Resistances were determined via electrochemical impedance spectroscopy (EIS) and 85% ohmic drop compensation was applied during the experiment. Gas samples were analyzed every 10 minutes using gas chromatography (Micro-GC, Agilent), equipped with two thermal conductivity detectors (TCD). One TCD used a CP-SIL 5B column to separate CO_2, CH_4, and C_2H_4, while the other TCD used a combination of MS5A and CP-PORABOND Q columns to separate H_2, O_2, N_2, CH_4, and CO.

6.3 Results and Discussion

6.3.1 Au and Pt CVs

Voltammograms of Au and Pt wires in 0.1 M H_2SO_4 were recorded in the designed cell (Figure 6.1) and compared to their established and well-known profiles to demonstrate that the cell functions as intended. Figure E.2 shows the CV of Au and Pt wires, respectively, where all the features align with a conventional and clean voltammogram of a polycrystalline surface [33–36]. The CVs were measured until 300 cycles were completed and it can be observed that the CVs exhibit the same features with a slight surface roughening after 300 cycles were completed and no contamination is observed.

The effect of pressure on the blank CV was evaluated on the Au wire. CVs were recorded as the cell pressure was changed from 0 barg to 50 barg in 0.1 M H_2SO_4 purged with argon as an inert gas (Figure 6.2). Before the pressure was increased, argon was purged into the electrolyte for at least 30 minutes while the potential was held at 0.2 V. There is no noticeable change in the CV after the cell pressure was increased from 0 barg to 50 barg, indicating that pressure does not affect the oxidation and reduction on the Au surface. This result is expected, as the increase in pressure primarily enhances gas dissolution in the electrolyte (and minimal liquid compression), and it is not expected that argon would influence the gold surface features. The pressure in the vessel is raised by an argon flow rate of

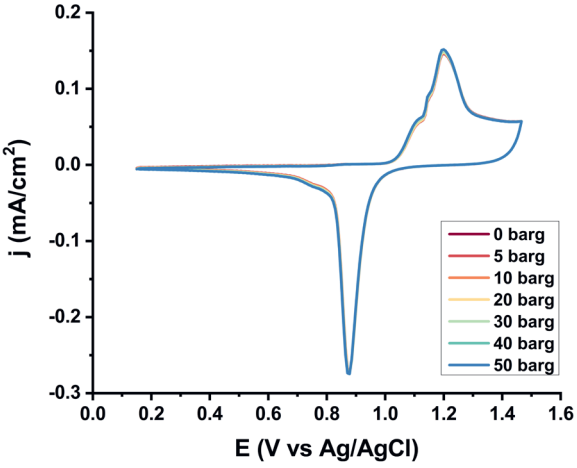

Figure 6.2 Cyclic voltammograms at different pressures on Au, using scan rate of 100 mV/s, in 0.1 M H_2SO_4 and at 22°C.

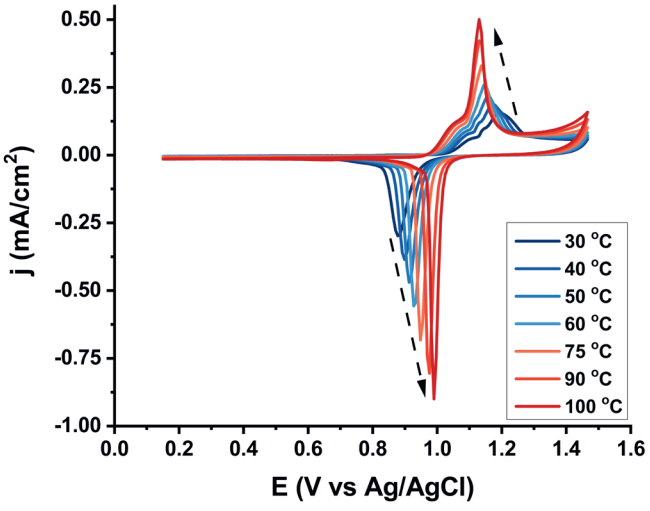

Figure 6.3 Cyclic voltammograms in 0.1 M H_2SO_4 at different temperatures: from 30°C to 100°C

150 mL min^{-1}, taking approximately 2 hours to increase from 0 barg to 50 barg. Consequently, we can also rule out the possibility that time (during this 2-hour test) affects the CV profile.

Temperature, on the other hand, can significantly alter the blank CVs of the electrodes since the kinetics of oxidation and reduction should be strongly temperature dependent, in addition to small changes in the corresponding thermodynamic redox potentials with temperature. To prevent electrolyte evaporation, Au CVs were recorded under a pressure of 30 barg at different temperatures and the results are shown in Figure 6.3. At this pressure, the boiling point of water exceeds 200°C, which guarantees the liquid phase with a reasonable safe margin for the tests shown in Figure 6.3. This Figure reveals that the reduction and oxidation peaks shift positively and negatively, respectively, with increasing temperature, demonstrating enhanced reversibility and peak sharpness. For instance, the reduction and oxidation peaks at 0.87 V and 1.20 V at 30°C, shift to 0.98 V and 1.12 V at 100°C, respectively. As illustrated in Figure 6.3, the designed cell facilitates the evaluation of surface changes under high-pressure and high-temperature conditions. However, it is important to mention that caution must be taken when working at elevated temperatures using Ag/AgCl reference electrodes. As depicted in Figure E.3 and further detailed in Note S1, Cl^- species may leak from the high-pressure reference electrode at temperatures exceeding 100°C, potentially leading to surface electrodissolution and compromising measurement accuracy. This can be prevented by storing the reference not in saturated KCl, but in a 0.1 M KCl solution. Additionally, we have evaluated the use of a high-pressure PdH reference electrode (Cormet Testing System), which does not contain any anion species. Therefore, we are able to get Cl^--free measurements but this reference electrode is highly sensitive to O_2. Consequently, this sensitivity limits measurements to very low currents, as O_2 can be produced in situ at the counter electrode. If the objective is solely focused on catalytic performance studies of the entire cell, the system can also be easily utilized without a reference electrode, and chronopotentiometry tests can be conducted while only recording cell voltage.

6.3.2 CO_2 reduction on Au at different temperatures and pressures using RDE mode

Next, the CO_2 reduction reaction on Au in an RDE mode was evaluated at higher pressures and moderate temperatures. The aim was to demonstrate that the

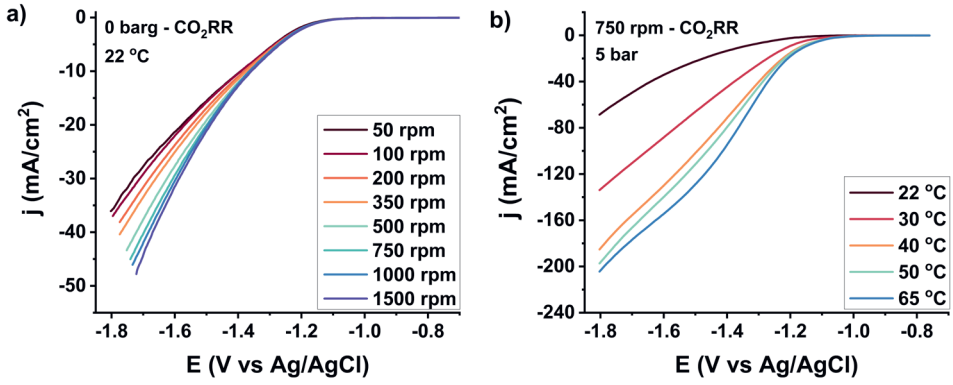

Figure 6.4 Linear sweep voltammograms (LSVs) in 0.1 M $KHCO_3$ at a) different scan rate recorded at 0 barg and 22°C; and b) different temperatures recorded at 5 barg and 750 rpm.

designed cell is suitable for studies involving the impact of different parameters such as mass transport, temperature, and pressure on CO_2 reduction under well-defined conditions. Figure 6.4a illustrates the effect of rotation speed on the linear sweep voltammogram of CO_2-saturated 0.1 M $KHCO_3$ electrolyte at 0 barg and room temperature. Goyal et al. [37] demonstrated that an increase in rotation speed of a disk Au electrode leads to a decrease in the overall current density in a CO_2-saturated $NaHCO_3$ electrolyte, which is opposite of Figure 6.4a. This decrease was attributed to the inhibition of HER caused by the reduction in local alkalinity near the electrode surface, thereby observed primarily at low current densities (up to 3.5 mA/cm^2), while other factors such as bubble formation and release become prevalent at higher current densities. We observe a similar behavior at lower current densities as shown in Figure E.4 and briefly described in Note 2 in the Supporting Information. Therefore, we attribute the enhancement in the overall current, more pronounced at current densities above 15 mA/cm^2, to the improved bubble removal facilitated by the higher rotation speed.

The impact of temperature on the CO_2RR and HER was investigated in a CO_2-saturated $KHCO_3$ electrolyte while maintaining constant rotation speed (750 rpm) and pressure (5 barg). Figure 6.4b reveals a pronounced effect of temperature on the overall current density. For instance, the current density of around -70 mA/cm^2 at -1.8 V and 22°C increased to around -200 mA/cm^2 at 65°C. However, CO_2 solubility generally decreases with increasing temperature, negatively impacting

the CO_2RR rate. Detangling the specific influence of temperature on CO_2RR and HER solely from Figure 6.4b is not possible. Nevertheless, previous work by Vos et al., [13] and Schellekens et al.[20] demonstrates that at ambient pressures, temperatures around 50°C can favor the production of multi-carbon products, such as ethylene, on Cu electrodes. Therefore, while increasing temperature might adversely affect CO_2 conversion due to decreased CO_2 solubility, it can simultaneously play a significant role by modifying catalytic rates and/or changing adsorption modes, potentially leading to a more selective product spectrum.

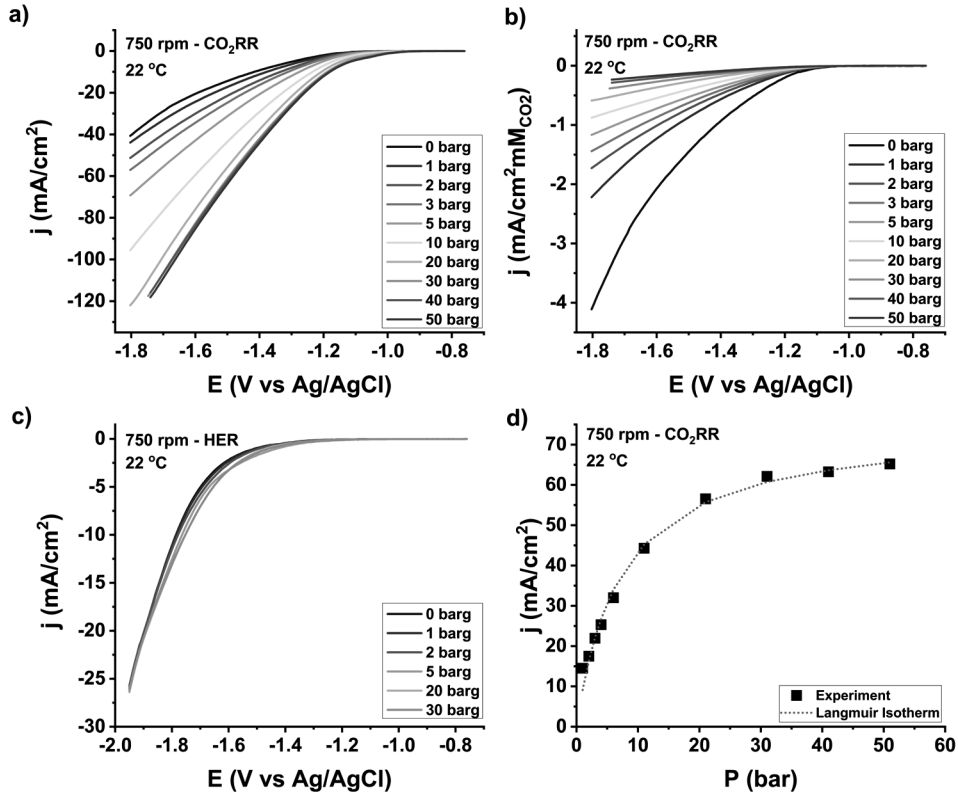

Figure 6.5 a) LSVs recorded in CO_2-saturated electrolyte at different pressures under 22°C and 750 rpm; b) LSVs recorded in CO_2-saturated electrolyte at 750 rpm and 22°C, but normalized by the CO_2 concentration; c) LSVs recorded in Ar-saturated electrolyte at 750 rpm and 22°C; and d) Langmuir isotherm fitting at -1.5V and 750 rpm using $j = j_{max} * (K * P)/(1 + K * P)$ equation.

Figures 6.5 illustrate the effect of pressure at a constant rotation rate of 750 rpm at room temperature. Figure 6.5a demonstrates the CO_2 pressure effect on the overall current when using a CO_2-saturated $KHCO_3$ electrolyte. Notably, the current density at -1.5 V increases roughly 5-fold as pressure rises from 0 barg to 50 barg. It has been reported that CO_2 solubility in water as a function of pressure has a logarithmic dependence [38–41]. However, at pressures below 50 bar, CO_2 solubility increases linearly with a rate of 0.0099 mol_{CO2}/L per bar increase [38]. Despite the linear rise in CO_2 concentration from 1 to 50 bar, no corresponding linear increase in current density is observed. Figure 6.5b illustrates the impact of pressure on the overall current density normalized by the CO_2 concentration at that pressure. The normalized current density exhibits a significant decrease from 0 barg to 50 barg. We hypothesize that the increase in CO_2 concentration might partially inhibit the competitive HER by the adsorption of either CO_2 or CO onto the gold electrode, which could also explain the overall decrease in the normalized current density.

Figure 6.5c support this hypothesis. In an Ar-saturated electrolyte, in which only HER takes place, the pressure minimally affects the overall current, indicating that the observed pressure effect in Figure 6.5a and 6.5b is primarily due to the CO_2 concentration. Furthermore, Figure 6.5d shows the total current density as function of CO_2 pressure at -1.5 V, which resembles a Langmuir isotherm, indicating that the current density is related with CO_2 pressure through an adsorption process. Specifically, by fitting the experimental data with $j = j_{max} \cdot (K * P)/(1 + K * P)$ Langmuir equation, where K is the adsorption coefficient, P is pressure, and j is the current density, we achieved a fitting with an R^2 value of 0.99. Therefore, the overall current density over pressure seems to be directly related to the CO_2 (or CO) adsorption. This would explain why the increase in current density levels off at higher pressures, as CO_2 adsorption cannot increase infinitely. Furthermore, it indicates that HER can be inhibited by increasing the CO_2 pressure as the increased CO_2 (or CO) coverage leaves less active sites for HER. Moreover, Figure E.5 suggests reversibility of the effect of CO_2 pressure as the current density returns to its initial range when the CO_2 pressure is reduced from 50 barg back to 0 barg. This observation further supports the hypothesis that the overall current density is primarily influenced by the CO_2 concentration in the electrolyte.

To evaluate the impact of temperature and pressure on the selectivity, gaseous products were measured using gas chromatography during 3h electrolysis at

constant potential. This is possible in our cell design as it is a system which can operate in semi-continuous mode, where CO_2 is continuously bubbled into electrolyte and out of the high pressure cell. This makes it possible to connect the cell to an online gas chromatograph to detect H_2 and CO. Figure 6.6a shows the impact of temperature on the FE to CO at 0 barg and 750 rpm. No liquid products were identified by liquid chromatography within the detection limit. H_2 was the sole byproduct detected, alongside CO from the CO_2RR process. As a general trend, for all evaluated potentials, the FE for CO slightly increases from room temperature to 50 °C before decreasing again at temperatures exceeding 50°C. H_2, on the other hand, follows the opposite direction. This result is consistent with our earlier findings [19], in which an optimal temperature of 55 °C for CO_2 conversion to CO on a gold electrode was observed, followed by a decrease at higher temperatures, attributed to the decreasing solubility of CO_2 at elevated temperatures, thereby favoring HER over CO_2RR. The initial increase of the FE towards CO with increasing temperature was ascribed to the differences in kinetics, as CO_2RR shows higher apparent activation energy and therefore the activity of CO_2RR increases faster with temperature than the HER activity. In that work, we concluded that an increase in CO_2 solubility would likely extend the optimal temperature for CO_2 reduction.

If the observed decrease is indeed primarily linked to CO_2 availability, increasing pressure could mitigate this decline at temperatures exceeding 50 °C, as the concentration of CO_2 would increase accordingly. Figure 6.6b illustrates the influence of temperature and pressure on the FE to CO at 750 rpm and -1.35 V. No liquid products were detected within the detection limit of the liquid chromatography, with H_2 as the sole byproduct from CO_2RR. Remarkably, the FE for CO increases from 42% at room temperature to 62% at 2 barg and approximately 86% at pressures exceeding 6 barg. At pressures exceeding 6 barg, there are minimal changes in FE with variations in temperature, although the partial current density for CO increases with pressure (Fig. 6c). Interestingly, the effect of temperature on the FE decreases by increasing the pressure. This may be due to the fact that even at room temperature the FE is already high, leaving less room for improvement at elevated temperatures. Another interesting observation is that the decline at temperatures exceeding 50°C is significantly mitigated by increasing pressure, confirming that CO_2 availability is a critical factor in suppressing HER at higher

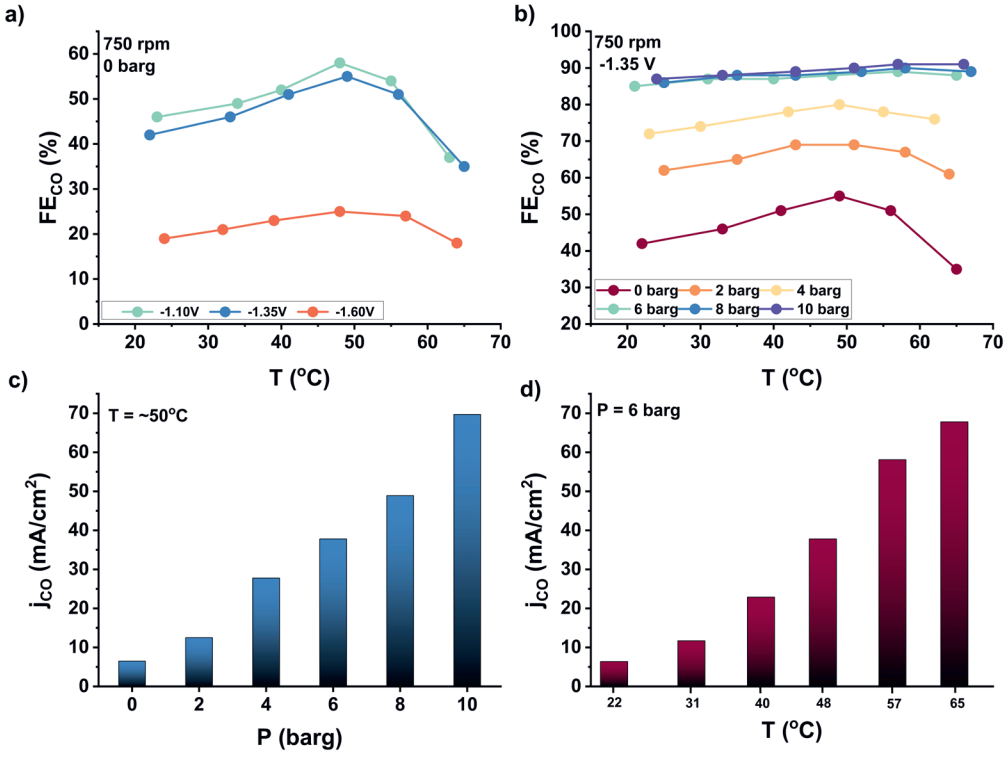

Figure 6.6 a) Faradaic efficiency to CO in different temperature at -1.1V, -1.35V, and -1.6V under 0 barg and rotation speed of 750 rpm. b) CO_2 reduction at different temperatures and pressures with constant potential of -1.35 V and constant rotation speed of 750 rpm; c) recorded current densities towards CO at different pressures at constant potential of -1.35 V and constant rotation speed of 750 rpm at 50°C; and d) recorded current densities towards CO at different temperatures at constant potential of -1.35 V and constant rotation speed of 750 rpm at 6 barg.

temperatures. It also corroborates our hypothesis raised in relation with Figure 6.5, where higher CO_2 concentration might partially inhibit the competitive HER, explaining the lower the current density normalized by the CO_2 concentration in different pressures. Thus, elevated pressures increase the FE towards CO and make the effect of temperature on the FE insignificant. However, temperature has still a positive effect on the current density towards CO as shown in Figure 6.6d. At the constant pressure of 6 barg, the current density increases one order of magnitude by increasing the temperature from room temperature to 65 °C, with no negative impact in the FE to CO (~90%). Therefore, Figure 6.6 demonstrates the substantial

impact of pressure and temperature on catalytic performance towards CO. When pressure and temperature are combined, there is potential to simultaneously enhance the FE and the overall current density, thereby providing opportunities for future studies on materials that are more active and selective for CO_2RR.

The CO_2RR at high pressure has been shown to exhibit an enhancement towards CO compared to atmospheric pressure. On similar electrode surfaces (polished flat surfaces), FE towards CO reaches approximately 80% under optimal conditions of potential, rotation speed, temperature, and electrolyte [19,37,42,43]. In this study, an FE of 90% was achieved at pressures exceeding 6 bar. This value could potentially be improved through further optimization. For instance, nanostructured gold electrodes, which have demonstrated >90% FE towards CO at atmospheric pressure [44], could be a promising class of materials to investigate at high pressure and temperature for enhanced current density and stability. Cu electrodes, capable of producing more valuable compounds such as ethylene, ethanol, and n-propanol, have not yet been comprehensively explored in terms of their fundamental aspects under both high pressure and temperature. There are numerous opportunities for further investigation in this direction. Additionally, different classes of metals, typically inactive for CO_2RR, may become active under high pressure and temperature conditions. Hara et. al [28] have already indicated this possibility. For instance, Fe electrodes, which exhibit low activity towards CO_2RR, demonstrated an FE of 40% towards formic acid under high pressure. If similar investigations are conducted under high temperature, "electrochemical Fisher-Tropsch" type reactions could potentially be discovered. Finally, we recently reported the impact of bubbles on HER [45,46], and expect that bubble dynamics will be pressure and temperature dependent. Such studies will be possible using the system presented in this work.

6.4 Conclusion

The impact of pressure, temperature, and mass transport on the CO_2 reduction on Au electrodes was successfully investigated using a high-pressure and high-temperature rotating disk electrode electrochemical cell. This system offers the opportunity for fundamental surface characterization without apparent metal contamination, as demonstrated by 300 reproducible cycles of the well-known blank voltammetry of polycrystalline Pt and Au in 0.1 M H_2SO_4. Additionally, we examined how Au cyclic voltammograms are affected by increasing temperature

and pressure up to 150°C and 50 bar, although Cl^- leakage from Ag/AgCl reference electrode may occur when operating at high temperatures. The system operates in a semi-continuous mode, with CO_2 (or any other gas) continuously bubbling into the electrolyte, and can be easily connected to an online gas chromatograph and mass spectrometry for investigating CO_2 reduction at different pressures and temperatures on the rotating disk electrode. Linear sweep voltammograms of CO_2RR on the Au electrode indicated that current densities were positively influenced by increasing rotation speed, temperature, and pressure. The total current density follows a Langmuir dependence on CO_2 concentration explaining the smaller pressure effect at the highest pressures and suggesting that CO_2 or CO adsorption may block active sites for the competing HER. Electrolysis experiments show that elevated pressure can inhibit the effect of temperature on the CO efficiency, but both pressure and temperature can significantly increase the current density towards CO. This result suggests that increasing both pressure and temperature allows for sustained CO_2 electrolysis at high activities outcompeting HER.

This work suggests several promising avenues for future investigations. On a fundamental level, voltammetry techniques can be employed to explore the surface changes on the electrode induced by variations in temperature and pressure. From a catalysis viewpoint, the designed high-pressure and high-temperature cell presents a platform for discovering novel catalysts for $CO_{(2)}RR$. As demonstrated here, using a gold electrode, these parameters dramatically enhance catalytic performance. Similar improvements are expected for Cu electrodes leading to the formation of more valuable C_{2+} products. As commented in the introduction, altering temperature and pressure pushes the electrochemical system towards the well-known thermochemical regime. Consequently, it is expected that previously inactive materials at ambient conditions might become active under temperature and/or pressure, leading to the discovery of new material classes for electrochemical conversion. Moreover, the system can be easily extended to investigations beyond CO_2 conversion, offering prospects for electro-oxidation studies, nitrogen-based reactions, and organic electrosynthesis.

References

1. da Silva, A. H. M., Karaiskakis, G., Vos, R. E. & Koper, M. T. M. *J Am Chem Soc* **145**, 15343–15352 (2023).
2. Kuhl, K. P., Cave, E. R., Abram, D. N. & Jaramillo, T. F. *Energy Environ Sci* **5**, 7050 (2012).
3. Hori, Y., Murata, A. & Takahashi, R. *Journal of the Chemical Society, Faraday Transactions 1: Physical Chemistry in Condensed Phases* **85**, 2309 (1989).
4. Hori, Y., Murata, A., Takahashi, R. & Suzuki, S. *J Chem Soc Chem Commun* 17 (1988)
5. Niu, J. *et al. Int J Hydrogen Energy* **47**, 9183–9200 (2022).
6. Shi, Y.-F., Ma, S. & Liu, Z.-P. *EES Catalysis* **1**, 921–933 (2023).
7. Gholami, Z. *et al. Catalysts* **12**, 174 (2022).
8. Davis, B. H. *Ind Eng Chem Res* **46**, 8938–8945 (2007).
9. Gholami, Z., Tišler, Z. & Rubáš, V. *Catalysis Reviews* **63**, 512–595 (2021).
10. Nitopi, S. *et al. Chem Rev* **119**, 7610–7672 (2019).
11. Hori, Y. in *Modern Aspects of Electrochemistry* 89–189 (Springer New York, New York, NY, 2008).
12. Zhan, C. *et al. ACS Catal* **11**, 7694–7701 (2021).
13. Vos, R. E. *et al. ACS Catal* **13**, 8080–8091 (2023).
14. Corral, D. *et al. Energy Environ Sci* **14**, 3064–3074 (2021).
15. Iglesias van Montfort, H.-P. & Burdyny, T. *ACS Energy Lett* **7**, 2410–2419 (2022).
16. Lobaccaro, P. *et al. Physical Chemistry Chemical Physics* **18**, 26777–26785 (2016).
17. Liu, X. *et al. Advanced Materials* **32**, (2020).
18. Lei, H., Wan, Q., Tan, S., Wang, Z. & Mai, W. *Advanced Materials* **35**, (2023).
19. Vos, R. E. & Koper, M. T. M. *ChemElectroChem* **9**, (2022).
20. Schellekens, M. P., Raaijman, S. J., T. M. Koper, M. & Corbett, P. J. *Chemical Engineering Journal* **483**, 149105 (2024).
21. Hara, K. & Sakata, T. *Bull Chem Soc Jpn* **70**, 571–576 (1997).
22. Morrison, A. R. T., Girichandran, N., Wols, Q. & Kortlever, R. *J Appl Electrochem* **53**, 2321–2330 (2023).
23. Hara, K., Kudo, A. & Sakata, T. *Journal of Electroanalytical Chemistry* **421**, 1–4 (1997).
24. Ramdin, M. *et al. Ind Eng Chem Res* **58**, 22718–22740 (2019).
25. Ramdin, M. *et al. Ind Eng Chem Res* **58**, 1834–1847 (2019).
26. Zong, S. *et al. Carbon Capture Science & Technology* **8**, 100133 (2023).
27. Huang, L. *et al. Nat Commun* **14**, 2958 (2023).
28. Hara, K., Kudo, A. & Sakata, T. *Journal of Electroanalytical Chemistry* **391**, 141–147 (1995).
29. Hara, K., Tsuneto, A., Kudo, A. & Sakata, T. *Journal of Electroanalytical Chemistry* **434**, 239–243 (1997).

30. Costamagna, J. A., Isaacs, M., Aguirre, M. J., Ramírez, G. & Azocar, I. in *N4-Macrocyclic Metal Complexes* 191–254 (Springer New York, New York, NY, 2006). doi:10.1007/978-0-387-28430-9_5.
31. Huo, S., Lu, J. & Wang, X. *Energy Sci Eng* **9**, 1042–1047 (2021).
32. Wei, X. *et al. Appl Surf Sci* **564**, 150423 (2021).
33. Jeyabharathi, C., Ahrens, P., Hasse, U. & Scholz, F. *Journal of Solid State Electrochemistry* **20**, 3025–3031 (2016).
34. Daubinger, P., Kieninger, J., Unmüssig, T. & Urban, G. A. *Phys. Chem. Chem. Phys.* **16**, 8392–8399 (2014).
35. Monteiro, M. C. O. & Koper, M. T. M. *Electrochim Acta* **325**, 134915 (2019).
36. Jacobse, L., Raaijman, S. J. & Koper, M. T. M. *Physical Chemistry Chemical Physics* **18**, 28451–28457 (2016).
37. Goyal, A., Marcandalli, G., Mints, V. A. & Koper, M. T. M. *J Am Chem Soc* **142**, 4154–4161 (2020).
38. Duan, Z. & Sun, R. *Chem Geol* **193**, 257–271 (2003).
39. Hemmati-Sarapardeh, A., Amar, M. N., Soltanian, M. R., Dai, Z. & Zhang, X. *Energy & Fuels* **34**, 4761–4776 (2020).
40. Zhang, P. *et al. RSC Adv* **9**, 8672–8683 (2019).
41. Khoshraftar, Z. & Ghaemi, A. *Case Studies in Chemical and Environmental Engineering* **7**, 100338 (2023).
42. Marcandalli, G., Goyal, A. & Koper, M. T. M. *ACS Catal* **11**, 4936–4945 (2021).
43. Noda, H., Ikeda, S., Yamamoto, A., Einaga, H. & Ito, K. *Bull Chem Soc Jpn* **68**, 1889–1895 (1995).
44. Zhao, S., Jin, R. & Jin, R. *ACS Energy Lett* **3**, 452–462 (2018).
45. Park, S., Lohse, D., Krug, D. & Koper, M. T. M. *Electrochim Acta* **485**, 144084 (2024).
46. Park, S. *et al. Nat Chem* **15**, 1532–1540 (2023).

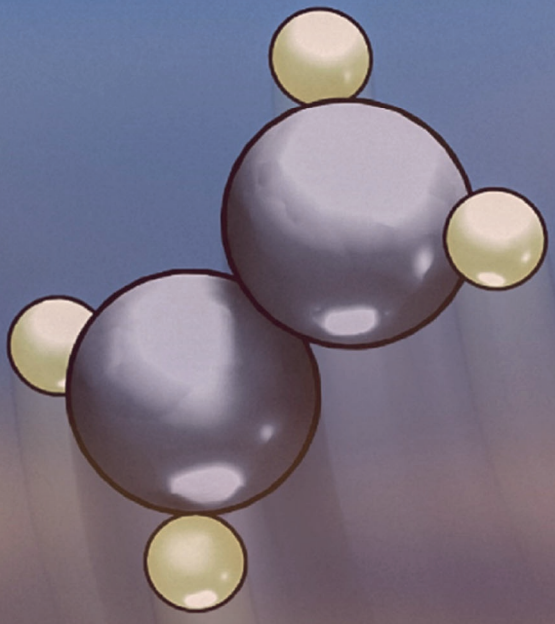

7

Change in the C-C coupling mechanism during CO_2 electroreduction on Cu at elevated temperature and pressure

This chapter is based on R.E. Vos, P. Sun, D. Schauermann, S. R. Hanselman, M.T.M. Koper, in preparation

Abstract

Future practical applications of the electrochemical CO_2 reduction reaction (CO2RR) will likely involve the use of higher pressures and temperatures. However, most research on e.g. the copper-catalyzed CO2RR is typically performed at ambient conditions, and hence the mechanistic conclusions drawn also pertain to these conditions. Using a special high-pressure high-temperature electrochemical cell, we show that on copper electrodes, the C-C coupling mechanism changes from the typical CO dimerization mechanism at low temperatures to a Fischer-Tropsch-like chain growth mechanism at temperatures above 125 °C (requiring higher pressure). Additionally, temperature influences the selectivity more significantly than pressure, however copper stability is compromised at elevated temperatures. The stability can be improved with increasing pressures, which also suppresses the competing hydrogen evolution reaction significantly. These results show that temperature and pressure are crucial parameters to consider in applied and mechanistic studies of the electrochemical reduction of CO_2.

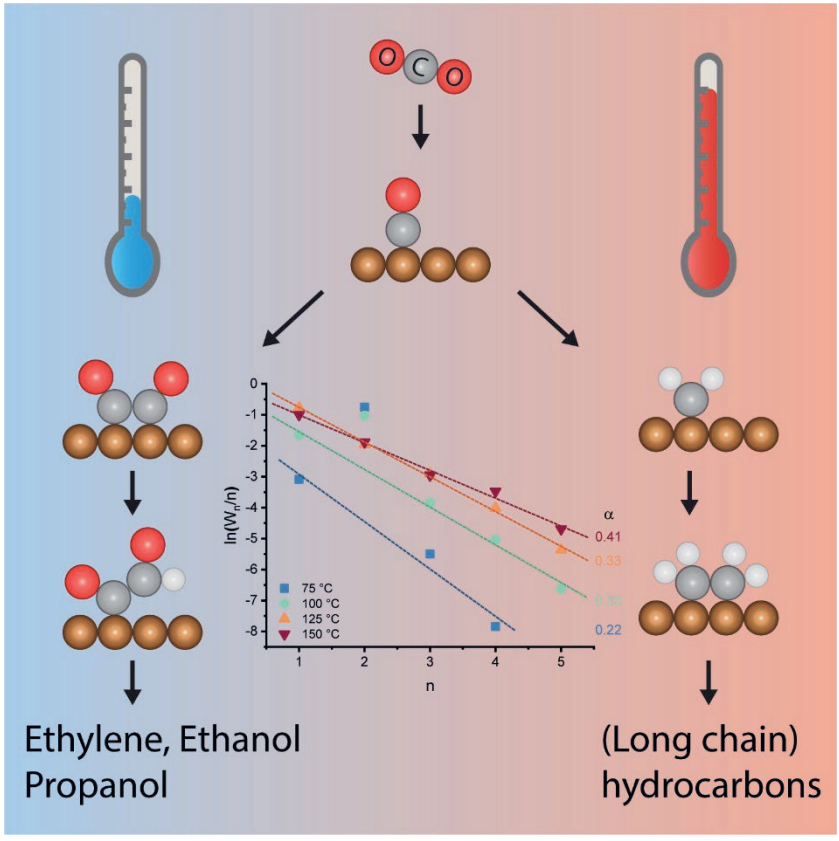

7.1 Introduction

Electrochemical CO_2 reduction (CO2RR) offers an interesting strategy to recycle CO_2 into fuels and chemicals using renewable electricity [1–4]. Copper is a unique catalyst for this reaction, as it is the only catalyst that can make C-C bonds with significant Faradaic efficiencies [5–7]. Multicarbon products in CO2RR are typically formed via a CO dimerization or carbonyl coupling mechanism [8–13], although recently research has provided evidence for a chain growth mechanism as alternative C-C coupling mechanism on for example Ni electrodes[14–17]. Many factors influencing the CO2RR on Cu have been studied, such as morphology [18–21], electrolyte effects [22–25] and electrode potential [7,11,24–26]. Recently, more attention has been given to parameters such as pressure [27–30] and temperature [14,31–34]. Electrochemistry research in general and CO2RR studies specifically are often performed at ambient pressure and temperature and hence conclusions and fundamental insights are drawn at these conditions. However, for practical applications, ambient conditions might not be the most relevant, as industrial electrolyzers typically operate at elevated temperatures [35], for example due to thermal losses [36–38] and/or hot feedstocks. Moreover, pressure and temperature can improve the selectivity and activity of CO2RR [27–29,31,32], open up new mechanistic pathways [30,39] and elevated pressure could enable better integration with up- and downstream processes [30,40,41].

Temperature has a significant effect on the activity and selectivity of CO2RR on Cu at ambient pressure [32]. Below 48 °C, increasing temperature has a positive effect on both the selectivity as activity towards C2+ products, but above 48 °C the competing hydrogen evolution reaction (HER) takes over. Other studies [27–30,40,42–44] have shown that increased CO_2 pressures can suppress the HER, which might mean that the optimum in C2+ selectivity with temperature changes at elevated pressures. Moreover, under elevated pressures the studied temperature window can be increased and experiments in aqueous electrolytes can even be performed above 100 °C. This could bridge the fields of electrocatalysis and thermal catalysis, where C-C bonds are made via a chain growth mechanism in the Fischer-Tropsch reaction [45–47] (although Cu produces mainly methanol in thermal heterogeneous catalysis [48–50]). This raises the question if the electrochemical CO_2 reduction on Cu at high temperatures in aqueous electrolyte is more similar to electrocatalysis at ambient conditions, to thermal catalysis or to neither of them.

Recently, we have developed an electrochemical cell in which both pressure and temperature can be regulated up to 200 °C and 140 bar [51]. In this study, we use this setup to study the combined effect of elevated pressure and temperature and we show a change in the C-C coupling mechanism on copper electrodes above 100

°C, at a pressure of 24 bar. Whereas at low temperatures C-C bonds are mostly formed via the traditional CO dimerization mechanism, at high temperatures the chain growth mechanism takes over and from 125 °C onwards this is the dominant mechanism making C-C bonds. Moreover, even up to 75 °C, both temperature and pressure already substantially influence the selectivity and activity of the traditional CO2RR products on Cu. This study illustrates that temperature and pressure are crucial parameters to consider in applied and fundamental studies of the electrochemical reduction of CO_2.

7.2 Experimental

7.2.1 Chemicals

The electrolyte was prepared from $KHCO_3$ (99.95%, Sigma-Aldrich) with Milli-Q water (≥18.2 MΩcm, TOC < 5 ppb) and stored with Chelex (100 sodium form, Sigma-Aldrich) to clean the electrolyte from any metal impurities [52]. H_2SO_4 (95-98%, Sigma-Aldrich), H_2O_2 (35%, Merck) and $KMnO_4$ (99%, Sigma-Aldrich) were used to clean the cells. Ar (5.0 purity, Linde) and CO_2 (4.5 purity, Linde) were used for purging the electrolytes.

7.2.2 HP cell setup

We used an adapted high-pressure, high-temperature cell from Parr instruments; this cell has been described in detail in a recent paper [51]. The cell was designed to work up to 140 bar and 200 ^{0}C. The cell was used in semi-continuous mode, where either CO_2 or a mixture of CO_2 and Ar were constantly purged through the cell. The outlet of the cell was coupled to a condenser and a cooler (Cool-Care, Van der Heijden Labortechnik GMbH) to keep all volatile products in the liquid phase in the setup. The outlet gas was analyzed every 6 min with a Micro-GC from Agilent with two TCD detectors. A combination of a MS6A and a CP-PORABOND Q column was used to detect H_2, CO and CH_4, and an Al_2O_3 column was used to detect the C2 and C3 hydrocarbons. For the detection of the higher hydrocarbons, another GC with an RTX-1 column and an FID detector was used. The experimental limitation in the first part of the paper were due to the limitations of the Micro-GC which could not handle too much CO_2. Later these limitations were solved by stripping the CO_2 with NaOH before injecting the outlet gas in the GC. This allowed for the use of a pure CO_2 stream and larger injection volumes in the GC, increasing the detection limit by a factor 40. The pressure in the cell was maintained by controlling both the inlet and outlet flow with flow controllers (SLA5850, Brooks Instruments), while for the mixed gas experiments the flow was also checked with a flow meter (Defender 530+, Mesalabs). The temperature was controlled with an electric heating mantle. A homemade two-compartment PEEK cup was used inside

the stainless steel chamber and all metal parts from the thermocouple and reference electrode were covered by Teflon tape. Moreover, the lid of the vessel was covered with Viton rubber to prevent any contamination from the stainless steel.

7.2.3 General electrochemistry

The homemade PEEK cup was cleaned prior to experiments by storing in permanganate solution overnight (0.5 M H_2SO_4, 1g/L $KMnO_4$). Afterwards, the cell was rinsed, submerged in a diluted mixture of H_2SO_4 and H_2O_2 to remove any traces of MnO_4 and MnO_2, rinsed again and boiled three times with Milli-Q water. A 1mm thick Cu wire (99.99%, Mateck) was used as working electrode. Before experiments, the working electrode was electropolished in 85% H_3PO_4 (Suprapure, Merck) by applying +3 V versus a graphite counter electrode for 20 s and subsequently rinsed with Milli-Q water. Due to the large difference in current at the various conditions used, 4 different sized wires were used to ensure the current stays between 10 mA (for product detection) and 200 mA (for stability of the system) during the experiment. The areas of different working electrodes were normalized using their double layer capacitance, measured from -0.3 to 0.2 V vs SHE at scan rates from 200 to 1400 mV/s [53]. The areas of the electrodes can be found in Table S1.

During experiments, a DSA counter electrode (Magneto) was separated from the working and reference electrode by a PiperION membrane (Versogen)[54,55]. The experiments were performed with a Gamry Interface 1010B potentiostat and current interrupt[56] was used to correct for the Ohmic drop. Experiments were performed for 60 or 90 minutes at constant potential. Gaseous products were determined every 6 min with GC as described above, while liquid products were determined afterwards by sampling the 65 ml catholyte and analyzing this using high performance liquid chromatography (HPLC, Shimadzu) with an Aminex HPX-87H column (Bio-rad). During experiments the pressure was maintained within an error of 0.1 bar, while temperature was maintained within an error of 2 °C. Before reaching the conditions used for the experiment (which typically takes up to an hour), the working electrode was always under potential control at a potential of -0.8 V vs Ag/AgCl. Due to time restraints, individual experiments have not been repeated and no error bars are plotted.

7.2.4 Reference electrode corrections

In this study, all potentials are reported vs SHE(T). During experiments, an Ag/AgCl electrode (Ultradeg, 0.1 M KCl, Corr Instruments) was used as a reference electrode. However, with changing temperature, one should make several corrections to convert the potential from Ag/AgCl to SHE. The Nernst equation is used to determine the shift of the Ag/AgCl reference electrode against SHE:

$$E_{Ag/AgCl} = E^0_{Ag/AgCl}(T) - \frac{\ln(10) * RT}{nF} * \log\left(a_{Cl^-}(T)\right) \qquad (7.1)$$

with E^0 being the standard potential, R the gas constant, T the temperature, n the number of electrons, F Faradays constant and a_{Cl^-} the activity of the chloride anion. The standard potential of Ag/AgCl vs SHE is a function of temperature and can be calculated using the following formula[57]:

$$E^0_{Ag/AgCl}(T) = -0.111658 + 0.011134 * T - 0.001757268 * T * \ln(T) \qquad (7.2)$$

The temperature dependence of the activity of the chloride ions can be determined from a formula from Bogaerts et al.[58] :

$$a_{Cl^-}(T) = exp\left[\log\left(a_{Cl^-}(25\,^\circ C)\right) - \frac{\sqrt{I_{Cl^-}}}{1+\sqrt{I_{Cl^-}}} * \left(A_\gamma^T - A_\gamma^{25\,^\circ C}\right)\right] \qquad (7.3)$$

where a_{Cl^-} is the activity of the chloride anion at room temperature[59], I_{Cl} is the ionic strength of the chloride anion, and A_γ is the Debye-Huckel parameter[58].

With these formulas, the shift between an Ag/AgCl reference and SHE could be determined at different temperatures as shown in Table S2. Even though the SHE potential is defined zero at all temperatures, there is a difference in potential between SHE(T) and SHE (25°C)[60]. One could correct for this difference too, but we decide to limit the corrections to the necessary corrections and therefore report on a SHE(T) scale. In previous studies we reported on the RHE(T) scale [14,31,32,61], but in this study the potential could not be reported vs. RHE because the pH should be known to convert SHE to RHE. However, it is impossible to measure the exact pH of the electrolyte at elevated CO_2 pressures and temperatures.

7.3 Results and Discussion

7.3.1 Screening temperature, pressure and potential

As the research space increases tremendously when pressure and temperature are opened up as parameters, we first screened the effect of these parameters at different potentials. We mainly focused on -1.4 V vs SHE as shown in Figures 7.1 and F.1. This potential corresponds to -1.0 V vs RHE at ambient conditions in 0.2 M $KHCO_3$, a potential which is commonly used for electrochemical CO_2 reduction on Cu. However, we also performed screening experiments at -1.3 and -1.5 V vs SHE (Figure F.2 and F.3), as the potential can change the effects of temperature and pressure [31,61]. Experiments have been performed from 25 to 125 °C and with pressures up to 40 bar. All screening experiments were performed with 50% CO_2 and 50% Ar. Moreover, all experiments have been performed in 0.2 M $KHCO_3$

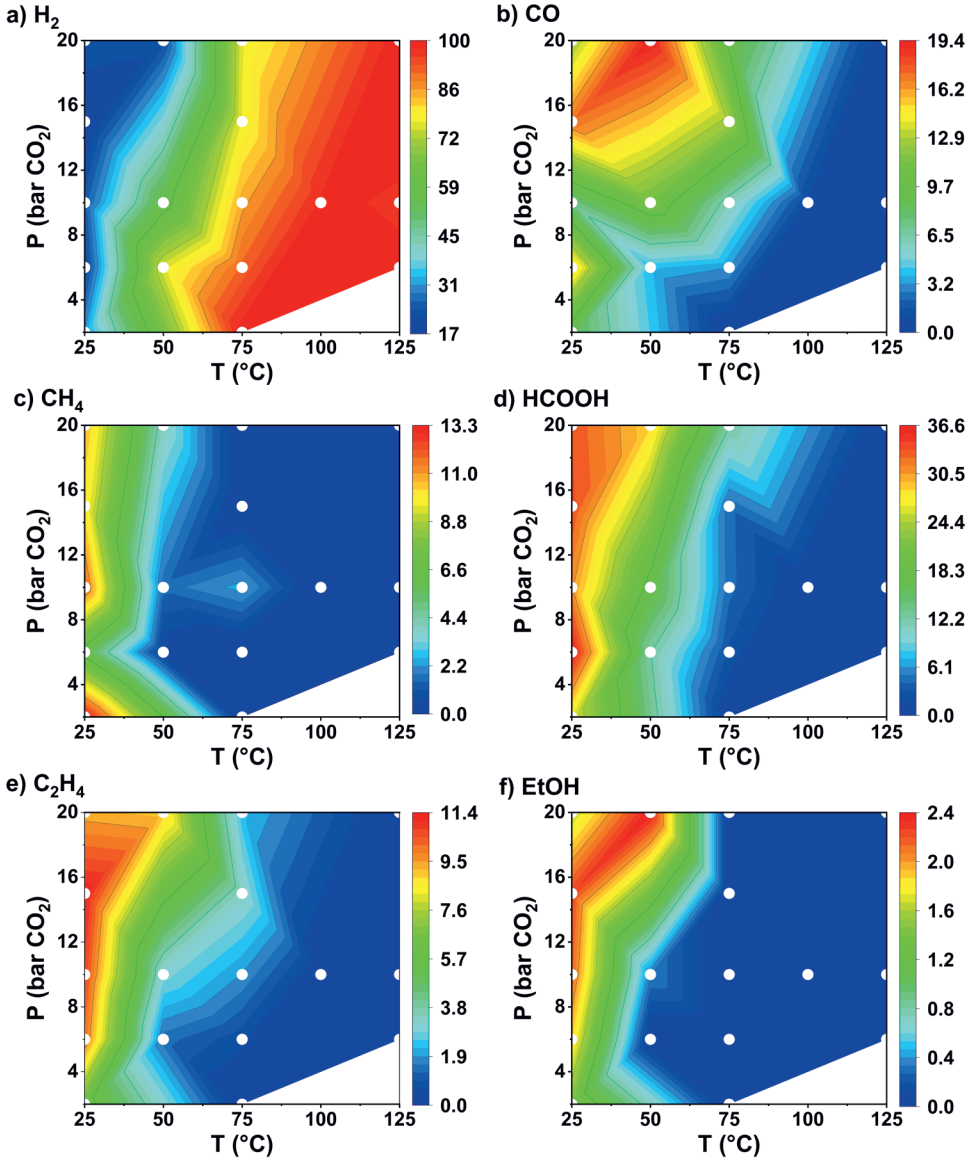

Figure 7.1 Faradaic efficiency towards the main CO2RR products as function of temperature and pressure at -1.4 V vs SHE in 0.2 M $KHCO_3$ with a 50/50 ratio of CO_2 and Ar. The white dots give the measured points and the maps are constructed via interpolation between these points. FE for a) hydrogen b) carbon monoxide c) formic acid d) methane e) ethylene and f) ethanol

because changing the electrolyte as well would increase the research space beyond reasonable measure.

Figure 7.1 shows that temperature has a more significant effect on the selectivity than pressure. With increasing temperature, more H_2 is generated and the selectivity for all CO2RR products decreases. With increasing pressure, the effect of temperature can be suppressed and the CO2RR stays active up to higher temperatures. At room temperature, there are only subtle effects on the selectivity, while the effect of pressure becomes more clear at 50 and 75 °C. These trends can also be observed at the other potentials. The exact values of the FE for the different products depends on the potential applied, but the overall trends for temperature and pressure seem independent of potential, at least in this potential window. Figure F.1 shows the 2D maps for the minor products. In general, the trends are similar to the major products in Figure 7.1, however the effect of pressure at room temperature is more clear, especially for methanol and acetate. Acetate and ethylene glycol seem to form even at very high temperatures. Moreover, we observe longer hydrocarbon formation (C3+) at the highest temperatures.

7.2 Switching mechanism at high pressure and high temperature

At the highest pressures and temperatures used in this study, above 100 °C, mainly hydrogen is produced, but also small amounts of interesting and unusual CO2RR products such as ethylene glycol, propene and butene. To detect these minor products, we have used a pure CO_2 flow which allowed for more sensitive product detection. Figure 7.2a shows the selectivity for CO2RR at temperatures up to 150 °C

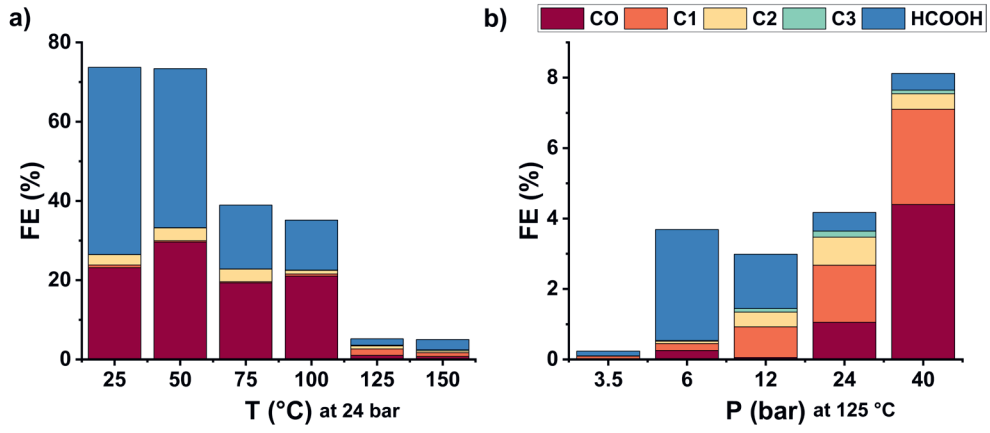

Figure 7.2 Faradaic efficiencies for the CO2RR products at function of a) temperature at 24 bar of CO_2 pressure b) pressure at 125 °C, both at -1.3 V vs SHE in 0.2 M $KHCO_3$. The remaining FE goes towards hydrogen, which is shown in Figure F.5.

at -1.3 V vs SHE. This potential was chosen as Cu is very unstable at higher overpotentials at temperatures above 100 °C, as can be seen in Figure F.4, and only produces H_2 within the total experiment time (Figure F.5b). However, at lower overpotentials some CO2RR is still possible, even at 150 °C. The product distribution changes from mainly CO and HCOOH to hydrocarbons, besides the dominant H_2 production, which is shown in Figure F.5. Figure 7.2b shows that pressure also influences the CO2RR selectivity compared to HER at 125 °C, where higher pressures lead to higher CO2RR rates and a more stable operation, as seen in Figure F.4a. The selectivity of the CO2RR products changes as well, as higher pressures lead to more CO and hydrocarbons, and less HCOOH. The selectivity has a less clear trend with potential, although a potential of -1.3 V vs SHE seems to be the optimum for hydrocarbon formation, as shown in Figure F.5b. Interestingly, the CO produced at high temperatures is mainly produced at the start of the experiment as shown in Figure F.7, while the hydrocarbons are produced throughout the measurement. This observation coincides with an significant change in the current at the start of the experiment, after which it stabilizes as shown in Figure F.4b. If only the gaseous products of the last 30 minutes are analyzed, almost no CO is produced and the optimum for the hydrocarbon formation becomes more apparent, as shown in Figure F.8.

Cu is known to be able to form C-C bonds and produce C2+ products. However, longer chain hydrocarbons are usually not observed on Cu. Either C1 or C2 hydrocarbons are formed, or C3 oxygenates, such as propionaldehyde and 1-propanol. In rare instances higher hydrocarbons have been observed before on Cu [62–64] although they are more often found on other electrochemical CO2RR catalysts [16,17,65–68], with the highest selectivities on Ni [14,15]. These longer hydrocarbons are presumed to be formed via a CH_x chain growth mechanism [15,67] similar to the thermal catalytic Fischer-Tropsch reaction, while Cu traditionally forms C-C bonds via a CO dimerization (pathway C-D-E in Figure 7.4) or carbonyl coupling mechanism (pathway F-G-E). Figure 7.2a shows that at low temperatures, mainly CO and HCOOH are formed at -1.3 V vs RHE, but also some ethylene is formed via the CO dimerization mechanism. When the temperature is increased, longer-chain products are detected and from 75 °C onwards an Anderson-Flory-Schultz (AFS) plot can be constructed, as C4 products such as butene and butane are observed. From the AFS plot in Figure 7.3, it can be seen that at 75 and 100 °C, two mechanisms are active to form C-C bonds on Cu. One is the chain growth mechanism previously observed on Ni, resulting in a linear relationship in the AFS plot. However, the C2 products do not fit this linear relationship, as they are also produced via the CO dimerization mechanism, which produces mainly ethylene, leading to a peak in the AFS plot. At 125 and 150 °C, the product distribution fits the linear relationship in the AFS plot, including the C2 products, which shows that

at these temperatures, all hydrocarbons are formed via the chain growth mechanism and the CO dimerization/carbonyl coupling mechanism has become inactive.

From the slope of the linear relationship in the AFS plot, the chain growth probability can be determined. The chain growth probability gives an indication for the product distribution, where a chain growth probability of 0 leads to only methane and a chain growth probability of 1 leads to very long hydrocarbons consisting of more than 20 carbon atoms. Figure 7.3 shows that the chain growth probability on Cu increases with increasing temperature. Table F.4 shows that pressure and potential also seem to influence the chain growth probability, decreasing with increasing pressure and higher overpotential.

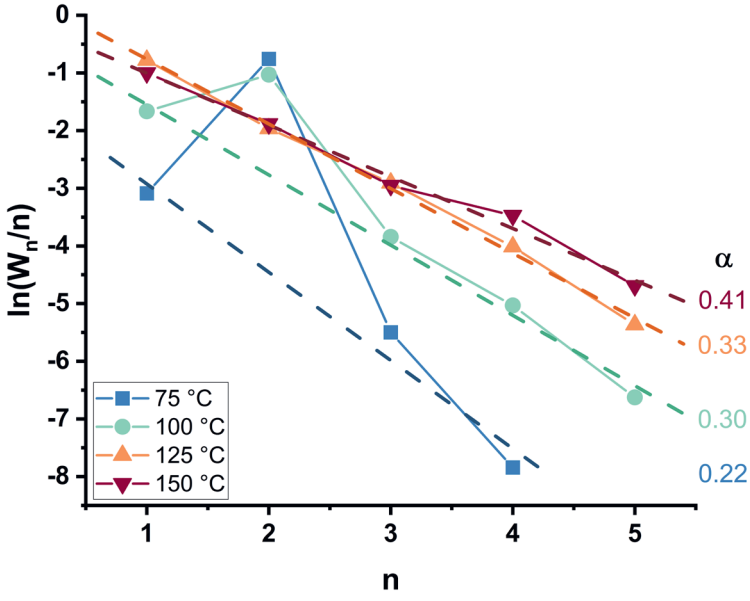

Figure 7.3 Anderson-Flory-Schultz plot (dotted lines) for Cu at -1.3 V vs SHE at 24 bar in 0.2 M $KHCO_3$ at as function of temperature. The slope of the graph gives the chain growth probability α as given on the left and in Table S3

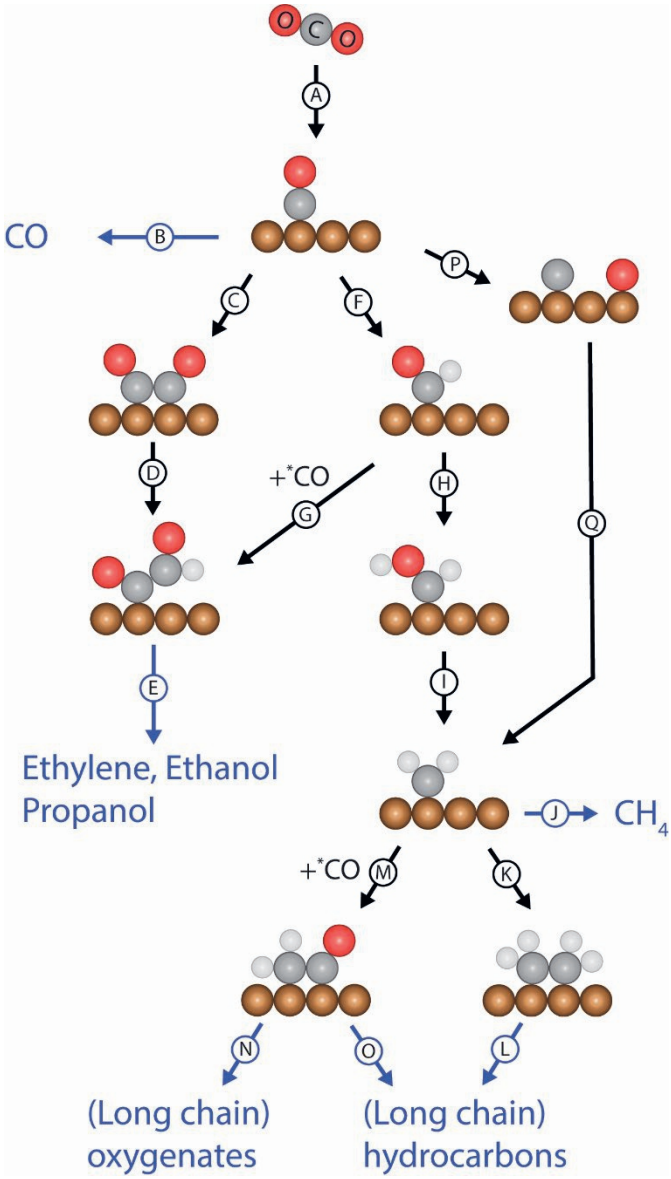

Figure 7.4 Overview of the different C-C coupling mechanisms on Cu. In blue the final products. Pathways are indicated with an arrow. We did not indicate the number of water molecules and electrons necessary for each pathway. A is the CO_2 reduction to form *CO, B the desorption of CO, C the CO dimerization and G is the carbonyl coupling to form the C-C bond. D, F, H, I and Q are the further hydrogenation of intermediates. P is the direct CO dissociation, K the CH_x coupling, M is CO insertion and E, J, L, N and O consist of multiple steps to form of the final hydrocarbons and oxygenates.

Figure 7.4 shows a overview of the different reaction pathways leading to C-C coupled products. At high temperatures the traditional C-C coupling pathways via C and G do not take place anymore as discussed above. This could be due to a lower *CO coverage, as this pathways is second order in *CO, and the *CO coverage is thus an important determinant for this pathway [69–73]. The chain growth mechanism is expected to take place via a CH_x intermediate [15,67] and would be less sensitive to the *CO coverage. Desorption of *CO (pathway B) should be faster at higher temperatures, which could lower the *CO coverage. However, we only observe little CO as product at high temperatures and only at the start of the reaction. This indicates that the *CO mostly reacts before it can desorb.

Hydrogenation is important in the chain growth mechanism and in all cases where this mechanism is observed during CO2RR, it is under conditions where HER is dominant and very little CO is formed [14,15,17,66–68]. Hydrogenation of the *CO can take place via a so-called H-assisted dissociation to form $*CH_x$ intermediates (Pathway F-H-I). Alternatively, in the thermo-catalytic Fischer-Tropsch reaction a direct dissociation of *CO is possible, which is followed by hydrogenation of the *C to form the $*CH_x$ intermediates (pathway P-Q). It might be that the latter pathway is opened up at high temperatures or that the high temperatures facilitate the fast dissociation of the *HCO. In any case, either F or P should become so fast that B and C are outcompeted. In both cases hydrogenation is important and therefore we can not distinguish between these pathways.

At low temperatures methane is already formed on Cu [7,11,73,74] via pathway F-H-I-J, but pathway M and K seem not possible as no longer hydrocarbons (apart from ethylene) have been observed. Therefore, for the chain-growth mechanism high temperatures should enhance the C-C coupling compared to CH_4 formation, as also shown by the increase in chain growth probability with temperature. The chain can grow either by CH_x coupling (Pathway K) or by CO insertion (Pathway M). It is still ambiguous which pathways is followed in the electrochemical chain-growth mechanism. However, we argue that on Cu at high temperatures the C-C bond is probably formed via CH_x coupling, because if pathway M would be active, pathway G is also expected to be active. However as discussed above, very little *CO is available, making these pathways unlikely. Moreover, pathway M should result in some oxygenates. However, neither long or short chain oxygenates have been detected at high temperatures. High temperatures should thus open up pathway K and must make this competitive to pathway J (the termination of the chain) to explain our results.

7.3 Effect of temperature

Temperature influences the stability and selectivity of Cu at temperatures much lower than 125 °C. Figure F.9 shows the effect of temperature on the FE of the major products at different pressures. These experiments were performed at -1.5 V vs SHE, as formation of C2+ products is increased at this potential. The trends at ambient pressure are very similar to the trends we reported before in a different setup [32]. However, in this study Cu is more unstable than observed before and no optimum in C2+ products with temperature is detected. Moreover, hydrogen evolution increases very rapidly with temperature, although this effect is suppressed by increasing the pressure (Figure F.11). Figure 7.5 shows the selectivity towards C_2H_4 as a function of temperature and time. Initially, at 1 bar, the effect of temperature is very similar to what we reported before. There is an optimum in ethylene selectivity at ca. 50 °C. However, in the setup used in this work the Cu seems to be less stable than before and with time the selectivity towards ethylene decreases, which gives a negative trend with temperature over the entire experiment. This electrochemical cell is very different to the design that we have used before, but also the electrode is now a wire instead of a disk, as it was previously. Additionally, the increased electrolyte concentration might explain the differences in stability. At 6 and 12 bar, similar behavior is observed, in the sense that with increasing time, the FE towards ethylene decreases. Interestingly, after 20 min, the selectivity towards ethylene remains high, even up to temperatures of 75 °C. This shows that even at a few bars of elevated pressure, formation of C2+ products can be performed at higher temperatures, most likely because the CO_2 concentration in the electrolyte is maintained at a reasonable concentration due to the increased pressure.

Figure F.12 shows the ratio in FE towards ethylene at 40 and 60 min compared to the initial FE at 20 min, as a descriptor for stability. This clearly shows that the Cu becomes less stable with increasing temperature, but increasing pressure can increase the stability. To make experiments at elevated temperatures on Cu possible, it is important to stabilize Cu at temperatures up to 75 °C, which are reasonable industrial operation temperatures [75,76], but also at higher temperatures, to utilize the chain growth mechanism discussed above. We hypothesize that the stabilization of Cu through pressure is due to the suppression of HER and an increase of the coverage of CO_2 and/or CO. However, other strategies are probably needed to obtain long term stability of the Cu catalyst at elevated temperatures. Some possible strategies may include pulsing of the potential or alloying the Cu to make it more stable at high temperatures [61].

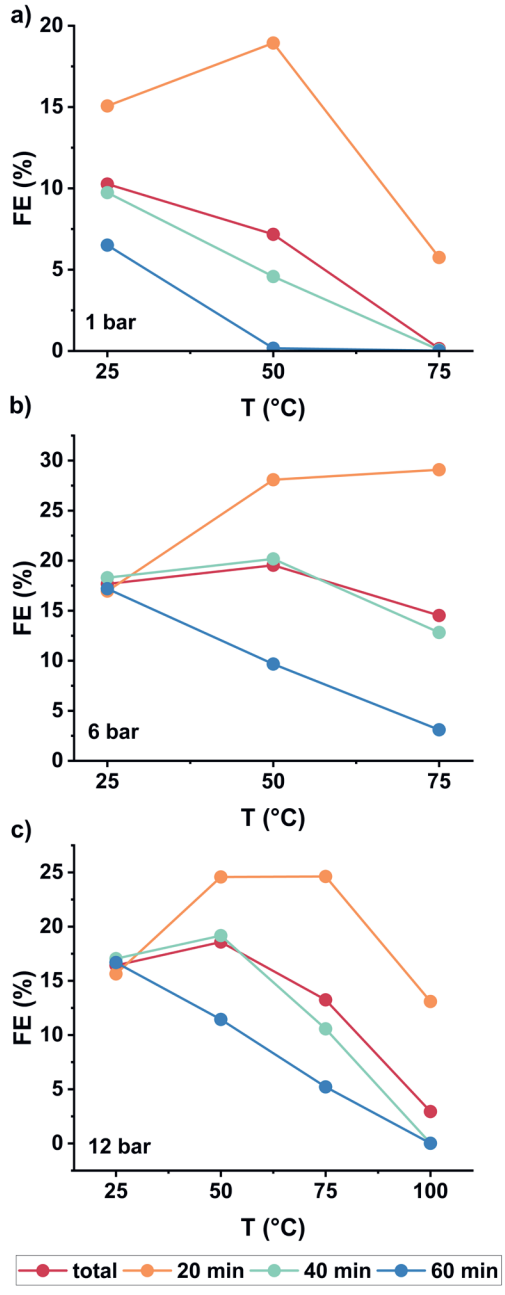

Figure 7.5 Faradaic efficiency towards ethylene as function of temperature after different electrolysis times at -1.5 V vs SHE in 0.2 M $KHCO_3$ at a) 1 bar b) 6 bar and c) 12 bar

7.4 Effect of pressure

Pressure does not only influence the stability of the Cu catalyst or increase the operating temperature window, but can itself also affect the activity and selectivity of the CO2RR. Figure 7.1 showed that the effect of pressure on the selectivity is smaller than the effect of temperature, but it is not negligible. Figure 7.6 shows the effect of pressure on the selectivity of the major products during CO2RR at -1.5 V vs SHE at room temperature, while the minor products are shown in Figure F.13. The pressure has been increased both with CO_2 and with Ar to be able to distinguish between the effect of pressure itself and of CO_2 pressure specifically.

Figures 7.6 and F.15 show that increasing CO_2 pressure can decrease the selectivity towards H_2 and that this effect already plateaus at a relatively low pressure of 3 and 6 bar at 25 and 75 °C, respectively. This same pressure is the optimum pressure for C_2H_4 selectivity, and for C2+ selectivity in general. At 25 °C, the initial pressure increase from 1 to 3 bar leads to a rapid increase in C2+ selectivity, but with further increasing pressure, the selectivity slowly decreases in favor of the simple C1 products CO and HCOOH, although the selectivity of the minor liquid products does keep increasing with increasing CO_2 pressure. Even though the selectivity towards HCOOH increases at high pressures, we never observe very selective CO2RR towards HCOOH as described in the literature [29,30]. Figure F.17 shows that this is not due to differences in electrolyte concentration between these studies.

During CO reduction on Cu, a continuous increase in C2+ selectivity with increasing pressure was observed [77,78] , which was attributed to the increasing *CO coverage. However, Figure 7.6 evidently shows this is not the case for CO_2 reduction, especially at higher pressures of 20 bar. It would be interesting to compare CO_2 and CO reduction at elevated pressures and temperatures but unfortunately, due to safety concerns, we are not able to perform CO reduction experiments at elevated pressures at this moment. Moreover, it would also be interesting to observe the *CO coverage during CO2RR at elevated pressures, which is unfortunately not possible with our current setup. However, from the product analysis, we hypothesize that the *CO coverage does not continuously increase with increasing CO_2 pressure, which might be due to faster desorption of CO due to increased CO_2 adsorption [51,79]. This limit in *CO coverage would explain the observed optimum in C2+ products at relatively low pressure and shift to simple C1 products with higher pressure.

Figure 7.6a evidently demonstrates that the suppression of H_2 at elevated pressures is due to the increase in CO_2 pressure. When the pressure is increased with Ar instead of CO_2, the FE towards H_2 increases at 25 °C, although at elevated temperatures Ar pressure does suppress HER slightly (Figure F.16a). This might be

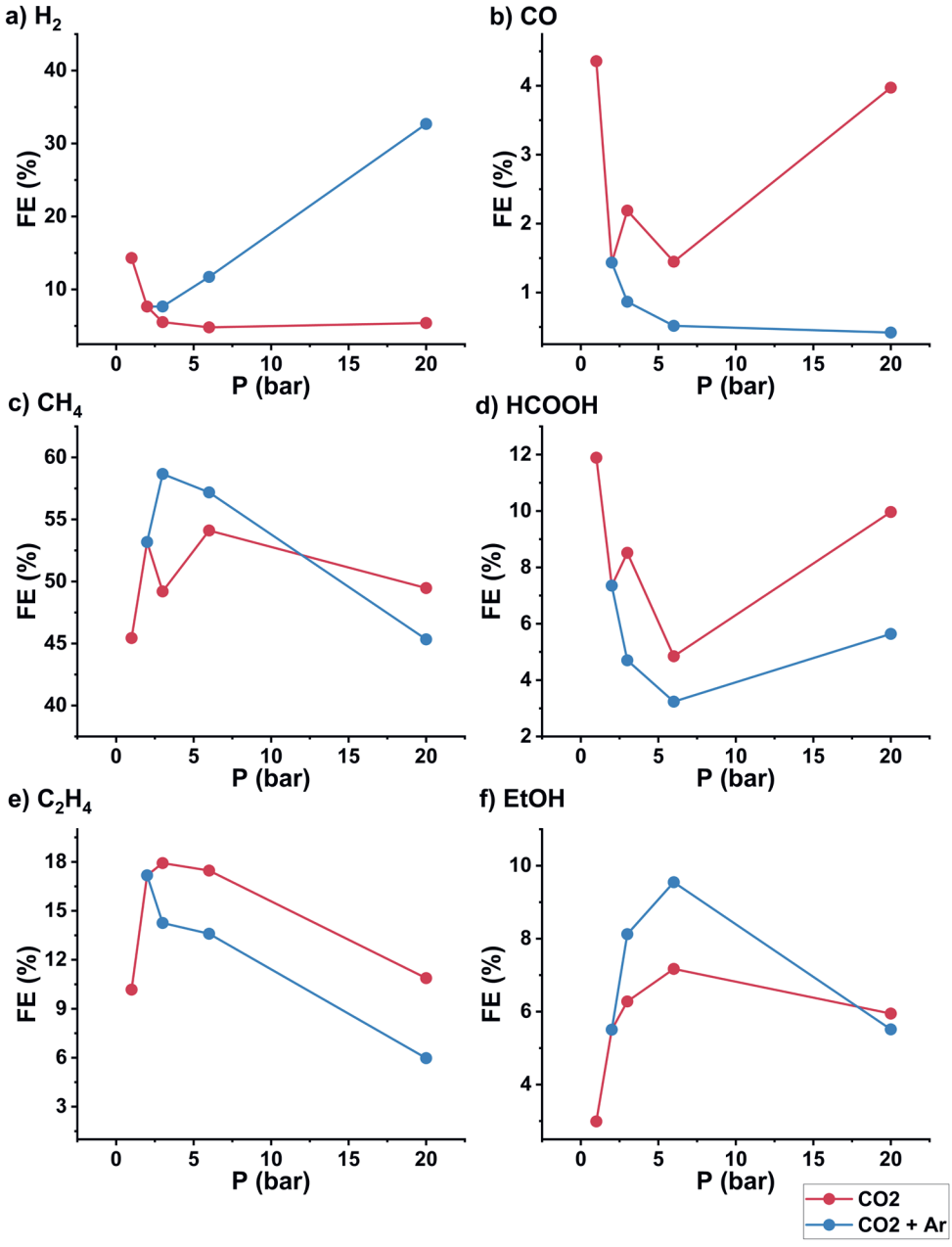

Figure 7.6 Faradaic efficiency towards the main CO2RR products as function of CO_2 and total pressure at -1.5 V vs SHE in 0.2 M $KHCO_3$ at 25 °C. Red lines are performed in pure CO_2 and blue lines are at 2 bar of CO_2 and pressure is increased with Ar. FE for a) hydrogen b) carbon monoxide c) methane d) formic acid e) ethylene and f) ethanol

due to the very high initial HER selectivity or the improved stability, even from Ar pressure. Moreover, when Ar is used to increase the pressure, most CO2RR products show lower selectivities than in a pure CO_2 atmosphere as shown in Figures 7.6 and F.13. For ethanol and methane this is not the case, but also for these products the activity is lower with Ar than in a pure CO_2 atmosphere as shown in Figure F.14 and F.16. So the increase in selectivity for these two CO2RR products is merely due to a relatively smaller decrease in activity compared to for example ethylene. These results show that the main reason for suppression of HER is not pressure itself, but CO_2 pressure, although Ar pressure might slightly help at elevated temperatures when HER is very active. We hypothesize that the HER suppression is due to competition of adsorption sides between CO_2 and H_2 intermediates, where elevated CO_2 pressures lead to less adsorption sites for HER [51].

7.4 Conclusion

In this study we have investigated the combined effect of pressure and temperature on the electrochemical CO_2 reduction on Cu. We show that temperature has a larger effect on the selectivity than pressure, although the effect of the latter is not negligible. Elevated pressures allow the performance of CO2RR at temperatures above 100 °C in aqueous systems. For the first time, we demonstrated CO2RR experiments at these high temperatures with liquid electrolytes. Although HER dominates at these conditions, we observed a change in the C-C coupling mechanism. Traditionally, C-C bonds are believed to form through a CO dimerization mechanism on Cu. However, by increasing the temperature, the chain growth mechanism, by which higher hydrocarbon chains can be formed, becomes more active, and it becomes dominant at 125 °C.

At temperatures below 100 °C, increasing the temperature can increase the FE towards traditional C2+ products and increasing the pressure can broaden the temperature range in which Cu catalysts can operate, both by increasing the CO_2 available and the Cu stability. At ambient temperature, increased CO_2 pressure itself can significantly suppress the competing hydrogen evolution reaction, even at a few bar. It is important to make the distinction between pressure and CO_2 pressure, as these do not have the same effect on the CO_2 reduction. For positive effects, it is in most cases crucial to increase the CO_2 pressure and not just the total pressure in the system.

In this study, we illustrate that temperature and pressure are crucial parameters to consider as they have significant effects both on selectivities and activities, but also on the mechanism for CO2RR. With our high-pressure, high-temperature electrochemical system we opened up the parameter space for much

broader study. This also means that there are too many parameters to investigate in this single study. In this study, all experiments were performed in 0.2 M $KHCO_3$ electrolyte, but it would be interesting to study the electrolyte effect at elevated pressures and temperatures. Moreover, it is important to study the stability of Cu at elevated pressures and especially elevated temperatures. We observe that at high temperatures, the Cu seems instable and new methods to increase the stability under these conditions must be developed. Alloying Cu with more stable metals or pulsed experiments are examples of possible ways to increase Cu stability. Furthermore, CO reduction instead of CO_2 reduction as well as experiments in different systems such as flow cell and GDE systems at both elevated pressures and temperatures are interesting and important to gain more insight into the combined effects of pressure and temperature.

References

1. Mertens, J. *et al. Joule* 7 442–449 (2023).
2. De Luna, P. *et al. Science (1979)* **364**, eaav3506 (2019).
3. Alerte, T. *et al. ACS Sustain Chem Eng* **11**, 15651–15662 (2023).
4. Roh, K. *et al. Green Chemistry* **22**, 3842–3859 (2020).
5. Bagger, A., Ju, W., Varela, A. S., Strasser, P. & Rossmeisl, J. *ChemPhysChem* **18**, 3266–3273 (2017).
6. Hori, Y. i. in *Modern aspects of electrochemistry* 89–189 (Springer, 2008).
7. Kuhl, K. P., Cave, E. R., Abram, D. N. & Jaramillo, T. F. *Energy Environ Sci* **5**, 7050–7059 (2012).
8. Kortlever, R., Shen, J., Schouten, K. J. P., Calle-Vallejo, F. & Koper, M. T. M. *Journal of Physical Chemistry Letters* **6**, 4073–4082 (2015).
9. Garza, A. J., Bell, A. T. & Head-gordon, M. (2018) doi:10.1021/acscatal.7b03477.
10. Nitopi, S. *et al. Chemical Reviews* 119 7610–7672 (2019).
11. Schouten, K. J. P., Kwon, Y., Van Der Ham, C. J. M., Qin, Z. & Koper, M. T. M. *Chem Sci* **2**, 1902–1909 (2011).
12. Kastlunger, G. *et al. ACS Catal* **12**, 4344–4357 (2022).
13. da Silva, A. H. M., Karaiskakis, G., Vos, R. E. & Koper, M. T. M. *J Am Chem Soc* **145**, 15343–15352 (2023).
14. Vos, R. E. & Koper, M. T. M. *ACS Catal* 4432–4440 (2024)
15. Zhou, Y. *et al. Nat Catal* **5**, 545–554 (2022).
16. Ma, X. & Yeo, B. S. *Current Opinion in Electrochemistry* 46 (2024).
17. Hwang, S. Y. *et al. Nano Energy* 109881 (2024)
18. da Silva, A. H. M. *et al. Journal of Electroanalytical Chemistry* **880**, (2021).
19. Jiang, K. *et al. ACS Energy Lett* **5**, 1206–1214 (2020).
20. Tang, W. *et al. Physical Chemistry Chemical Physics* **14**, 76–81 (2012).
21. Dutta, A., Rahaman, M., Luedi, N. C., Mohos, M. & Broekmann, P. *ACS Catal* **6**, 3804–3814 (2016).
22. Schouten, K. J. P., Pérez Gallent, E. & Koper, M. T. M. *Journal of Electroanalytical Chemistry* **716**, 53–57 (2014).
23. Varela, A. S., Kroschel, M., Reier, T. & Strasser, P. *Catal Today* **260**, 8–13 (2016).
24. Resasco, J., Lum, Y., Clark, E., Zeledon, J. Z. & Bell, A. T. *ChemElectroChem* **5**, 1064–1072 (2018).
25. Resasco, J. *et al. J Am Chem Soc* **139**, 11277–11287 (2017).
26. Ren, D., Fong, J. & Yeo, B. S. *Nat Commun* **9**, (2018).
27. Hara, K., Kudo, A. & Sakata, T. *Journal of Electroanalytical Chemistry* 391 (1995).
28. Hara, K., Tsuneta, A., Kudo, A. & Sakata, T. *J. Electrochem. Soc* 141 (1994).
29. Huang, L. *et al. Nat Commun* **14**, (2023).
30. Girichandran, N., Saedy, S. & Kortlever, R. *Chemical Engineering Journal* **487**, (2024).
31. Vos, R. E. & Koper, M. T. M. *ChemElectroChem* **9**, e20220023 (2022).
32. Vos, R. E. *et al. ACS Catal* **13**, 8080–8091 (2023).
33. Ahn, S. T., Abu-baker, I. & Palmore, G. T. R. *Catal Today* **288**, 24–29 (2017).

34. Hori, Y., Kikuchi, K., Murata, A. & Suzuki, S. *Chem Lett* **15**, 897–898 (1986).
35. Krause, R. *et al. Chemie Ingenieur Technik* **92**, 53–61 (2020).
36. Lobaccaro, P. *et al. Physical Chemistry Chemical Physics* **18**, 26777–26785 (2016).
37. Iglesias Van Montfort, H. P. & Burdyny, T. *ACS Energy Lett* **7**, 2410–2419 (2022).
38. Corral, D. *et al. Energy Environ Sci* **14**, 3064–3074 (2021).
39. Raaijman, S. J., Schellekens, M. P., Corbett, P. J. & Koper, M. T. M. *Angewandte Chemie - International Edition* **60**, 21732–21736 (2021).
40. Ramdin, M. *et al. Ind Eng Chem Res* **60**, 17862–17880 (2021).
41. Alerte, T. *et al. ACS Energy Lett* **6**, 4405–4412 (2021).
42. Li, J. *et al. J Am Chem Soc* **142**, 7276–7282 (2020).
43. Todoroki, M., Hara, K., Kudo, A. & Sakata, T. *Journal of Electroanalytical Chemistry* vol. 394 (1995).
44. Lamaison, S. *et al. Joule* **4**, 395–406 (2020).
45. Van Der Laan, G. P. & Beenackers, A. A. C. M. *Catal Rev Sci Eng* **41**, 255–318 (1999).
46. Van Santen, R. A., Markvoort, A. J., Filot, I. A. W., Ghouri, M. M. & Hensen, E. J. M. *Physical Chemistry Chemical Physics* **15**, 17038–17063 (2013).
47. ten Have, I. C. & Weckhuysen, B. M. *Chem Catalysis* 1 339–363 (2021).
48. Niu, J. *et al. International Journal of Hydrogen Energy* 47 9183–9200 (2022).
49. Nielsen, N. D., Jensen, A. D. & Christensen, J. M. *J Catal* **393**, 324–334 (2021).
50. Grabow, L. C. & Mavrikakis, M. *ACS Catal* **1**, 365–384 (2011).
51. da Silva, A. H. M., Vos, R. E., Schrama, R. J. C. & Koper, M. T. M. *Electrochim Acta* **498**, 144612 (2024).
52. Wuttig, A. & Surendranath, Y. *ACS Catal* **5**, 4479–4484 (2015).
53. Morales, D. M. & Risch, M. *Journal of Physics: Energy* **3**, 34013 (2021).
54. Wang, J. *et al. Nat Energy* **4**, 392–398 (2019).
55. Achrai, B. *et al. J Electrochem Soc* **167**, 134518 (2020).
56. Heenan, A. R., Hamonnet, J. & Marshall, A. T. *ACS Energy Lett* **7**, 2357–2361 (2022).
57. Öijerholm, J., Forsberg, S., Hermansson, H.-P. & Ullberg, M. *J Electrochem Soc* **156**, P56 (2009).
58. Bogaerts, W. F. & Haute, A. A. Van. *J. Electrochem. Soc.* **131**, 68–72 (1984).
59. Dash, D., Kumar, S., Mallika, C. & Mudali, U. K. *ISRN Chemical Engineering* **2012**, 1–5 (2012).
60. Bosch, R. W., Bogaerts, W. F. & Zheng, J. H. *CORROSION SCIENCE SECTION* 162 (2003).
61. Vos, R. E., Smaak, J. P. & Koper, M. T. M. *J Catal* **436**, (2024).
62. Rihm, S. D., Kovalev, M. K., Lapkin, A. A., Ager, J. W. & Kraft, M. *Energy Environ Sci* **16**, 1697–1710 (2023).
63. Shibata, H., Moulijn, J. A. & Mul, G. *Catal Letters* **123**, 186–192 (2008).
64. Lee, S., Kim, D. & Lee, J. *Angewandte Chemie* **127**, 14914–14918 (2015).
65. Dong, S. T., Xu, C. & Lassalle-Kaiser, B. *Chem Sci* **14**, 550–556 (2022).
66. Maeng, J. Y., Hwang, S. Y., Kim, S. Y., Rhee, C. K. & Sohn, Y. *J Environ Chem Eng* **12**, (2024).
67. Kim, Y. J., Maeng, J. Y., Hwang, S. Y., Rhee, C. K. & Sohn, Y. *Appl Catal B* **338**, (2023).
68. Yang, J. H. *et al. ACS Appl Mater Interfaces* **16**, 3368–3387 (2024).

69. Zhan, C. *et al. ACS Catal* **11**, 7694–7701 (2021).
70. Kong, X. *et al. Nano Lett* **22**, 3801–3808 (2022).
71. Huang, Y., Handoko, A. D., Hirunsit, P. & Yeo, B. S. *ACS Catal* **7**, 1749–1756 (2017).
72. Moradzaman, M. & Mul, G. *Journal of Physical Chemistry C* **125**, 6546–6554 (2021).
73. Liu, K. *et al. Sci Bull (Beijing)* **67**, 1042–1048 (2022).
74. Bai, H. *et al. Sci Bull (Beijing)* **66**, 62–68 (2021).
75. Lei, H., Wan, Q., Tan, S., Wang, Z. & Mai, W. *Advanced Materials* **35**, (2023).
76. Liu, X. *et al. Advanced Materials* **32**, (2020).
77. Yang, W. *et al. Journal of Energy Chemistry* **85**, 102–107 (2023).
78. Hou, J., Chang, X., Li, J., Xu, B. & Lu, Q. *J Am Chem Soc* **144**, 22202–22211 (2022).
79. De Jesús-Cardona, H., Del Moral, C. & Cabrera, C. R. *Journal of Electroanalytical Chemistry* 513 (2001).

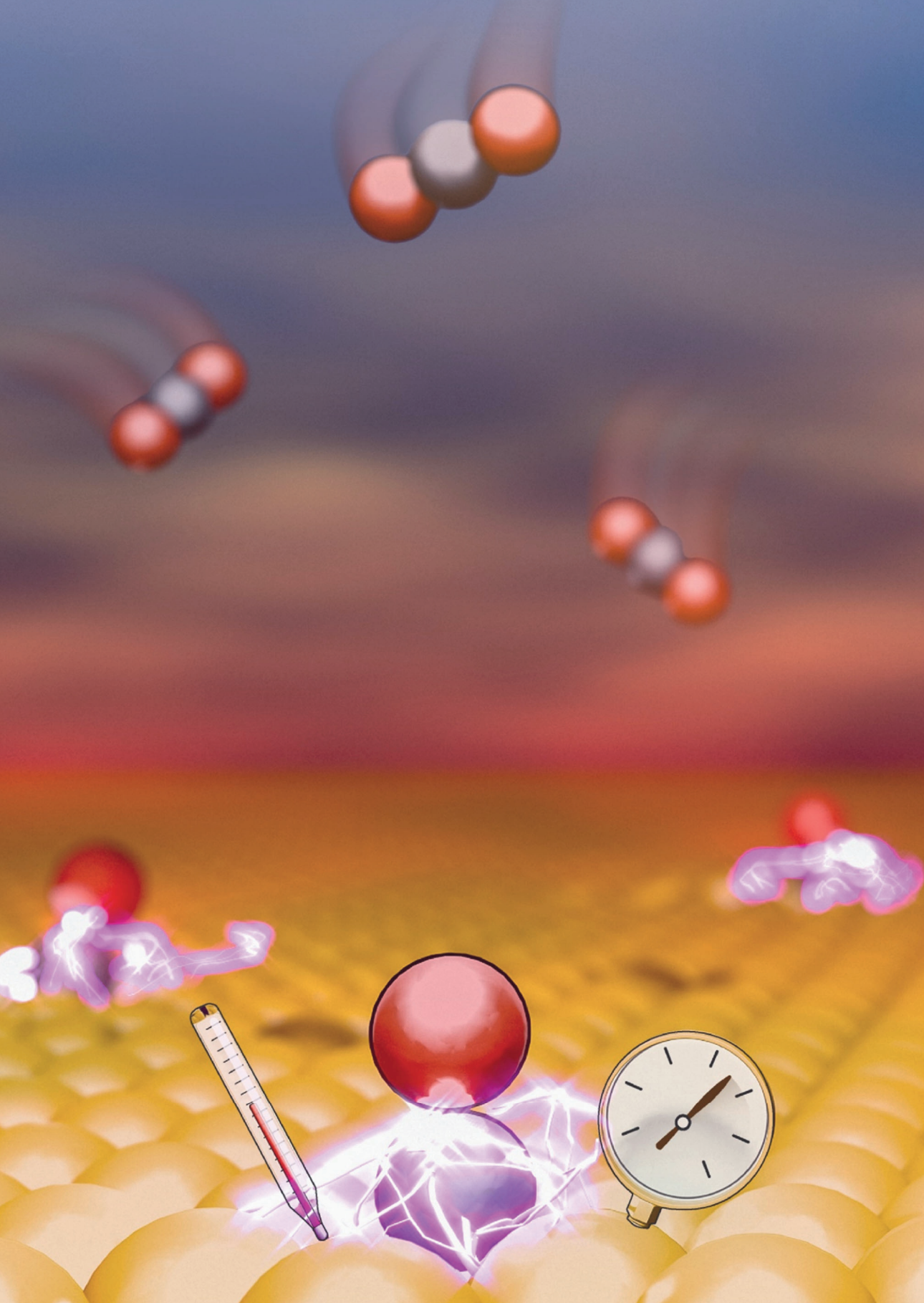

8

Screening of various metals for electrochemical CO_2 reduction at elevated temperatures and pressures

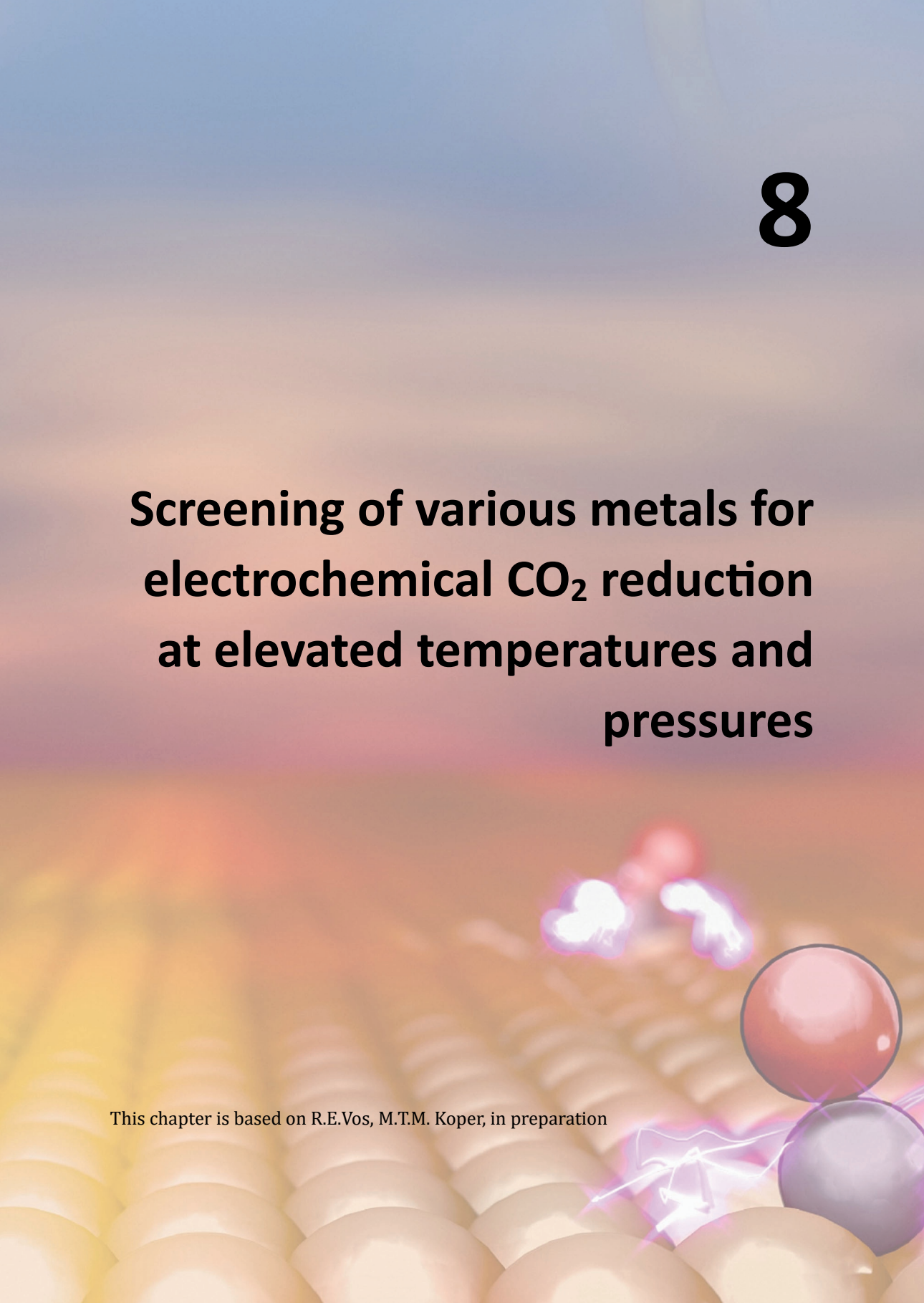

This chapter is based on R.E.Vos, M.T.M. Koper, in preparation

Abstract

Traditionally, the catalysts for the electrochemical CO_2 reduction reaction (CO2RR) have been categorized in 4 groups, producing mainly H_2, CO, HCOOH or C2+ products. However, this categorization is based on experiments at ambient conditions. With our high-pressure, high-temperature electrochemical cell, we are able to perform CO_2 reduction at vastly different conditions. In this study we have screened 20 metal catalysts for their ability to perform CO_2 reduction at conditions up to 30 bar and 100 °C in aqueous electrolyte. We show that catalysts that have average activity at ambient conditions, can reach near 100% efficiency for CO2RR at 30 bar and maintain this at high temperatures. Both temperature and pressure can increase the CO2RR activity significantly. However, if a catalyst does not perform CO2RR at ambient conditions, increasing pressure and temperature will only increase CO2RR selectivity to maximum 30%. Nevertheless, some of these inferior CO2RR catalysts do show interesting products beyond CO and HCOOH, such as long chain hydrocarbons and methanol.

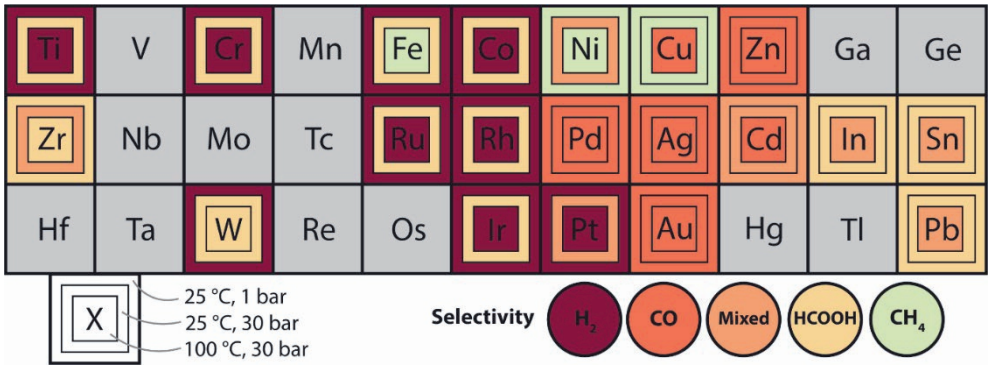

8.1 Introduction

The electrochemical CO_2 reduction reaction (CO2RR) is an interesting reaction to study as it could produce sustainable fuels and feedstocks for the chemical industry, and in this way fits in a sustainable green society [1–4]. Metals can be excellent catalysts for this reaction and these catalysts are traditionally classified in 4 groups [5,6]; metals as Au, Ag an Zn produce mainly CO from CO_2, metals such as Pb, Sn and In form mainly HCOOH, and Cu is the special one being able to form C-C bonds and produce products such as ethanol and ethylene. Lastly, there are metals such as Pt, Pd and Ni which are more active for the competing hydrogen evolution reaction (HER). This classification is based on data at ambient conditions, but these are probably not the typical conditions under industrial applications. Therefore, it is important to study the effect of temperature and pressure on a wide range of metal catalysts for CO2RR.

Temperature has been shown to increase the selectivity towards CO2RR compared to HER on Au, Cu and Ni at ambient pressures [7–9]. Often an optimal temperature is found, as too high temperatures can lead to too low CO_2 concentrations in electrolyte, or to instability of the metal catalyst. Temperature not only influences the selectivity but also significantly enhances the activity, both of CO2RR and HER. These trends are not only observed in H-cell configurations, but also in GDE setups, with catalyst such as Ag[10] and Sn[11].

Pressure can also significantly influence the CO_2 reduction reaction. Hara et al.[12] showed that even catalysts which at ambient conditions mainly produce H_2, such as Zr and Pt, could produce some CO2RR products at 30 bar. Also for catalysts of the other categories, pressure can improve the activity and selectivity towards CO or HCOOH[13,14]. Moreover, elevated pressures could even lead to new products, for example hydrocarbons on Ni[15], oxygenates on Ag[16] and 2-propanol on Cu[17].

Recently, we have developed a high-pressure, high-temperature electrochemical cell, which can be used to study the CO2RR at both high temperature and high pressure simultaneously[18]. This combination gives us the opportunity to study this reaction under new experimental conditions and perform experiments at or above 100 °C in aqueous electrolyte. The combination of elevated pressure and temperature can improve both selectivity and activity, as has been shown for CO on Au[18] and for ethylene on Cu. Moreover, at high temperatures and pressures new reaction pathways can be open up, such as the chain growth mechanism for C-C coupling on Cu as shown in the previous chapter.

In this study, we use our high-pressure high-temperature electrochemical cell to screen 20 metal catalysts for CO2RR. The effect of pressure and the combined

effect of high temperature and pressure on these metals is studied to establish if poor CO2RR catalysts can become decent, and if decent catalysts can become excellent. We study how selectivity and activity changes with experimental conditions and if new products are produced. We show that elevated pressures can inhibit HER significantly and CO2RR can reach almost 100% FE, even at 100 °C. Although traditional HER catalysts do not reach very high FEs for CO2RR, even at high pressures, some of them do produce interesting products such as long chain hydrocarbons and methanol. This study shows what is possible and which interesting directions exist to further understand electrochemical CO_2 reduction at high temperatures and pressures in aqueous systems.

8.2 Experimental

8.2.1 Chemicals

The 0.1 M electrolyte was made from $KHCO_3$ (99.95%, Sigma-Aldrich) with Milli-Q water (≥18.2 MΩcm, TOC < 5 ppb) and stored with Chelex (100 sodium form, Sigma-Aldrich) to clean the electrolyte from any metal impurities.[19] H_2SO_4 (95-98%, Sigma-Aldrich), H_2O_2 (35%, Merck) and $KMnO_4$ (99%, Sigma-Aldrich) were utilized to clean the cells. CO_2 (4.5 purity, Linde) was used for purging the electrolyte.

8.2.2 HP cell setup

An adapted high pressure, high temperature cell from Parr instruments with an Ag/AgCl reference from Corr instruments was used in this study. More details on the cell have been described before in a recent paper[18]. The cell was designed to work up to 140 bar and 200 ^{0}C and was used in semi-continuous mode where CO_2 was constantly purged through the cell with a flow rate of 150 ml/min. After going through a condenser coupled to a cooler (Cool-Care, Van der Heijden Labortechnik GMbH) to keep all volatile products in the liquid phase in the setup, the outlet gas was analyzed every 6 min with a Micro-GC from Agilent with two TCD detectors. A combination of a MS6A and CP-PORABOND Q column was used to detect H_2, CO and CH_4 and a Al_2O_3 column was used to detect the C2 and C3 hydrocarbons. The pressure in the cell was maintained by controlling both the inlet and outlet flow with flow controllers (SLA5850, Brooks Instruments). The temperature was controlled with an electric heating mantle. A homemade two-compartment PEEK cup was used inside the stainless steel chamber and all metal parts from the thermocouple and reference electrode were covered by Teflon tape. Moreover, the lid of the vessel was covered with Viton rubber to prevent any contamination from the stainless steel.

8.2.3 Electrochemical experiments

The homemade PEEK cup was cleaned prior to experiments by storing in permanganate solution overnight (0.5 M H_2SO_4, 1g/L $KMnO_4$). Afterwards, the cell was washed, cleaned in diluted mixture of H_2SO_4 and H_2O_2 to remove any traces of MnO_4 and MnO_2, washed again and boiled three times with Milli-Q water. As working electrodes, 1mm thick wires were used. Table G.1 gives an overview of the supplier and the purity of the wires. The wires were used as received, except for the Cu, which was electropolished in 85% H_3PO_4 (Suprapure, Merck) by applying +3 V versus a graphite counter electrode for 20 s before the experiment. The working electrode was separated from a DSA counter electrode (Magneto) with a PiperION membrane (Versogen)[20,21]. The experiments were performed with a Gamry Interface 1010B potentiostat and current interrupt[22] was used to correct for the Ohmic drop. Experiments were performed for 60 minutes at constant potential, in principle -1.5 V vs SHE. Gaseous products were determined every 6 min with GC as described above, while liquid products were determined afterwards by sampling the 65 ml catholyte and analyzing this using high performance liquid chromatography (HPLC, Shimadzu) with an Aminex HPX-87H column (Bio-rad). Methanol was not detected with HPLC but using a liquid GC with a SH-I-MS column (Nexis GC 2030 with AOC-30i autosampler, Shimadzu). During experiments the pressure was maintained within an error of 0.1 bar, while temperature was maintained within an error of 2 °C. Before reaching the conditions used for the experiment (which could take up to an hour), the working electrode was always under potential control at a potential of -0.8 V vs Ag/AgCl. Due to time restraints, individual experiments have not been repeated and no error bars are plotted.

8.2.4 Reference electrode corrections

In this study, all potentials are reported vs SHE(T). During experiments, a high pressure Ag/AgCl electrode (Ultradeg, 0.1 M KCl, Corr Instruments) was used as a reference electrode. However, with changing temperature, one should make several corrections to convert the potential from Ag/AgCl to SHE as we described previously (REF to HP Cu paper). The Nernst equation is used to determine the shift of the Ag/AgCl reference electrode against SHE:

$$E_{Ag/AgCl} = E^0_{Ag/AgCl}(T) - \frac{\ln(10) * RT}{nF} * \log\left(a_{Cl^-}(T)\right) \qquad (8.1)$$

with E^0 the standard potential, R the gas constant, T the temperature, n the number of electrons, F Faradays constant and a_{Cl} the activity of the chloride anion. The standard potential of Ag/AgCl is a function of temperature and can be calculated using the following formula[23]:

$$E^0_{Ag/AgCl}(T) = -0.111658 + 0.011134 * T - 0.001757268 * T * \ln(T) \qquad (8.2)$$

The temperature dependence of the activity of the chloride ions can be determined from a formula from Bogaerts et al.[24] :

$$a_{Cl^-}(T) = exp\left[\log\left(a_{Cl^-}(25\,^\circ C)\right) - \frac{\sqrt{I_{Cl^-}}}{1+\sqrt{I_{Cl^-}}} * \left(A_\gamma^T - A_\gamma^{25\,^\circ C}\right)\right] \qquad (8.3)$$

where a_{Cl^-} is the activity of the chloride at room temperature[25] I_{Cl} is the ionic strength and A_γ is the Debye-Huckel parameter[24]

With these formulas, the shift between an Ag/AgCl reference and SHE could be determined at different temperatures, as shown in Table G.2. The potential could not be reported in RHE as the pH should be known to convert SHE to RHE. However, it is impossible to measure the exact pH of the electrolyte at elevated CO_2 pressures and temperatures.

8.3 Results

8.3.1 Selective screening

We have performed experiments on a selection of metal catalysts for CO2RR at elevated pressures and temperatures. Because our setup opens up the parameter space for both pressure and temperature, many combinations of conditions are possible, especially when electrolyte composition and potential are also taken into account. Therefore, in this study we have limited the parameter space and all experiments are in principle performed in 0.1 M $KHCO_3$ at -1.5 V vs SHE, which is equivalent to -1.1 V vs RHE at ambient conditions. Moreover, we study six temperature and pressure combinations for seven main metal catalysts. Ambient conditions are studied as reference point, room temperature and 30 bar to study the effect of pressure, and to be able to compare with known literature. The effect of temperature is studied at 50 and 100 °C, at 30 bar, and to observe the effect of pressure at these temperatures also experiments at 5 bar were performed. Figure 8.1 shows part of the periodic table and the main CO2RR products of these metals at ambient conditions [5,6]. We have chosen to study Cu, as it is the only one making products beyond CO. Zn and Ag are studied as typical CO producing catalysts, while Cd and Sn typically make HCOOH. Ni and Pd are studied to complete the set with catalysts that at ambient conditions produce mainly H_2. With the exception of Sn, the studied metals all surround Cu as we expect this gives the highest chance to observe products beyond CO when the temperature and pressure are altered. Besides these 7 metals, 16 other metal catalysts such as Au, Pb, Pt and Fe are studied as well, although in less detail, in Figure 8.4.

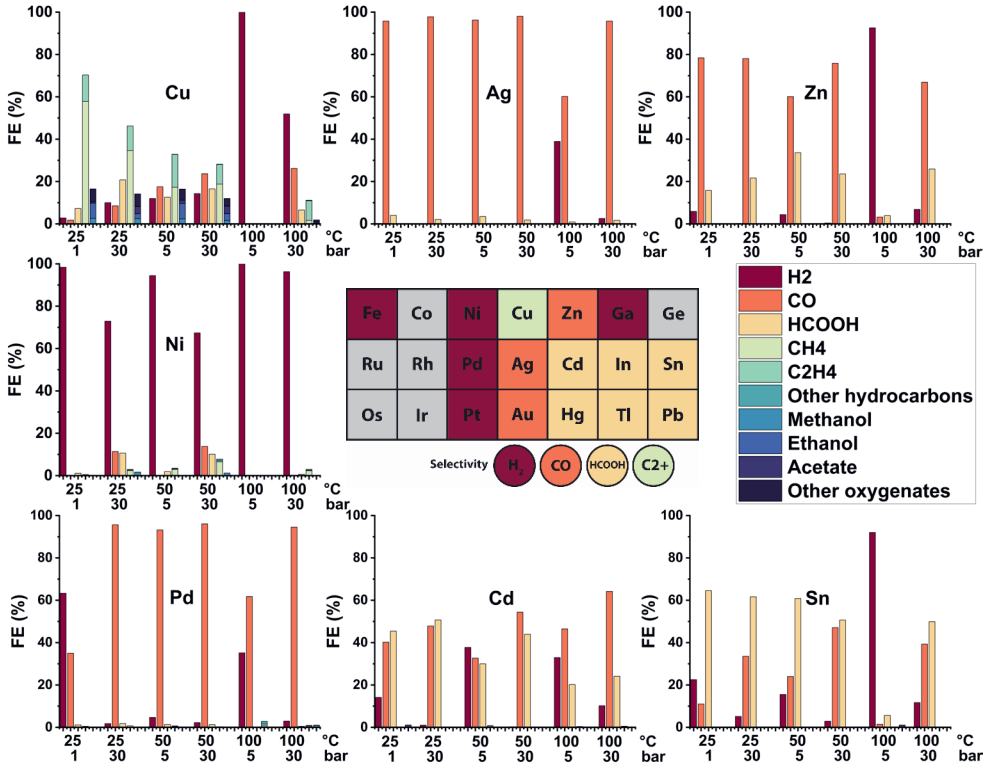

Figure 8.1 Faradaic efficiency at six different conditions for Cu, Ag, Zn, Ni, Pd, Cd and Sn at -1.5 V vs SHE in 0.1 M $KHCO_3$. These metals were studied as they represent the different groups of metals as shown in the Periodic Table in the middle(REF); hydrogen as main product, CO or HCOOH and Cu as catalyst able to make C2+ products.

Figure 8.1 shows the Faradaic efficiency towards the main products at the different pressure and temperature combinations for Cu, Ag, Zn, Ni, Pd, Cd and Sn. The competing hydrogen evolution reaction can be significantly suppressed on most of these metals at elevated pressures. Ag, Zn, Cd and even Pd show hardly any H_2 at 30 bar at room temperature, while Cu and Sn only produce up to 10%. Only Ni still produces significantly amounts of H_2 at these conditions, although with 70% also significantly less than the almost 100% at ambient conditions. With increasing temperature up to 50 °C, the HER efficiency remains low. At 100 °C, H_2 selectivity rises slightly for most metals, although only very significantly for Cu and Ni. At elevated temperatures, high pressures are needed to keep HER suppressed as at 5 bar the H_2 selectivity increases again, especially at 100 °C, where it starts to dominate not only on Ni, but also on Cu, Sn and Zn. The dominance of hydrogen at 100 °C and 5 bar is not simply due to low CO_2 solubility, as at this condition the CO_2

solubility is higher than at ambient conditions but CO_2 reduction performance is worse.

Low efficiency towards H_2 means that most current is used to make CO2RR products. While Pd and Ag are very selective and produce almost 100% CO at elevated pressures, Cd, Sn and Zn produce both CO and HCOOH. While at ambient conditions Zn and Sn produce mainly the product they are expected to produce (CO and HCOOH respectively)[5,6], Cd already produces a mixture of CO and HCOOH at these conditions even though it is expected to produce mainly HCOOH. How the ratio between CO and HCOOH changes in general with pressure and temperature, will be discussed in more detail in section 8.3.3. It is interesting to notice that when almost 100% efficiency towards CO2RR is reached, it is either towards CO (for Pd and Ag) or towards a mixture of CO and HCOOH (for Cd, Sn and Zn), but never only towards HCOOH. In the literature, HCOOH has been observed as the dominating CO2RR product at elevated pressures, even reaching efficiencies above 90% [26]. However, the FE towards HCOOH strongly depends on potential[26], so it might be that we are not at the optimal potential for the formation of HCOOH.

At high pressure and low to medium temperatures, Ni is able to perform CO2RR in significant amounts and it produces a mixture of products; not only CO and HCOOH, but also hydrocarbons. These hydrocarbons are mainly methane, but also ethane, ethylene, propene and trace amounts of C4 products are observed. The formation of ethane and propene indicates that a chain growth mechanism is active, as has been shown before for Ni [9,27]. Interestingly, not only Ni produces these longer chain hydrocarbons but also Cu and Pd produce some longer chain hydrocarbons at elevated temperatures. Cu produces a mixture of products, as expected. At ambient conditions, mainly hydrocarbons are produced on Cu, but the selectivity towards these decrease with both temperature and pressure and at 50 °C and 30 bar there is a relatively equal mixture of all product categories. These trends fit with the trends observed before in a more detailed study to the combined effect of pressure and temperature on Cu in Chapter 7. The only metals that are able to produce oxygenates in detectable amounts besides Cu are again Ni and Pd. Both metals can produce methanol, but only under very specific conditions. On Pd, a trace of acetate has been detected at 100 °C and 30 bar. From literature it is known that Ag can produce oxygenates at elevated CO pressures [16], but we did not observe any during CO2RR. Besides that we use CO_2 and not CO, these rates are also so small that it would not lead to any significant amount of FE for these oxygenates. Moreover, Kuhl et al.[28] have shown that several metals can produce methane and methanol, even at ambient conditions, such as Zn, Ag and Au. However, this was only observed at very specific potentials and with very low activity.

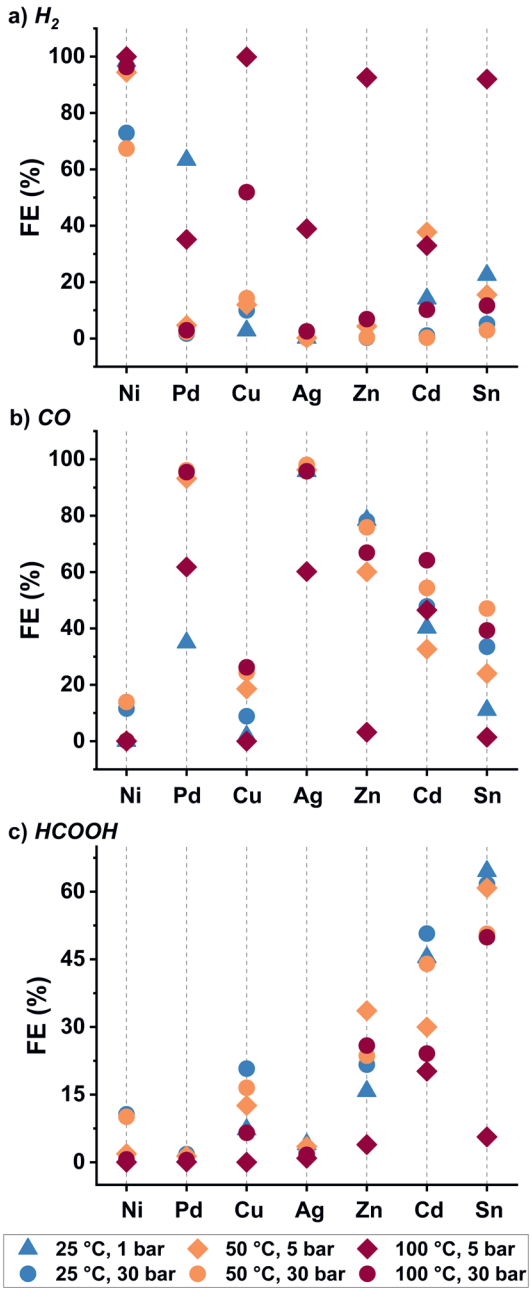

Figure 8.2 Faradaic efficiency for a) hydrogen b) carbon monoxide and c) formic acid at six different conditions for Cu, Ag, Zn, Ni, Pd, Cd and Sn at -1.5 V vs SHE in 0.1 M $KHCO_3$

Figure 8.2 shows the same data of Figure 8.1, but plotted in a different way, to gain further insights in the trends. It shows how the selectivity towards the main products CO, HCOOH and H_2 changes with the different conditions on the different metal catalysts. Figure 8.2a gives an even more pronounced illustration than Figure 8.1 how H_2 selectivity is influenced by pressure and temperature. H_2 can be almost completely suppressed with increasing pressure except on Ni. This suppressing effect can be maintained with increasing temperature. However at high temperatures, elevated pressures are needed to maintain high CO2RR selectivity because high FE towards H_2 are mainly observed at 100 °C and 5 bar.

Pd and Ag produces CO with almost 100% FE under most conditions. Cu, Zn, Cd and Sn show more variation in the CO selectivity with temperature and pressure. On Zn, the selectivity towards CO remains fairly constant at low temperatures and only slightly decreases at 100 °C, or at the combination of elevated temperatures and low pressures. For Cu, Cd and Sn, the FE towards CO seems to increase with increasing temperature, although mainly at 30 bar. For the selectivity towards HCOOH, it is apparent that the highest efficiencies are reached at room temperature, especially for the metals known for producing formic acid. With increasing temperatures, these catalysts are becoming less selective towards HCOOH, which is similar to what has been observed before on Cu under ambient pressures [8] and on Sn and In at elevated pressures[29]. Although in general higher pressures increase the selectivity towards formic acid (for example at room temperature on Cu, Zn and Cd), in some cases higher pressure actually decreases the selectivity towards formic acid (50 °C on Zn and Sn).

Figure 8.3 shows the partial current densities which accompany the selectivities of Figure 8.1 and 8.2. Note the breaks in the y-axis. These breaks are necessary to be able to spot the details at low current densities, while also showing the few extreme cases. Especially for H_2, the partial current densities can go to very high values at high temperatures, mainly in combination with low pressure. In these conditions, some metals are not very stable and produce large amounts of H_2. To illustrate this, the current vs time for Cu and Ni at high temperature and low pressure have been plotted in Figure G.3. For all products, the highest current densities are observed at 100 °C. For the CO2RR products, the effect of pressure on the partial current densities is also apparent as the highest current densities are reached at elevated pressures. Even though the FE towards HCOOH decreases often with temperature as discussed above, the partial current density still increases significantly. When the metal catalyst is stable, increasing either pressure or temperature is an effective strategy to increase the activity of CO_2 reduction, as is illustrated for Ag, Zn and Cd in Figure G.3 and as shown before in the same setup for Au[18].

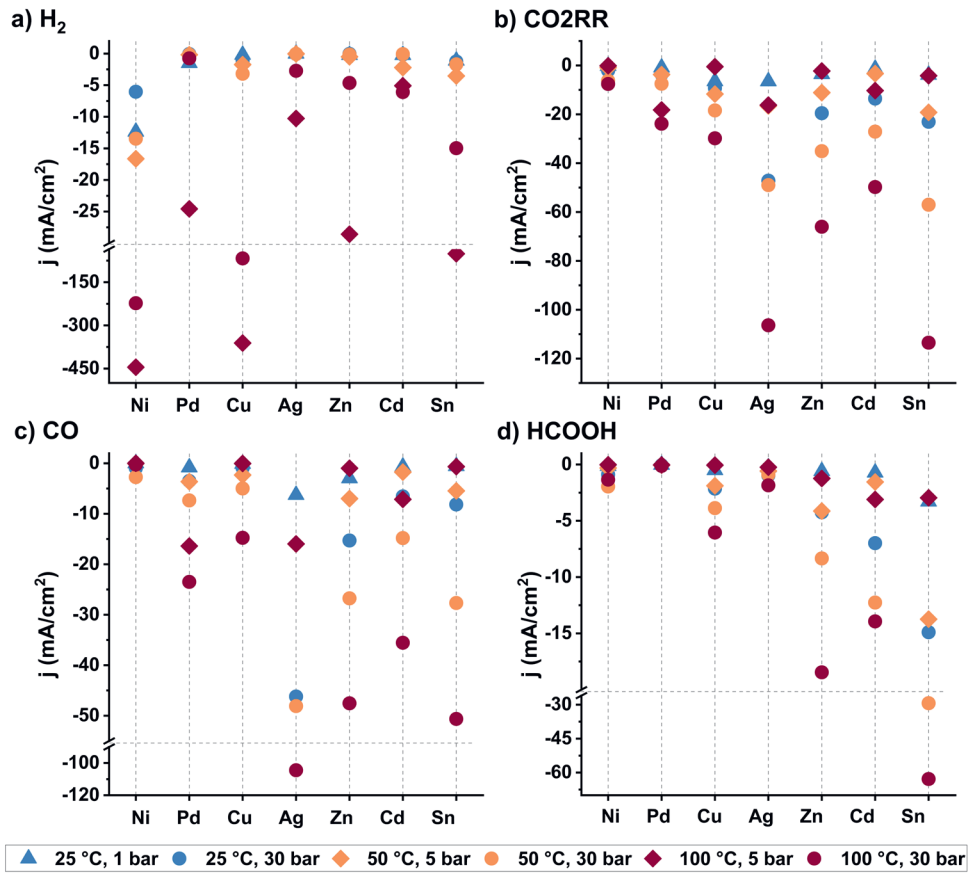

Figure 8.3 Partial current densities for a) hydrogen b) all CO2RR products c) carbon monoxide and d) formic acid at six different conditions for Cu, Ag, Zn, Ni, Pd, Cd and Sn at -1.5 V vs SHE in 0.1 M $KHCO_3$.

8.3.2 Broader screening

In the above discussion, we have studied a small selection of possible metal catalysts. However, many more metals could be studied, of which some are known to be good CO2RR catalysts at ambient conditions. However, it is also interesting to investigate the catalysts that produce mainly H_2 at ambient conditions to study if a poor CO2RR catalyst can turn into a good catalyst when the conditions, such as pressure and temperature, are optimal. Ni and Pd are examples of the this, where both significantly improve their CO2RR activity and selectivity under the right conditions. Therefore, we decided to study a larger range of metals and see what the effect of pressure and temperature is on the CO2RR. To limit the parameter space, we only study these catalysts under three conditions, namely ambient

conditions as reference point, room temperature and 30 bar to study the effect of pressure, and 100 °C and 30 bar to observe the effect of temperature. These conditions have been chosen as Figures 8.1 and 8.2 show that elevated temperature with low pressure is not a good combination for CO2RR. Moreover, the difference between 50 and 100 °C is in most cases not that significant at 30 bar, but at 100 °C some other products have been observed on Pd and Cu. Ni does show that for a poor CO2RR catalyst, 100 °C might be too high and leads to mainly H_2, but in that case the 50 °C does not provide much more insight than the case at 25 °C and 30 bar. Therefore, it was decided to study 100 °C and not 50 °C for this broader screening.

Figure 8.4 shows the effect of pressure and temperature on the CO2RR on Ti, Zr, Cr, W, Fe, Ru, Co, Rh, Ir, Pt, Au, In and Pb. The last three metals are known to be good catalysts at ambient conditions for CO2RR, while the others mainly produce H_2 at these conditions. While Au, In and Pb can reach very high CO2RR selectivities at high pressures both at 25 and 100 °C, the other catalysts remain producing mostly hydrogen at all conditions. Thus, a poor CO2RR catalyst at ambient conditions can not become a good catalyst by simply changing the pressure and temperature, as further illustrated in Figure 8.5.

In Figure 8.5 we plot the Faradaic efficiency towards CO2RR at different conditions against each other to clearly illustrate how these conditions improve the CO2RR selectivity (compared to HER). For example, Figure 8.5a show the effect of pressure on the CO2RR selectivity by plotting the FE for CO2RR at 30 bar and 25 °C vs the FE for CO2RR at 1 bar and 25 °C. This Figure shows that a poor CO2RR catalyst at ambient conditions (on the far left side of the graph) cannot be turned in a good one by increasing the pressure (on the top side of the graph). A poor catalyst can be turned in a slightly better catalyst at best, as shown in Figure 8.5b, where none of the catalysts reaches much more than 25% FE towards CO2RR. However, a reasonable CO2RR catalyst with FE toward CO2RR as low as 30% at ambient conditions (at these potentials), such as Au, In and Pd, can become a very good catalyst with less than 10% FE for HER at elevated pressures (Figure 8.5a), even at high temperatures (Figure 8.5c and d).

Even though the poor CO2RR catalysts do not have high CO2RR selectivity, there are still some interesting observation to be made from Figure 8.4. For these poor CO2RR catalysts, the main product at high T and p is HCOOH. Pt and Zr are exceptions, as they produce also significant amounts of CO. Coincidently, from all the poor CO2RR catalysts, Pt and Zr also produce the least hydrogen at elevated pressures. Moreover, we observe that some of these catalysts are able to produce long chain hydrocarbons and methanol, which we will discuss in more detail in section 8.3.3.

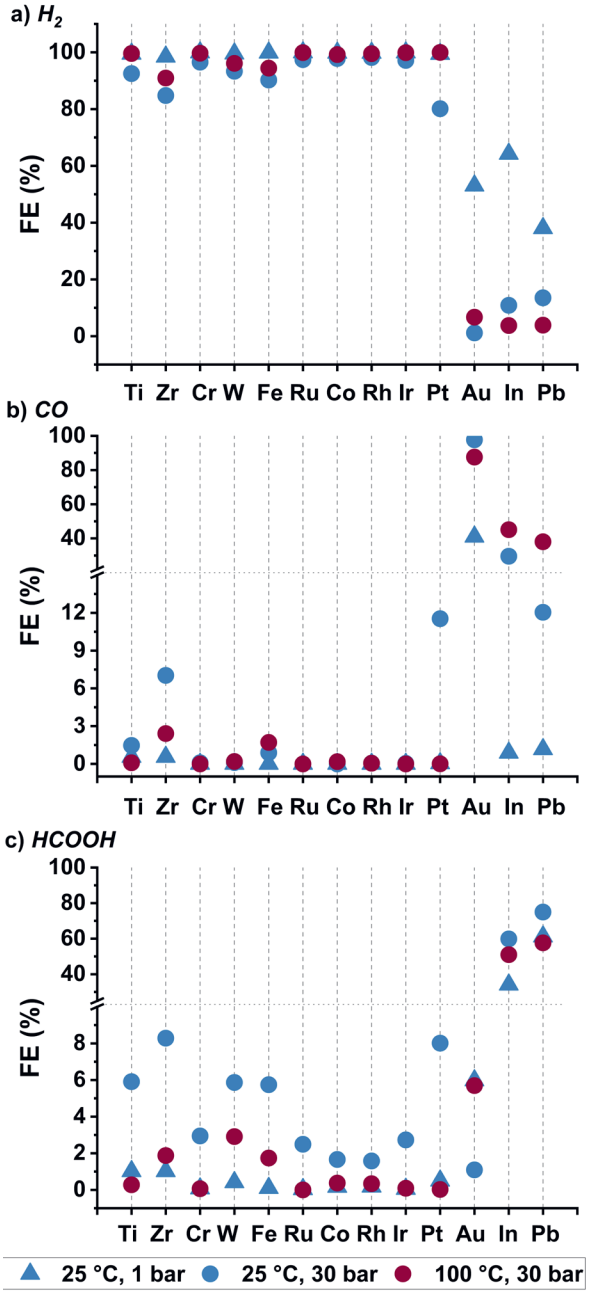

Figure 8.4 Faradaic efficiency for a) hydrogen b) carbon monoxide and c) formic acid under the three main conditions (ambient, high pressure, high temperature and pressure) for a variety of metal catalysts at -1.5 V vs SHE in 0.1 M $KHCO_3$.

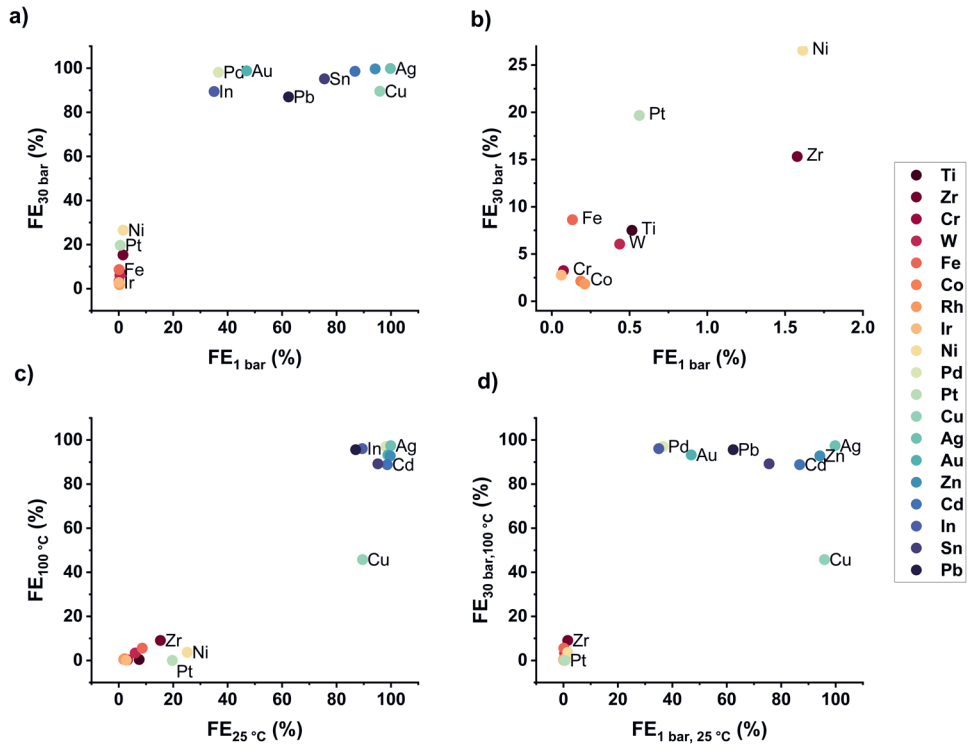

Figure 8.5 The Faradaic efficiency towards CO2RR plotted against different conditions as an illustration of the improvement (p,T) conditions can have. For example, a) shows the effect of pressure at room temperature, where medium CO2RR catalysts at ambient conditions can become very good at high pressure, but poor catalysts at ambient conditions at best become mediocre. b) is a zoomed-in version of a) showing the poor CO2RR catalysts. c) shows the effect of temperature at 30 bar and d) shows the combined effect of pressure and temperature.

The poor CO2RR catalysts at ambient conditions do not become very active at elevated pressures, not even at room temperature. This is different than observed before by Hara et al.[12] as they observed reasonably high FE for CO2RR on metals as Zr (40%), Pt (57%) and Rh (80.8%). Figure G.4 compares our results with the results of Hara et al. and Figure G.4c indeed shows that for the poor CO2RR catalysts, we observe significantly more H_2 than Hara et al. However, for some of the good CO2RR catalysts, we observe much more CO than Hara et al. There is not a systematic difference between the studies of Hara et al. and this study for H_2 and CO, although we observed in general less HCOOH for the most active HCOOH

producing metals as Pb and Sn. Both studies were performed in the same electrolyte, at similar pressures and temperatures, but a key difference is that we employ constant potential measurements while Hara et al. employ constant current measurements. Therefore, the potential in their experiments can be very different depending on the metal studied, and this might explain the different results between the two studies. A comparison between the study of Hori[5] and this study in Figure G.5 leads to a similar observations. However, the HCOOH efficiency in the study of both Hara and Hori is exceptionally high and was not reached in many other studies[30–33], or only at certain conditions of potential, electrode roughness and temperature [26,34,35]. Therefore, we expect that under (slightly) different conditions, near 100% FE towards HCOOH should also be achievable in our setup.

8.3.3 Discussion activity, stability, selectivity

Figure G.6 shows that the activity towards CO2RR increases with both increasing temperature and pressures. This is similar to what we have shown before in a more detailed study on Au using this setup [18]. Only under conditions where CO_2 availability becomes limited, or when the catalyst becomes unstable, this relationship does not hold. In Figure G.6 this is most clearly illustrated by the data points at 100 °C and 5 bar, which are often lower than expected based on the other results. Moreover, Figure G.3 illustrates that not all metals are stable under the conditions applied in this study. Especially at high temperatures and low CO_2 pressures, we observe instabilities, which are illustrated by the increase of the total current due to the increase in HER selectivity in time. This instability also influences the product distribution, as can be seen in Figure 8.5c and d, because the instabilities lead to more HER and relatively less CO2RR. Therefore, while all other reasonable CO2RR catalyst cluster together in the top right corner of Figure 8.5c, Cu is the only one significant below that. This means that for most CO2RR catalyst, they produce very little H_2 when the pressure is increased to 30 bar and this remains the case even at 100 °C because they are stable. However, Cu becomes unstable at these temperatures and as a consequence starts producing significant amounts of H_2, which lowers the CO2RR selectivity and makes Cu and outlier in Figure 8.5c.

The selectivity of the reaction and especially the competition between the main products CO and HCOOH is analyzed in more detail in Figures G.8, G.9 and G.10. Figure G.8 shows the selectivity towards hydrogen, formic acid and CO plotted against the H* binding energy calculated by Bagger et al.[6] They argue that H* binding energy is the key descriptor predicting the main product, although recently it has been argued that the crystal lattice also works as descriptor[36]. In these plots, the different classes of CO2RR catalysts can clearly be seen and seem to reasonably

hold even at these different conditions. However, there are some exceptions of which Pd is a clear example. Based on its *H energy, Pd is expected to produce mainly H_2, as it was classified before by Bagger et al.[6] However, we observed that HER can be suppressed almost entirely on Pd, maybe because one should consider a palladium hydride surface instead[37–41]. Also Ni and Pt move away from the cluster on top, but only at elevated pressures. Even though the H* binding energy still seems a reasonable descriptor even at high temperature and pressure, the difference between the CO and HCOOH producing metals becomes less sharp and more gradual in these conditions. Zn, which is classified as producing CO, makes relatively less CO by increasing pressure and temperature while Cd and the HCOOH-producing metal move in opposite direction and seem to produce more CO with increasing pressure and temperature. Figure G.8 illustrates that with increasing pressure the Faradaic efficiency towards HCOOH can either increase or decrease and this seems to depend on the *H binding energy. For metals known for producing HCOOH, the FE decreases with increasing temperature, while the metals with stronger *H binding energies slightly increase their selectivity towards HCOOH. As formic acid and CO are the main CO2RR products for most catalysts, it is interesting to see how the ratio between these products changes with changing operation conditions. Figure G.9 illustrates that both with increasing pressure and temperature in most cases the CO selectivity increases more than the HCOOH selectivity, at least for the potential and electrolyte used here.

Figure G.10 shows that some metal catalysts (Fe, Co, Ni, Pd, Cu) have the ability to make hydrocarbons at high pressures, sometimes only in combination with high temperatures (Zr and Cd). Various metals show some methane production and others show even longer hydrocarbons. These efficiencies are very low, but not uninteresting as this shows that these metals are capable of producing C2+ products and this is not limited to Cu only. Because no other liquid C2+ products are detected at any other metal than Cu (except for trace of acetate on Pd) and because these metals are able to produce longer hydrocarbons, we expect that these metals perform C-C coupling via a chain growth mechanism instead of the traditional CO dimerization mechanism. Maybe not coincidentally, some of the metals that perform this electrochemical chain growth mechanism are also able to do this thermocatalytically and are active for the Fischer-Tropsch reaction[42–44], such as Fe, Co and Ni, although Ru does not show the formation of hydrocarbons in this study. Also interestingly, some metals are able to produce methanol as well (Figure G.11). Fe produces methanol both at 25 and 100 °C at 30 bar, while Ni and Cu only produce it at 25 and 50 °C and Pd only at 100 °C. Curiously, the only metals that produce methanol also produce longer hydrocarbons, which could indicate that that these products share a common intermediate, such as *HCO[28,45]. Based on this, one might expect Co to also be able to form methanol, even though this was not observed in

our experiments. Moreover, Ru has shown to be active in methanol production before, but no methanol was found in these experiments. However, in the literature often RuO_2 is used instead of metallic Ru and lower overpotentials are applied[46].

8.4 Conclusion

Figure 8.6 summarizes the trends and observations of this study, showing the selectivity of all the metals studied at ambient conditions, at elevated pressure and for the combination of elevated pressure and temperature. Section G.9 contains the details how this figure was constructed. The top periodic table shows the selectivity towards CO2RR compared to HER. Increasing the CO_2 pressure can significantly improve CO2RR and intermediate CO2RR catalysts at ambient conditions can

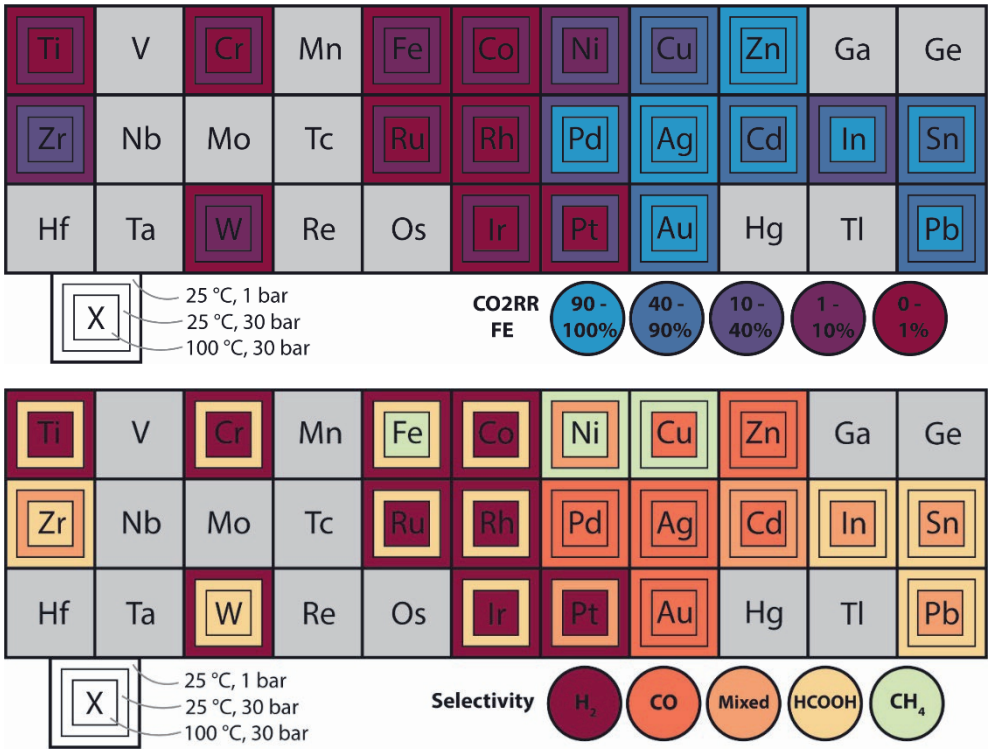

Figure 8.6 Periodic table to summarize the trends with pressure and temperature at a big variety of metal catalysts for electrochemical CO_2 reduction at -1.5 V vs SHE in 0.1 M $KHCO_3$. The upper Periodic table shows the selectivity towards CO2RR in competition with HER. The lower Periodic table shows the selectivity of the CO2RR products, unless so little is produced which leads to a red color for HER. Per metal, the outer box gives shows the results at ambient conditions, the middle box at high pressure and the inner box at high pressure and temperature.

become very good as HER is significantly suppressed by increasing pressure. The CO producing metals can reach very high FE with increasing pressure, even at 100 °C, while for the HCOOH producing catalysts, this high efficiency is reached at high pressures but at different temperatures depending on the catalyst. The left side of the periodic table stays more red and only at elevated pressures Faradaic efficiencies for CO2RR above 1% can be reached, although hardly ever exceeding 10%. The bottom periodic table shows the product distribution of the CO_2 reduction reaction. It can be seen that the CO producing metals always keep producing CO, while Cu and the HCOOH producing metals produce relatively more CO at elevated temperatures. The poor CO2RR catalysts produce mainly HCOOH as CO2RR product at high pressures and low temperatures. Cu is not the only metal able to produce hydrocarbons, as also Ni and Fe can produce them in significant amounts under the high pressures and temperatures.

This study has screened various metals as electrocatalysts for CO_2 reduction and specifically looked at the effect of temperature and pressure. Potential and electrolyte were kept constant during all experiments, because otherwise the parameter space would be too large. However, these parameters can have significant influence on catalyst performance [26,34,47–50]. Therefore, this screening study gives first insights, but further in-depth studies are needed in which the effect of potential and electrolyte are studied on selected catalysts. Moreover, we only studied six temperature-and-pressure combinations. Medium pressures of 10-20 bar and medium temperatures of 50-75 °C may still yield deviating results. This study therefore gives guidance in deciding future experiments. The most interesting catalysts to study for CO2RR appear to be the known catalysts as Cu, Ag and Zn, but also Pd, Ni, Fe, Zr and Pt, especially at elevated pressures and temperatures. Beyond the pure metal catalysts, these metals could also be studied as carbides, nitrides and phosphides for example [9,27,51,52]. Moreover, combining these metals in metal alloys could lead to new results and improve activity or selectivity beyond the performance of a single metal [53–58].

References

1. Mertens, J. *et al.* Carbon capture and utilization: More than hiding CO_2 for some time. *Joule* vol. 7 442–449 Preprint at https://doi.org/10.1016/j.joule.2023.01.005 (2023).
2. De Luna, P. *et al.* What would it take for renewably powered electrosynthesis to displace petrochemical processes? *Science (1979)* **364**, eaav3506 (2019).
3. Alerte, T. *et al.* Scale-Dependent Techno-Economic Analysis of CO2 Capture and Electroreduction to Ethylene. *ACS Sustain Chem Eng* **11**, 15651–15662 (2023).
4. Roh, K. *et al.* Early-stage evaluation of emerging CO_2 utilization technologies at low technology readiness levels. *Green Chemistry* **22**, 3842–3859 (2020).
5. Hori, Y., Wakebe, H., Tsukamoto, T. & Koga, O. Electrocatalytic process of CO selectivity in electrochemical reduction of CO_2 at metal electrodes in aqueous media. *Electrochim Acta* **39**, 1833–1839 (1994).
6. Bagger, A., Ju, W., Varela, A. S., Strasser, P. & Rossmeisl, J. Electrochemical CO_2 Reduction: A Classification Problem. *ChemPhysChem* **18**, 3266–3273 (2017).
7. Vos, R. E. & Koper, M. T. M. The Effect of Temperature on the Cation-Promoted Electrochemical CO_2 Reduction on Gold. *ChemElectroChem* **9**, e20220023 (2022).
8. Vos, R. E. *et al.* How Temperature Affects the Selectivity of the Electrochemical CO_2 Reduction on Copper. *ACS Catal* **13**, 8080–8091 (2023).
9. Vos, R. E. & Koper, M. T. M. Nickel as Electrocatalyst for $CO_{(2)}$ Reduction: Effect of Temperature, Potential, Partial Pressure, and Electrolyte Composition. *ACS Catal* 4432–4440 (2024) doi:10.1021/acscatal.4c00009.
10. Dufek, E. J., Lister, T. E., Stone, S. G. & McIlwain, M. E. Operation of a Pressurized System for Continuous Reduction of CO 2. *J Electrochem Soc* **159**, F514–F517 (2012).
11. Löwe, A. *et al.* Influence of Temperature on the Performance of Gas Diffusion Electrodes in the CO_2 Reduction Reaction. *ChemElectroChem* **6**, 4497–4506 (2019).
12. Hara, K., Kudo, A. & Sakata, T. *Electrochemical Reduction of Carbon Dioxide under High Pressure on Various Electrodes in an Aqueous Electrolyte*. *Journal of Electroanalytical Chemistry* vol. 391 (1995).
13. Ramdin, M. *et al.* High Pressure Electrochemical Reduction of CO2 to Formic Acid/Formate: A Comparison between Bipolar Membranes and Cation Exchange Membranes. *Ind Eng Chem Res* **58**, 1834–1847 (2019).
14. Gabardo, C. M. *et al.* Combined high alkalinity and pressurization enable efficient CO2 electroreduction to CO. *Energy Environ Sci* **11**, 2531–2539 (2018).
15. Kudo, A., Nakagawa, S., Tsuneta, A. & Sakata, T. Electrochemical Reduction of High Pressure CO_2 on Ni Electrodes. *J. Electrochem. Soc* **140**, 1541–1545 (1993).
16. Raaijman, S. J., Schellekens, M. P., Corbett, P. J. & Koper, M. T. M. High-Pressure CO Electroreduction at Silver Produces Ethanol and Propanol. *Angewandte Chemie - International Edition* **60**, 21732–21736 (2021).
17. Girichandran, N., Saedy, S. & Kortlever, R. Electrochemical CO_2 reduction on a copper foam electrode at elevated pressures. *Chemical Engineering Journal* **487**, (2024).

18. da Silva, A. H. M., Vos, R. E., Schrama, R. J. C. & Koper, M. T. M. Design of a Rotating Disk Electrode setup operating under high pressure and temperature: Application to CO_2 reduction on gold. *Electrochim Acta* **498**, 144612 (2024).
19. Wuttig, A. & Surendranath, Y. Impurity Ion Complexation Enhances Carbon Dioxide Reduction Catalysis. *ACS Catal* **5**, 4479–4484 (2015).
20. Wang, J. *et al.* Poly(aryl piperidinium) membranes and ionomers for hydroxide exchange membrane fuel cells. *Nat Energy* **4**, 392–398 (2019).
21. Achrai, B. *et al.* A Direct Ammonia Fuel Cell with a KOH-Free Anode Feed Generating 180 mW cm −2 at 120 °C . *J Electrochem Soc* **167**, 134518 (2020).
22. Heenan, A. R., Hamonnet, J. & Marshall, A. T. Why Careful iR Compensation and Reporting of Electrode Potentials Are Critical for the CO_2 Reduction Reaction. *ACS Energy Lett* **7**, 2357–2361 (2022).
23. Öijerholm, J., Forsberg, S., Hermansson, H.-P. & Ullberg, M. Relation Between the SHE and the Internal Ag⁄AgCl Reference Electrode at High Temperatures. *J Electrochem Soc* **156**, P56 (2009).
24. Bogaerts, W. F. & Haute, A. A. Van. Determination of Activity Coefficients for KCl at Elevated Temperatures. *J. Electrochem. Soc.* **131**, 68–72 (1984).
25. Dash, D., Kumar, S., Mallika, C. & Mudali, U. K. New Data on Activity Coefficients of Potassium, Nitrate, and Chloride Ions in Aqueous Solutions of KNO_3 and KCl by Ion Selective Electrodes. *ISRN Chemical Engineering* **2012**, 1–5 (2012).
26. Todoroki, M., Hara, K., Kudo, A. & Sakata, T. *Electrochemical Reduction of High Pressure CO 2 at Pb, Hg and In Electrodes in an Aqueous KHCO 3 Solution*. *Journal of Electroanalytical Chemistry* vol. 394 (1995).
27. Zhou, Y. *et al.* Long-chain hydrocarbons by CO_2 electroreduction using polarized nickel catalysts. *Nat Catal* **5**, 545–554 (2022).
28. Kuhl, K. P. *et al.* Electrocatalytic Conversion of Carbon Dioxide to Methane and Methanol on Transition Metal Surfaces. *J Am Chem Soc* **136**, 14107–14113 (2014).
29. Mizuno, T. *et al.* Effect of temperature on electrochemical reduction of high-pressure CO_2 with In, Sn, and Pb electrodes. *Energy Sources* **17**, 503–508 (1995).
30. Feaster, J. T. *et al.* Understanding Selectivity for the Electrochemical Reduction of Carbon Dioxide to Formic Acid and Carbon Monoxide on Metal Electrodes. *ACS Catal* **7**, 4822–4827 (2017).
31. Pander, J. E., Baruch, M. F. & Bocarsly, A. B. Probing the Mechanism of Aqueous CO2 Reduction on Post-Transition-Metal Electrodes using ATR-IR Spectroelectrochemistry. *ACS Catal* **6**, 7824–7833 (2016).
32. Pander, J. E., Lum, J. W. J. & Yeo, B. S. The importance of morphology on the activity of lead cathodes for the reduction of carbon dioxide to formate. *J Mater Chem A Mater* **7**, 4093–4101 (2019).
33. Bitar, Z., Fecant, A., Trela-Baudot, E., Chardon-Noblat, S. & Pasquier, D. Electrocatalytic reduction of carbon dioxide on indium coated gas diffusion electrodes-Comparison with indium foil. *Appl Catal B* **189**, 172–180 (2016).

34. Hegner, R., Rosa, L. F. M. & Harnisch, F. Electrochemical CO2 reduction to formate at indium electrodes with high efficiency and selectivity in pH neutral electrolytes. *Appl Catal B* **238**, 546–556 (2018).
35. He, Z. *et al.* Electrochemically created roughened lead plate for electrochemical reduction of aqueous CO2. *Catal Commun* **72**, 38–42 (2015).
36. Christensen, O., Bagger, A. & Rossmeisl, J. The Missing Link for Electrochemical CO2 Reduction: Classification of CO vs HCOOH Selectivity via PCA, Reaction Pathways, and Coverage Analysis. *ACS Catal* **14**, 2151–2161 (2024).
37. Ohkawa, K., Hashimoto, K., Fujishima, A., Noguchi, Y. & Nakayama, S. *Electrochemical Reduction of Carbon Dioxide on Hydrogen-Storing Materials Part 1. The Effect of Hydrogen Absorption on the Electrochemical Behavior on Palladium Electrodes*. *J. Electroanal. Chem* vol. 345 (1993).
38. Guo, S. *et al.* Robust palladium hydride catalyst for electrocatalytic formate formation with high CO tolerance. *Appl Catal B* **316**, (2022).
39. Tackett, B. M., Lee, J. H. & Chen, J. G. Electrochemical Conversion of CO2to Syngas with Palladium-Based Electrocatalysts. *Acc Chem Res* **53**, 1535–1544 (2020).
40. Abdellah, A. M. *et al.* Impact of palladium/palladium hydride conversion on electrochemical CO2 reduction via in-situ transmission electron microscopy and diffraction. *Nat Commun* **15**, (2024).
41. Min, X. & Kanan, M. W. Pd-Catalyzed Electrohydrogenation of Carbon Dioxide to Formate: High Mass Activity at Low Overpotential and Identification of the Deactivation Pathway. *J Am Chem Soc* **137**, 4701–4708 (2015).
42. Jahangiri, H., Bennett, J., Mahjoubi, P., Wilson, K. & Gu, S. A review of advanced catalyst development for Fischer-Tropsch synthesis of hydrocarbons from biomass derived syn-gas. *Catalysis Science and Technology* vol. 4 2210–2229 Preprint at https://doi.org/10.1039/c4cy00327f (2014).
43. Martinelli, M., Gnanamani, M. K., LeViness, S., Jacobs, G. & Shafer, W. D. An overview of Fischer-Tropsch Synthesis: XtL processes, catalysts and reactors. *Applied Catalysis A: General* vol. 608 Preprint at https://doi.org/10.1016/j.apcata.2020.117740 (2020).
44. Arsalanfar, M., Mirzaei, A. A., Bozorgzadeh, H. R. & Samimi, A. A review of fischer-tropsch synthesis on the cobalt based catalysts. *Physical Chemistry Research* vol. 2 179–201 Preprint at https://doi.org/10.22036/pcr.2014.5786 (2014).
45. Albo, J., Alvarez-Guerra, M., Castaño, P. & Irabien, A. Towards the electrochemical conversion of carbon dioxide into methanol. *Green Chemistry* **17**, 2304–2324 (2015).
46. Popic, J. P., Avramov, M. L. & Vukovic, N. B. Reduction of carbon dioxide on ruthenium oxide and modified ruthenium oxide electrodes in 0.5 M NaHCO 3. *Journal of Electroanalyticai Chemistry* **421**, 105–110 (1997).
47. Ummireddi, A. K., Sharma, S. K. & Pala, R. G. S. Influence of tetraethylammonium cation on electrochemical CO2 reduction over Cu, Ag, Ni, and Fe surfaces. *J Catal* **406**, 213–221 (2022).
48. Pan, H., Wang, F., Zhang, Z. & Min, S. Interfacial modification of Zn foil electrode with cationic surfactants enables efficient and selective CO production from CO2 electroreduction. *Sustain Energy Fuels* **6**, 2149–2154 (2022).

49. Hatsukade, T., Kuhl, K. P., Cave, E. R., Abram, D. N. & Jaramillo, T. F. Insights into the electrocatalytic reduction of CO_2 on metallic silver surfaces. *Physical Chemistry Chemical Physics* **16**, 13814–13819 (2014).
50. Hwang, S. Y. *et al.* Electrochemical Fisher-Tropsch chemistry across transition metals: a paradigm shift in sustainable liquid fuel production. *Nano Energy* 109881 (2024) doi:10.1016/j.nanoen.2024.109881.
51. Yin, Z. *et al.* Cu3n nanocubes for selective electrochemical reduction of co2 to ethylene. *Nano Lett* 8658–8663 (2019) doi:10.1021/acs.nanolett.9b03324.
52. Handoko, A. D. *et al.* Two-Dimensional Titanium and Molybdenum Carbide MXenes as Electrocatalysts for CO2 Reduction. *iScience* **23**, (2020).
53. Jia, Y., Li, F., Fan, K. & Sun, L. Cu-based bimetallic electrocatalysts for CO2 reduction. *Advanced Powder Materials* vol. 1 Preprint at https://doi.org/10.1016/j.apmate.2021.10.003 (2022).
54. He, J., Johnson, N. J. J., Huang, A. & Berlinguette, C. P. Electrocatalytic Alloys for CO2 Reduction. *ChemSusChem* vol. 11 48–57 Preprint at https://doi.org/10.1002/cssc.201701825 (2018).
55. Mahyoub, S. A. *et al.* Rational design of low loading Pd-alloyed Ag nanocorals for high current density CO2-to-CO electroreduction at elevated pressure. *Mater Today Energy* **24**, (2022).
56. Cai, C. *et al.* Heteroatoms Induce Localization of the Electric Field and Promote a Wide Potential-Window Selectivity Towards CO in the CO2 Electroreduction. *Angewandte Chemie - International Edition* **61**, (2022).
57. Xu, X. *et al.* Pd-Decorated Cu2O-Ag Catalyst Promoting CO2 Electroreduction to C2H4 by Optimizing CO Intermediate Adsorption and Hydrogenation. *ACS Appl Mater Interfaces* **16**, 16243–16252 (2024).
58. Vos, R. E., Smaak, J. P. & Koper, M. T. M. The temperature dependence of electrochemical CO_2 reduction on Ag and CuAg alloys. *J Catal* **436**, (2024).

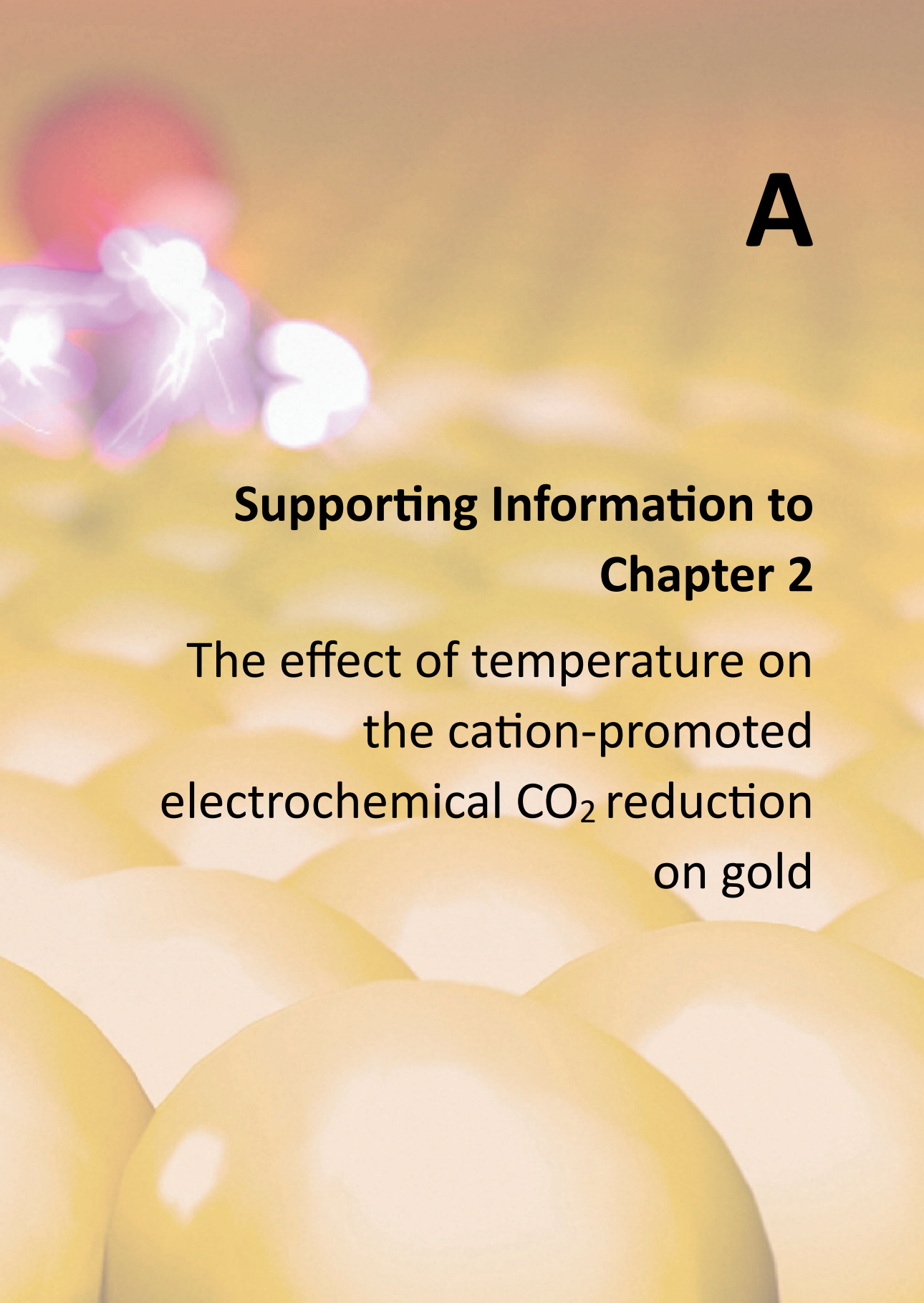

A

Supporting Information to Chapter 2

The effect of temperature on the cation-promoted electrochemical CO_2 reduction on gold

A.1 Standard equilibrium potential

The standard equilibrium potential of CO_2 reduction towards CO has a temperature dependence itself. Using equations A.1a and A.1b, and the thermodynamic data tabulated in Table A.1, we can calculate the equilibrium potential at different temperatures. Table A.2 shows that the equilibrium potential shifts towards more negative potentials with increasing temperature, although the shift is relatively small.

$$\Delta G = -nFE \qquad (A.1a)$$

$$\Delta G = \Delta H - T\Delta S \qquad (A.1b)$$

$$CO_2 + 2\,e^- + 2H^+ \rightarrow CO + H_2O \qquad (A.2a)$$

$$H_2 \rightarrow 2\,e^- + 2H^+ \qquad (A.2b)$$

Table A.1 The tabulated enthalpies and entropies for species involved in the CO2 reduction towards CO

	ΔH (kJ/mol)	ΔS (J/mol)
CO2	-393.509	213.74
CO	-110.525	197.674
H2O	-285.8	69.9
H2	0	130.7

Assuming the entropy and enthalpy are constants in this temperature range, the standard equilibrium potentials can be obtained at different temperatures as seen in Table A.2.

Table A.2 Equilibrium potential versus RHE of CO2RR towards CO with temperature

T (°C)	$E^0(V)$
25	-0.104
30	-0.106
35	-0.108
40	-0.110
45	-0.112
50	-0.114
55	-0.116
60	-0.118
65	-0.120

A.2 Exchange current density determination

Figure A.1 is an example of a Tafel plot used to determine the exchange current density by extrapolation.

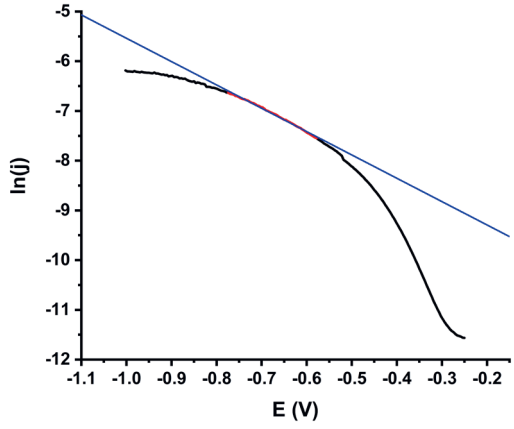

Figure A.1 Determination of the exchange current density using an extrapolation in the Tafel plot of the partial current density for CO formation

A.3 Plateau in activity of CO formation

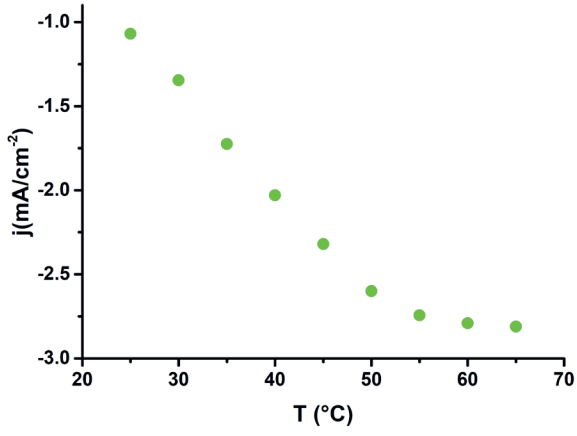

Figure A.2 The partial current density of CO2RR towards CO formation at -0.7V vs RHE plotted against temperature in 0.1M $NaHCO_3$ to illustrate the plateau in the activity starting around 55 ^{0}C.

A.4 SHE scale

When pH dependent studies have been performed on CO2RR, it has been argued before that the partial current densities of CO should be plotted on an SHE scale as this reaction is pH independent [1,2]. Because in our experiments the RHE and the SHE scale are not exactly similar, we have plotted our data on a SHE scale as well (Figure A.3). This shows that there is no qualitative difference between the SHE and RHE scale in the temperature range used in this study. Moreover, for the quantitative data obtained in the kinetic analysis later in this study, the differences are minor. So, we decided to show our data on a RHE scale in this study as this was the reference scale used to measure and requires no further operations.

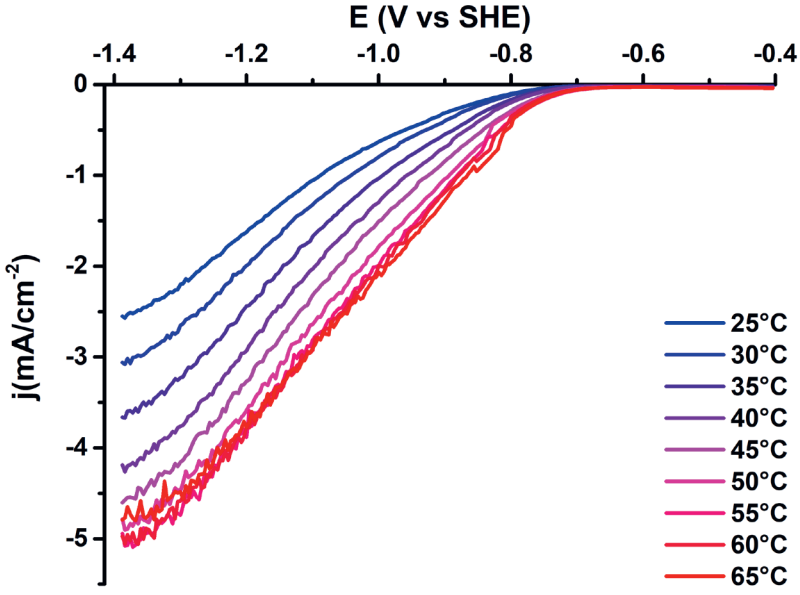

Figure A.3 The partial current density for CO formation in 0.1M $NaHCO_3$ on a gold RRDE at 2500 rpm and 20 mV/s at different temperatures plotted on a SHE scale

A.5 Temperature dependent variables

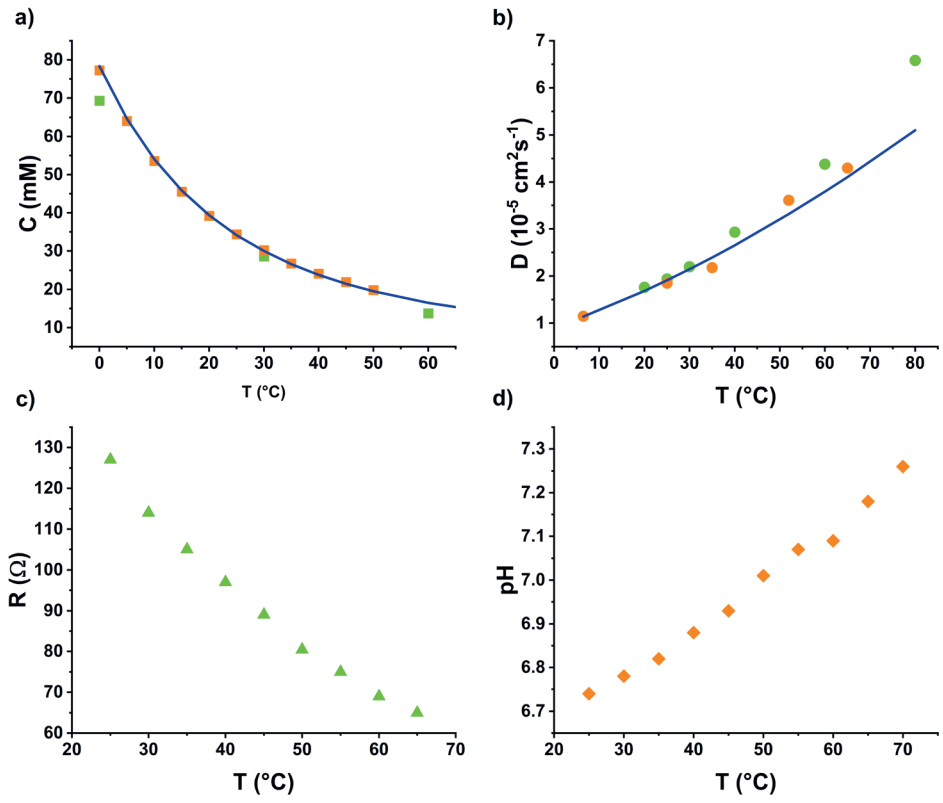

Figure A.4 Different parameters which change with temperature, (some values originate from literature); a) the CO_2 concentration in water (orange[3], green[4], blue[5]), b) the diffusion coefficient of CO_2 in water (orange[6], green[7], blue[8]), c) the resistance of 0.1M $NaHCO_3$, d) the pH of 0.1M CO2 saturated $NaHCO_3$

A.6 Partial pressure experiments

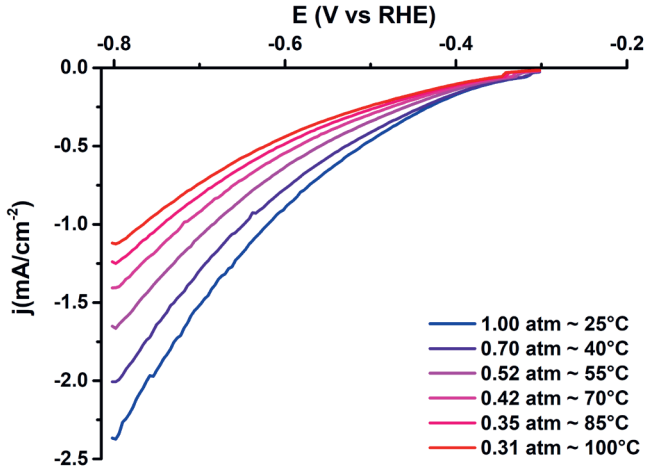

Figure A.5 The partial current density for CO formation at different partial pressures of CO_2 (and the equivalent temperature with 1 atm of CO_2) on a gold RRDE at 2500 rpm and 20 mV/s in 0.1 M $NaHCO_3$.

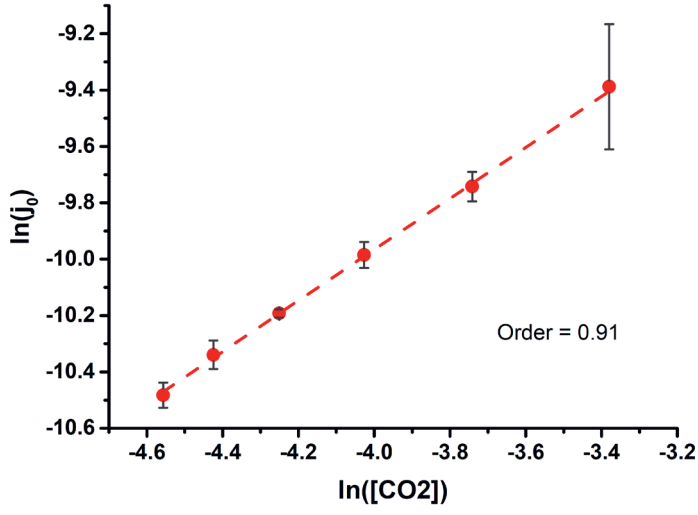

Figure A.6 The ln of the exchange current density at different concentrations of CO_2 to determine the reaction order of CO_2

A.7 Limiting current densities and Koutecky Levich plot

Levich equation

$$j_L = 0.201nFD^{\frac{2}{3}}\omega^{\frac{1}{2}}\upsilon^{-\frac{1}{6}}C = B_L\omega^{\frac{1}{2}} \qquad (A.3)$$

Koutecky-Levich equation

$$\frac{1}{j_m} = \frac{1}{j_K} + \frac{1}{j_{MT}} = \frac{1}{j_K} + \frac{1}{B_L\omega^{0.5}} \qquad (A.4)$$

where j_L is the Levich current, n moles of electrons transferred, D is the diffusion coefficient, ω the angular rotation rate in rpm, υ the kinematic viscosity, C the concentration of the CO_2, B_L the Levich constant, j_m the measured partial current density j_K the kinetic current density and j_{MT} the mass transport current density

Table A.3 The limiting current densities at different temperatures and 2500 rpm calculated using the Levich equation [5,8]

J (mA/cm²)	T (K)	D (cm²/s)	v (cm²/s)	C (mmol/ml)
103.98	298.12	1.92E-05	8.90E-03	0.034
100.41	303.15	2.16E-05	8.00E-03	0.030
97.34	308.15	2.40E-05	7.24E-03	0.027
94.68	313.15	2.66E-05	6.60E-03	0.024
92.49	318.15	2.93E-05	6.03E-03	0.021
90.77	323.15	3.21E-05	5.50E-03	0.019
89.19	328.15	3.50E-05	5.11E-03	0.018
88.13	333.15	3.80E-05	4.70E-03	0.016
87.12	338.15	4.11E-05	4.41E-03	0.015

Table A.4 Kinetic current density and Levich constant from data of Figure A.4

T (K)	j_K (mA)	1/B ((s*rpm)$^{0.5}$/C)
298	1.9	3317
313	4.9	4354
328	10.6	5677

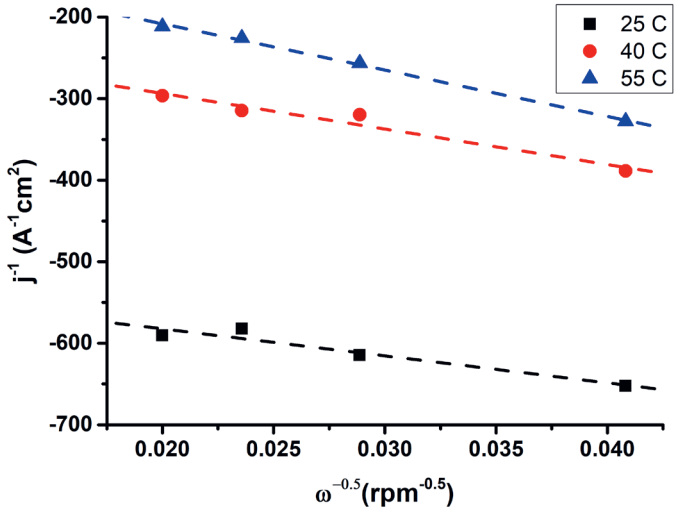

Figure A.7 Koutecky-Levich plot of CO2RR towards CO at -0.8V vs RHE

A.8 Hydrogen evolution reaction with increasing temperature

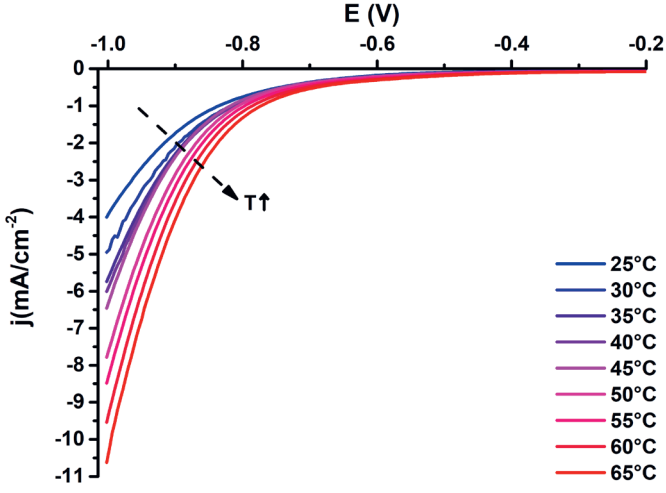

Figure A.8 The current density of HER in 0.1M Ar saturated $NaHCO_3$ on a gold RRDE at 2500 rpm and 20 mV/s

A.9 Qualitative effect of temperature on CO formation rates

Table A.5 The ratios between the partial current densities towards CO at different temperatures compared to the partial current density at 25 ^{0}C

	30 °C	35 °C	40 °C	45 °C	50 °C	55 °C	60 °C	65 °C
-0.4 V	1.18	1.71	1.97	3.36	3.44	3.89	3.16	3.34
-0.5 V	1.33	1.80	2.15	2.72	3.35	3.46	3.55	3.65
-0.6 V	1.24	1.64	1.99	2.35	2.77	2.92	3.11	3.06
-0.7 V	1.29	1.70	1.96	2.26	2.56	2.63	2.66	2.71
-0.8 V	1.26	1.56	1.82	2.06	2.22	2.32	2.24	2.26
-0.9 V	1.23	1.49	1.69	1.88	1.96	1.97	2.01	1.95
-1.0 V	1.23	1.48	1.65	1.81	1.86	1.95	1.95	1.82

A.10 Apparent activation energies

The Arrhenius equation can be used to determine the apparent activation energy.

$$k = Ae^{\frac{-E_a}{RT}} \qquad (A.5)$$

where k is the reaction rate constant, A is the pre-exponential factor, E_a is the activation energy, R is the gas constant and T the absolute temperature. Since the exchange current density depends on the reaction rate constant, the j_0 will also follow an Arrhenius relation. We can substitute equation A.6 in equation A.5 to get equation A.7a. This equation can be rewritten to equation A.7b to obtain the apparent activation energy.

$$j_0 = nFk^0C \qquad (A.6)$$

$$j_0 = nFCAe^{\frac{-E_a}{RT}} = A'e^{\frac{-E_a}{RT}} \qquad (A.7a)$$

$$\ln(j_0) = \ln(A') - \frac{E_a}{R} * \frac{1}{T} \qquad (A.7b)$$

where j_0 is the exchange current density, F the Faraday constant, k the reaction rate constant, n the number of electrons transferred, and C the concentration of CO_2. However, we need to correct for the temperature dependence of the CO_2 concentration:

$$j_0' = j_0 \frac{C_{25°C}}{C_T} \qquad (A.8)$$

where C_{25C} is the concentration of CO_2 at 25 ^{0}C and C_T the concentration of CO_2 at the temperature of the experiment. Instead of equation A.6, equation A.8 can now be substituted in equation A.5 to get equation A.9a. This equation can be rewritten to equation A.9b. Substituting equation A.8 back in equation A.9b and equation A.9c is obtained.

$$j_0' = A' e^{\frac{-E_a}{RT}} \qquad (A.9a)$$

$$\ln(j_0') = \ln(A') - \frac{E_a}{R} * \frac{1}{T} \qquad (A.9b)$$

$$\ln(j_0) + \ln\left(\frac{C_{25℃}}{C_T}\right) = \ln(A') - \frac{E_a}{R} * \frac{1}{T} \qquad (A.9c)$$

So, to correct for the changing concentration of CO_2 with temperature, we use the correction factor $\ln\left(\frac{C_{25℃}}{C_T}\right)$.

The standard equilibrium potential changes with temperature as can be seen in Table A.2. This change has been taken into account in the Arrhenius plot of Figure 2.5. For each temperature, the exchange current density has been calculated at the corresponding standard equilibrium potential according to Table A.2.

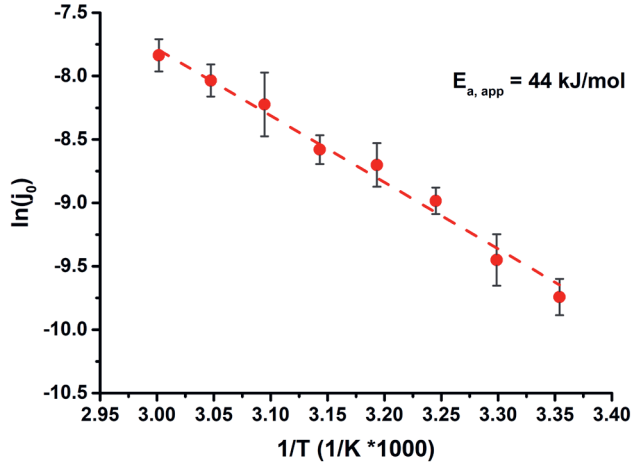

Figure A.9 Arrhenius plot of CO_2 reduction in 0.1M $NaHCO_3$ in the temperature range of 25-60 ^{0}C, not corrected for the changes in CO_2 concentration with temperature

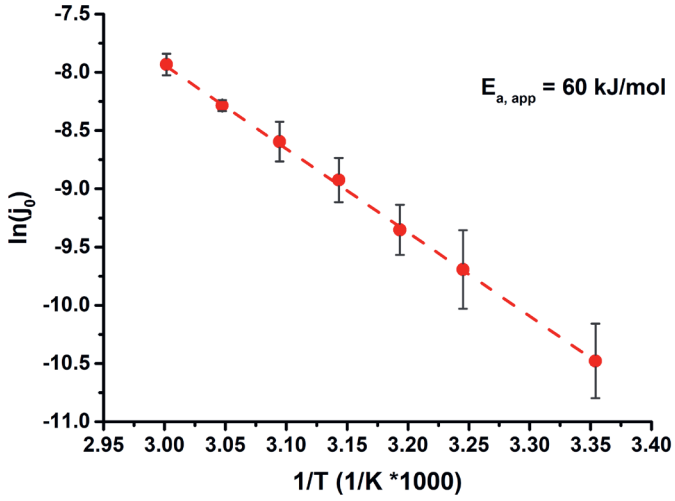

Figure A.10 Arrhenius plot of CO2RR towards CO formation in 0.1M $NaHCO_3$ using data from Figure 2.2, so at constant CO_2 concentration

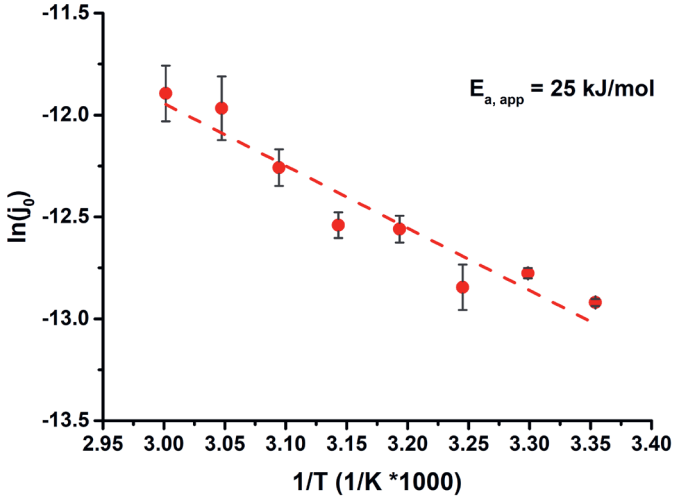

Figure A.11 Arrhenius plot of HER in Ar saturated 0.1M $NaHCO_3$

A.11 Transfer coefficient

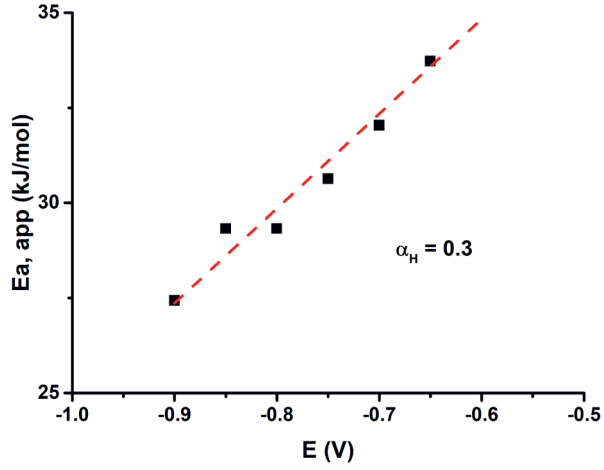

Figure A.12 The apparent activation energy of CO2 reduction towards CO formation in 0.5M NaHCO3 plotted against the applied potential

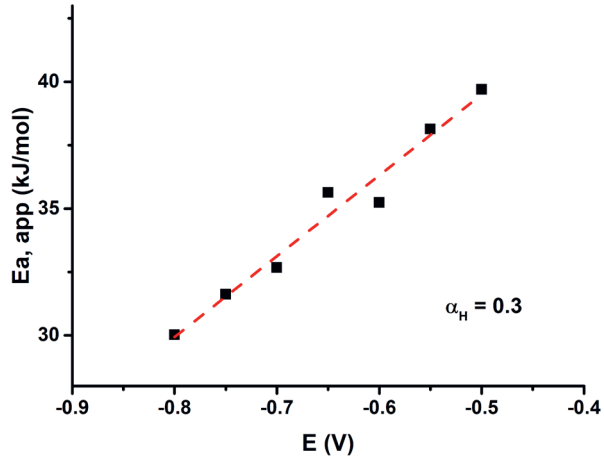

Figure A.12 The apparent activation energy of CO2 reduction towards CO formation in 0.1M CsHCO3 plotted against the applied potential

The entropic contribution to the transfer coefficient can be determined from the slope of the ln of the pre-exponential factors with potential [9].

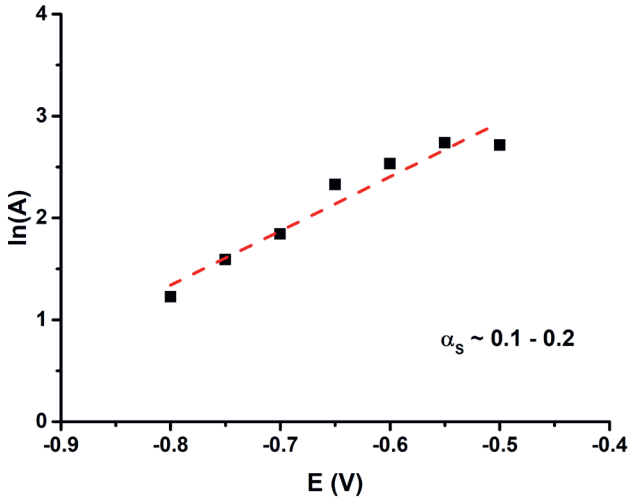

Figure A.14 The ln of the pre-exponential factor plotted against the applied potential for CO_2 reduction towards CO in 0.1M $NaHCO_3$

A.12 Cation volume occupation

Assuming 1.5M of K^+ at the surface [10], and an effective interfacial cation radius of 4.5 for K^+ [11], the volume these cations occupy is percent:

$$\left(1.5 * 6.022E23 * \frac{4}{3}\ \pi\ (6E-10)^3\ \right) / 10^{-3}\ * 100\% \ = 34\%$$

References

1. Resasco, J., Lum, Y., Clark, E., Zeledon, J. Z. & Bell, A. T. *ChemElectroChem* **5**, 1064–1072 (2018).
2. Ringe, S. *et al. Nature Communications* **11**, (2020).
3. Harned, H. S. & Davis Jr, R. *Journal of the American Chemical Society* **65**, 2030–2037 (1943).
4. Duan, Z. & Sun, R. *Chemical Geology* **193**, 257–271 (2003).
5. Plummer, L. N. & Busenberg, E. *Geochimica et Cosmochimica Acta* **46**, 1011–1040 (1982).
6. Unver, A. A. & Himmelblau, D. M. *Journal of Chemical and Engineering Data* **9**, 428–431 (1964).
7. Tamimi, A., Rinker, E. B. & Sandall, O. C. *Journal of Chemical and Engineering Data* **39**, 330–332 (1994).
8. Lu, W., Guo, H., Chou, I. M., Burruss, R. C. & Li, L. *Geochimica et Cosmochimica Acta* **115**, 183–204 (2013).
9. Gojković, S. L., Zečević, S. K. & Dražić, D. M. *Journal of Electroanalytical Chemistry* **399**, 127–133 (1995).
10. Weitzner, S. E. *et al. Journal of Physical Chemistry Letters* **11**, 4113–4118 (2020).
11. Ringe, S. *et al. Energy & Environmental Science* 17–25 (2019) doi:10.1039/c9ee01341e.

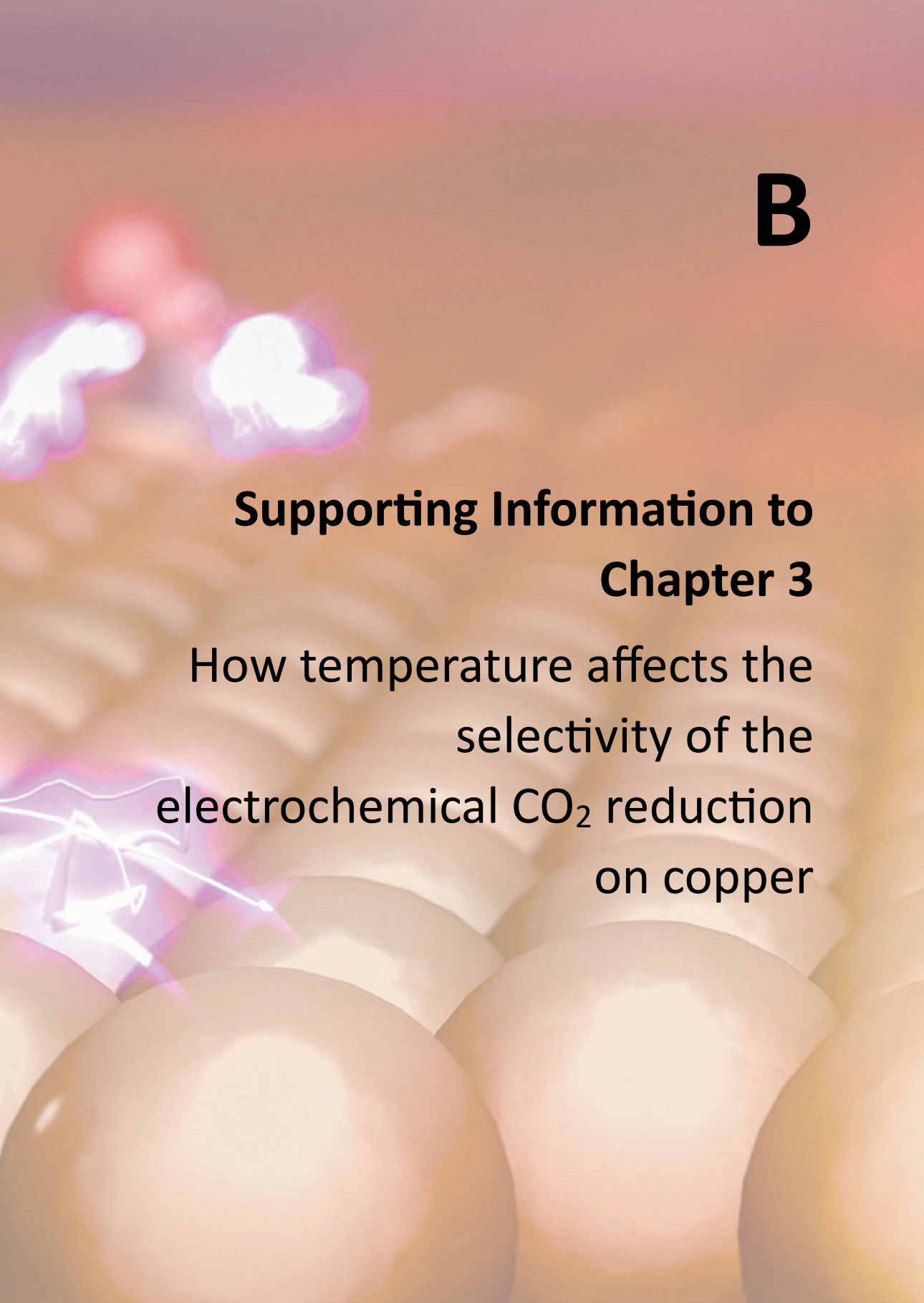

B

Supporting Information to Chapter 3

How temperature affects the selectivity of the electrochemical CO_2 reduction on copper

B.1 Photo and scheme of the H-cell and jacket

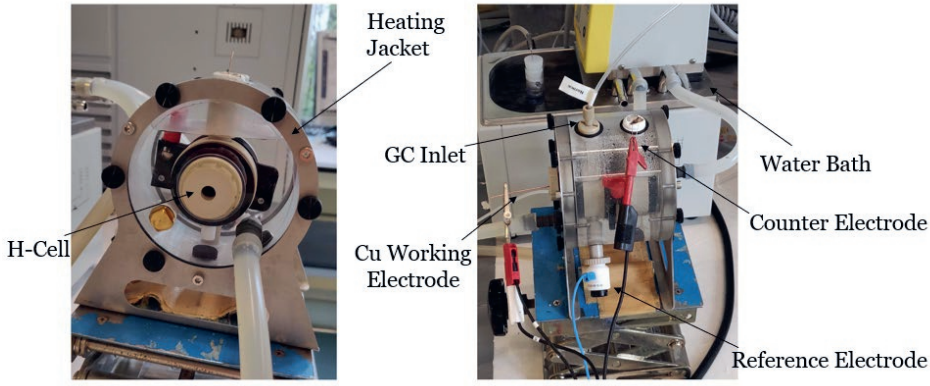

Figure B.1 Photos from the H-cell surrounded by the water jacket used to control the temperature

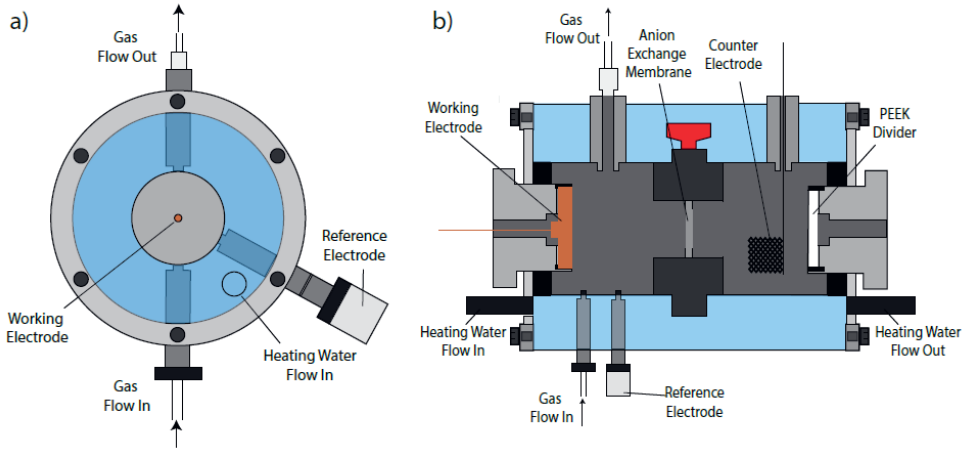

Figure B.2 Schematics of the H-cell surrounded by the water jacket used to control the temperature. a) Frontal-section of the cathodic chamber and (b) cross-section of the electrochemical H-cell with heating jacket

B.2 CO_2 reduction selectivity and activity at -1.1V vs. RHE

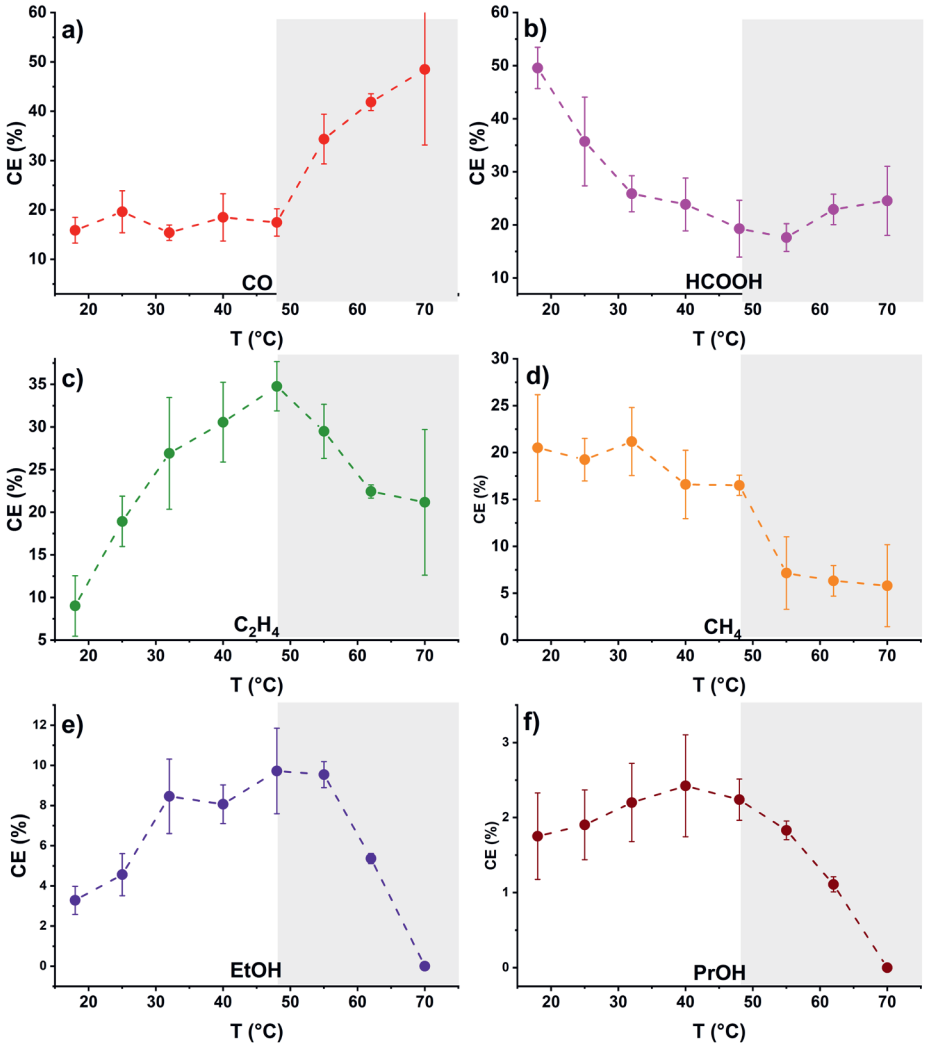

Figure B.3 Carbon Efficiency of CO2RR at different reaction temperatures in 0.1 M KHCO3 at -1.1 V vs. RHE for a) CO b) formic acid c) ethylene d) methane e) ethanol, and f) 1-propanol. The error bars are determined from at least 3 separate experiments. The gray background indicates the second regime and the dotted lines are a guide to the eye.

Table B.1 Faradaic and Carbon efficiency for CO2RR at different temperatures at -1.1V vs. RHE

-1.1 V	FE/CE (%)							
	18 °C	25 °C	32 °C	40 °C	48 °C	55 °C	62 °C	70 °C
H_2	29.4 / -	27 / -	28.7 / -	29.3 / -	41.0 / -	48.7 / -	62.3 / -	84.0 / -
CO	4.7 / 15.9	6.4 / 19.6	5.3 / 15.4	5.9 / 18.5	4.5 / 17.5	7.7 / 34.4	5.9 / 41.9	1.9 / 48.5
CH_4	21.5 / 20.5	17.9 / 19.3	20.1 / 21.2	18.1 / 16.6	13.5 / 16.5	6.6 / 7.2	4.2 / 6.3	1.2 / 5.8
C_2H	5.9 / 9.0	13.5 / 18.9	18.8 / 26.9	21.1 / 30.6	21.9 / 34.8	16.6 / 29.5	9.9 / 22.4	2.2 / 21.2
HCOOH	13.3 / 49.6	11.3 / 35.7	9.9 / 25.9	6.5 / 23.9	4.7 / 19.3	3.5 / 17.6	3.7 / 22.9	1.2 / 24.5
EtOH	2.6 / 3.3	4.1 / 4.6	6.4 / 8.5	7.2 / 8.1	6.9 / 9.7	4.4 / 9.5	2.6 / 5.4	0.6 / 0.1
PrOH	1.4 / 1.8	1.8 / 1.9	1.7 / 2.2	2.1 / 2.4	1.6 / 2.2	0.9 / 1.8	0.5 / 1.1	0.0 / 0.0

B.3 CO_2 reduction selectivity and activity at -0.95V vs. RHE

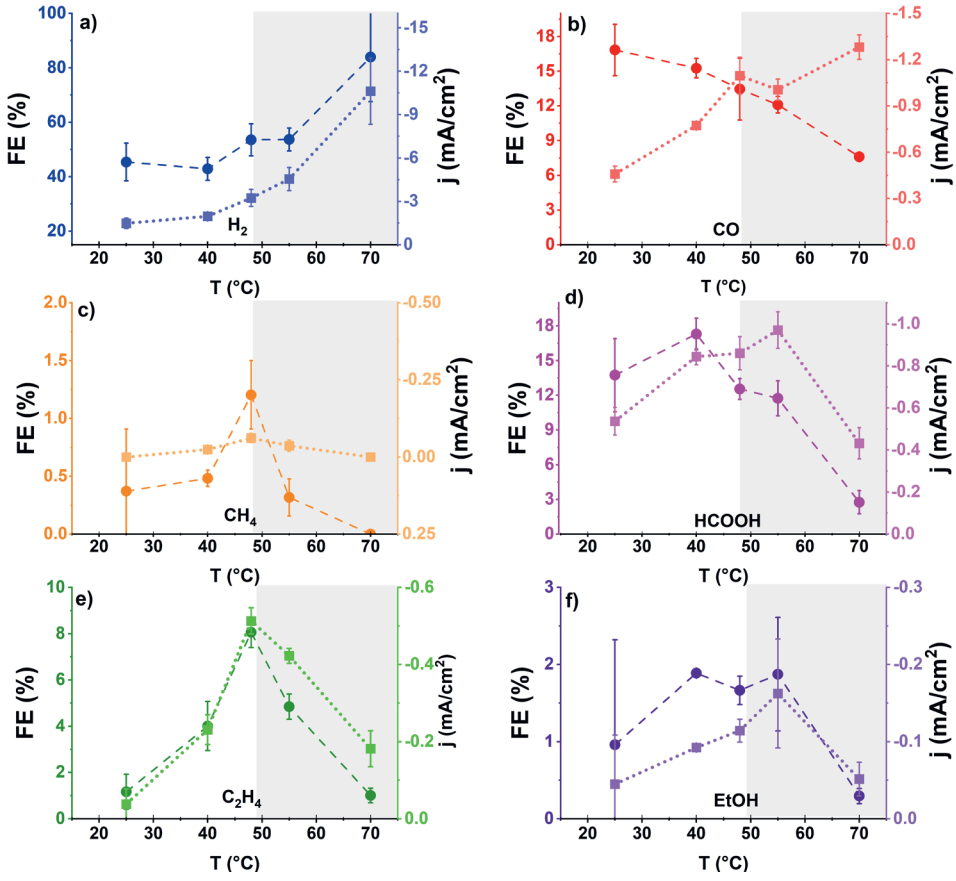

Figure B.4 Faradaic efficiency (in dark circles) and partial current density (in light squares) of CO2RR at different temperatures in 0.1M $KHCO_3$ at -0.95V vs. RHE for a) hydrogen b) CO c) methane d) formic acid e) ethylene f) ethanol g) 1-propanol. Dotted lines are a guide to the eye and error bars are determined from at least 3 measurements.

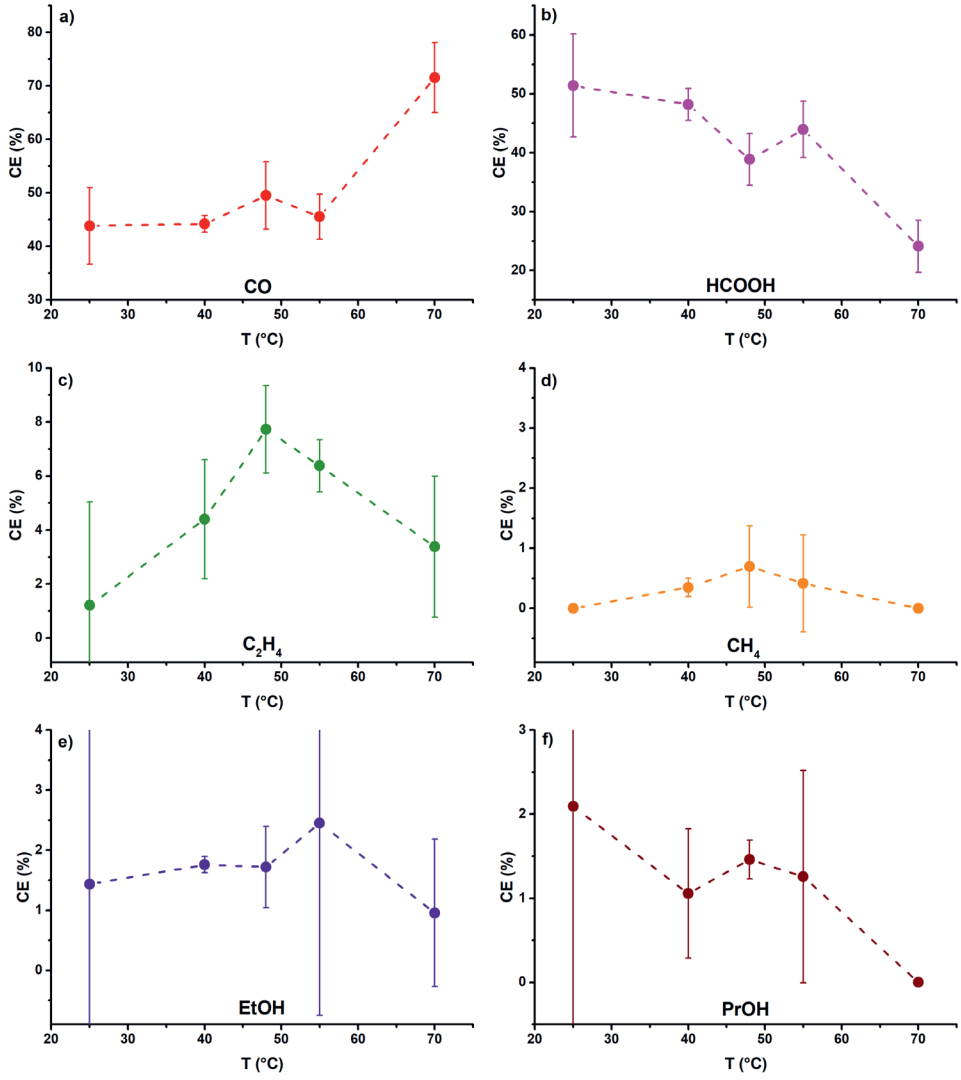

Figure B.5 Carbon efficiency of CO2RR at different temperatures in 0.1 M $KHCO_3$ at -0.95 V vs. RHE for a) formic acid b) CO c) ethylene d) methane e) ethanol f) 1-propanol. Dotted lines are a guide to the eye and error bars are determined from at least 3 measurements.

Table B.2 Faradaic and Carbon efficiency for CO2RR at different temperatures at -0.95V vs. RHE

-0.95 V	FE/CE (%)				
	25 °C	40 °C	48 °C	55 °C	70 °C
H_2	45.4 / -	42.9 / -	53.5 / -	53.7 / -	83.9 / -
CO	16.8 / 43.8	15.3 / 44.2	13.5 / 49.5	12.1 / 45.5	7.6 / 71.6
CH_4	0.4 / 0.1	0.5 / 0.3	1.2 / 0.7	0.3 / 0.4	0.0 / 0.0
C_2H	1.2 / 1.2	4.0 / 4.4	8.1 / 7.7	4.8 / 6.4	1.0 / 3.4
HCOOH	13.7 / 51.4	17.3 / 48.2	12.5 / 38.9	11.7 / 44.0	2.8 / 24.1
EtOH	1.0 / 1.4	1.9 / 1.8	1.7 / 1.7	1.9 / 2.5	0.3 / 1.0
PrOH	1.5 / 2.1	1.1 / 1.1	1.4 / 1.5	1.0 / 1.3	0.0 / 0.0

B.4 CO_2 reduction selectivity and activity at -0.7 V vs. RHE

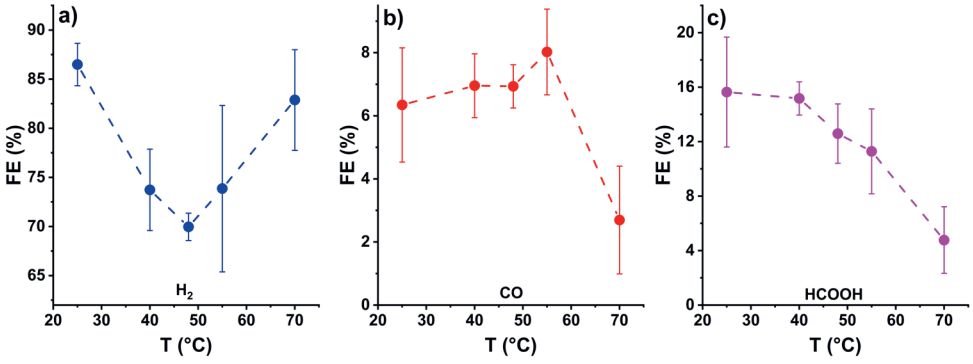

Figure B.6 Faradaic efficiency of CO2RR at different temperatures in 0.1 M $KHCO_3$ at -0.7 V vs. RHE for a) hydrogen b) CO c) formic acid

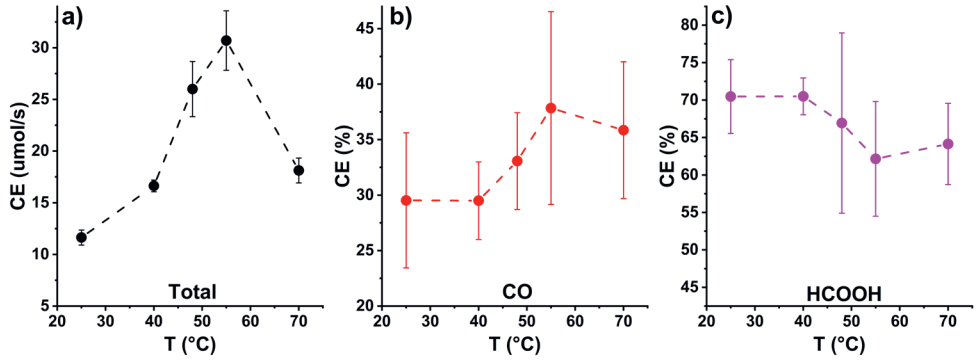

Figure B.7 a) Total consumption of CO_2 of CO2RR at different temperatures in 0.1 M $KHCO_3$ at -0.7 V vs. RHE and the carbon efficiency towards b) CO and c) HCOOH. Dotted lines are a guide to the eye and error bars are determined from at least 3 measurements.

Table B.3 Faradaic and Carbon efficiency for CO2RR at different temperatures at -0.7V vs. RHE

-0.70 V			FE/CE (%)		
	25 °C	40 °C	48 °C	55 °C	70 °C
H_2	86.5 / -	73.7 / -	70.0 / -	73.9 / -	82.9 / -
CO	6.3 / 29.5	7.0 / 29.5	6.9 / 33.1	8.0 / 37.8	2.7 / 35.9
HCOOH	15.6 / 70.5	15.2 / 70.5	12.6 / 66.9	11.3 / 62.2	4.8 / 64.1

B.5 Partial pressure experiments

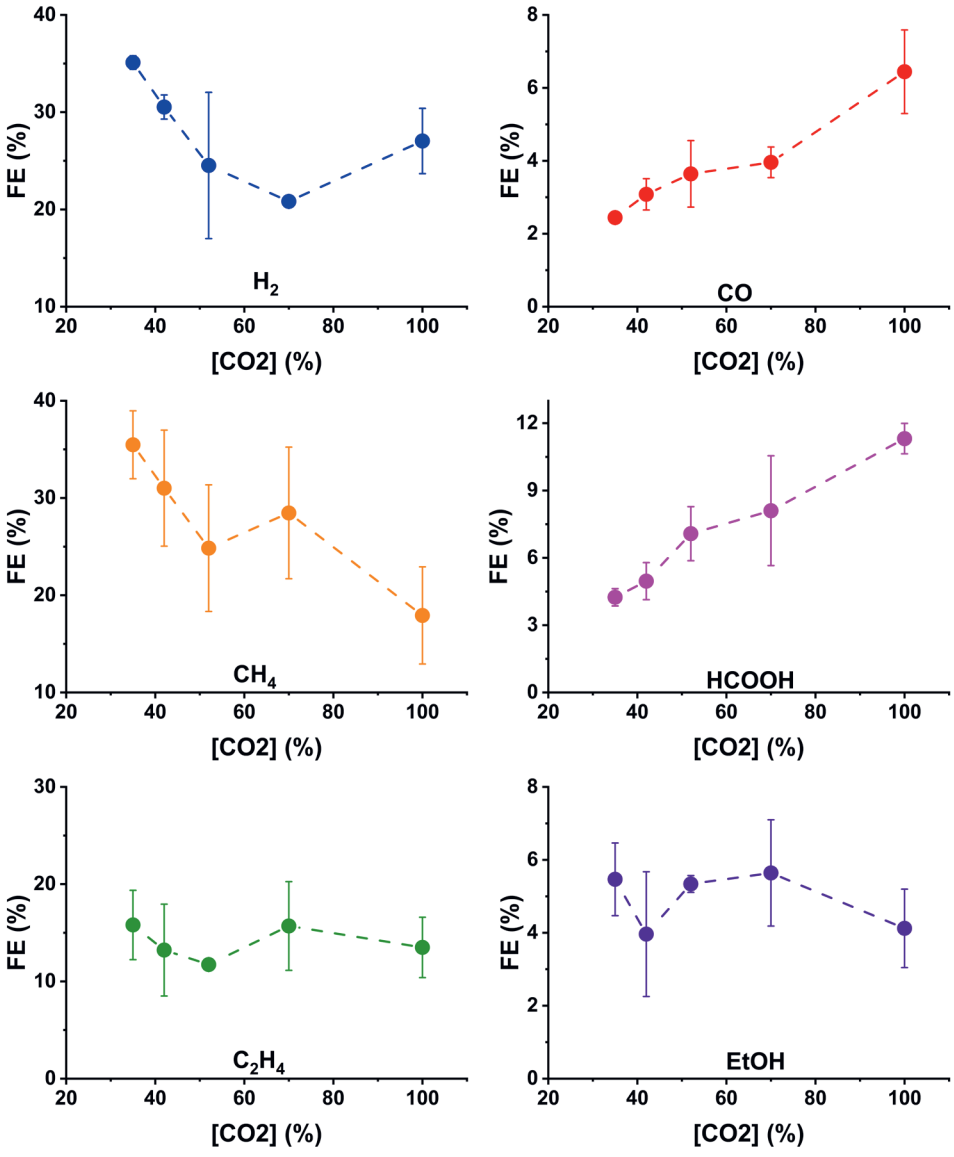

Figure B.8 Faradaic efficiency of CO2RR at different CO_2 bulk concentrations by changing the partial pressure in 0.1 M $KHCO_3$ at -1.1 V vs. RHE for a) hydrogen b) CO c) methane d) formic acid e) ethylene f) ethanol g) 1-propanol. Dotted lines are a guide to the eye and error bars are determined from at least 3 measurements.

Table B.4 Faradaic efficiency of CO2RR at different CO_2 bulk concentrations by changing the partial pressure in 0.1M $KHCO_3$ at -1.1V vs. RHE

Partial pressure	FE (%)				
[CO_2]	100 %	70 %	52 %	42 %	35 %
H_2	27.0	20.8	24.5	30.5	35.1
CO	6.4	4.0	3.6	3.1	2.4
CH_4	17.9	28.5	24.8	31.0	35.5
C_2H	13.5	15.7	11.7	13.2	15.8
HCOOH	11.3	8.1	7.1	5.0	4.2
EtOH	4.1	5.6	5.3	4.0	5.5
PrOH	1.8	1.8	1.2	1.2	1.3

Table B.5 Faradaic efficiency of CO2RR at different temperatures with constant CO_2 bulk concentrations by changing the partial pressure in 0.1M $KHCO_3$ at -1.1 V vs. RHE

[CO_2] constant	FE (%)			
	25 °C	40 °C	55 °C	70 °C
H_2	26.3	35.7	55.5	86.5
CO	3.3	4.9	5.5	1.8
CH_4	32.5	13.7	4.5	0.7
C_2H	13.7	17.0	16.6	1.7
HCOOH	6.5	5.8	5.0	1.3
EtOH	3.8	7.9	5.9	0.4
PrOH	1.2	1.7	1.4	0.0

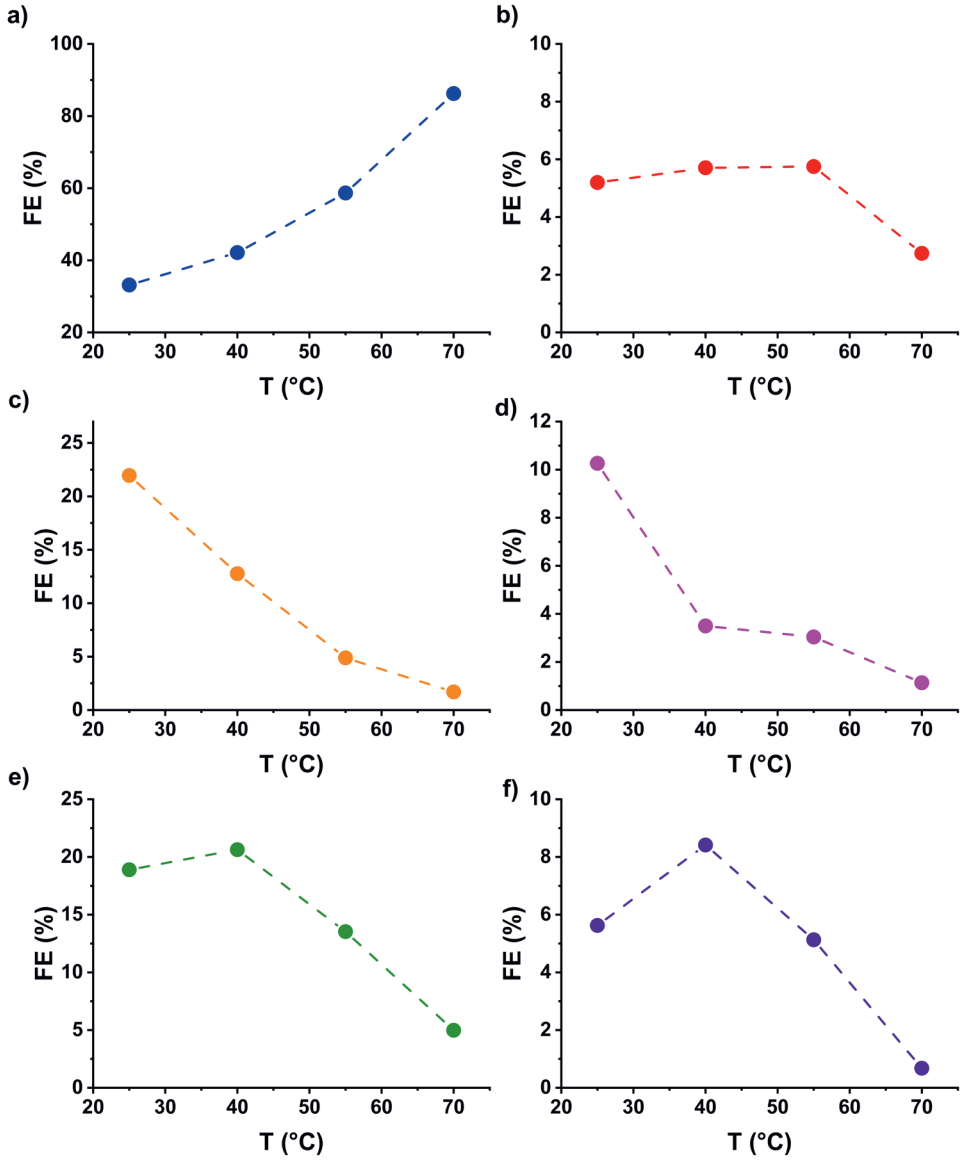

Figure B.9 Faradaic efficiency of CO2RR at different temperatures with constant CO_2 bulk concentrations by changing the partial pressure in 0.1 M $KHCO_3$ at -1.1 V vs. RHE a) hydrogen b) CO c) methane d) formic acid e) ethylene f) ethanol, and g) 1-propanol. Dotted lines are a guide to the eye and error bars are determined from at least 3 measurements.

B.6 Stirring experiments

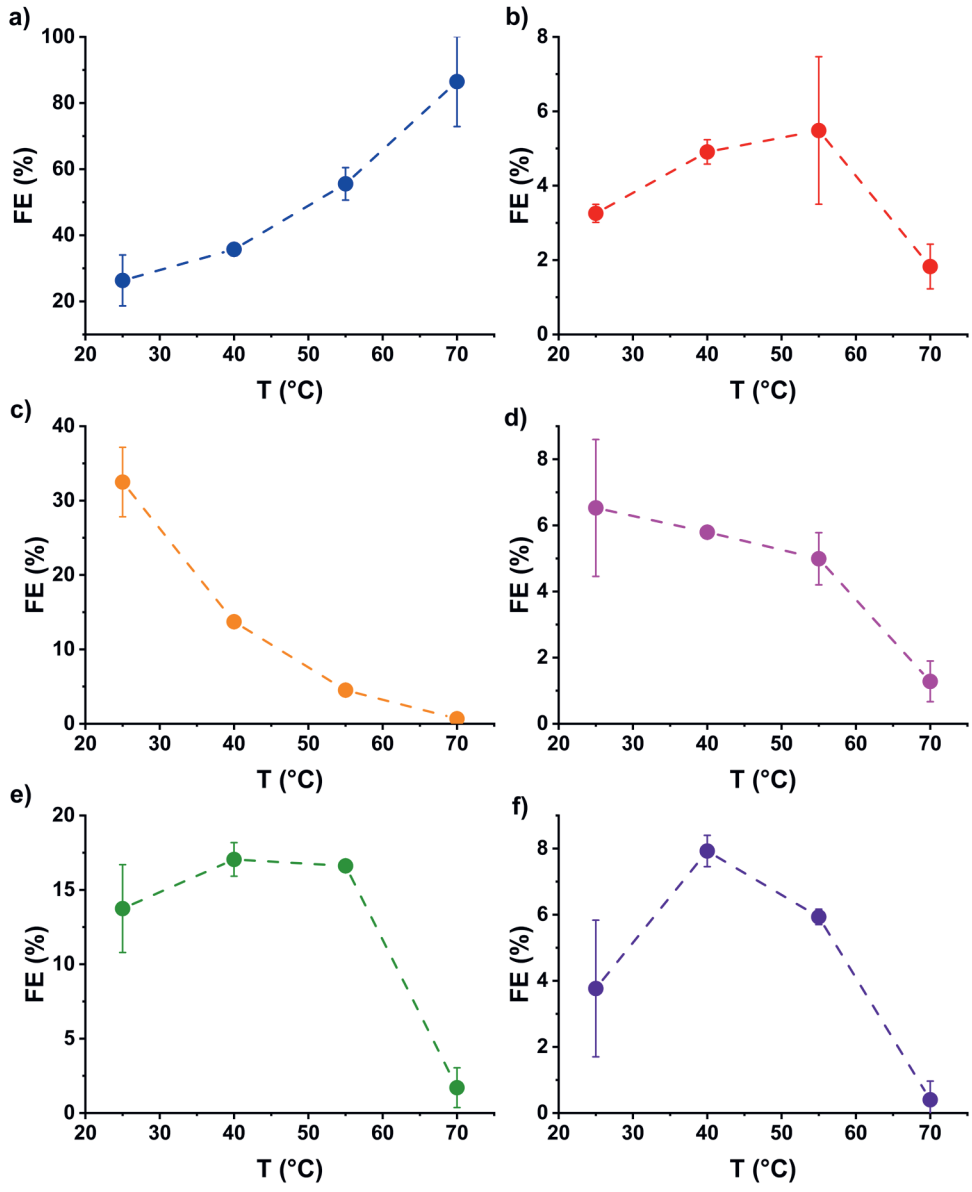

Figure B.10 Faradaic efficiency of CO2RR at different temperatures while stirring with a stirring bar at 1000 rpm in 0.1 M $KHCO_3$ at -1.1 V vs. RHE for a) hydrogen b) CO c) methane d) formic acid e) ethylene f) ethanol, and g) 1-propanol. Dotted lines are a guide to the eye and error bars are determined from at least 3 measurements.

Table B.6 Faradaic efficiency for CO2RR at different temperatures at -1.1V vs. RHE while stirring with at stirring bar at 1000 rpm

stirring		FE (%)		
	25 °C	40 °C	55 °C	70 °C
H_2	33.2	42.1	58.7	86.2
CO	5.2	5.7	5.8	2.7
CH_4	22.0	12.8	4.9	1.7
C_2H	18.9	20.6	13.5	5.0
HCOOH	10.3	3.5	3.0	1.1
EtOH	5.6	8.4	5.1	0.7
PrOH	3.4	2.6	1.2	0.0

B.7 Raman spectroscopy measurements

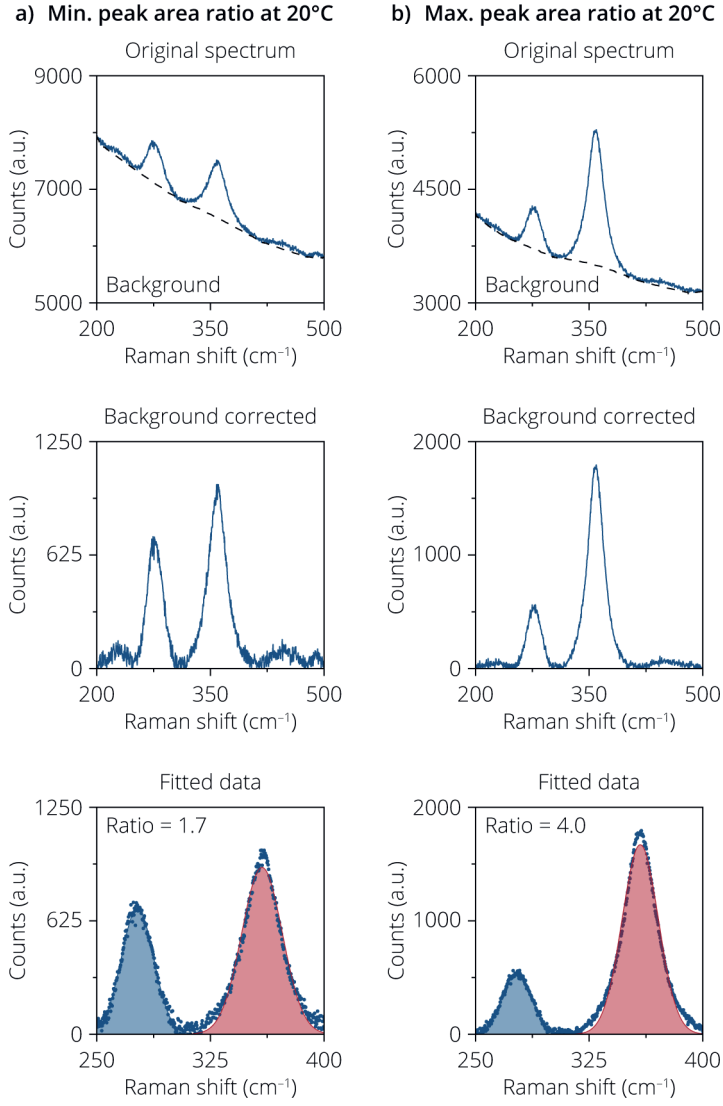

Figure B.11 Example of the data processing of the Raman data. Panel a) shows an example with small peak area ratios and b) with large peak area ratios. From top to bottom the Figure B.hows the original spectrum, the background corrected spectrum and then the data that is fitted with a Gaussian peak fitting procedure to calculate the area of the 280 cm^{-1} and 360 cm^{-1} peaks in blue and red, respectively.

Supporting Discussion: As mentioned in the experimental section, the obtained spectra were baseline corrected using the SNIP algorithm for background elimination. [1] After this background correction, a Gaussian fit was performed on the individual spectra to calculate the area of the 280 and 360 cm^{-1} features. The Raman shift window between 250 and 400 cm^{-1} was used for the fits, with a set boundary between the two peaks at 310 cm^{-1}. The ratio of the 360 and 280 cm^{-1} peaks areas was then used to determine the CO coverage qualitatively.

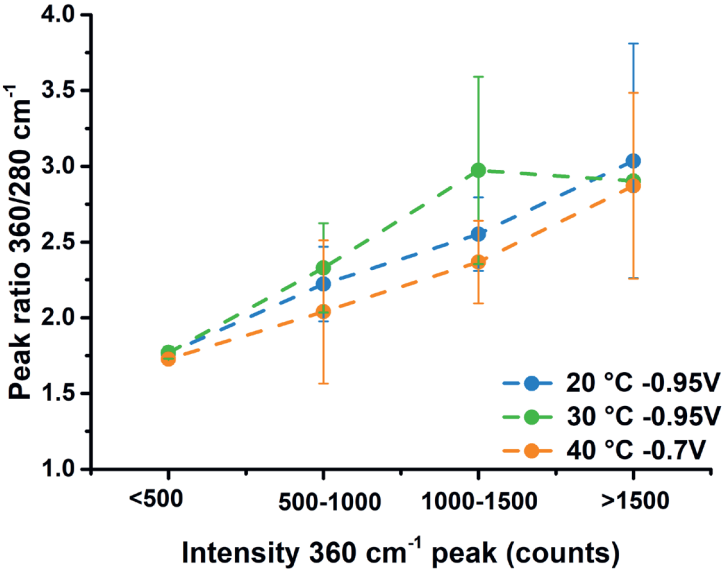

Figure B.12 The ratio between 360 and 280 cm^{-1} peak areas on Cu in 0.1 M $KHCO_3$ vs. the peak intensity of the 360 cm^{-1} peak, which is used as a proxy for the intensity of the Raman spectra. Three different conditions are shown to illustrate that this trend is not a coincidence. It can be seen that the ratio depends on the intensity of the peaks: at higher intensities the peak area ratio increases.

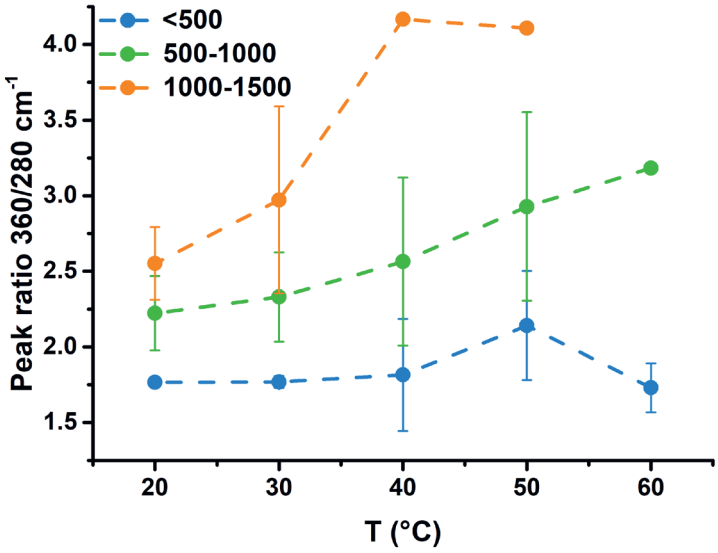

Figure B.13 The ratio between 360 and 280 cm^{-1} peak area on Cu in 0.1 M $KHCO_3$ vs. temperature at -0.95 V vs. RHE. It can be seen that the intensity of the Raman spectra, here indicated by the peak intensity of the 360 cm^{-1} peak, influences the peak ratio. The effect of temperature on the peak ratio and thus the CO coverage is more pronounced with more intense peaks.

Supporting discussion: In Figure 3b, the 280 and 360 cm^{-1} Raman features with the lowest intensities were not taken into account, because we observe that the peak area ratio also seems to depend on the intensity of these peaks, as can be seen in Figure B.12. When the spectra are more intense, as indicated by the peak height of the 360 cm^{-1} feature, the peak area ratio increases as well. This might be caused by the inhomogeneity of the copper surface or by the extent to which the different bands respond to the surface enhancement. Therefore, we isolate the effect of temperature on the peak area ratio by only comparing peak area ratios of spectra with similar intensity, as can be seen in Figure B.13. It can be seen that at all intensities, the CO coverage increases with temperature, although the trend becomes more pronounced when the peak area is larger. When all measured points are taken into account, the trends of Figure 3 are still observed, as can be seen in Figure B.14. However, at -0.7 V the trend is less pronounced due to the data point at 50 °C, as the measurements at this temperature contained many low intensity peaks with a lower ratio. At -0.95 V the entire trend is less pronounced as there are more low intensity peaks in general. Additionally, the peak position is potential

dependent due to the electrochemical Stark shift (Figures S15 and S16), but we find that this has negligible effect on the calculated peak ratios. From this analysis of the Raman spectra, we thus conclude an increasing trend in CO coverage with temperature, independently of the exact methods used to analyze the data.

The interfacial electric field that is generated at the electrode/electrolyte interface has implications for the energetics of the vibrational modes of the adsorbed intermediates. This is known as the vibrational Stark effect and has been researched for Raman spectroscopy during the CO2RR, where the adsorbed CO vibrations are known to show an electrochemical Stark shift due to the large dipole moment and sensitive interaction with the electrode surface. [2,3] Since the direction of the molecular vibration associated with the 280 cm^{-1} (assigned to the restricted rotation vibration of adsorbed CO) and 360 cm^{-1} (assigned to the Cu–Co stretching vibration) Raman bands with respect to the electric field is different, the expected Stark effect for these two vibrations should also be different. The molecular vibration associated with the 280 cm^{-1} Raman band is parallel to the electric field, while the molecular vibration associated with the 360 cm^{-1} Raman band is perpendicular to the electric field, hence a positive and negative Stark tuning is expected, respectively. Figure B.14 shows this positive and negative Stark tuning for the 280 and 360 cm^{-1} Raman bands, as they move in the opposite direction. These Raman spectroscopy measurements were conducted at the same applied potential and temperature, but at different locations at the Cu electrode surface. This indicates that there is an inhomogeneity in the experienced interfacial electric field per measurement spot, showing the necessity to perform these experiments at multiple measurements spots as has been done in this study.

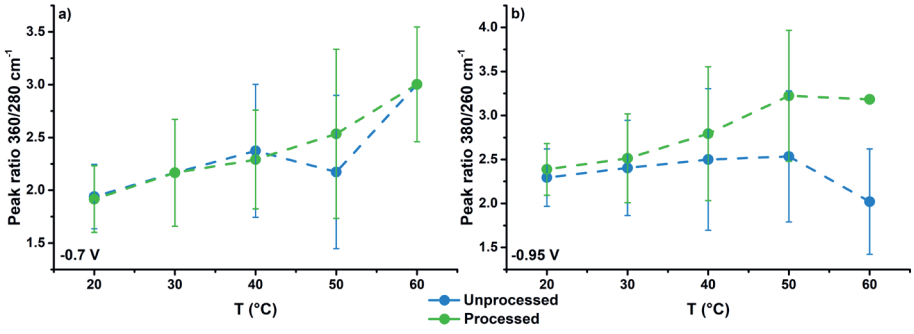

Figure B.14 The ratio between 360 and 280 cm^{-1} peak areas on Cu in 0.1 M $KHCO_3$ vs. different temperatures at a) -0.7 V and b) -0.95 V. The blue line shows the average when all measured data points are taken into account, the green line shows the average when the peaks with low intensity are not taken into account.

The previously mentioned Gaussian fits resulted in values for the peak maxima for both the 280 and 360 cm^{-1} peaks. These values are plotted in S15, showing their dependency on applied potential and temperature. The 280 cm^{-1} peak position seems to change little with applied potential (-0.7 V and -0.95 V vs. RHE, blue and orange lines, respectively). The 360 cm^{-1} peak position, however, shifts more drastically towards higher Raman shifts with higher applied potential. Both the 280 and 360 cm^{-1} peak position seem to shift towards lower Raman shift at the highest temperature measured, which might indicate a change in the interfacial potential at elevated temperatures.

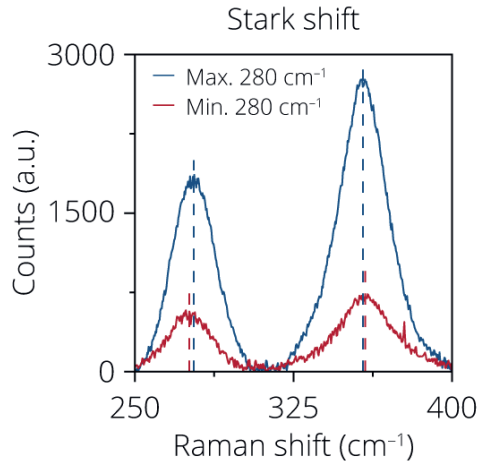

Figure B.15 Raman spectra to highlight the changing 280 and 360 cm^{-1} peak position at different measurement spots on the same Cu electrode. The spectra were both measured at 20 °C and -0.7 vs. RHE. The blue line shows the highest 280 cm^{-1} peak position, while the orange line shows the lowest 280 cm^{-1} peak position. The dashed lines indicate the peak maxima obtained from the Gaussian fitting procedure

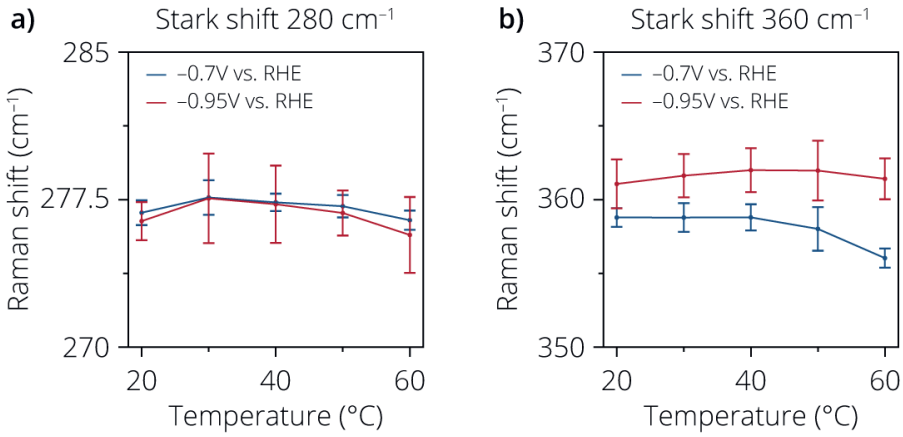

Figure B.16 Temperature- and potential-induced Stark tuning of the 280 cm^{-1} (left) and 360 cm^{-1} (right) peak maxima. The blue lines show the measurements at -0.7V vs. RHE, the orange lines at -0.95V vs. RHE. The data points are the average of 5–10 spots measured at every potential and temperature and the error bar shows the standard deviation of the peak positions of these spots.

The previously mentioned Gaussian fits resulted in values for the peak maxima for both the 280 and 360 cm^{-1} peaks. These values are plotted in S15, showing their dependency on applied potential and temperature. The 280 cm^{-1} peak position seems to change little with applied potential (-0.7 V and -0.95 V vs. RHE, blue and orange lines, respectively). The 360 cm^{-1} peak position, however, shifts more drastically towards higher Raman shifts with higher applied potential. Both the 280 and 360 cm^{-1} peak position seem to shift towards lower Raman shift at the highest temperature measured, which might indicate a change in the interfacial potential at elevated temperatures.

B.8 CO reduction experiments

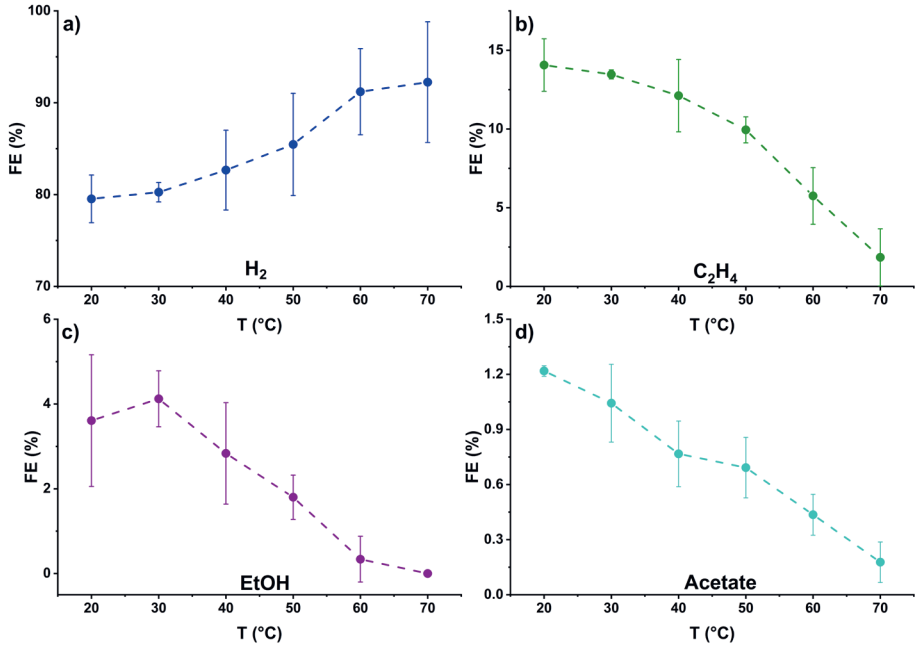

Figure B.17 Faradaic efficiency of CO reduction at different temperatures in 0.1 M KOH + 0.2 M K_2SO_4 at -0.7 V vs. RHE for a) hydrogen b) ethylene c) ethanol, and d) acetate. Dotted lines are a guide to the eye and error bars are determined from at least 3 measurements.

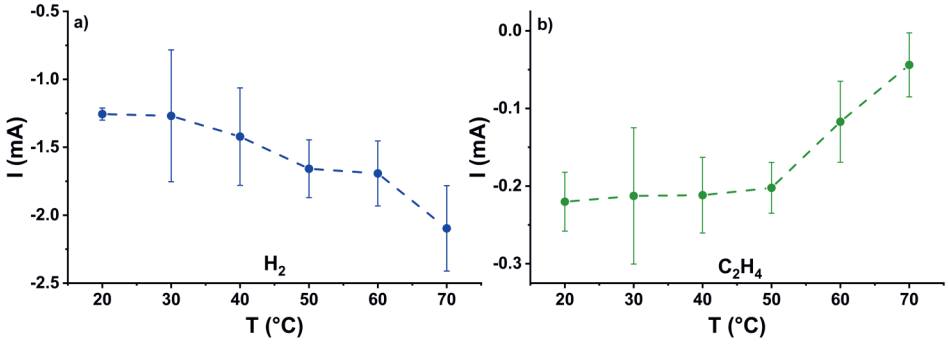

Figure B.18 Currents for CO reduction at different temperatures in 0.1 M KOH + 0.2 M K_2SO_4 at -0.7 V vs. RHE for a) hydrogen and b) ethylene. Dotted lines are a guide to the eye and error bars are determined from at least 3 measurements.

B.9 Activation Energy

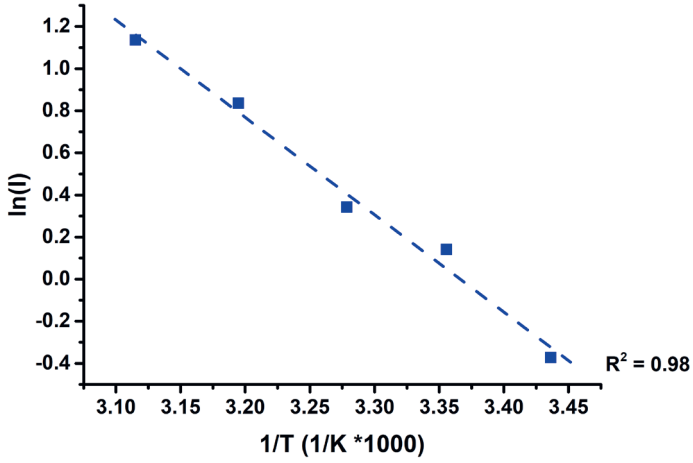

Figure B.19 Arrhenius plot of H_2 production during CO2RR at -1.1 V vs. RHE in -0.1 M $KHCO_3$. The striped line gives the trendline with the corresponding R^2 value to illustrate the linearity of the trendline.

Supporting discussion: We have shown previously that on a gold electrode, the (apparent) E_a for the CO2RR towards CO is higher than for the HER, which results in an increase in CO selectivity with increasing temperature. [4] However, Zong et al. [5] showed that on copper, the HER seems to have the highest apparent activation energy. We have tried to determine the apparent activation energy from our dataset as well, however this does not give straightforward results (Figure B.19 and S20). Ethylene and ethanol give semi-linear trends up to 48 °C. If the data point at 18 °C is not considered, they exhibit E_a of 27 ± 7 and 31 ± 8 kJ/mol, respectively, comparable to the results by Zong et al.. However, including the 18 °C data point, the E_a increases to 53 ± 16 and 50 ± 12 kJ/mol, respectively, showing that our data set is not sufficient to determine a reliable E_a. Unfortunately, the other products show non-linear trends. Only for HER we are able to determine a relatively accurate value (Figure B.19). Interestingly, the E_a for H_2 determined from our experiments is significantly lower than the value determined by Zong et al. (38 ± 2 kJ/mol vs. ~ 60 kJ/mol, respectively).

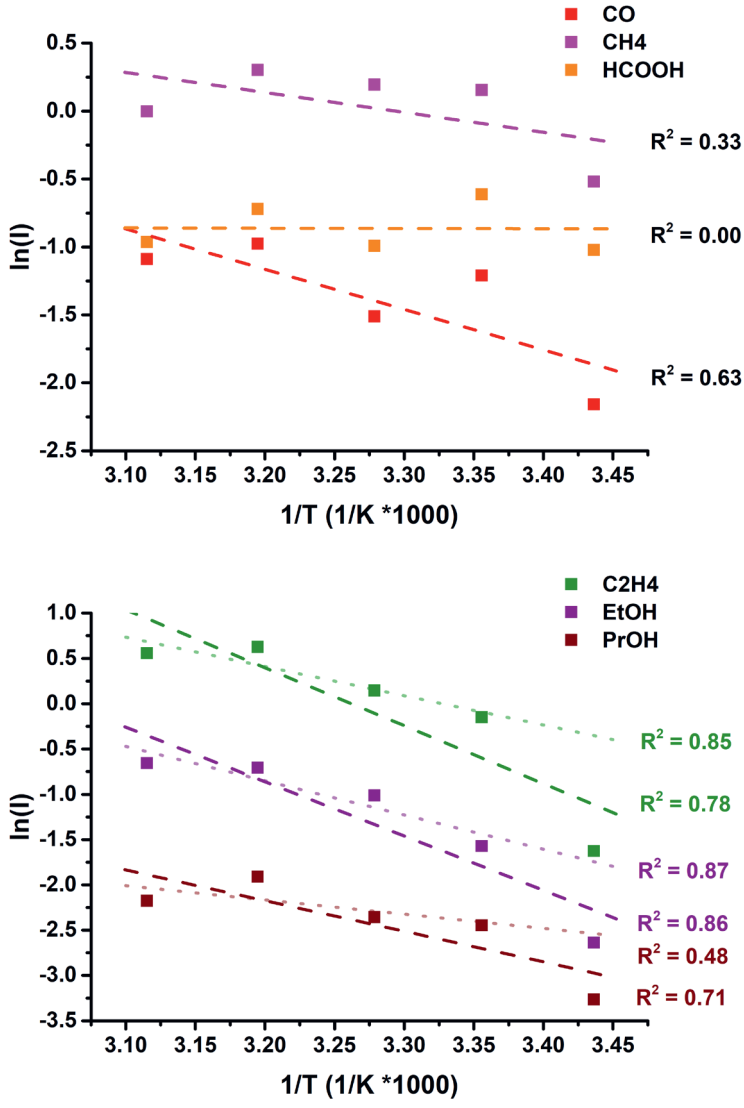

Figure B.20 Arrhenius plots of a) CO, methane, formic acid production and b) ethylene, ethanol and 1-propanol during CO2RR at -1.1 V vs. RHE in -0.1M $KHCO_3$. The striped lines gives the trendline with the corresponding R^2 value to illustrate the linearity of the trendline. The light doted lines for the C2+ products are the trendlines without the point at 18 °C. It can be seen that the slope changes significantly.

B.10 Pb UPD experiments

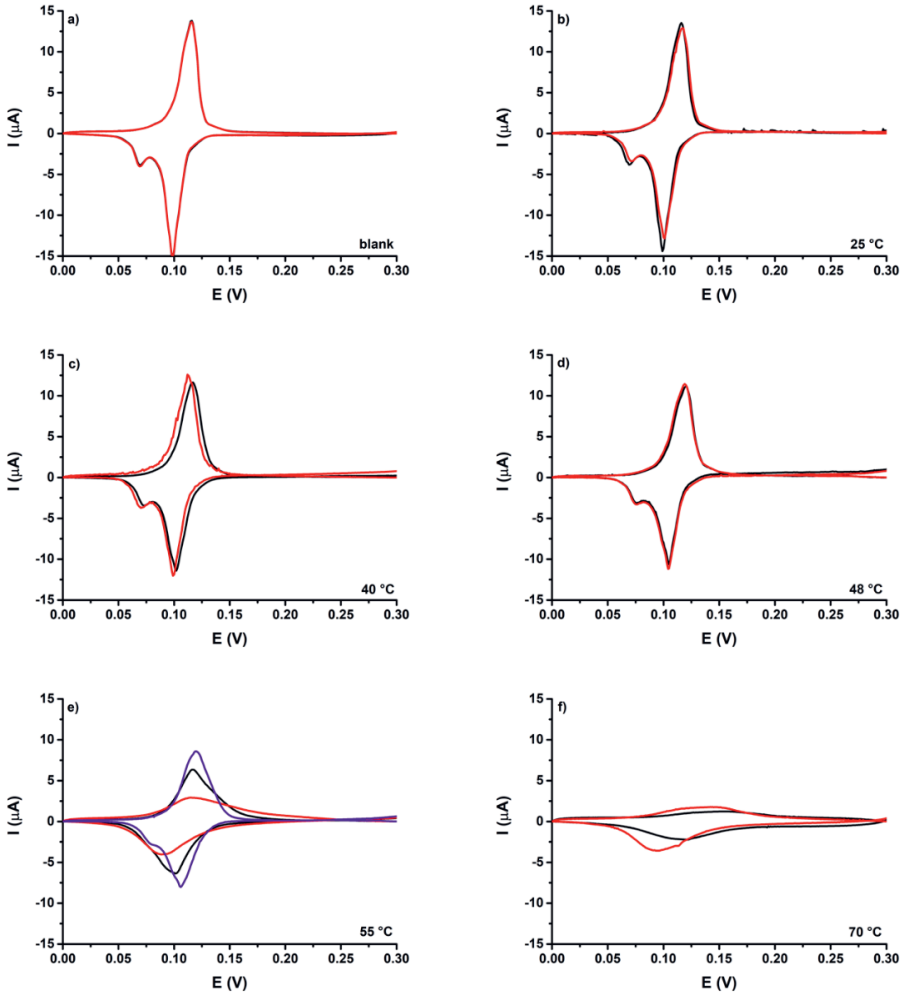

Figure B.21 Pb UPD CVs from 0.3 to 0.0 V vs. RHE at 5 mV/s in 0.1 M $NaClO_4$ + 1mM NaCl + 2 mM $PbClO_4$. A) blank CV after only polishing before CO2RR and after CO2RR for 20 min at -1.1V vs. RHE in 0.1M $KHCO_3$ at b) 25 °C c) 40 °C d) 48 °C e) 55°C f) 70 °C. The red, black and purple lines are separate experiments to illustrate reproducibility.

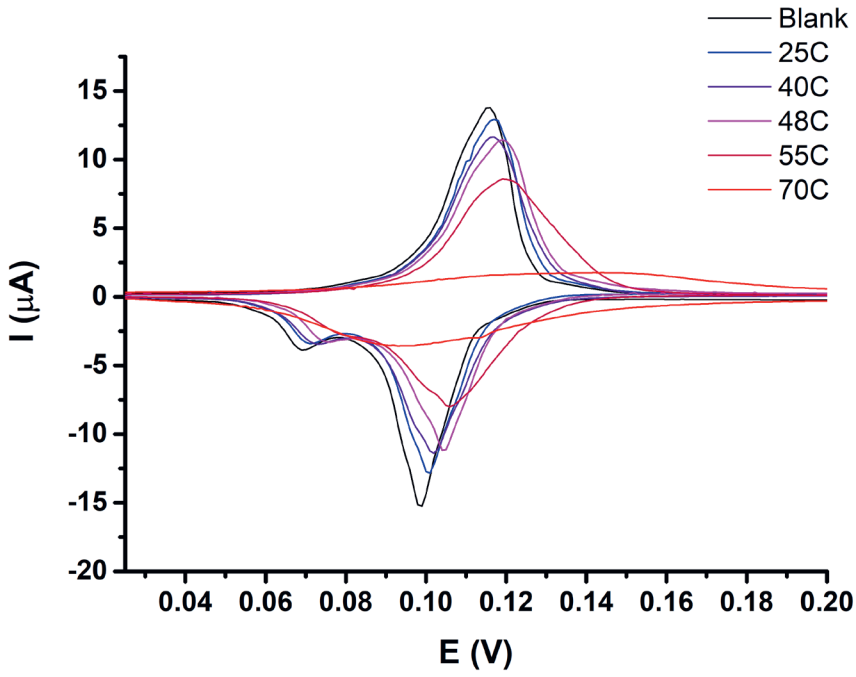

Figure B.22 Pb UPD CVs from 0.3 to 0.0 V vs. RHE at 5 mV/s in 0.1 M $NaClO_4$ + 1mM NaCl + 2 mM $PbClO_4$. The copper sample was first used for CO2RR for 20 min at -1.1V vs. RHE in 0.1 M $KHCO_3$ at different temperatures, while the blank is before CO2RR was performed.

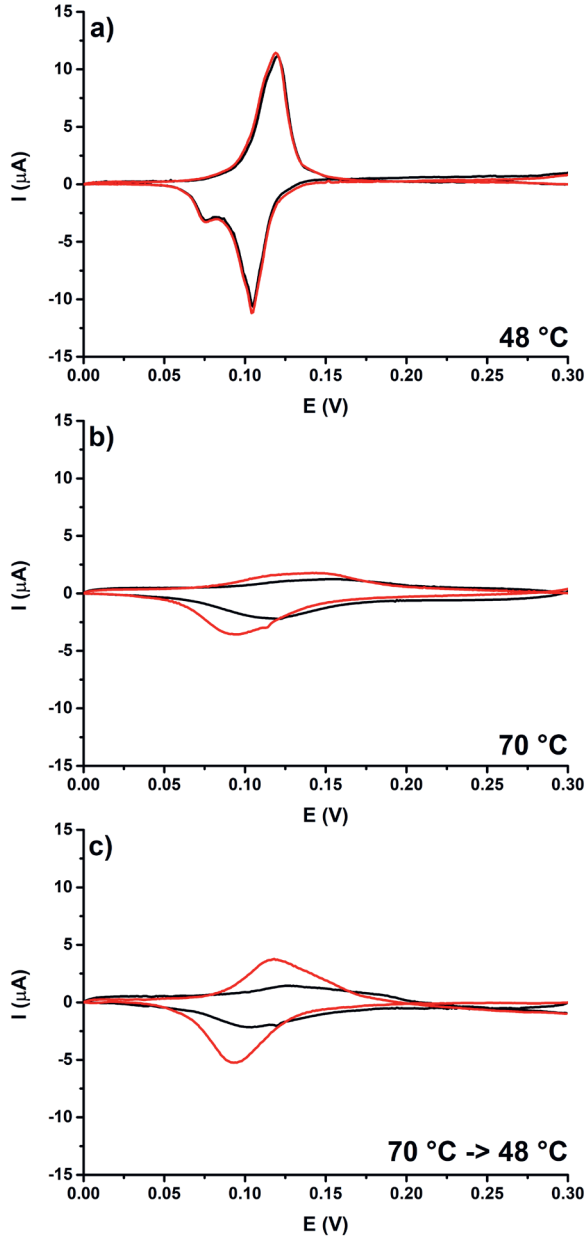

Figure B.23 Pb UPD CVs from 0.3 to 0.0 V vs. RHE at 5 mV/s in 0.1 M $NaClO_4$ + 1mM NaCl + 2 mM $PbClO_4$. a) after CO2RR for 20 min at -1.1V vs. RHE in 0.1M $KHCO_3$ at a) 48 ^{0}C b) 70 ^{0}C and c) 20 min at 70 °C and 30 min at 48 °C. The red and black line represent two different measurements.

B.11 SEM-EDX measurements

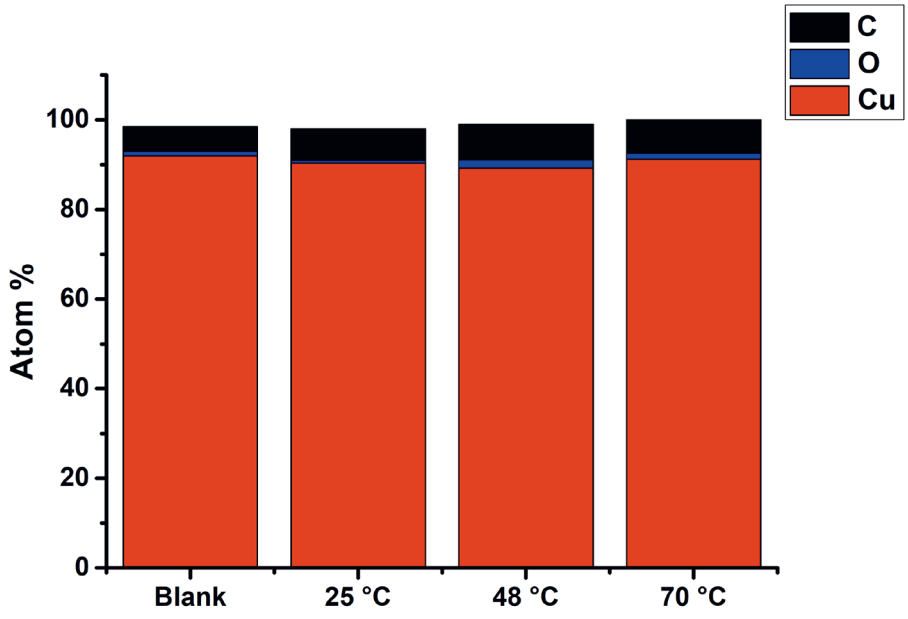

Figure B.24 Elemental composition measured using SEM-EDX of the copper surface after CO2RR at -1.1V at different temperatures and the blank before CO2RR

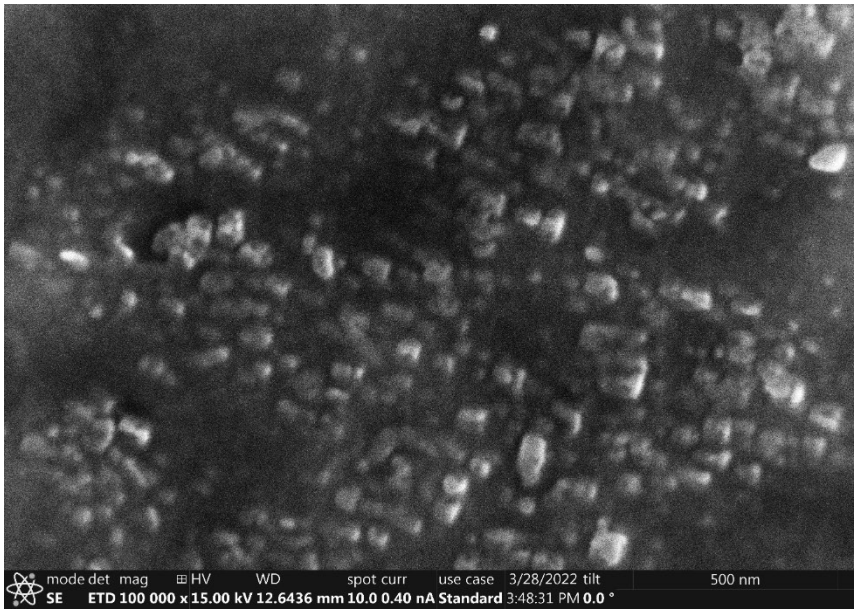
mode det mag HV WD spot curr use case 3/28/2022 tilt 500 nm
SE ETD 100 000 x 15.00 kV 12.6436 mm 10.0 0.40 nA Standard 3:48:31 PM 0.0 °

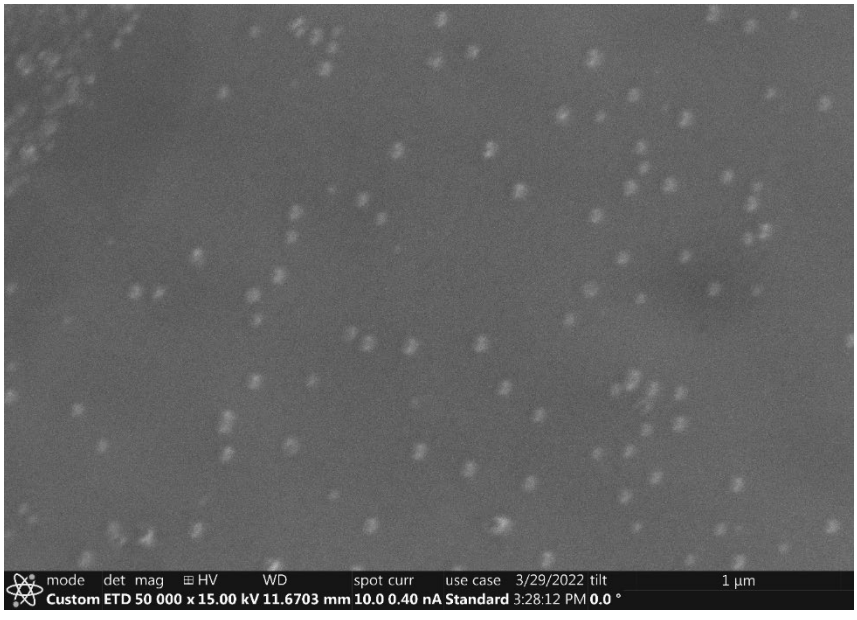
mode det mag HV WD spot curr use case 3/29/2022 tilt 1 µm
Custom ETD 50 000 x 15.00 kV 11.6703 mm 10.0 0.40 nA Standard 3:28:12 PM 0.0 °

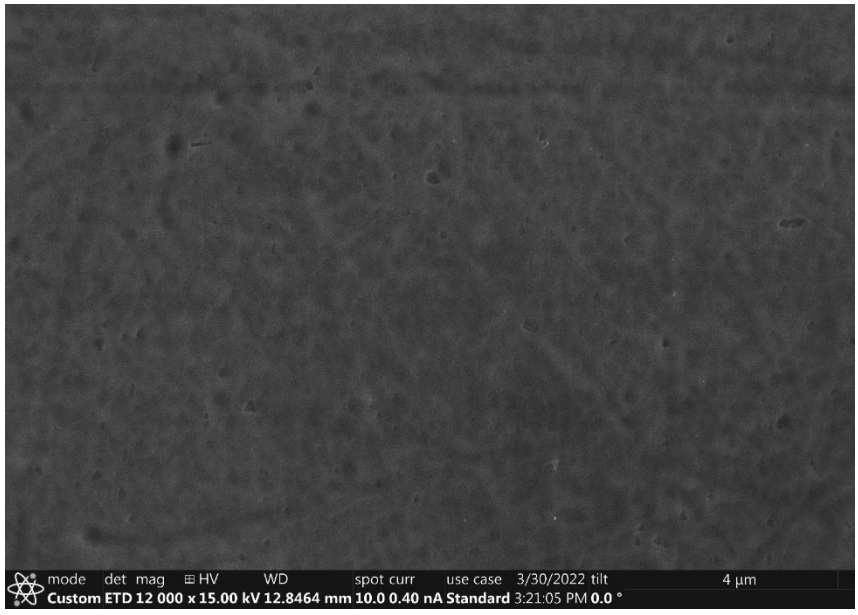

Figure B.25 SEM micrographs after CO2RR at -1.1V vs. RHE at a) 25 °C b) 48 °C c) 70 °C

B.12 Double layer capacitance measurements

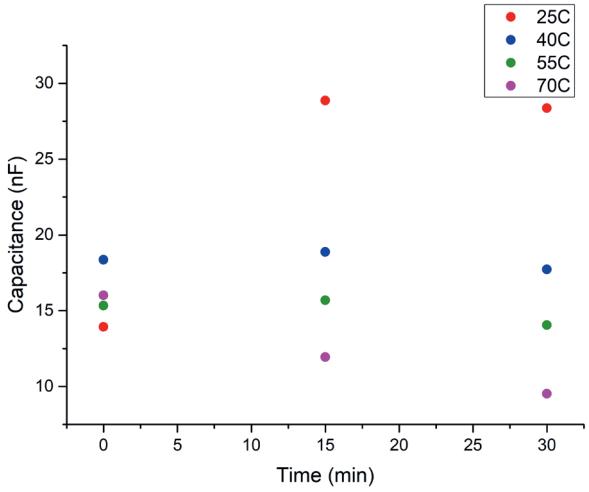

Figure B.26 Capacitance measured by double layer capacitance studies from CVs in the range -0.2 to 0.3 V vs. RHE at scan rates from 200 to 1400 mV/s before and after 15 and 30 min of CO2RR at different temperatures. The capacitance was determined at 0.0 V vs. RHE.

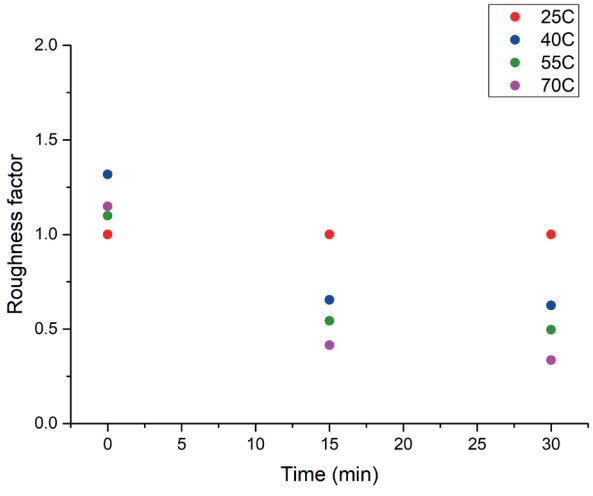

Figure B.27 Roughness factor determined from the data from Figure B.23 by setting the capacitance at 25 °C as 1 at every time interval and normalize the other values.

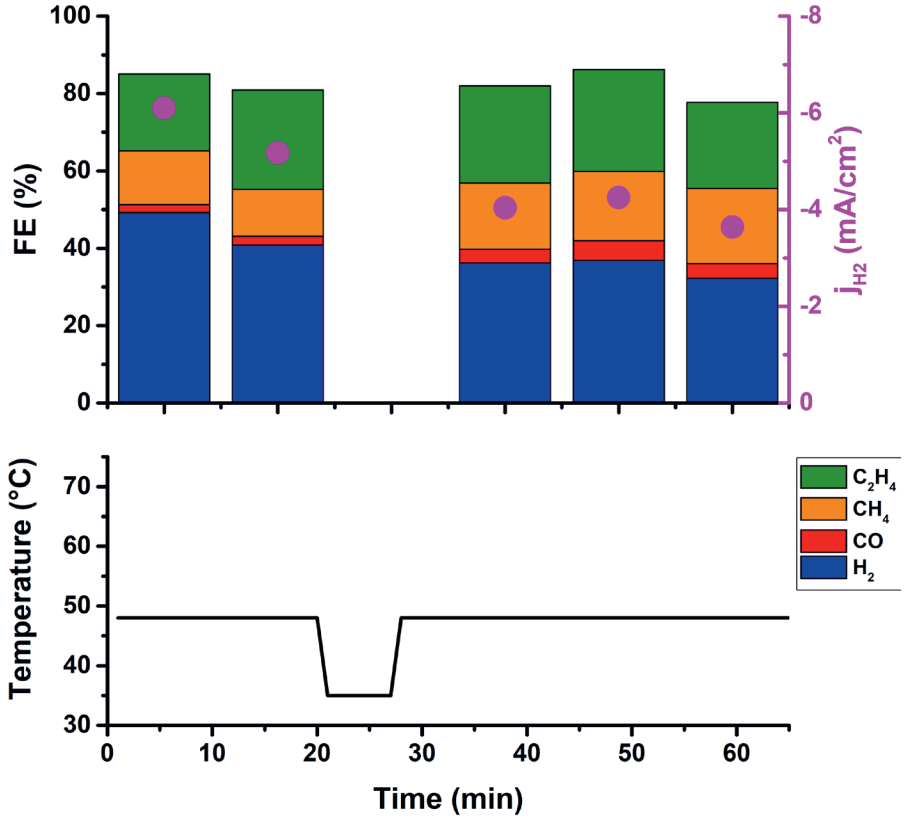

Figure B.28 Reversibility experiments, control experiment to Figure 6. The upper panel shows the Faradaic Efficiency of the gaseous products of CO2RR at -1.1V vs. RHE after 5 and 19 min at 48 °C, and after cooling down at 5, 19 and 32 min at 48 °C. The magenta dots show the patial current density towards H_2. The lower panel shows the temperature profile.

References

1. Caccia, M. *et al. Educational Note* **2**, ED3163 (2013).
2. Chernyshova, I. V, Somasundaran, P. & Ponnurangam, S. *Proceedings of the National Academy of Sciences* **115**, E9261–E9270 (2018).
3. Chang, X. *et al. Catal Sci Technol* **11**, 6825–6831 (2021).
4. Vos, R. E. & Koper, M. T. M. *ChemElectroChem* **9**, e20220023 (2022).
5. Zong, Y., Chakthranont, P. & Suntivich, J. *Journal of Electrochemical Energy Conversion and Storage* **17**, 1–7 (2020).

C

Supporting Information to Chapter 4

The temperature dependence of electrochemical CO_2 reduction on Ag and CuAg alloys

C.1 Picture and scheme of the H-cell and jacket

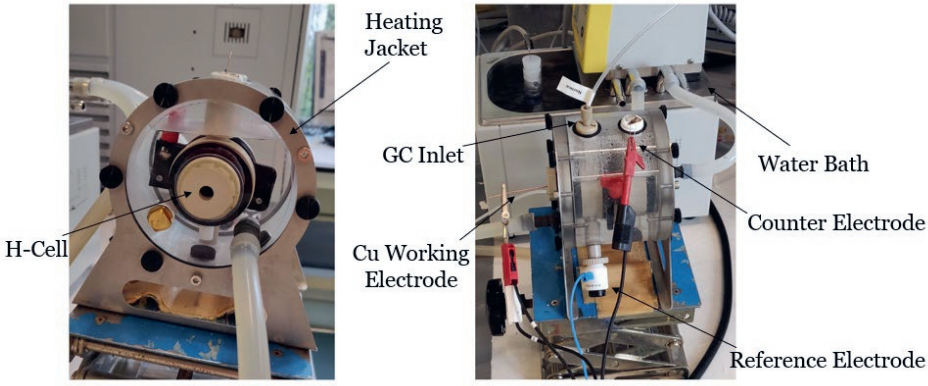

Figure C.1 Photos from the H-cell surrounded by the water jacket used to control the temperature

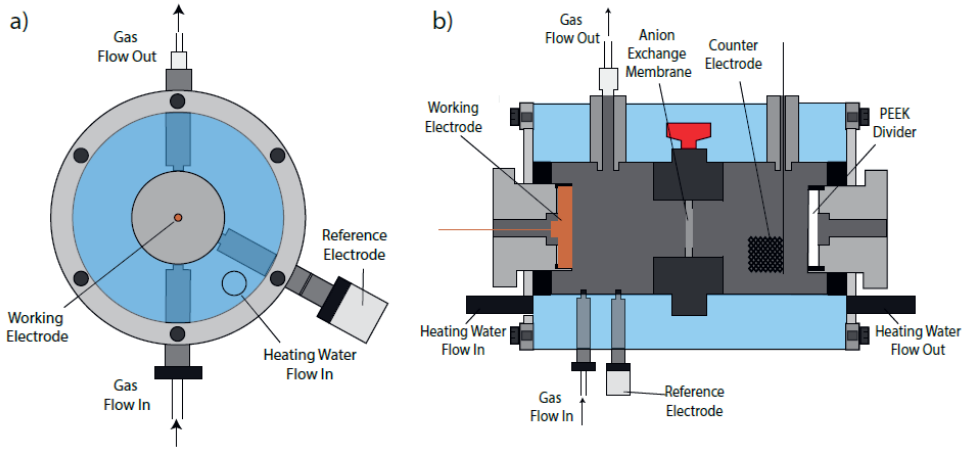

Figure C.2 Schematics of the H-cell surrounded by the water jacket used to control the temperature. a) Frontal-section of the cathodic chamber and (b) cross-section of the electrochemical H-cell with heating jacket

C.2 CO_2 concentration as function of temperature

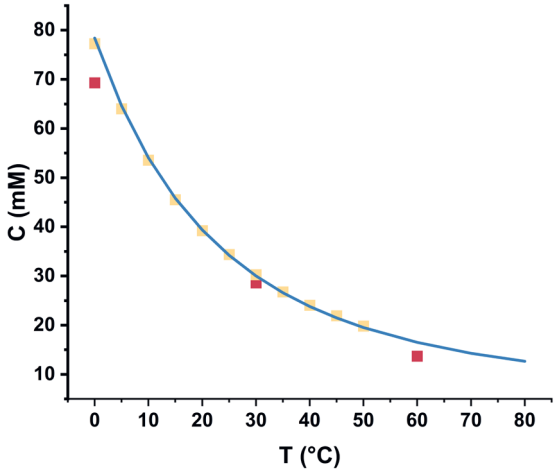

Figure C.3 the CO_2 concentration in water (yellow[1], red[2], blue[3]) as function of temperature

C.3 Partial pressure experiments

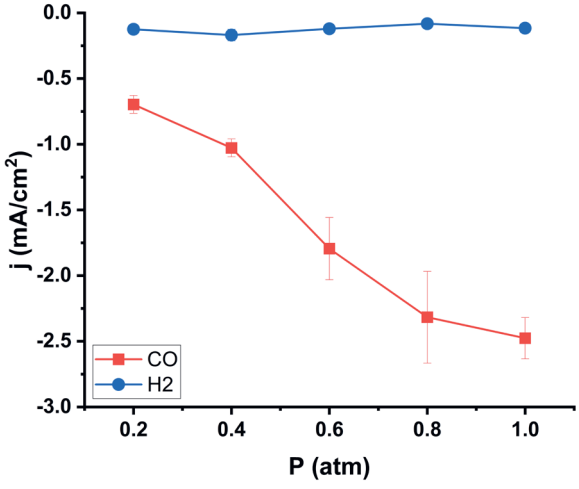

Figure C.4 Partial current densities at different partial pressures to change the bulk concentration of CO_2 at -1.1 V vs RHE at 20 °C in 0.1 M $KHCO_3$

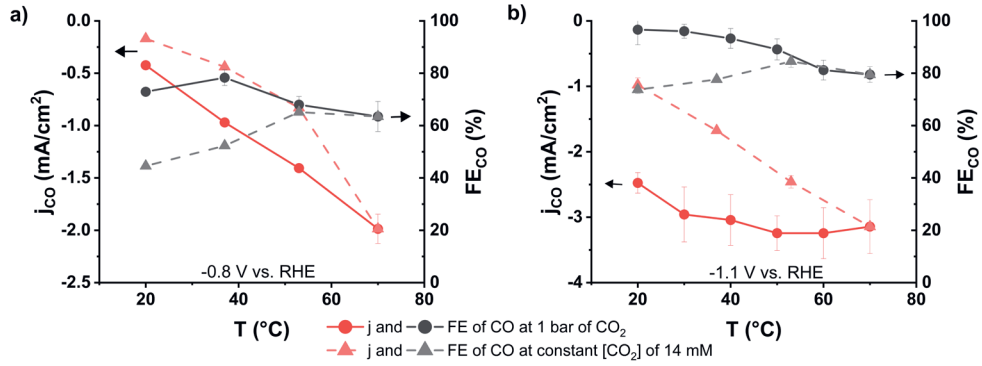

Figure C.5 Temperature effect of the partial current densities for CO and the FE for CO on Ag in 0.1 M $KHCO_3$ at constant CO_2 pressure of 1 bar for the full dark circles and at constant CO_2 concentration in electrolyte of 14 mM by changing the partial pressure accordingly in dashed light triangles at a) at -0.8 V and b) -1.1 V vs RHE

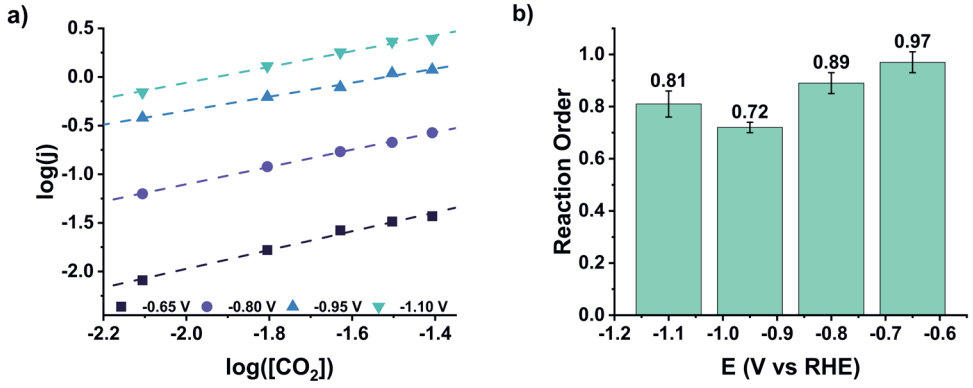

Figure C.6 Reaction order of CO_2 at different potentials in 0.1 M $KHCO_3$. From the plot in a) the reaction order in b) has been determined

C.4 Au map of temperature and potential dependence

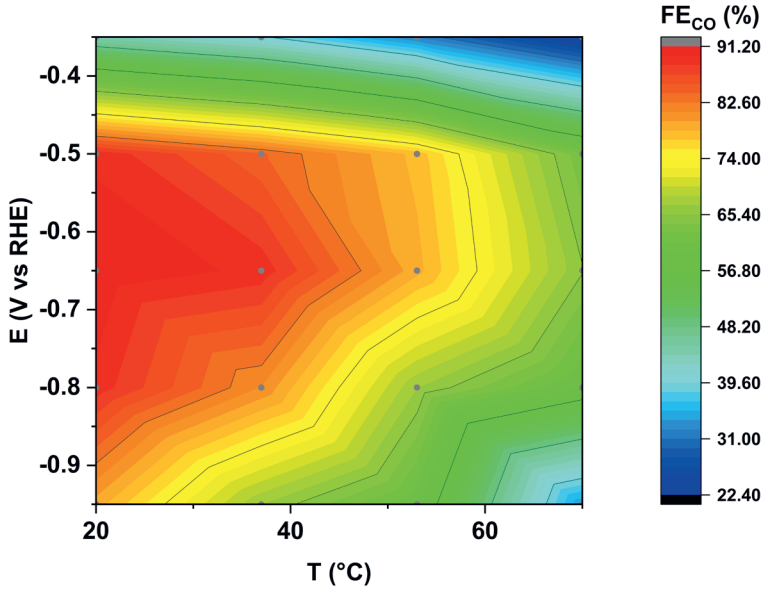

Figure C.7 Map of the Faradaic efficiency of CO on Au in the GC setup vs temperature and pressure in 0.1 M $KHCO_3$

C.5 Mass transport effect

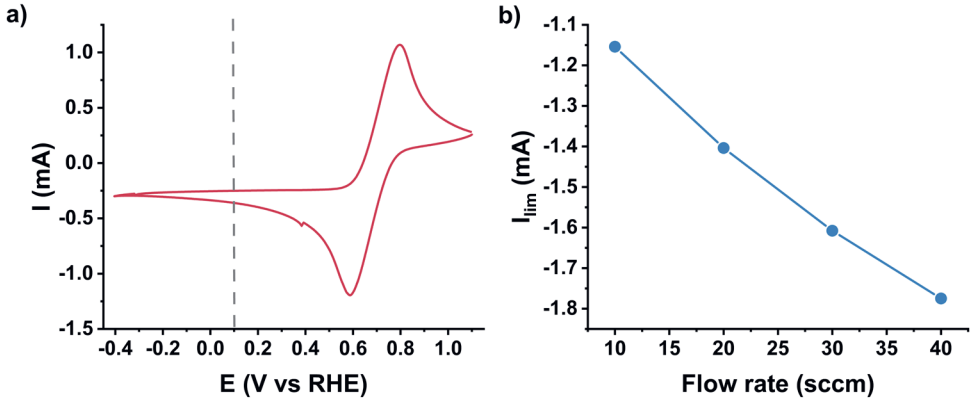

Figure C.8 a) the CV of $K_3Fe(CN)_6$ at 20 mV/s without an flow in CO_2 saturated 0.1 M $KHCO_3$ b) the limiting current of $K_3Fe(CN)_6$ at 0.1 V vs RHE in the GC cell showing that increased flow rates lead to improved mass transport

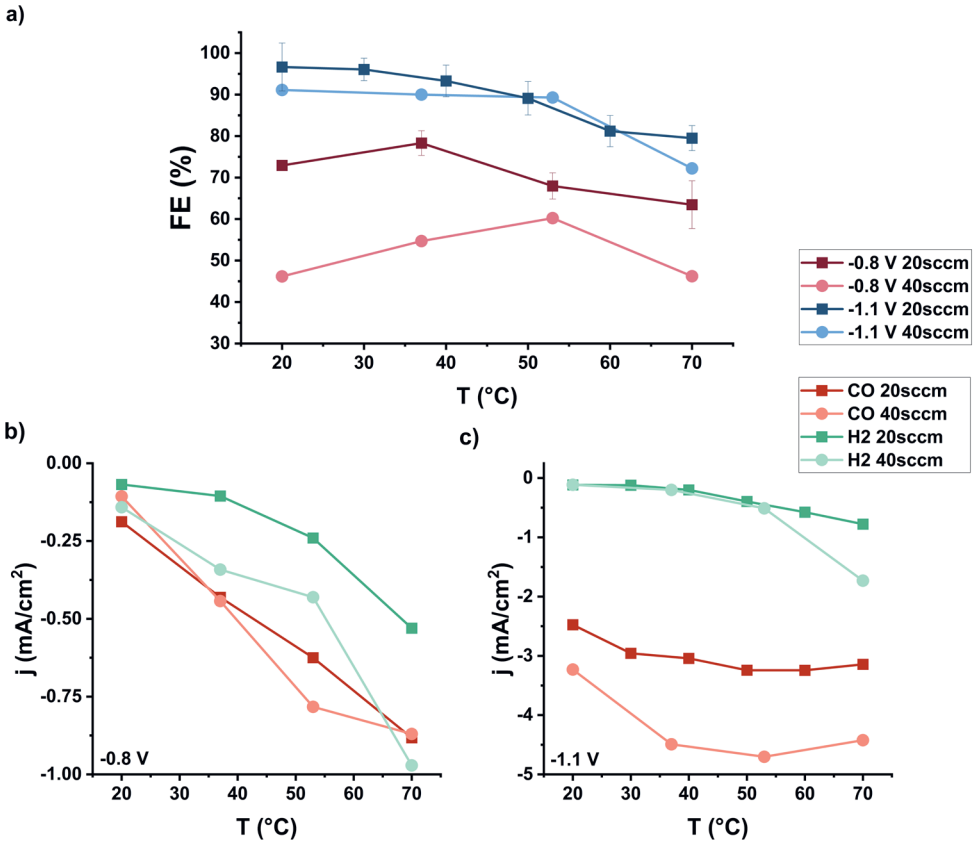

Figure C.9 Effect of mass transport on the CO_2 reduction on Ag in the GC cell in 0.1 M $KHCO_3$ on a) the Faradaic efficiency at different temperatures and the effect on the partial current densities to CO and H_2 at b) -0.8 V and c) -1.1 V vs RHE.

C.6 Different CuAg surface alloys

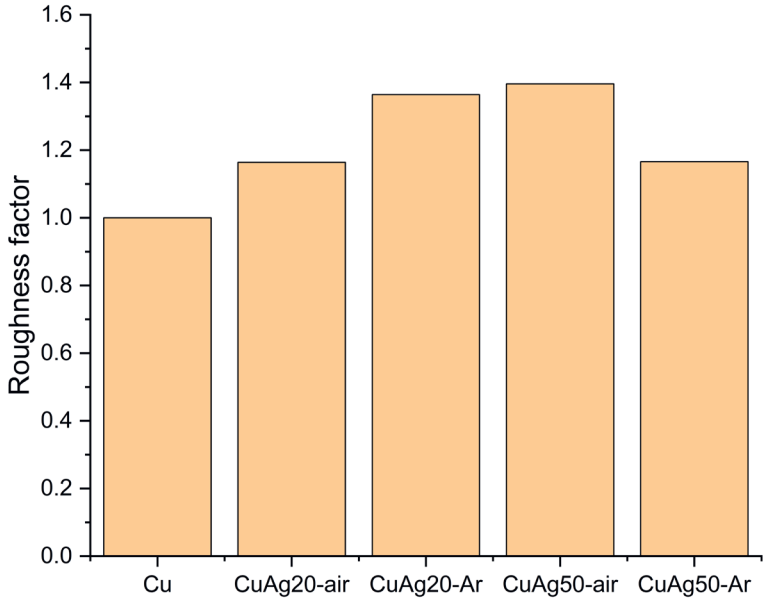

Figure C.10 Roughness factor determined from the double layer capacitance normalized to pure Cu

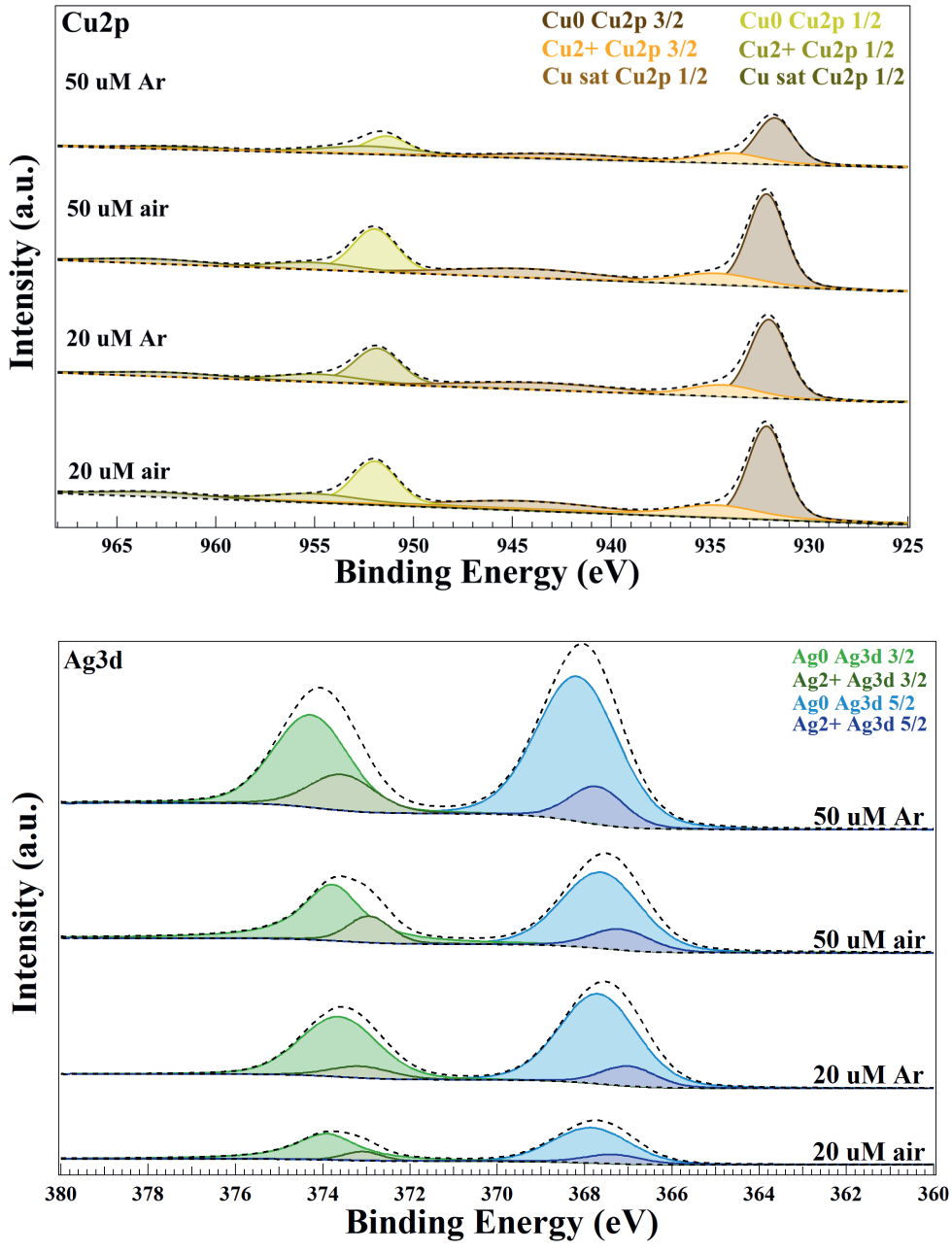

Figure C.11 the fitted Cu2p and Ag3d peaks determined with XPS

Table C.1 The area's from the Cu2p and the Ag3d peak and the calculated concentrations for the different CuAg samples

	Cu (Area)	Ag (Area)	Cu %	Ag %
20 µM $AgNO_3$ in air	8662156.76	596090.53	95.28	4.72
20 µM $AgNO_3$ in Ar	17175963.16	2665294.88	89.95	10.05
50 µM $AgNO_3$ in air	19319787.10	2429221.06	91.70	8.30
50 µM $AgNO_3$ in Ar	10443265.50	4545023.51	76.14	23.86

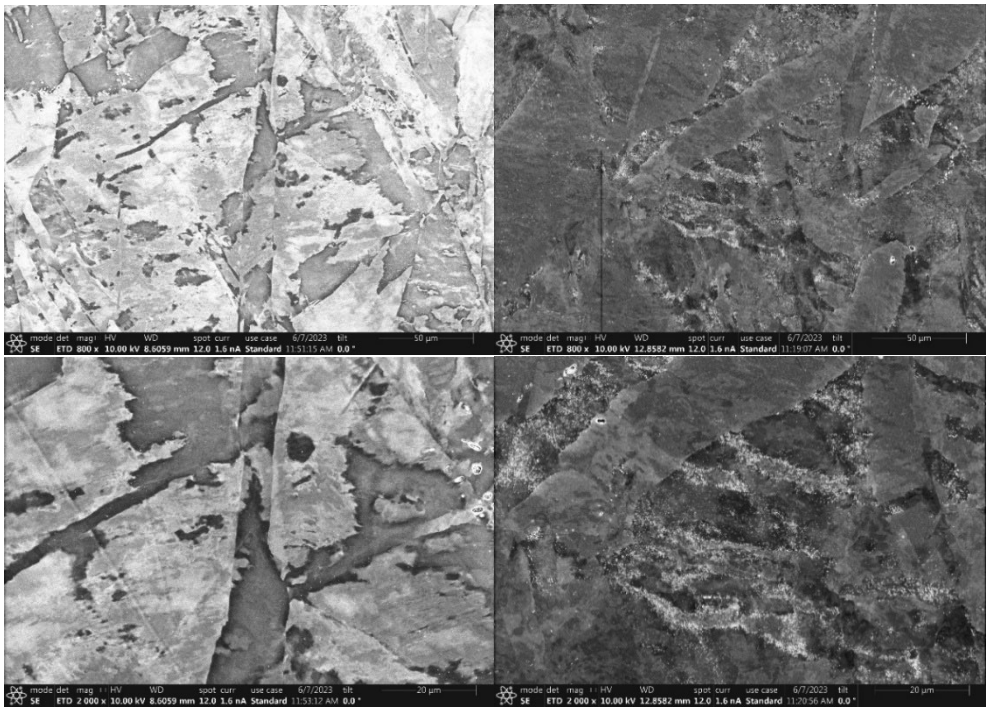

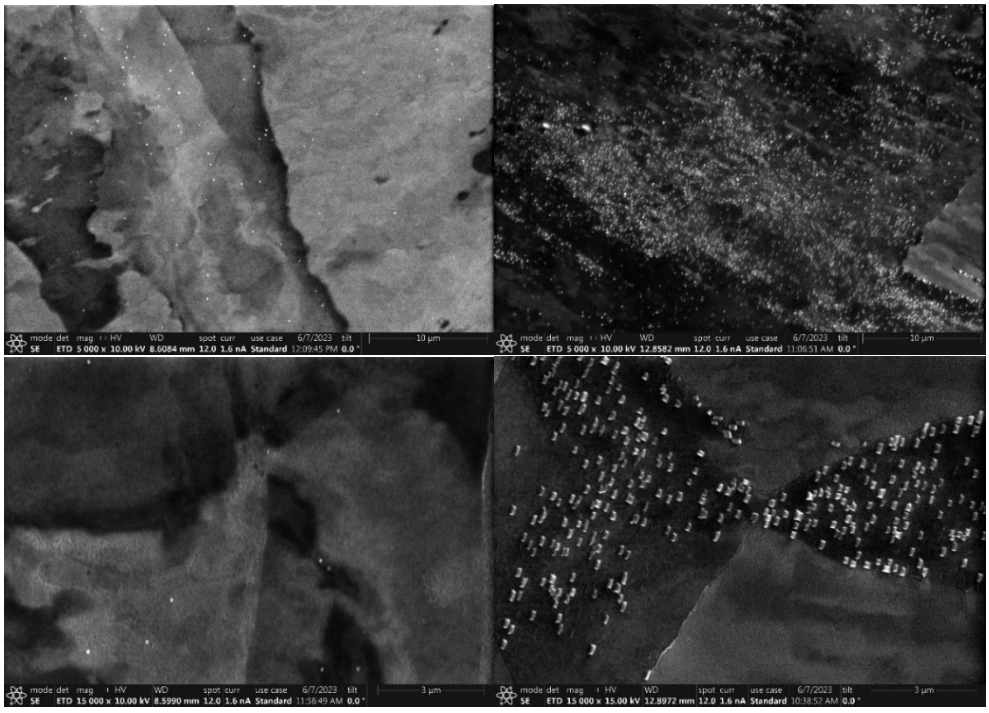

Figure C.12 SEM of CuAg20 on the left and CuAg50 on the right at different magnifications (800, 2000, 5000, 15000x)

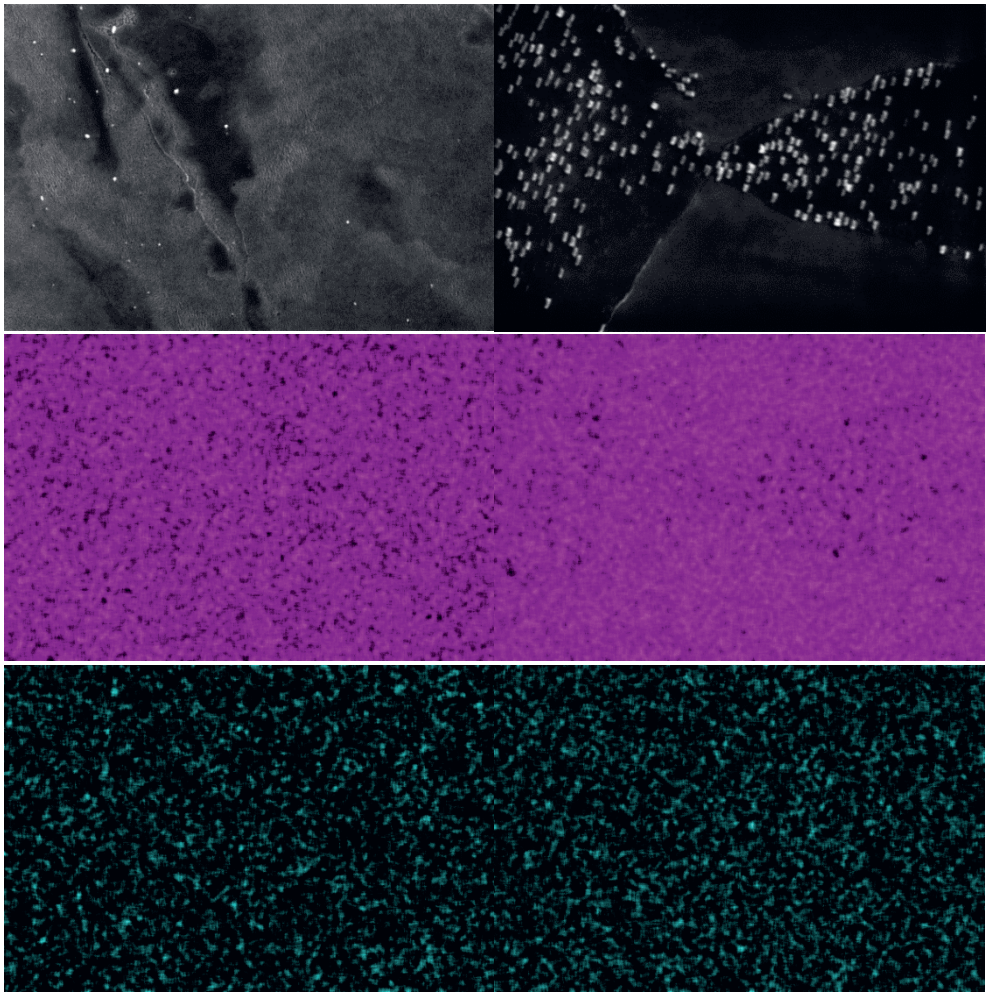

Figure C.13 EDX maps of the CuAg20 catalyst on the left and the CuAg50 catalysts on the right; pink is Cu, blue for Ag. The EDX map shows that Ag is uniformly distributed over the surface in both catalyst, as expected from galvanic exchange.

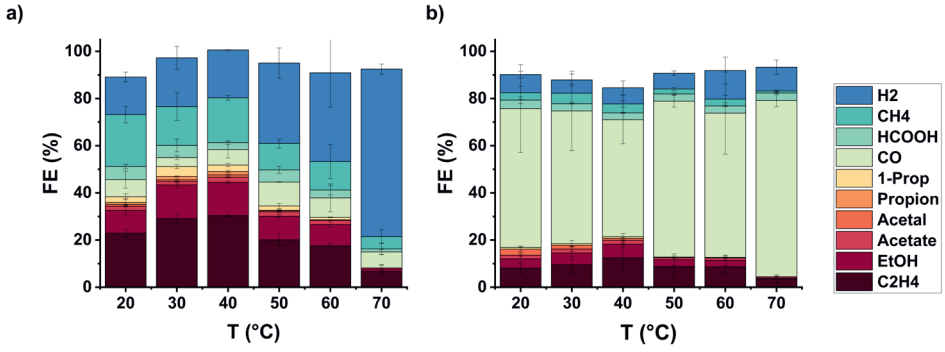

Figure C.14 Faradaic efficiencies for a) CuAg20 b) CuAg50 as function of temperature at -1.1 V vs RHE in 0.1 M $CsHCO_3$

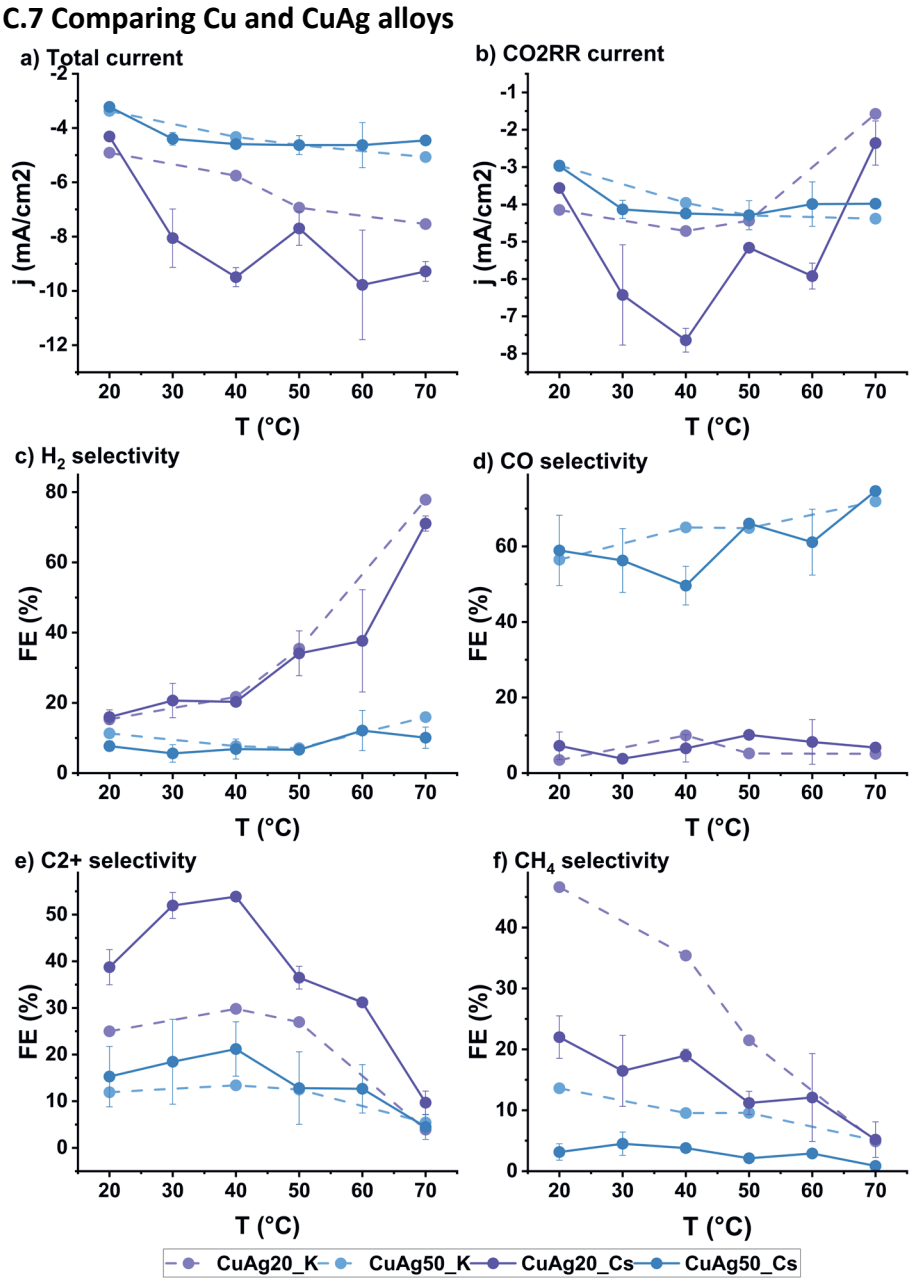

Figure C.15 a) Total current density and b) current density towards CO2RR and faradaic efficiency for c) hydrogen d) CO e) C2+ products f) CH4 for CuAg20 in purple and CuAg50 in blue at -1.1 V vs RHE in 0.1 M $KHCO_3$ (light dashed) and in 0.1 M CsHCO3 (dark full line)

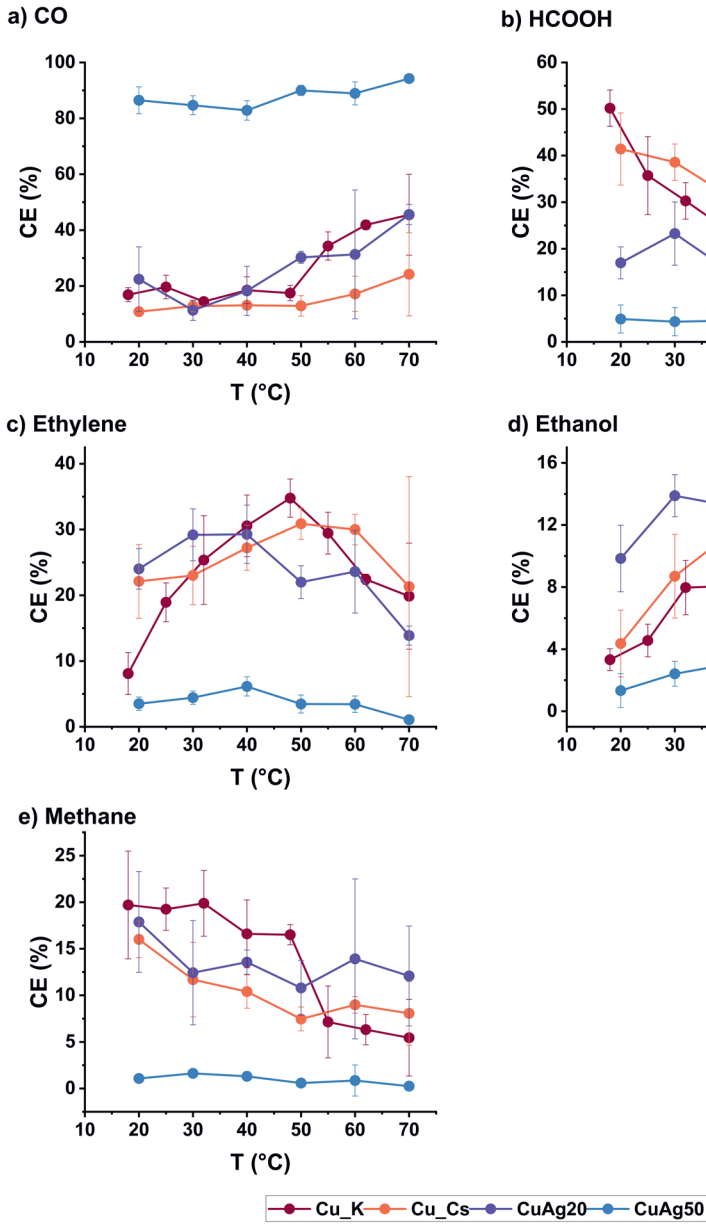

Figure C.16 Comparison of the Carbon efficiency for a) CO b) HCOOH c) ethylene d) ethanol e) methane for Cu, CuAg20 and CuAg50 at -1.1V vs RHE in 0.1 M CsHCO3 and also in 0.1 M $KHCO_3$ for Cu.

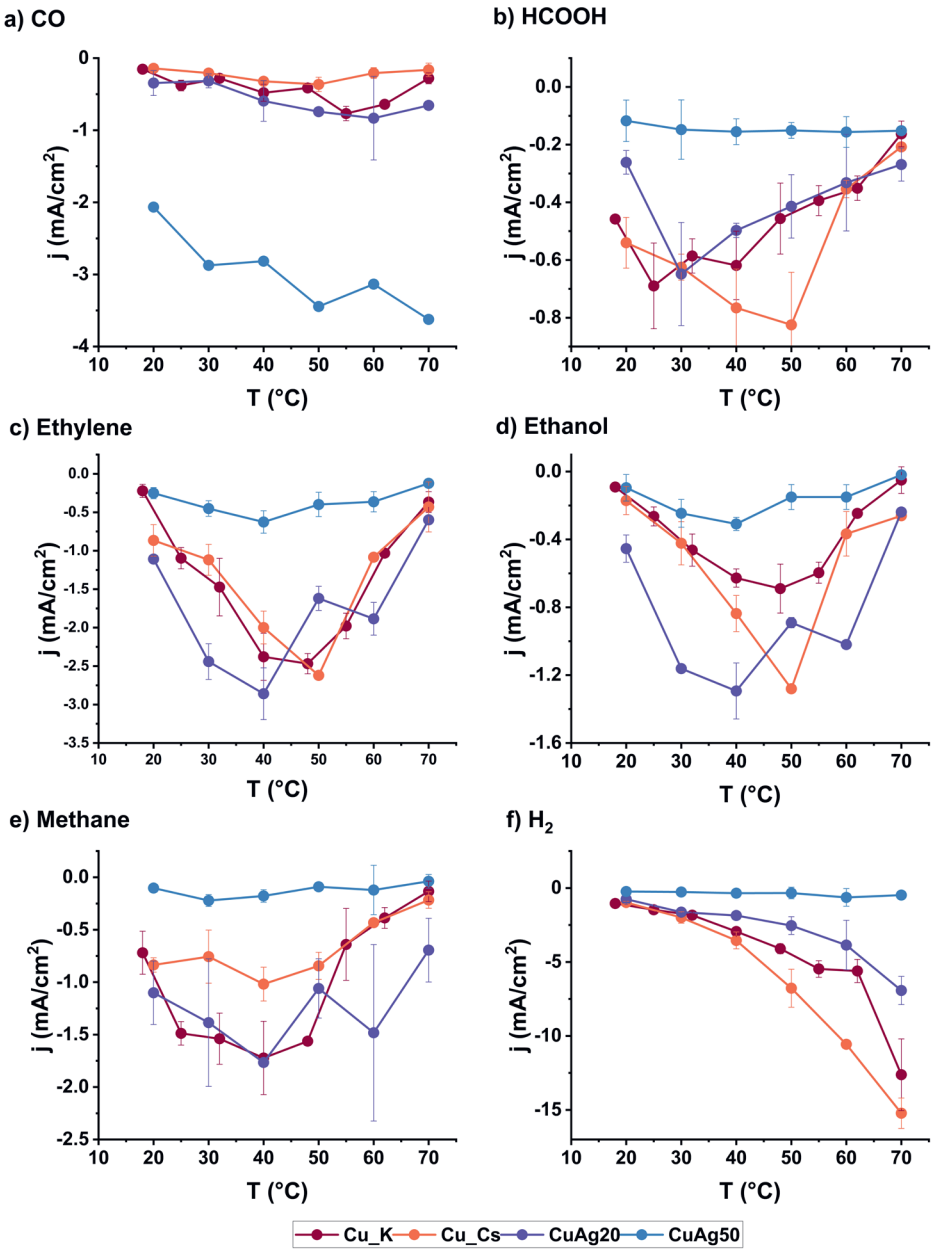

Figure C.17 Comparison of the partial current densities for a) CO b) HCOOH c) ethylene d) ethanol e) methane f) for Cu, CuAg20 and CuAg50 at -1.1V vs RHE in 0.1 M CsHCO3 and also in 0.1 M $KHCO_3$ for Cu.

C.8 Minor CO2RR products on CuAg20

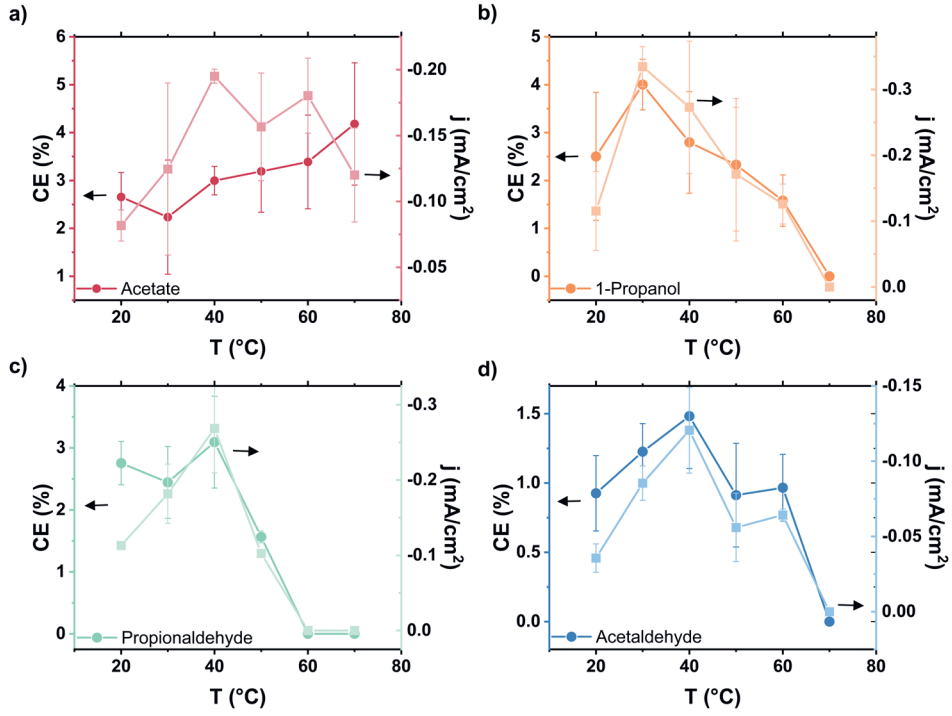

Figure C.18 Carbon efficiency and partial current density for minor liquid products on CuAg20 at -1.1 V vs RHE in $CsHCO_3$ a) acetate b) 1- propanol c) propionaldehyde and d) acetaldehyde based on the HPLC data

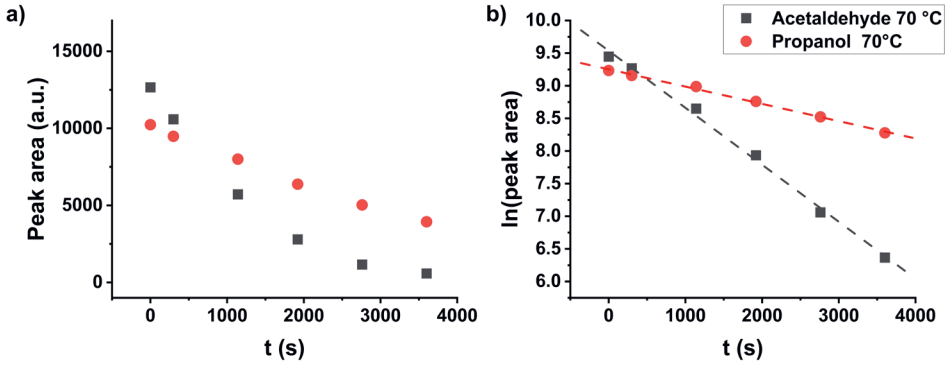

Figure C.19 Illustration of the evaporation experiments, a) the peak area and b) ln of the peak area of acetaldehyde and propanol at 70 °C vs. time

Some liquid products have low boiling points and could evaporate during the experiment, especially at elevated temperatures. To ensure this does not influence the measurements we have performed controlled evaporation studies. A solution containing 0.5 mM ethanol, 1-propanol, acetaldehyde and propionaldehyde was tested in the normal electrolysis setup, so with CO_2 flow rates of 40 sccm. After 0, 5, 19, 32, 46 and 60 min a liquid sample was taken and analyzed with HPLC. This experiment was performed at 20, 30, 40, 50, 60, 70 °C. The evaporation experiments show a 'first-order-like' behaviour, where the amount of evaporation depends on the concentration of the species in solution as can be seen in Figure C.13.

$$\text{Rate}_{\text{evaporation}} = \frac{dc}{dt} = -k_1 c \qquad \text{(S1)}$$

$$\ln(c) = -k_1 t + \ln(c_0) \qquad \text{(S2)}$$

Where c is the concentration, t is time in seconds and k_1 is the rate constant of evaporation. Equation S1 can be integrated to get equation S2, which illustrates that the rate constant can be obtained from the slope of Figure C.13b. This can be done for every product at every single temperature. If we assume the electrochemical production rate is constant over the experiment, we can define k_2 as the rate constant of the electrochemical reaction.

Then the accumulation of the product in the electrolyte is:

$$\text{Rate}_{\text{accumulation}} = \frac{dc}{dt} = -k_1 c + k_2 \qquad \text{(S3)}$$

Solving this differential equation gives

$$c(t) = \frac{k_2}{k_1} + x e^{-k_1 t} \qquad \text{(S4)}$$

Where c is the concentration, t is time in seconds and k_1 is the rate constant of evaporation, k_2 is the rate of the electrochemical reaction and x is a variable. This equation can be solved as we have 2 boundary conditions:

A: At t_0 c = 0

B: At t_{3600} c = the measured amount in the HPLC of a particular measurement

With boundary condition A we can fill in equation S4:

$$c(t) = \frac{k_2}{k_1} - \frac{k_2}{k_1} e^{-k_1 t} \qquad \text{(S5)}$$

$$k_2 = \frac{c(3600) * k_1}{1 - e^{-k_1 * 3600}} \qquad (S6)$$

And we can solve for k_2 with boundary condition B for every individual experiment and the electrochemically produced amount of the volatile liquid product is then given by: k_2 *3600

For the aldehydes, significant amounts of product evaporate. For the alcohols, only at the very high temperatures we see some evaporation, which is still very minor. Interestingly, the C3 products evaporate more than the C2 products, so propanol evaporates more than ethanol and acetaldehyde evaporates more than propionaldehyde. This is probably caused by the constant purging of the electrolyte. We also observe that without purging, hardly any of these compounds evaporate, even at 70 °C. We have corrected the graphs of the minor products from Figure C.12 and the result can be seen in Figure C.14. This correction for the evaporations does not influence the trends significantly. Only for propionaldehyde now also an optimum at 40 °C can be observed.

References

1. Harned, H. S. & Davis Jr, R. *J Am Chem Soc* **65**, 2030–2037 (1943).
2. Duan, Z. & Sun, R. *Chem Geol* **193**, 257–271 (2003).
3. Plummer, L. N. & Busenberg, E. *Geochim Cosmochim Acta* **46**, 1011–1040 (1982).

D

Supporting Information to Chapter 5

Nickel as electrocatalyst for $CO_{(2)}$ reduction; effect of temperature, potential, partial pressure and electrolyte composition

D.1 SEM-EDX images

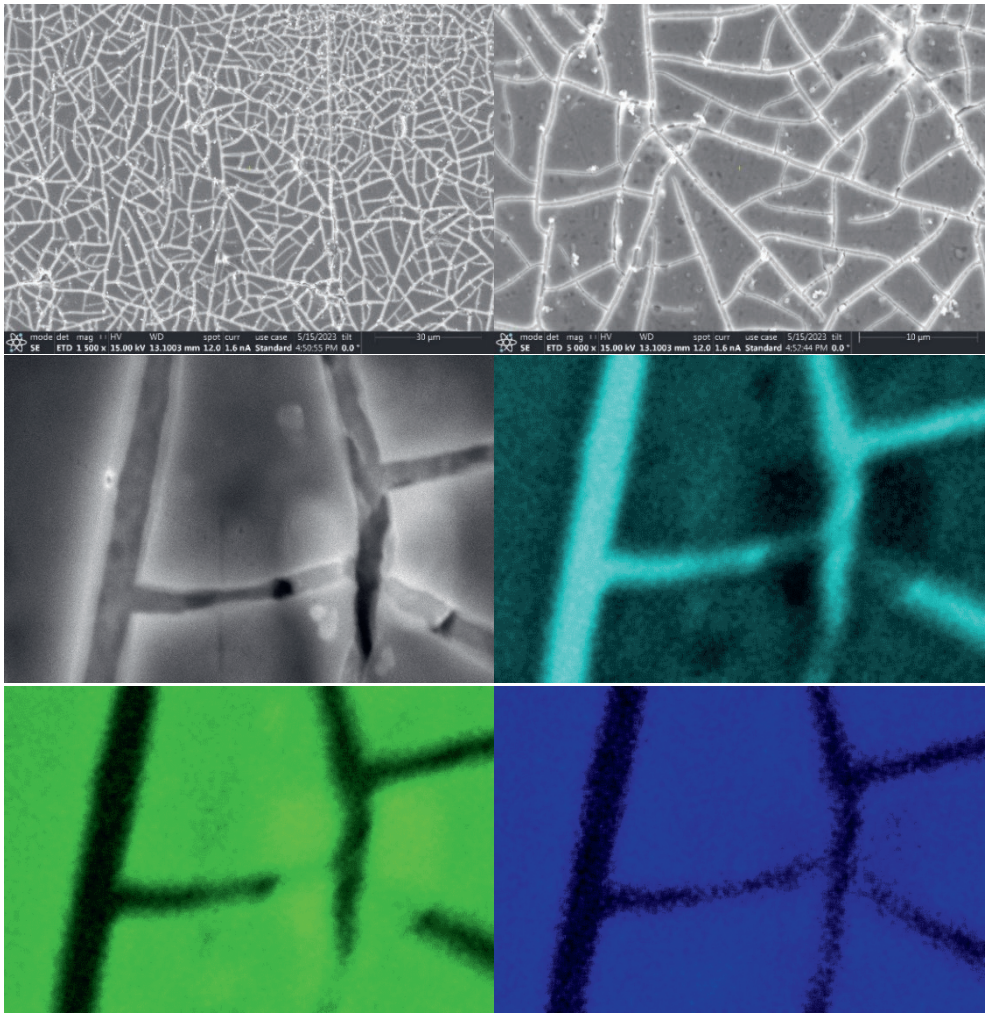

Figure D.1 SEM image of the Ni deposited electrode before CO2RR at respectively a) 1500 and b) 5000 magnification. EDX maps at 50 000 magnification showing c) the SEM image d) nickel e) oxygen f) phosphor.

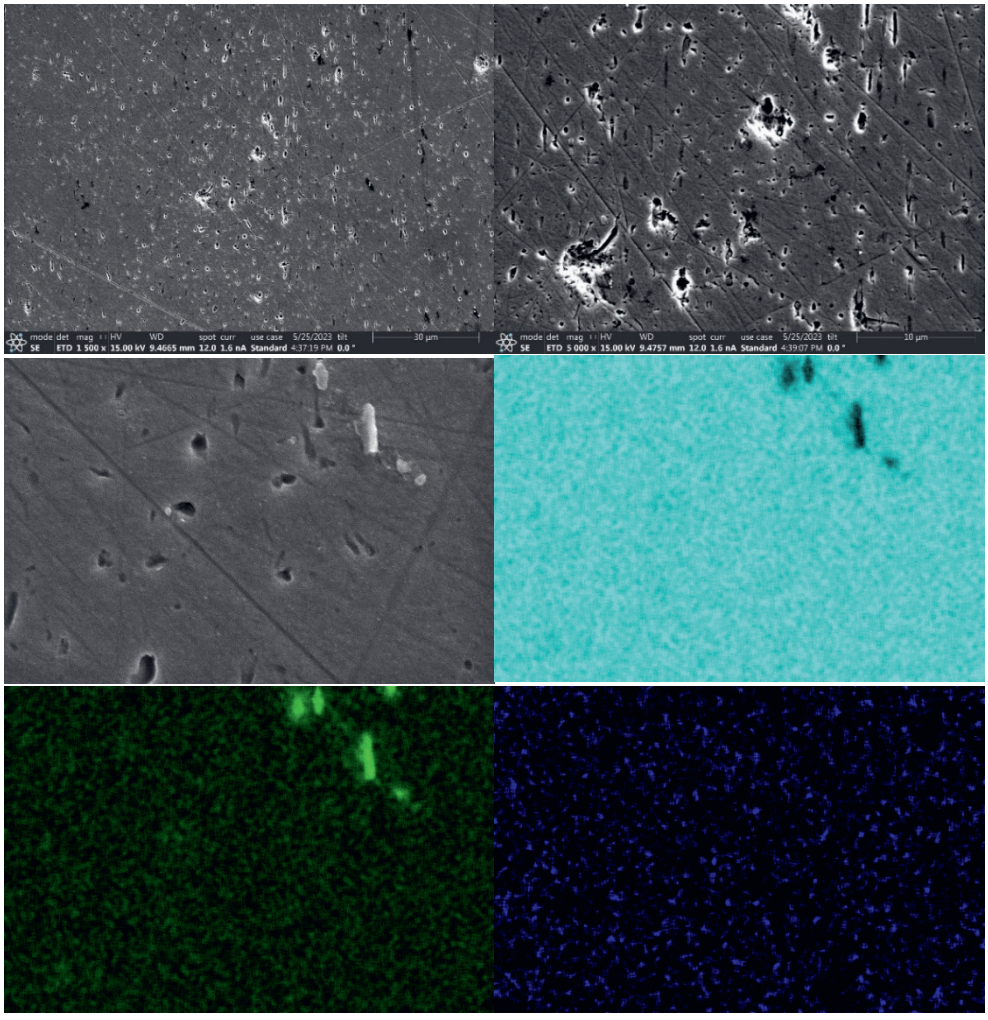

Figure D.2 SEM image of the Ni deposited electrode after CO2RR for 32 minutes at respectively a) 1500 and b) 5000 magnification. EDX maps at 50 000 magnification showing c) the SEM image d) nickel e) oxygen f) phosphor.

D.2 Effect of deposition

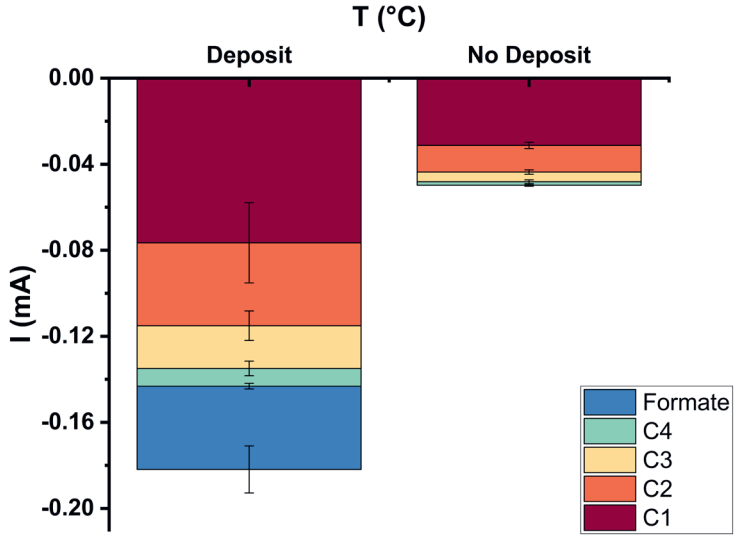

Figure D.3 Activity for CO_2 reduction on a polished polycrystalline Ni electrode with and without Ni deposition. Deposition shows higher activities at -1.175 V vs RHE at 18 °C

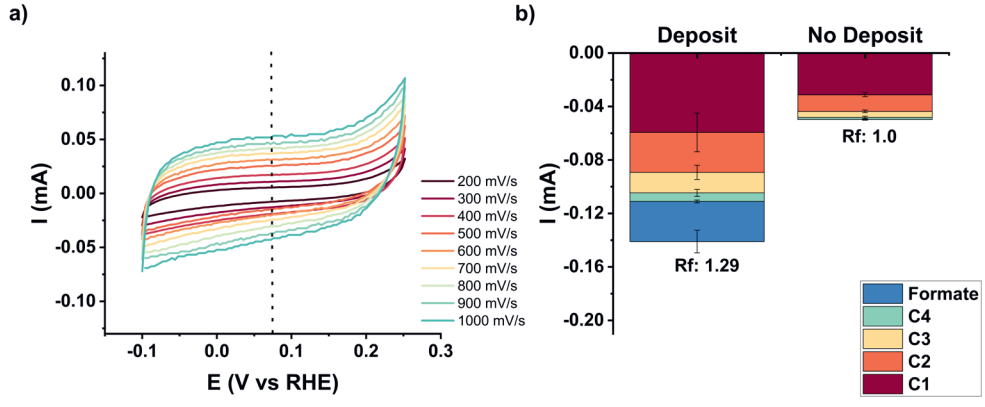

Figure D.4 a) Determination of the double layer capacitance by cyclic voltammetry. The double layer capacitance was determined at 0.075 V vs RHE and used to calculate a roughness factor (Rf). b) the roughness factor was used to normalize the deposited layer to the non-deposited catalyst, showing that the enhancement is not due to a roughness effect.

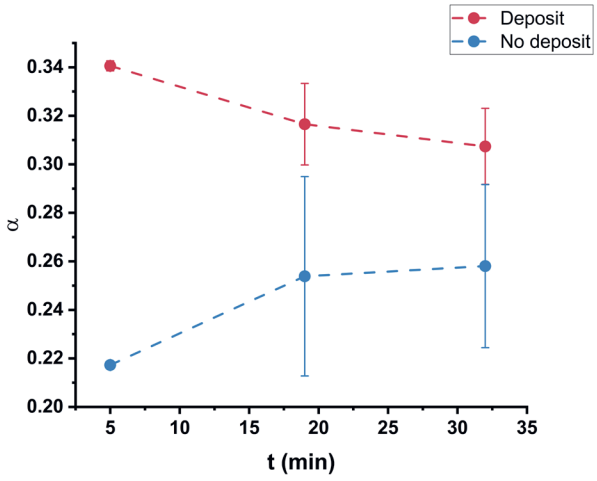

Figure D.5 Chain growth probability for CO_2 reduction on a polished polycrystalline Ni electrode with and without Ni deposition at -1.175 V vs RHE at 18 °C. Deposition shows higher chain growth probability

D.3 Anderson-Flory-Schultz plot

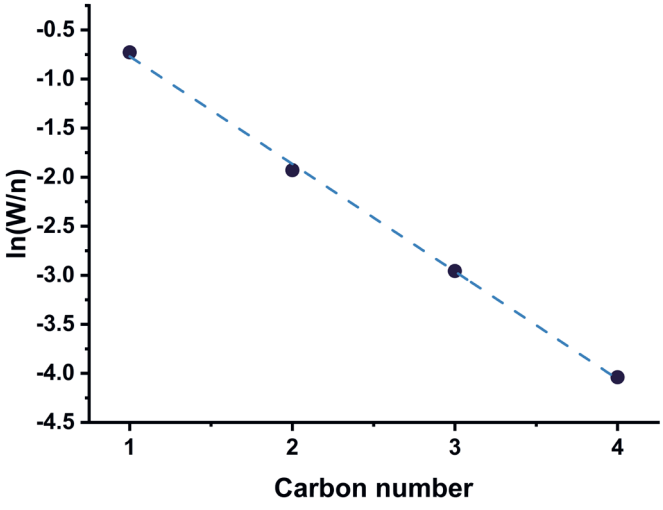

Figure D.6 Example of an Anderson-Flory plot to obtain the chain growth probability on the Ni electrode

D.4 Faradaic efficiency; temperature effect

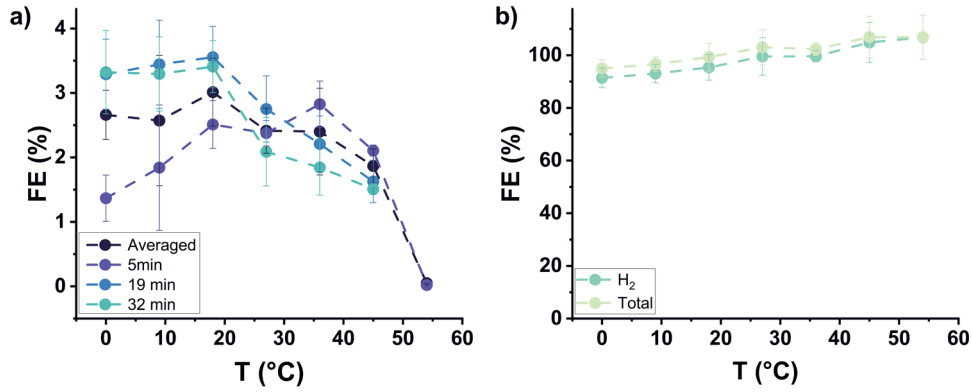

Figure D.7 Faradaic efficiency as function of temperature on Ni in 0.1 M $KHCO_3$ at -1.175 V vs RHE towards a) the total hydrocarbon formation (C1 up to C4 hydrocarbons) during CO_2 reduction both averaged and as function of time and b) towards H_2 and total FE

D.5 Deactivation by coke formation

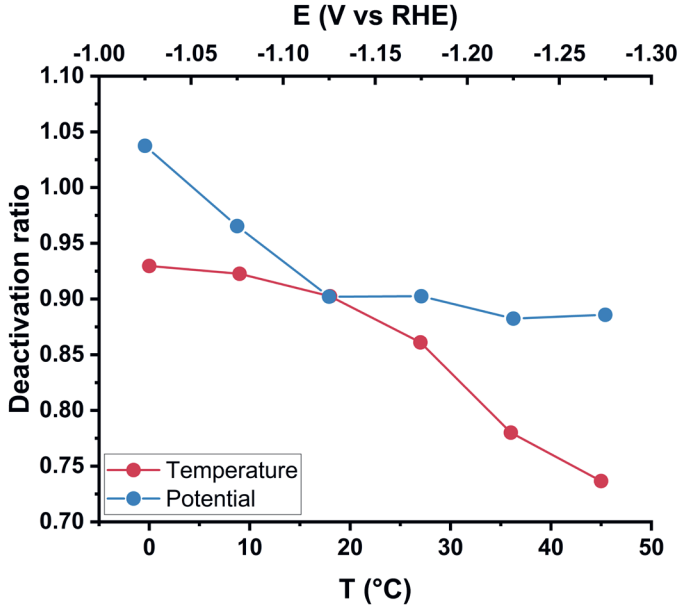

Figure D.8 Deactivation ratio as function of temperature and potential

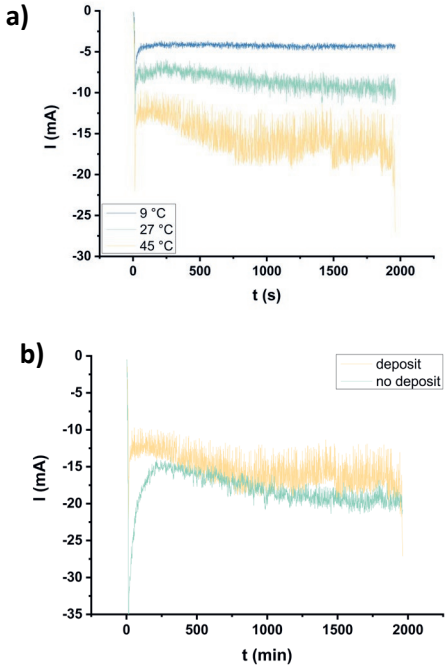

Figure D.9 a) Time dependence of current at different temperatures b) Time dependence of current at 45 °C both with the deposited electrode and the plain Ni electrode

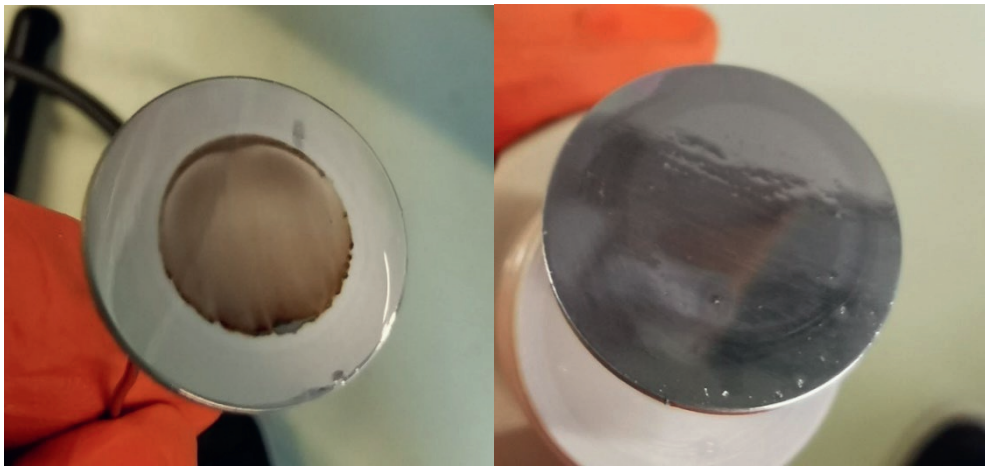

Figure D.10 Photographs of the electrode after a) CO2RR and b) HER showing that the coke only forms after CO2RR

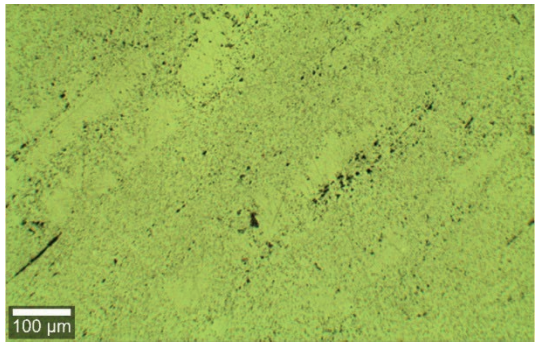

Figure D.11 Microscopy picture of the electrode after CO2RR showing the black deposits on the surface.

D.6 Faradaic efficiency; potential effect

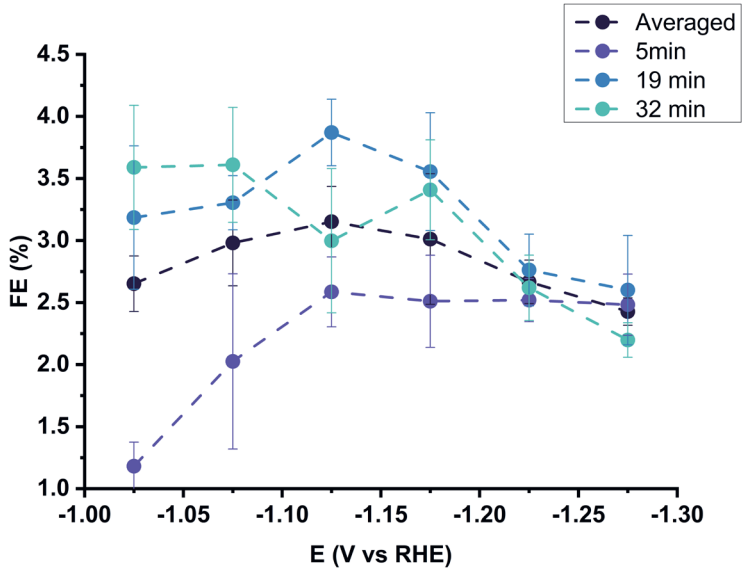

Figure D.12 Faradaic efficiency as function of potential and time on Ni in 0.1 M $KHCO_3$ at 18 °C

D.7 Comparing chain growth probabilities

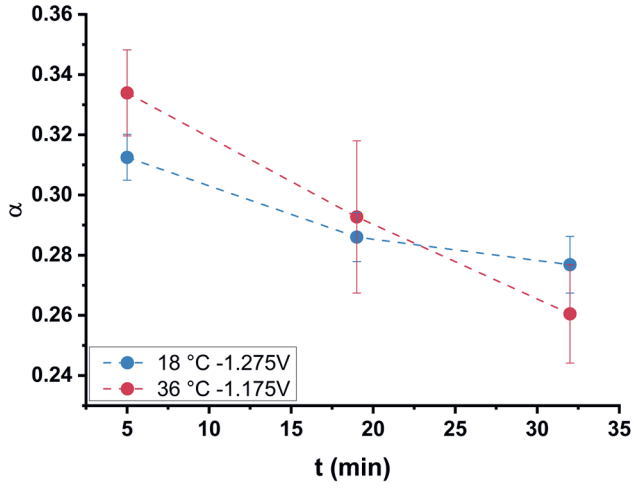

Figure D.13 Chain growth probability in time for 2 different experiments with similar activity showing that higher temperature causes deactivation of the catalyst

D.8 Cation dependence of the deactivation ratio

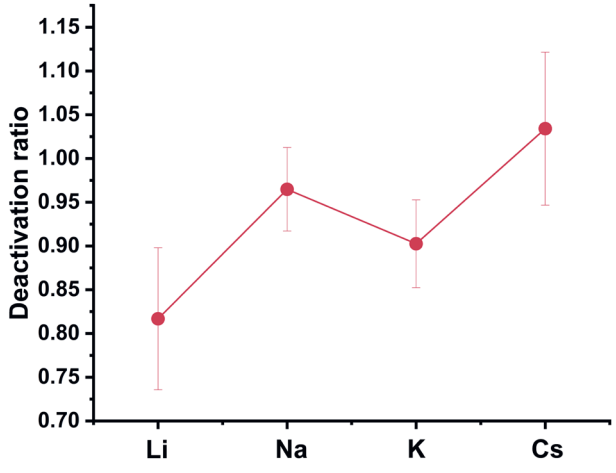

Figure D.13 Deactivation ratio as function of cation identity

D.9 Arrhenius plots

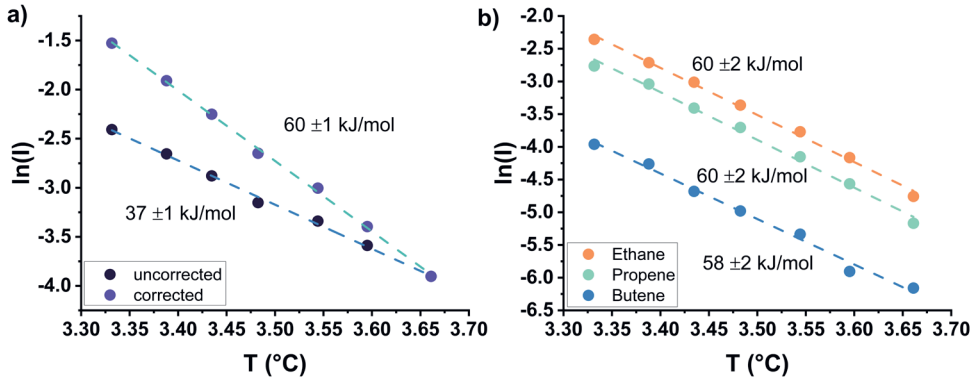

Figure D.15 a) Arrhenius plot after 5 min for methane, b) and for the other hydrocarbons which have similar activation energies

D.10 Relationship chain growth probability and activity

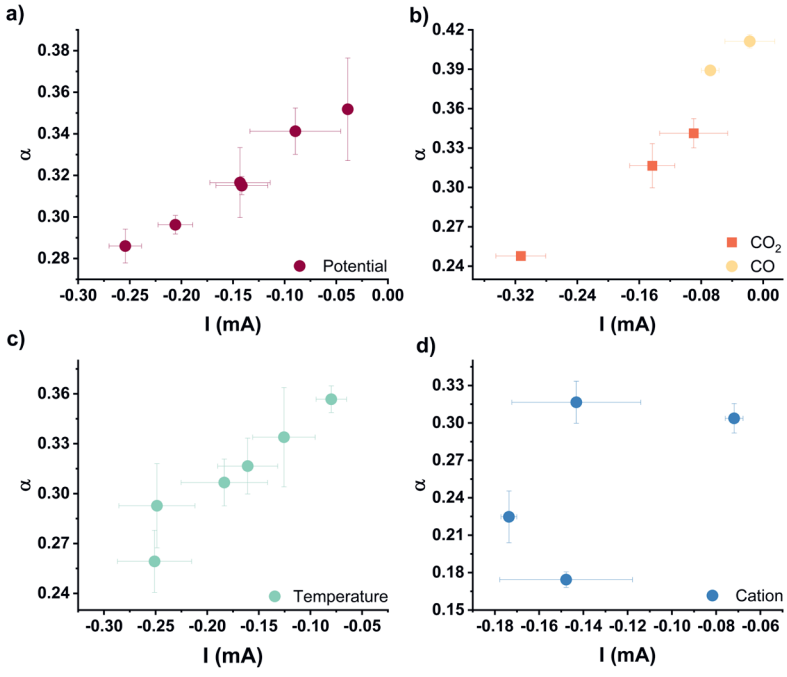

Figure D.16 chain growth probability α plotted vs the activity at different conditions: a) at different potentials (data from figure 3) b) at different anions and with CO or CO_2 as reactant (data from Figure 5) c) at different temperature (data from Figure 1) d) with different cations (data from Figure 4)

E

Supporting Information to Chapter 6

Design of a Rotating Disk Electrode setup operating under high pressure and temperature: application to CO_2 reduction on gold

E.1 High-pressure and High-temperature Rotating Disk Electrode (RDE) electrochemical cell design

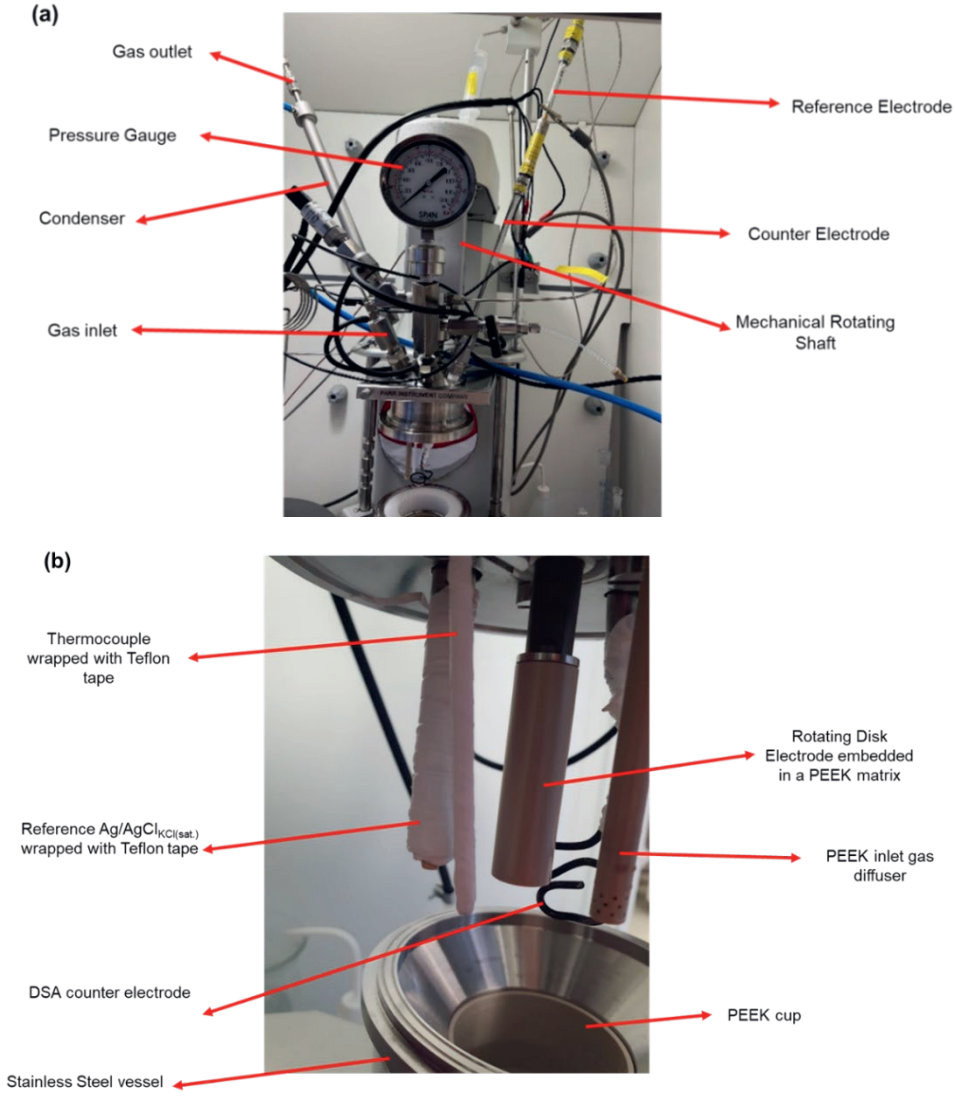

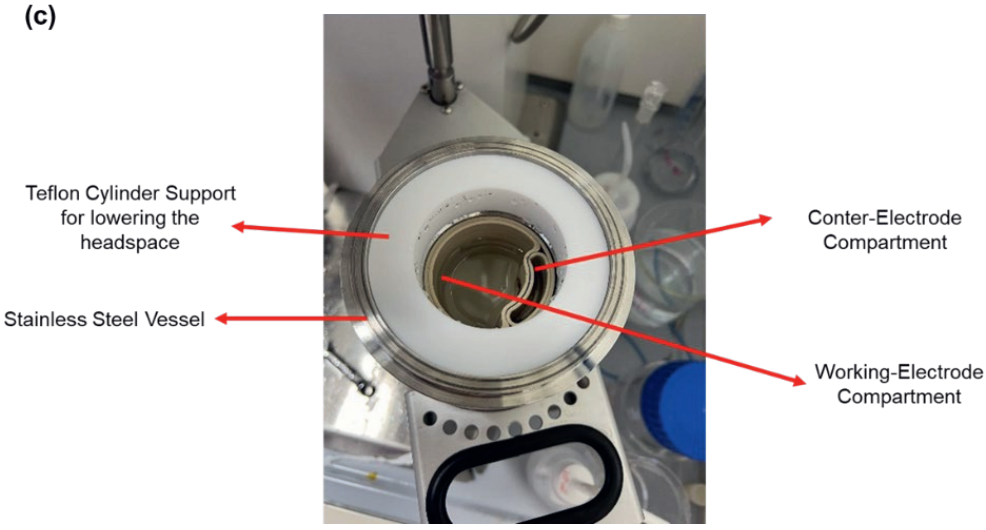
(c)
Teflon Cylinder Support for lowering the headspace
Stainless Steel Vessel
Conter-Electrode Compartment
Working-Electrode Compartment

(d)

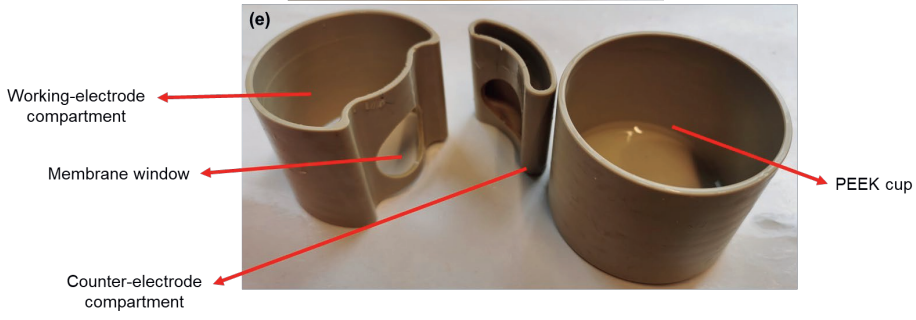
(e)
Working-electrode compartment
Membrane window
Counter-electrode compartment
PEEK cup

Figure E.1 Several pictures from the high-pressure electrochemical rotating disk electrode cell and its components (a) main mechanical parts of the high-pressure cell; (b) electrochemical parts of the high-pressure cell; (c) PEEK cup and membrane separator, and Teflon cylinder in the stainless steel vessel; (d-f) PEEK cup and membrane separator; (g) rotating disk electrode (gold); (h-i) reference electrode, thermocouple, and all other metal surface covered with Teflon tape; and (j) Teflon cylinder used to decrease headspace.

E.2 Cyclic voltammograms of Au and Pt

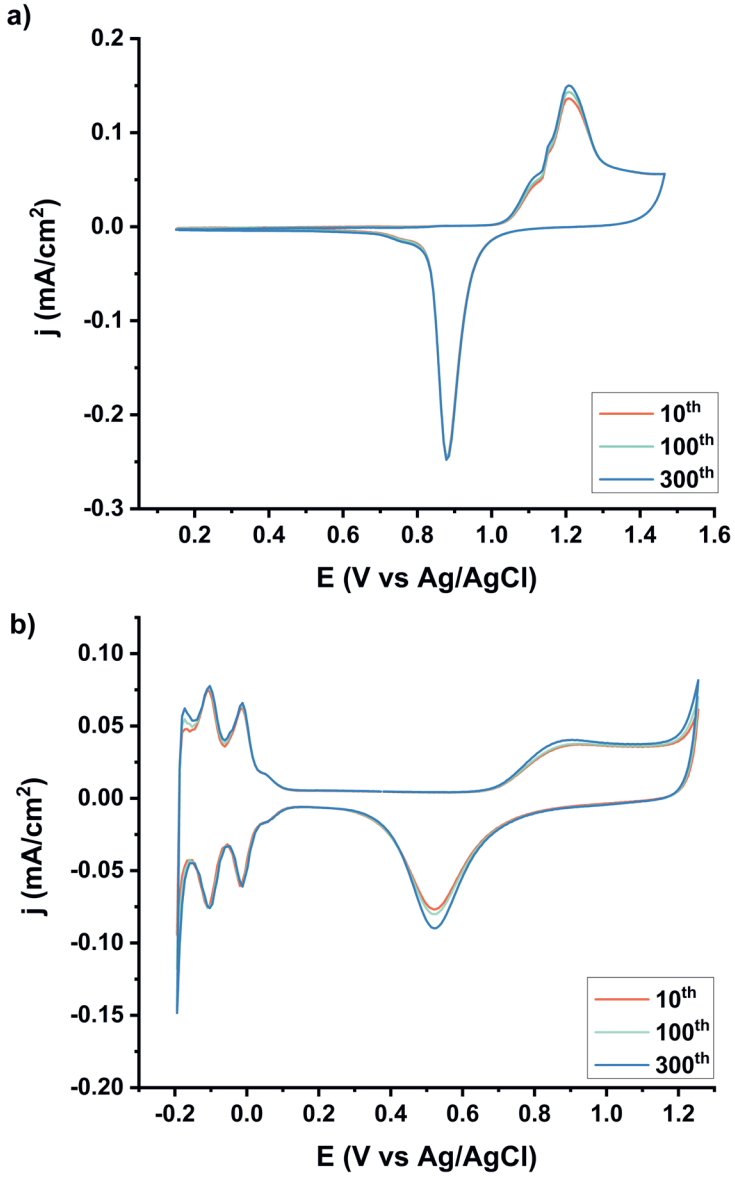

Figure E.2 Cyclic voltammograms of a) Au and b) Pt in 0.1M H_2SO_4 at scan rate of 100 mV/s, 0 barg, and 22°C.

E.3 Gold CVs at temperatures exceeding 100°C

Initially, when the temperature exceeds 100°C, an oxidative peak is observed when the potential is swept to negative potentials in the Au CVs, as shown at 1.10V (Figure E.3a). Additionally, the reduction peaks were drastically suppressed even though the oxidation peaks increased in intensity from 100°C to 145°C, indicating that phenomena other than the surface oxidation of Au were taking place. When the cell was cooled down and the temperature reached 40°C, the Au CV exhibited a marked change from the starting point (Figure E.3b), indicating a significant surface change and/or electrolyte contamination. This CV profile is very similar to the Au CV in the presence of Cl^- species, as shown in Figure E.3b, representing an Au CV recorded in 0.1M H_2SO_4 containing 100 μM KCl. These tests indicate that leakage of Cl species from the Ag/AgCl reference contaminated the electrolyte, and higher leakage is enhanced at higher temperatures.

We have identified that we can extend the operating limit up to 125°C by storing the reference electrode in 0.1 M KCl instead of saturated KCl. By rinsing the reference electrode surface thoroughly with ultrapure water and replacing the Teflon tape covering before each measurement, we did not observe electrodissolution behavior at temperatures up to 125°C. This indicates that Cl^- contamination originates from the liquid junction rather than the internal compartment of the reference electrode. However, at present, we lack sufficient information to ascertain whether very small amounts of chloride also release over time, which can potentially be a problem for long-term measurements.

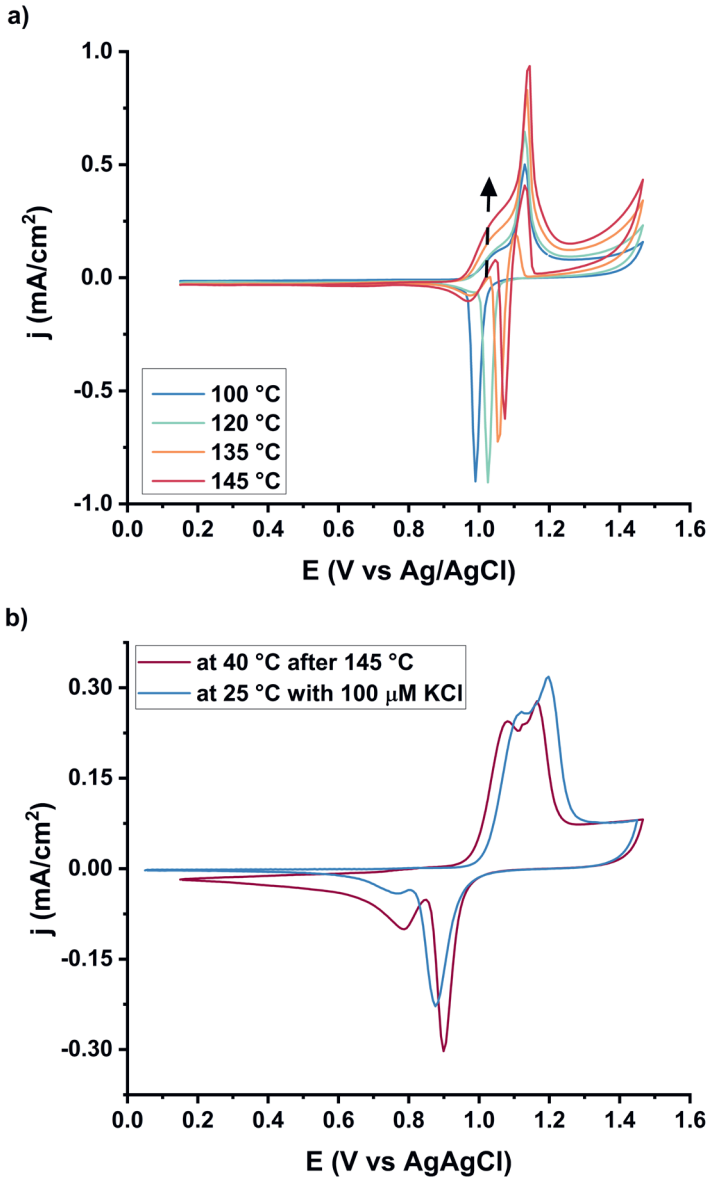

Figure E.3 Cyclic voltammograms in 0.1M H_2SO_4 at different temperatures: (a) from 30°C to 100°C; (b) at 100°C; (c) from 100°C to 145°C; (d) at 145°C; (e) after cooling the temperature down from 145°C to 40°C; (f) and at 25°C in a fresh electrolyte containing 100 µM KCl. All measurements were recorded at 0 barg and with scan rate of 100 mV/s.

E.4 Linear Sweep Voltammogram at different rotation speed

Figure E.5 shows, at different current density scales, the effect of rotation speed on the linear sweep voltammogram (LSV) of CO_2-saturated 0.1 M $KHCO_3$ electrolyte at 0 barg and room temperature for 500, 700, and 1000 rpm (data extracted from Figure 6.4a). At high current densities, the higher the rotation speed (ω), the higher the measured current (Figure E.4a and Figure 6.4a). However, at lower current densities, the opposite is observed in agreement with Goyal et al [1] as shown in Figure 6.4b. They argue that this decrease in current with rotation is due to suppression of HER by improved mass transport of OH^-. We hypothesize that the increase in current with rotation at higher current densities is due to improved bubble removal facilitated by the higher rotation speed.

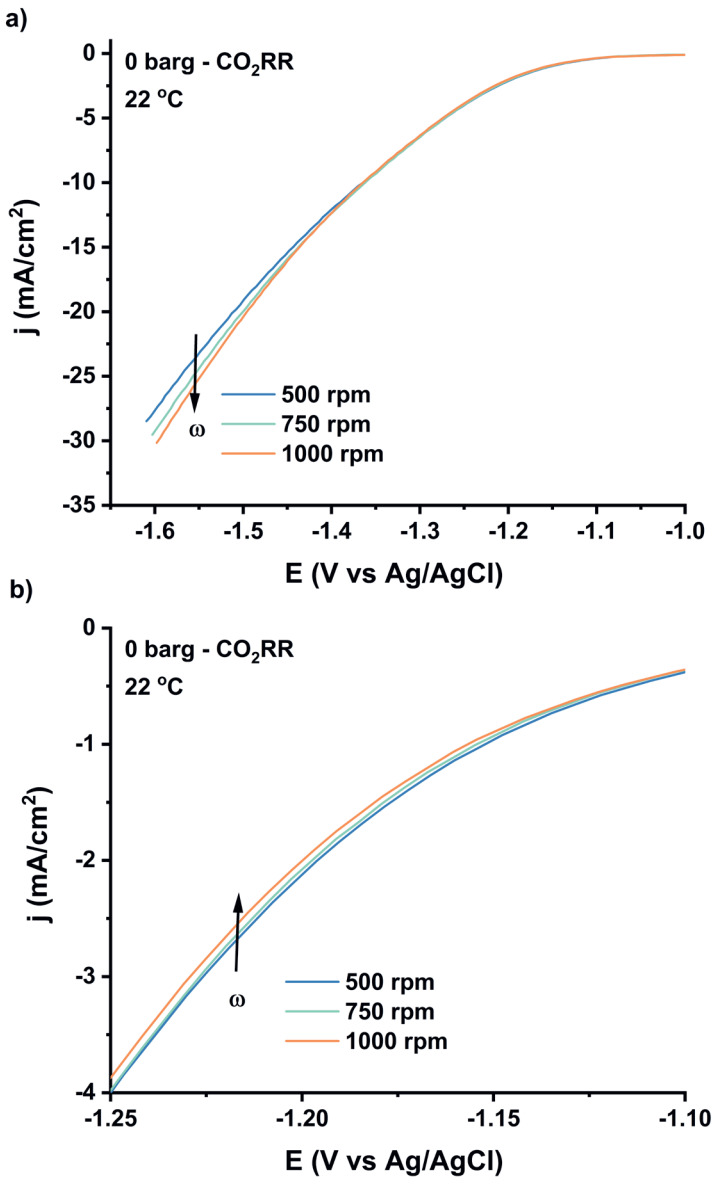

Figure E.4 Linear sweep voltammograms (LSVs) in 0.1 M $KHCO_3$ at different scan rates. b) is zoomed in of a) at lower current densities. LSVs recorded at 0 barg and 22°C.

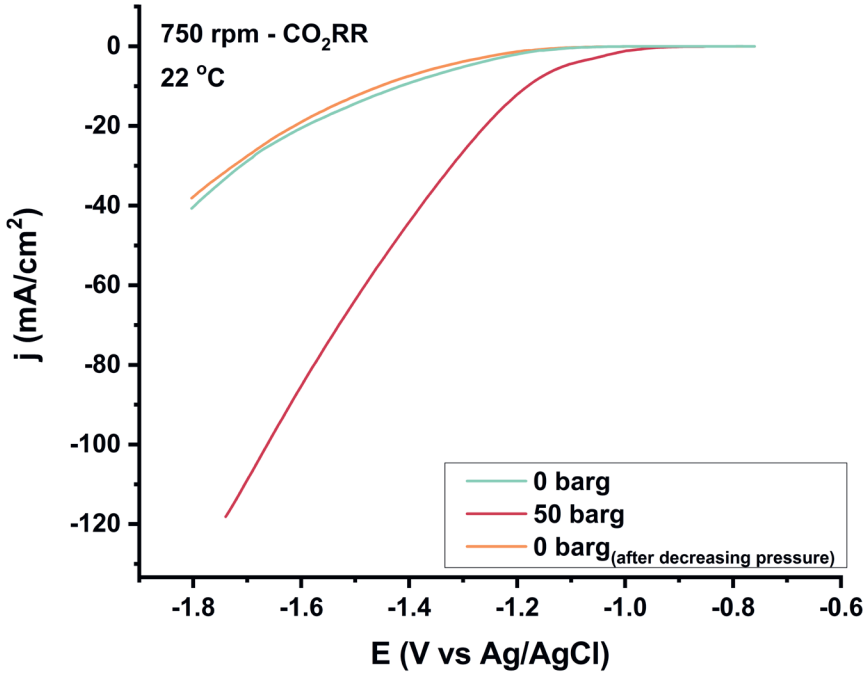

Figure E.5 Comparison of Linear sweep voltammograms (LSVs) in CO_2-saturated 0.1M $KHCO_3$ before increasing pressure, then at 50 barg, and then returning pressure to 0 barg.

Reference

1. Goyal, A., Marcandalli, G., Mints, V. A. & Koper, M. T. M. *J Am Chem Soc* **142**, 4154–4161 (2020).

F

Supporting Information to Chapter 7

Change in the C-C coupling mechanism during CO_2 electroreduction on Cu at elevated temperature and pressure

F.1 Working and reference electrode

Table F.1 Geometric electrode area based on double layer capacitance measurements. A, B, C and D are 1 mm Cu wires of different lengths, while E is a reference Cu disk (8mm diameter) with known geometric surface area

Electrode	A	B	C	D	E
C [µF]	252	139	44.3	21.1	27.8
Area [cm^2]	4.556	2.513	0.8010	0.3815	0.5027

Electrode A was used for experiments at all potentials and 25 °C, -1.3 V vs SHE up to 75 °C, -1.2 V vs SHE and 125 °C,

Electrode B was used for experiments at -1.5/-1.4 V vs SHE and 50 °C, -1.3 V vs SHE and 100 to 125 °C

Electrode C was used for experiments at -1.5 V and 75 °C, -1.4 V vs SHE and 75 to 125 °C, -1.3 V vs SHE and 150 °C

Electrode D was used for experiments at -1.5 V vs SHE above 75 °C

Table F.2 Shift of the Ag/AgCl reference with 0.1 M KCl at different temperatures, compared to SHE(T)

T [°C]	25	50	75	100	125	150
$E^{\mathrm{Ag\|AgCl}}(T)$ [mV]	230.3	214.5	195.9	174.6	151.1	125.5

F.2 Screening temperature, pressure and potential

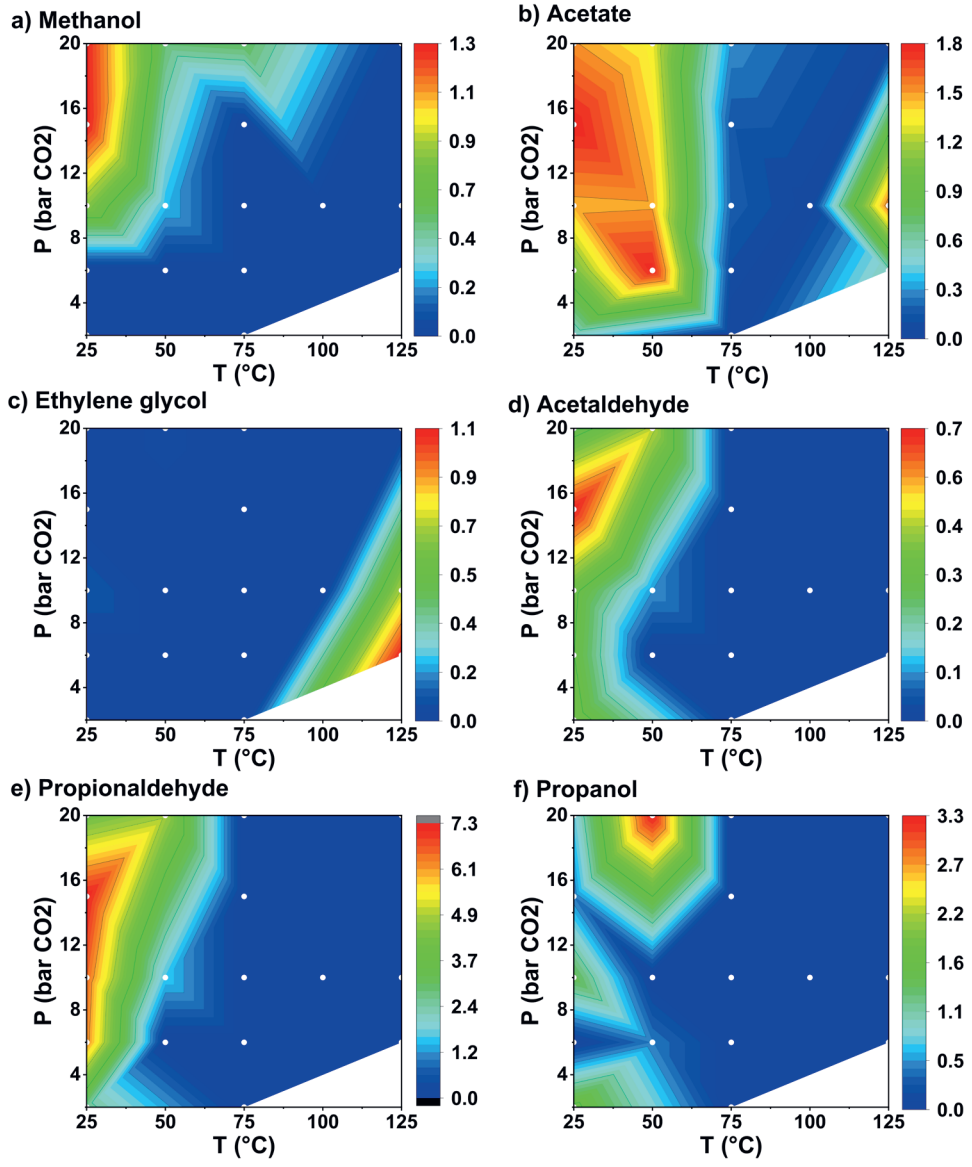

Figure F.1 Faradaic efficiency towards the minor CO2RR products as function of temperature and pressure at -1.4 V vs SHE in 0.2 M $KHCO_3$ with a 50/50 ratio of CO_2 and Ar. The white dots give the measured points and the maps are constructed via interpolation between these points. FE for a) methanol b) acetate c) ethylene glycol d) acetaldehyde e) propionaldehyde and f) 1-propanol

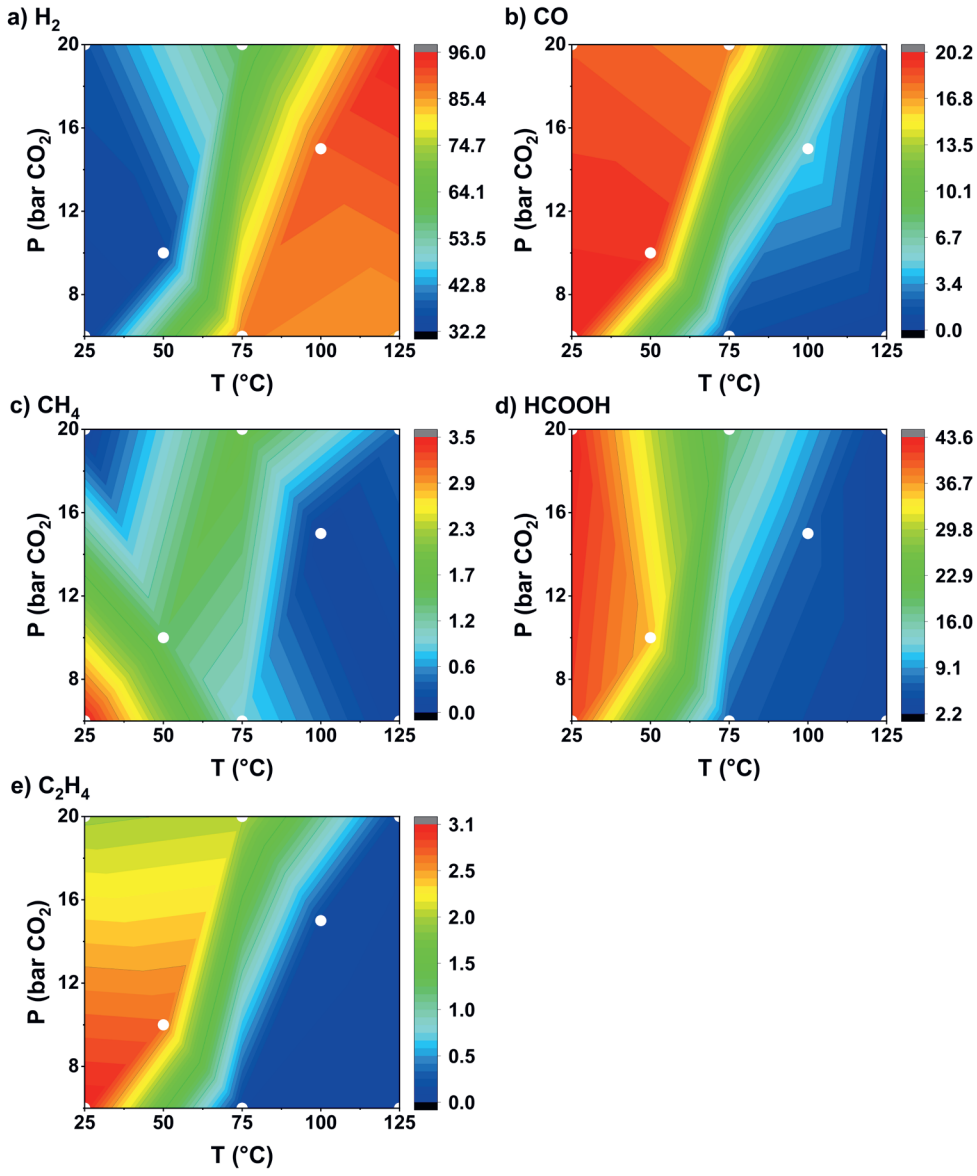

Figure F.2 Faradaic efficiency towards the main CO2RR products as function of temperature and pressure at -1.3 V vs SHE in 0.2 M $KHCO_3$ with a 50/50 ratio of CO_2 and Ar. The white dots give the measured points and the maps are constructed via interpolation between these points. FE for a) hydrogen b) carbon monoxide c) formic acid d) methane e) ethylene and f) ethanol

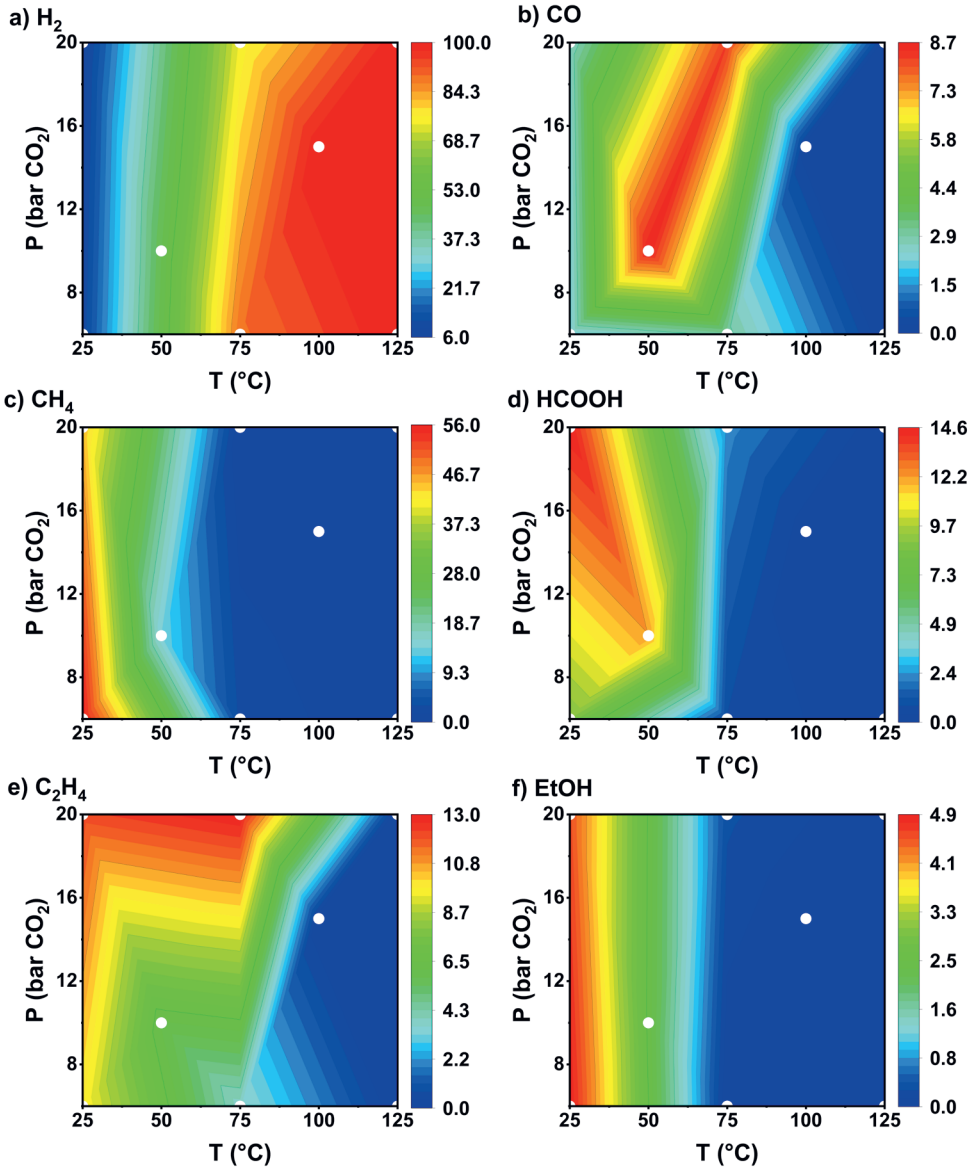

Figure F.3 Faradaic efficiency towards the main CO2RR products as function of temperature and pressure at -1.5 V vs SHE in 0.2 M $KHCO_3$ with a 50/50 ratio of CO_2 and Ar. The white dots give the measured points and the maps are constructed via interpolation between these points. FE for a) hydrogen b) carbon monoxide c) formic acid d) methane e) ethylene and f) ethanol

F.3 Instable currents at elevated temperatures

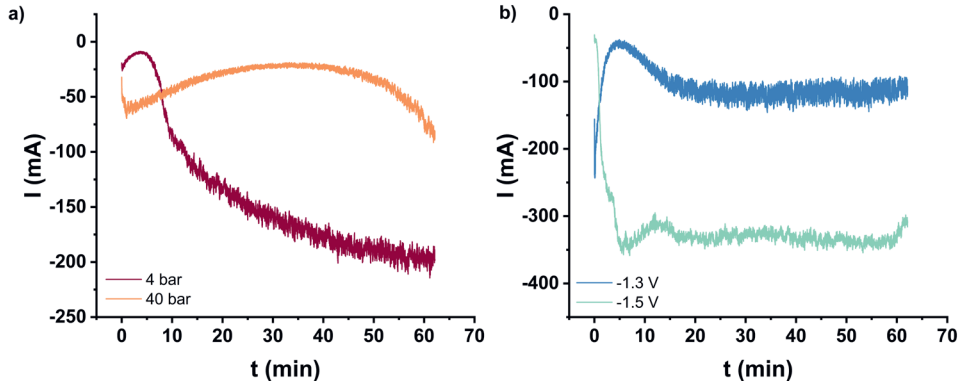

Figure F.4 Current as function of time for a) 4 and 40 bar at -1.5 V vs SHE at 75 °C and b) 24 bar at 125 °C at -1.3 V and -1.5 vs SHE. This illustrates that at elevated temperatures the current is not stable, especially at low pressures as seen in a). In b) the typical current profile at 125 °C and -1.3 V is observed, where the current is unstable in the first 20 minutes and first decreases and then increases again after which it stabilizes. It also shows the instability at higher overpotentials, where even the smallest electrode goes to currents above -300 mA, while at the start is was only -30 mA.

F.4 Switching mechanism at high pressure and high temperature

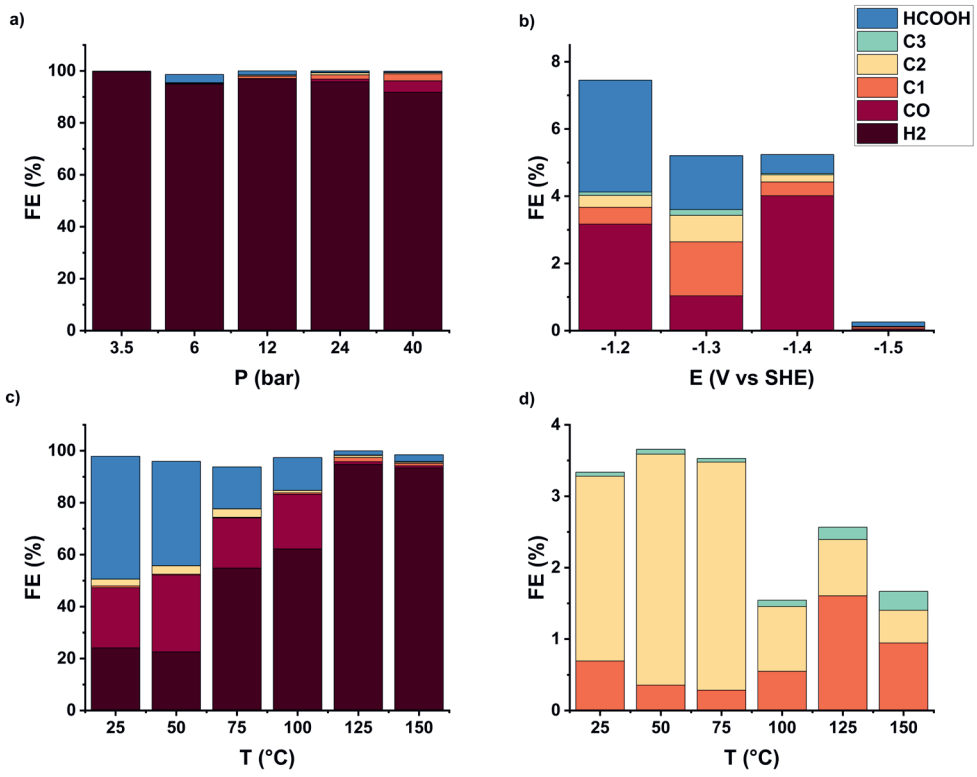

Figure F.5 Faradaic efficiencies for the CO2RR reduction as function of a) pressure at 24 bar and -1.3 V vs SHE b) potential at 24 bar and 125 °C and c and d) temperature at 24 bar and -1.3 V vs SHE. a) and c) show total FE. b) shows the CO2RR products with the remaining FE being H2 and d) shows only the hydrocarbons

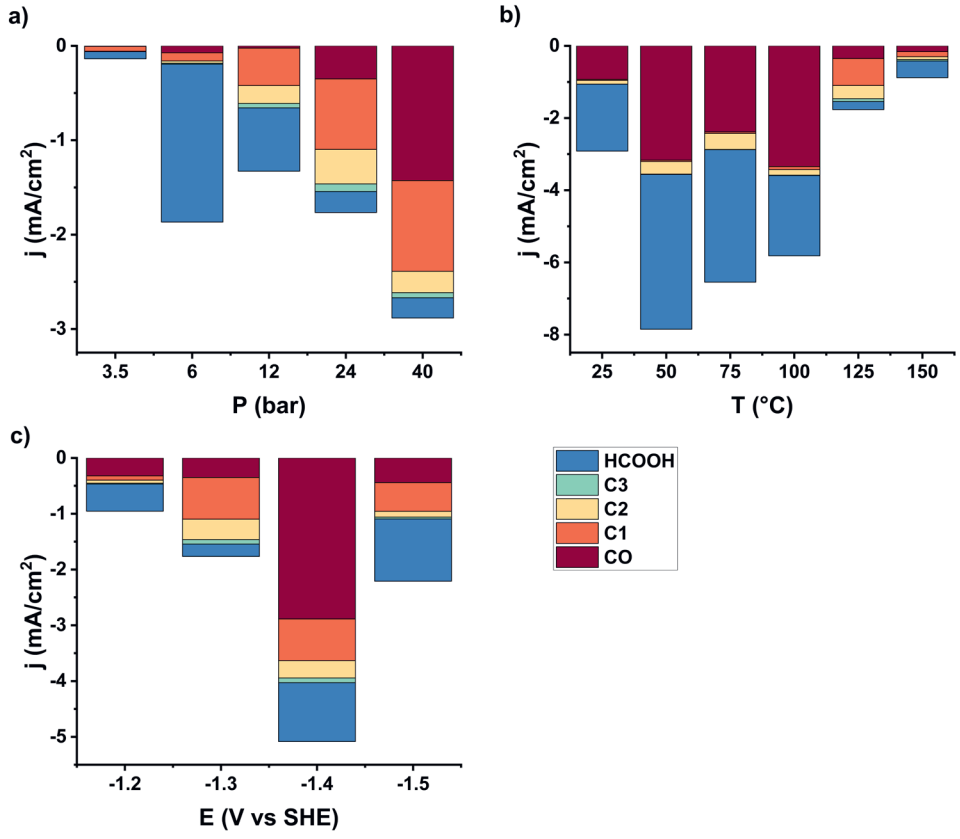

Figure F.6 Partial current density for the CO2RR products as function of a) pressure at 24 bar and -1.3 V vs SHE b) temperature at 24 bar and -1.3 V vs SHE c) potential at 24 bar and 125 °C.

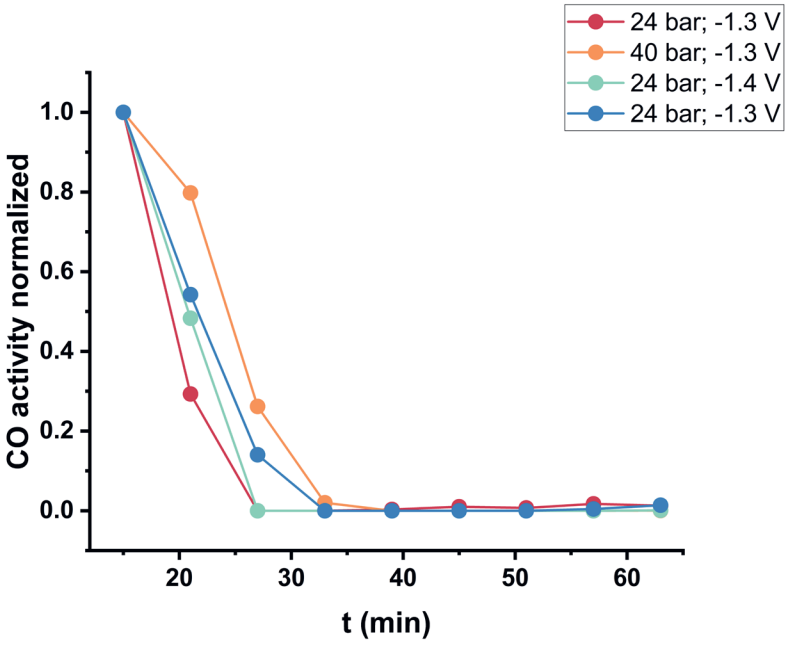

Figure F.7 The normalized CO activity as function of time for several conditions, all at 125 °C. This illustrates that CO is only produced at the start of the experiment as it decreases rapidly and from 32 min the activity is 0

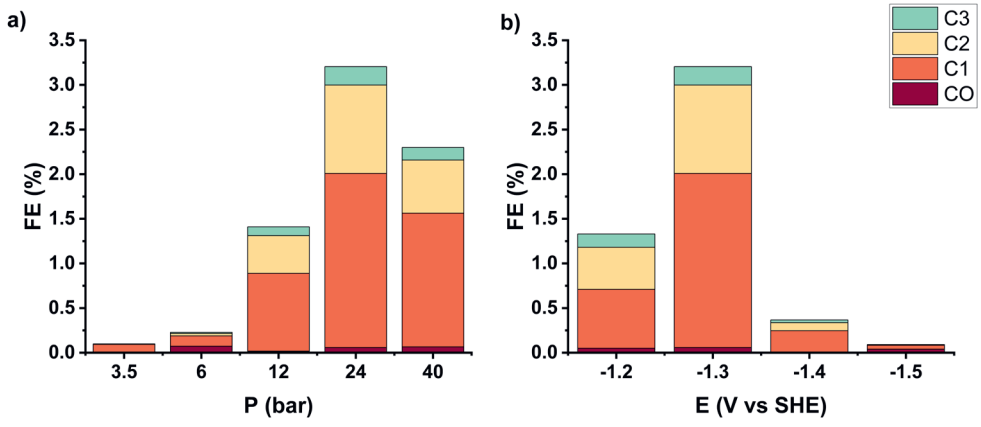

Figure F.8 Partial current density for the CO2RR products at function of as function of a) pressure at 24 bar and -1.3 V vs SHE b) temperature at 24 bar and -1.3 V vs SHE, but only taking into account the gaseous products during the last 30 minutes of the experiment.

Table F.4 Chain growth probability as function of temperature, pressure and potential

Temperature (°C)	Pressure (bar)	Potential (V vs SHE)	Chain growth probability
75	24	-1.3	0.22
100	24	-1.3	0.30
125	24	-1.3	0.33
150	24	-1.3	0.41
125	12	-1.3	0.35
125	40	-1.3	0.30
125	24	-1.2	0.41
125	24	-1.4	0.34
125	24	-1.5	0.31

F.5 Effect of temperature on the CO2RR at -1.5 V vs SHE

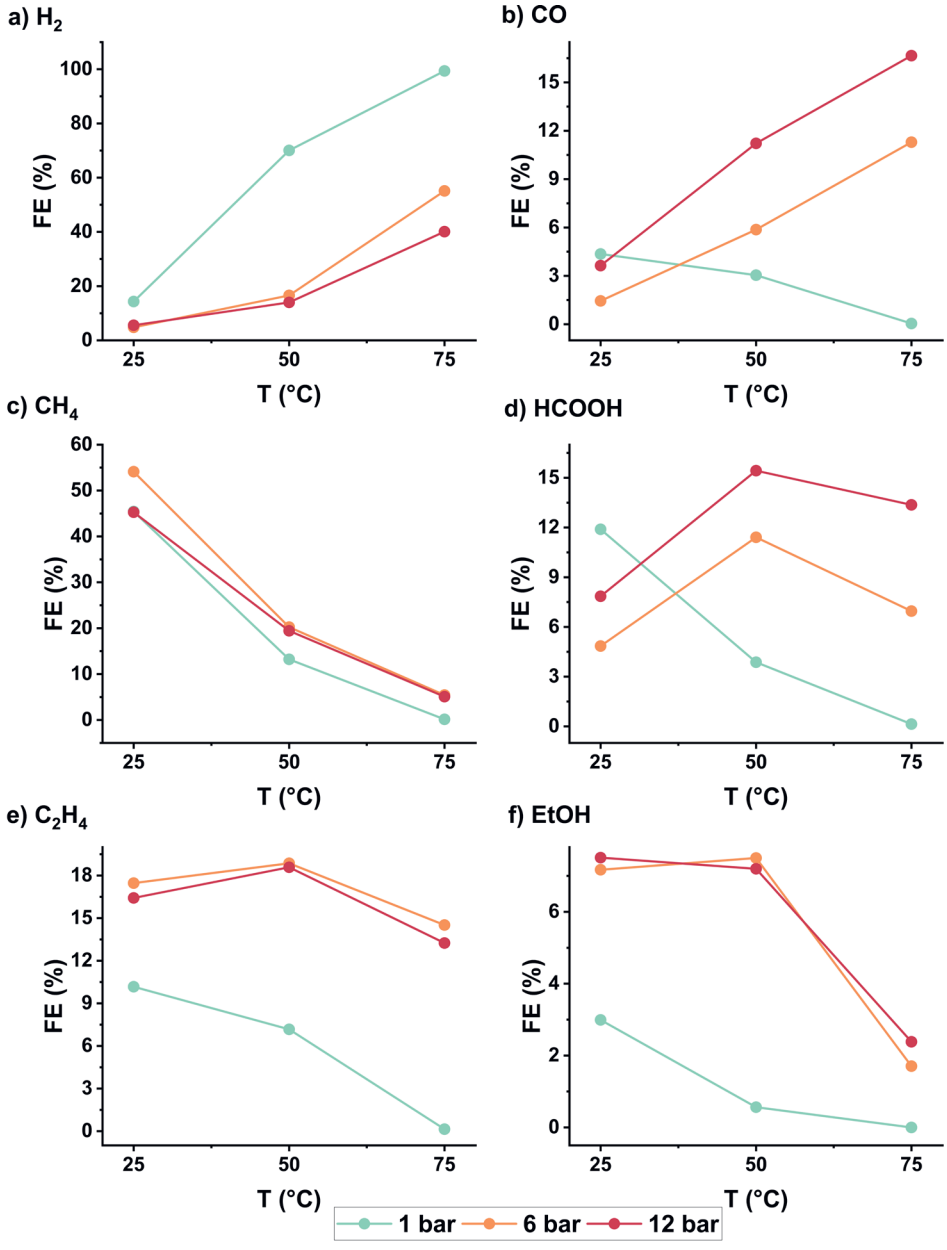

Figure F.9 Faradaic efficiency towards the main CO2RR products at different pressures as function of temperature at -1.5 V vs SHE in 0.2 M $KHCO_3$. FE for a) hydrogen b) carbon monoxide c) formic acid d) methane e) ethylene and f) ethanol

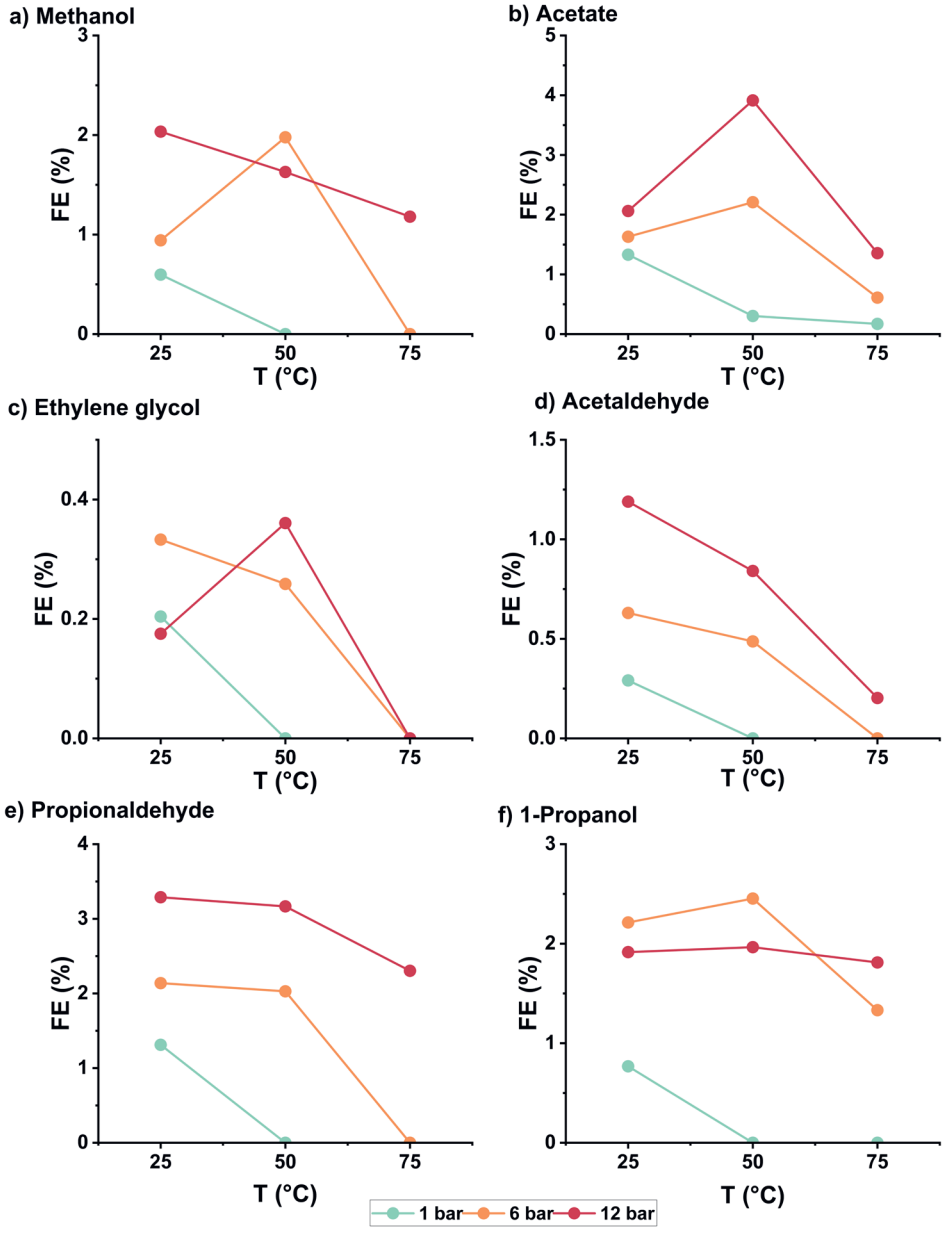

Figure F.10 Faradaic efficiency towards the minor CO2RR products at different pressures as function of temperature at -1.5 V vs SHE in 0.2 M $KHCO_3$. FE for a) methanol b) acetate c) ethylene glycol d) acetaldehyde e) propionaldehyde f) 1-Propanol

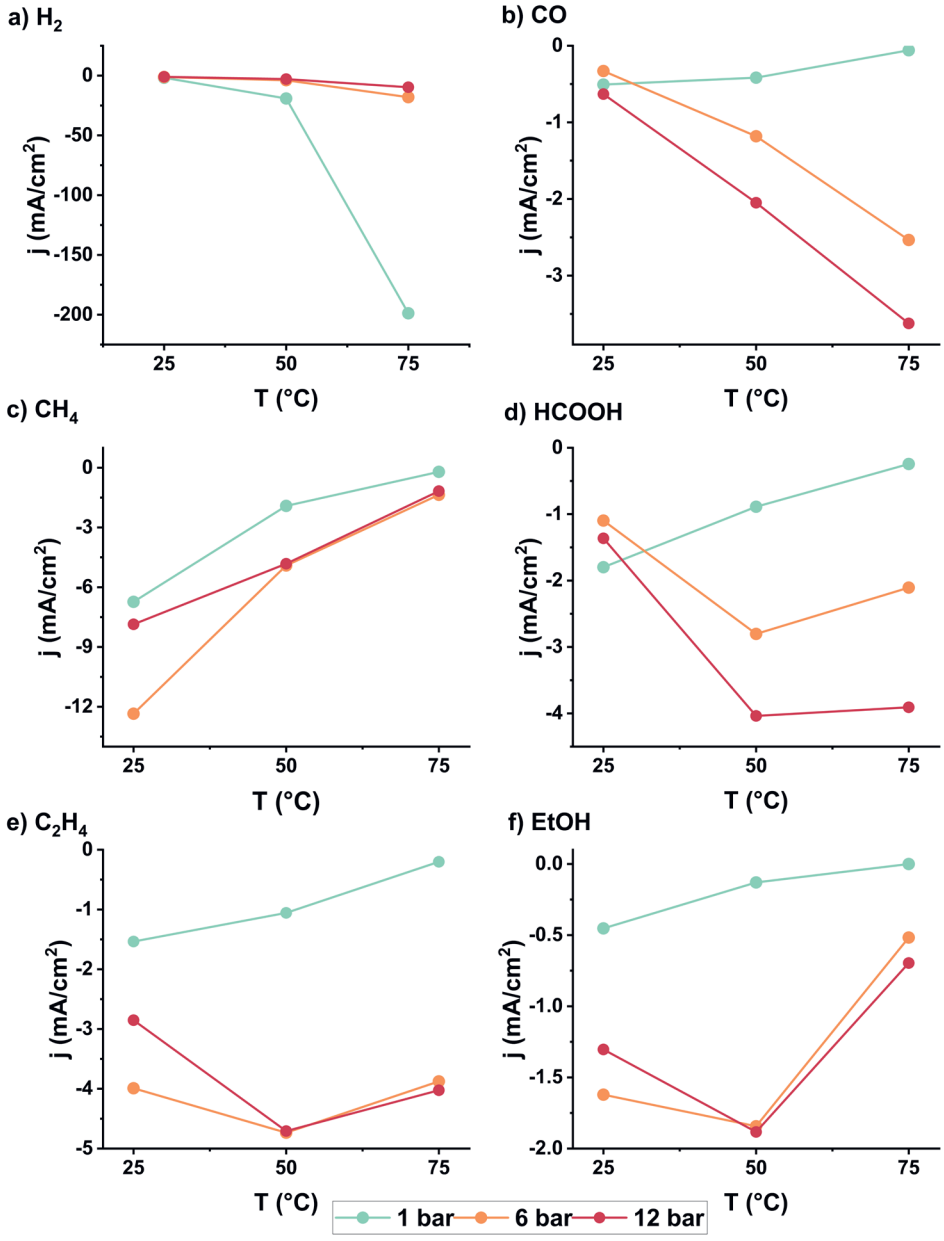

Figure F.11 Partial current density towards the main CO2RR products at different pressures as function of temperature at -1.5 V vs SHE in 0.2 M $KHCO_3$. FE for a) hydrogen b) carbon monoxide c) formic acid d) methane e) ethylene and f) ethanol

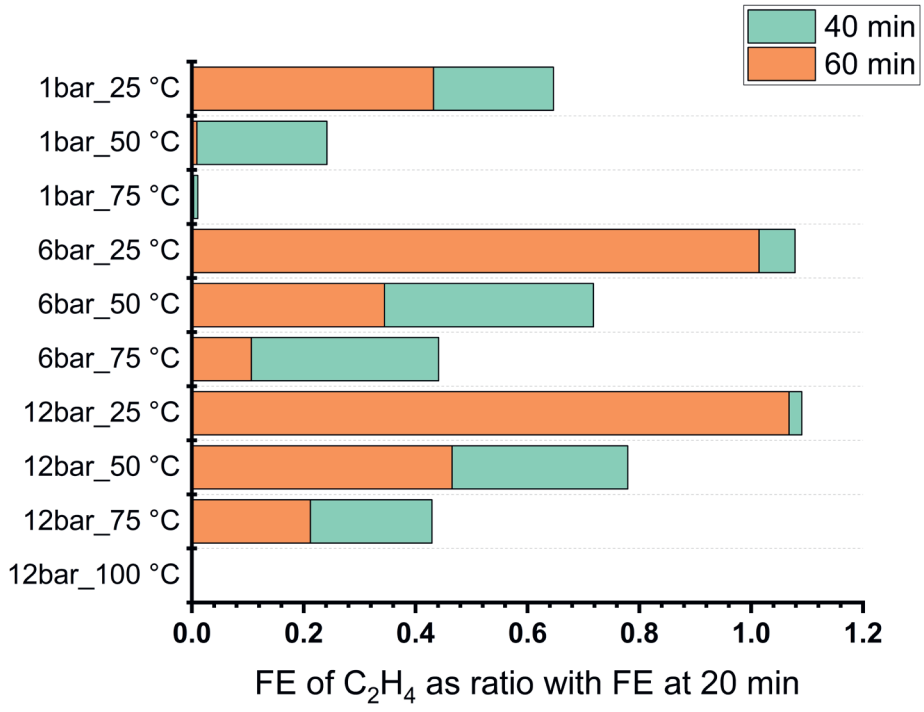

Figure F.12 Stability as function of temperature and pressure. Stability is here defined as the FE that remains after 40 and 60 minutes compared to the FE at 20 minutes at a certain condition.

F.6 Effect of pressure on the CO2RR at -1.5 V vs SHE

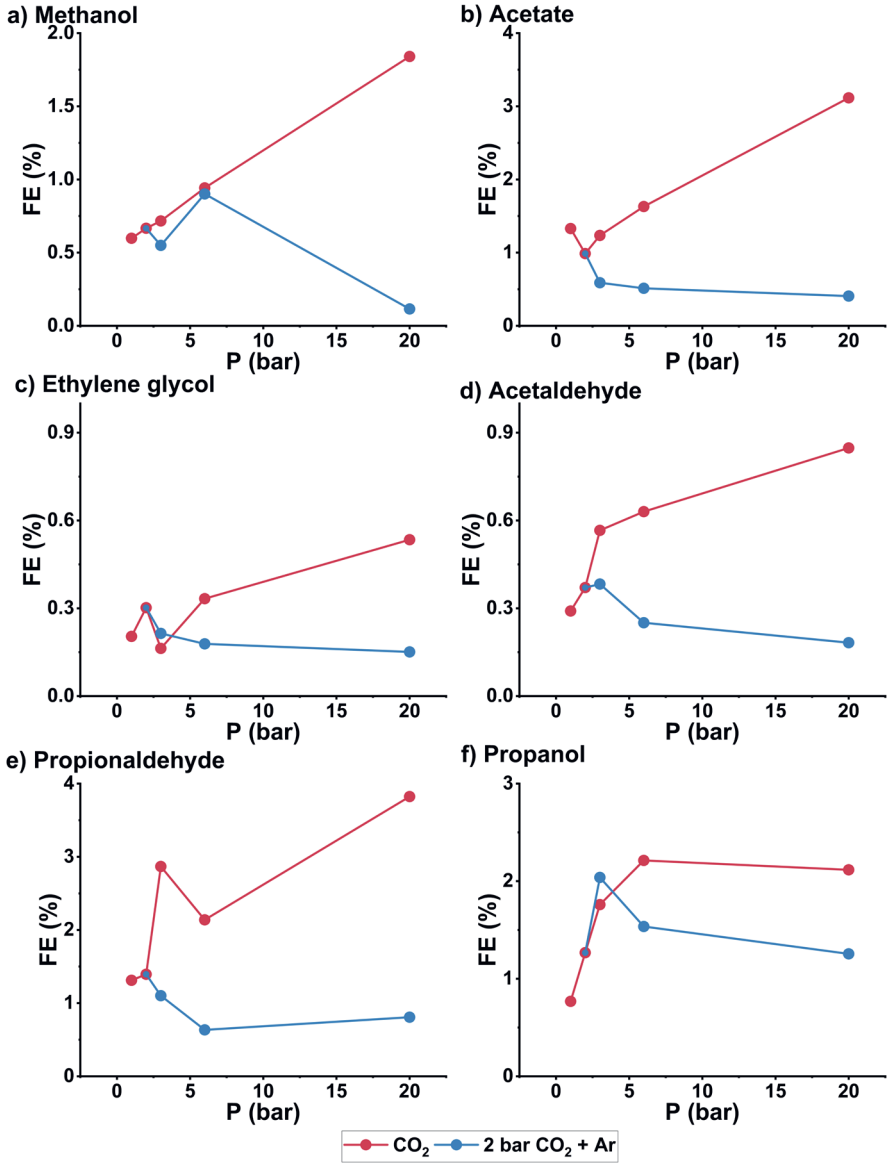

Figure F.13 Faradaic efficiency towards the minor CO2RR products as function of CO_2 and total pressure at -1.5 V vs SHE in 0.2 M $KHCO_3$ at 25 °C. Red lines are performed in pure CO_2 and blue lines are at 2 bar of CO_2 and pressure is increased with Ar. FE for a) methanol b) acetate c) ethylene glycol d) acetaldehyde e) propionaldehyde and f) 1-propanol

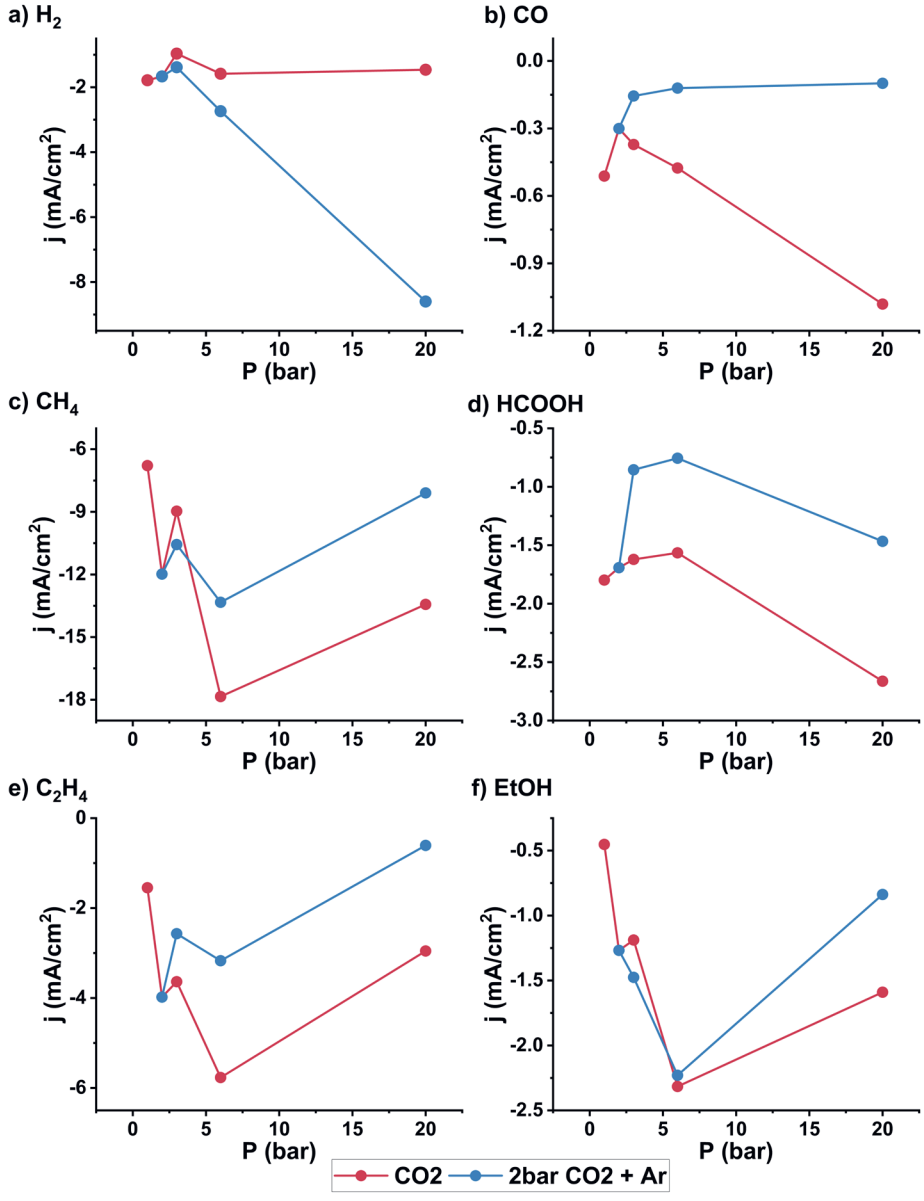

Figure F.14 Partial current density towards the main CO2RR products as function of CO_2 and total pressure at -1.5 V vs SHE in 0.2 M $KHCO_3$ at 25 °C. Red lines are performed in pure CO_2 and blue lines are at 2 bar of CO_2 and pressure is increased with Ar. FE for a) hydrogen b) carbon monoxide c) formic acid d) methane e) ethylene and f) ethanol

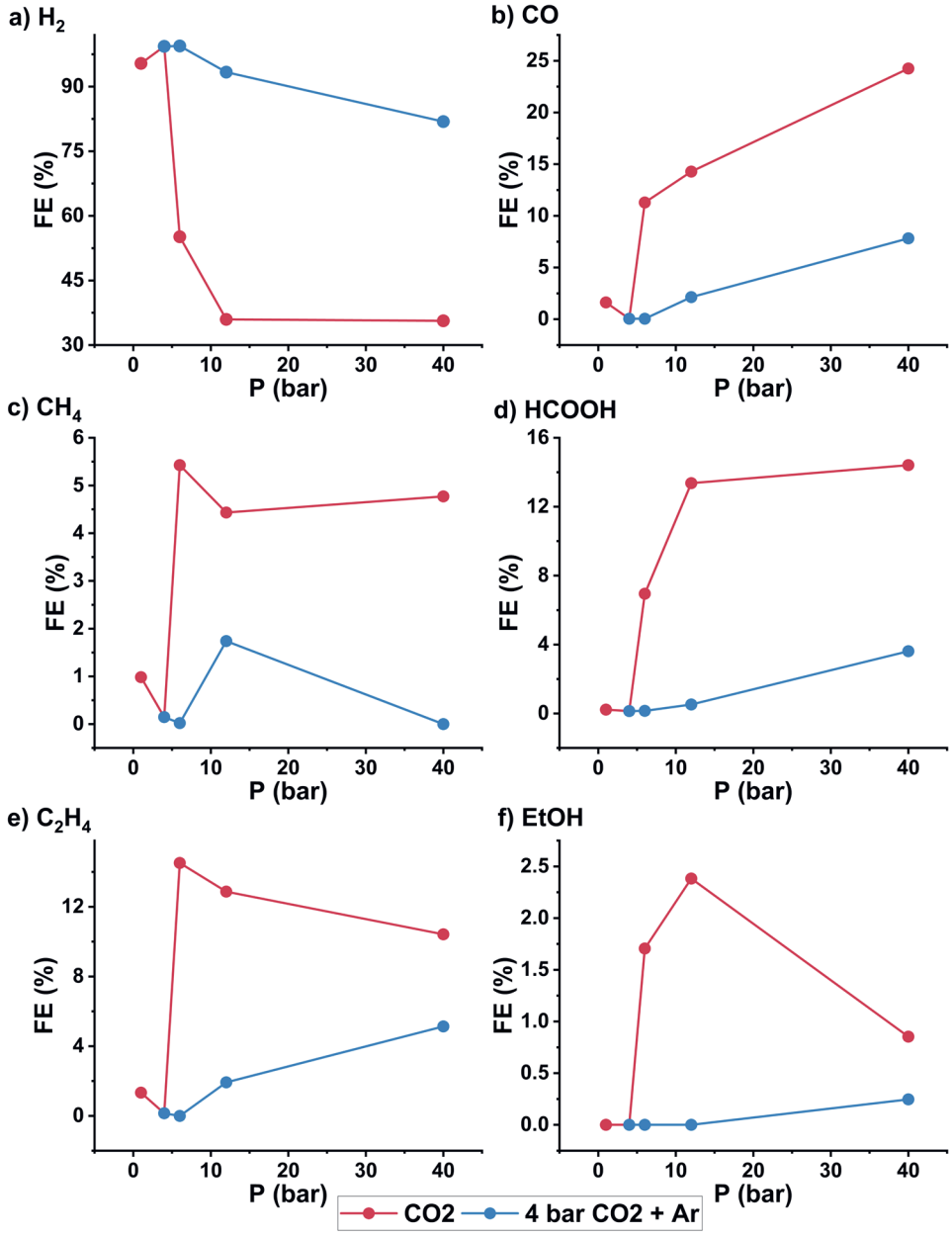

Figure F.15 Faradaic efficiency towards the main CO2RR products as function of CO_2 and total pressure at -1.5 V vs SHE in 0.2 M $KHCO_3$ at 75 °C. Red lines are performed in pure CO_2 and blue lines are at 2 bar of CO_2 and pressure is increased with Ar. FE for a) hydrogen b) carbon monoxide c) formic acid d) methane e) ethylene and f) ethanol

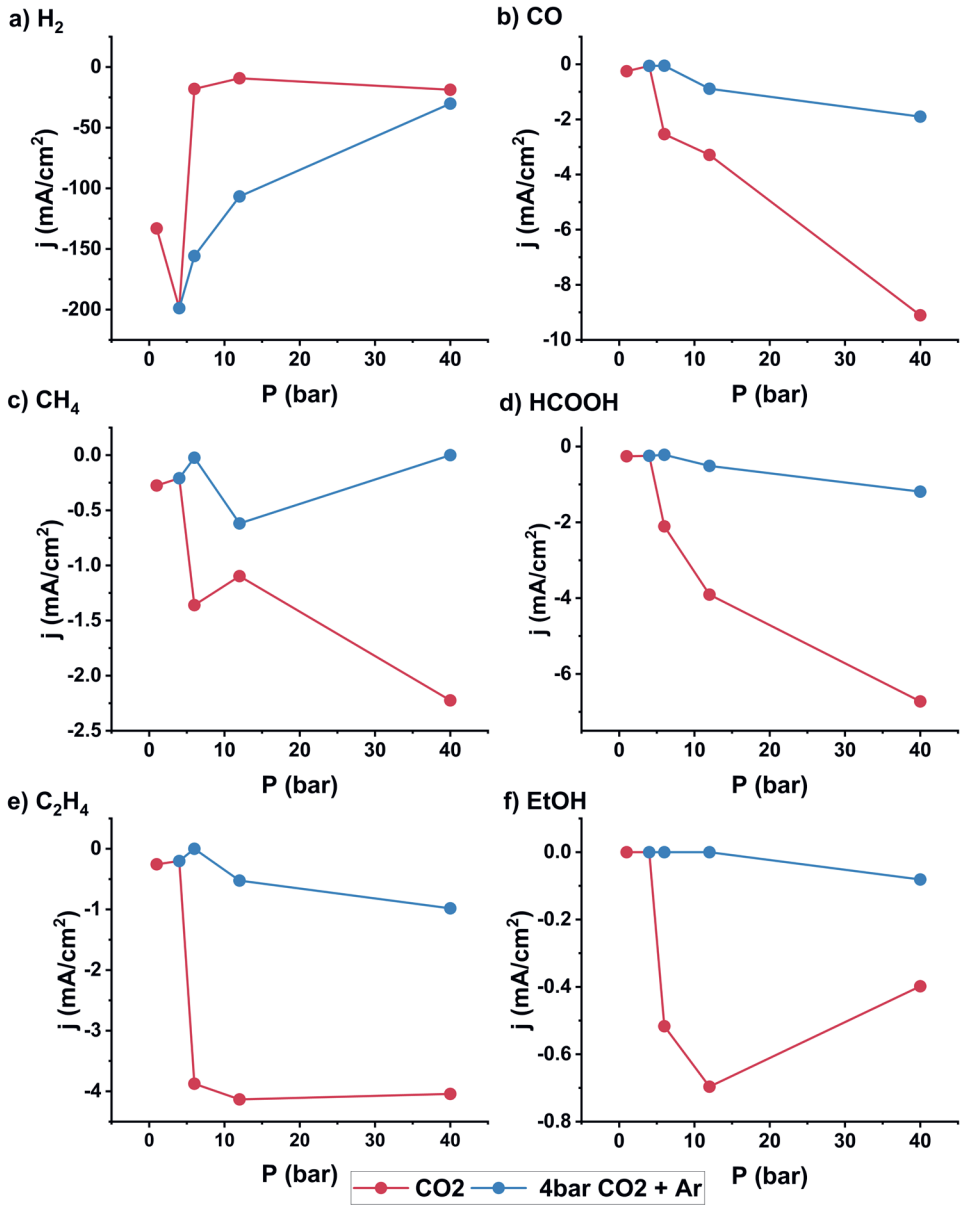

Figure F.16 Partial current densities towards the main CO2RR products as function of CO_2 and total pressure at -1.5 V vs SHE in 0.2 M $KHCO_3$ at 75 °C. Red lines are performed in pure CO_2 and blue lines are at 2 bar of CO_2 and pressure is increased with Ar. FE for a) hydrogen b) carbon monoxide c) formic acid d) methane e) ethylene and f) ethanol

The behavior of CO2RR with increasing CO_2 pressure at 75 °C as shown in Figure F.15 is similar for the C2+ products as at room temperature (Figure 7.5). An initial increase in pressure is needed as at low pressures and high temperatures no significant C2+ products are observed due to the instability of the Cu as discussed above. At 6 bar there is a sharp rise in C2+ activity (Figure S16) and selectivity, which slowly decreases with further increase of pressure. For the simple C1 products CO and HCOOH, the behavior at 75 °C is a bit different than at 25 °C, as the FE towards these products increases with increasing CO_2 pressure. At 25 °C, the FEs first decrease, but at 75 °C this is not possible as they already start near 0 at low pressures. Moreover, for most CO2RR products, the selectivity increases even when the pressure is increased with only Ar, contrary to the case at 25 °C.

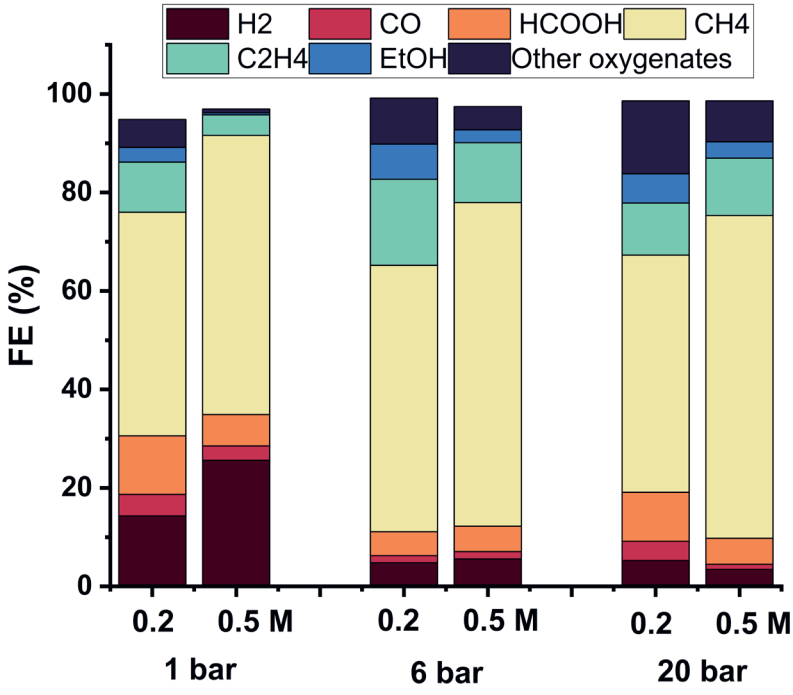

Figure F.17 Faradaic efficiency as function of pressure and electrolyte concentration at room temperature and -1.5 V vs SHE.

G

Supporting Information to Chapter 8

Screening of various metals for electrochemical CO_2 reduction at elevated temperatures and pressures

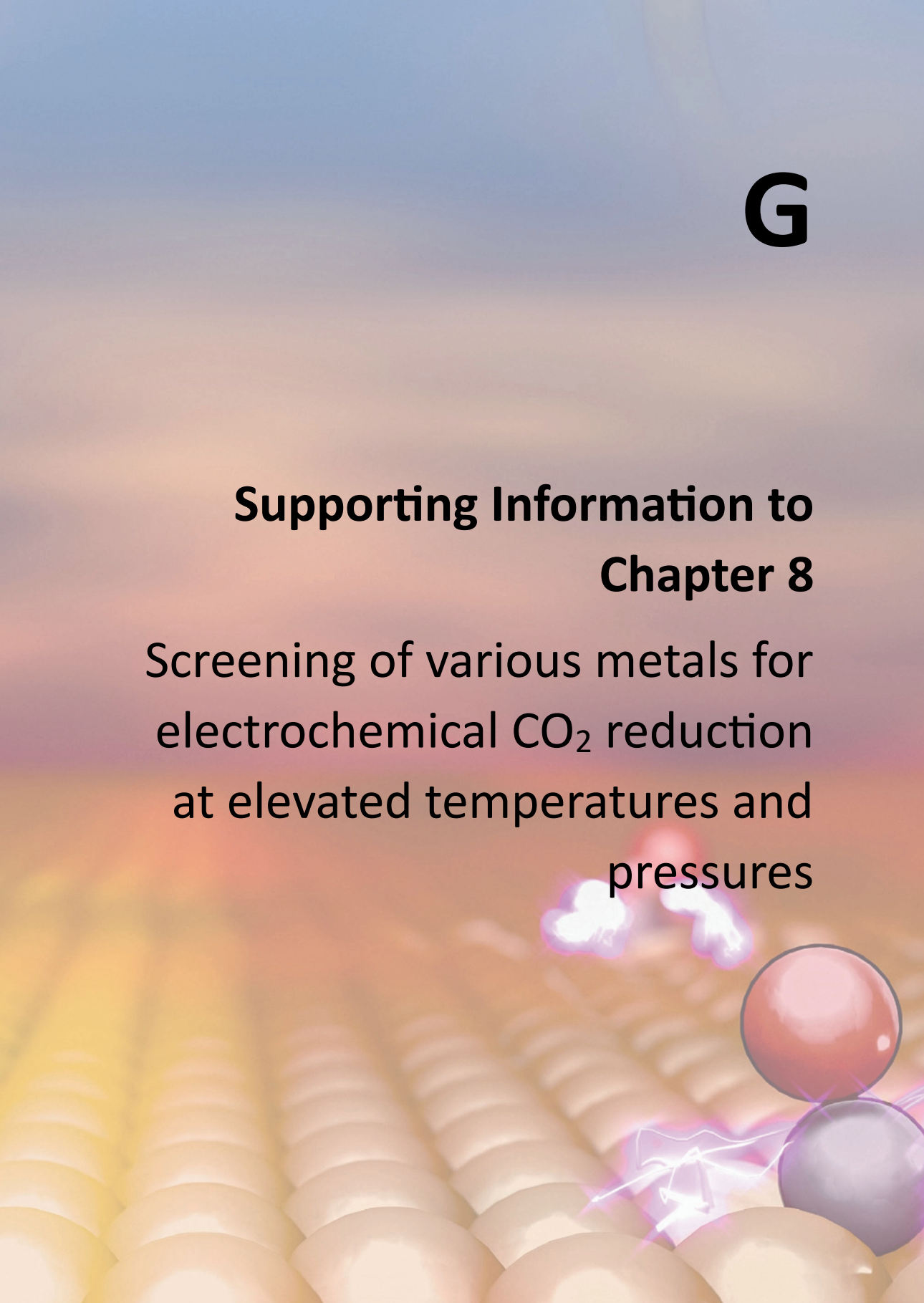

G.1 Catalyst overview

Table G.1 Overview of metal wires used with suppliers and purity

Metal	Supplier	Purity
Ti	Thermo Fischer	99.99
Zr	Mateck	99
Cr	Mateck	99.95
W	Mateck	99.95
Fe	Mateck	99.99
Ru	Mateck	99.95
Co	Mateck	99.995
Rh (0.5 mm diameter)	Goodfe llow	99.9
Ir	Mateck	99.9
Ni	Mateck	99.99
Pd	Mateck	99.9
Pt	Mateck	99.99
Cu	Mateck	99.99
Ag	Mateck	99.99
Au	Mateck	99.99
Zn	Mateck	99.999
Cd	Mateck	99.999
In	Mateck	99.99
Sn	Mateck	99.9
Pb	Thermo Fischer	99.998

Table G.2 Shift of the Ag/AgCl reference with 0.1 M KCl at different temperatures, compared to SHE(T)

T [°C]	25	50	75	100	125	150
$E^{\mathrm{Ag\|AgCl}}(T)$ [mV]	230.3	214.5	195.9	174.6	151.1	125.5

Table G.3 Overview with some of the highest reported Faradaic Efficiencies towards the CO2RR products in literature for the metals studied in this study. Only metal wires and foils in aqueous electrolyte in an H-cell configuration have been considered as these are comparable to this study.

Catalyst	Product	Efficiency	Conditions	Ref
Ti	HCOOH	4.6%	-1.57 V vs Ag/AgCl, 0.1 M $KHCO_3$, 30 bar	1
Zr	CO	32.5%	-1.73 V vs Ag/AgCl, 0.1 M $KHCO_3$, 30 bar	1
	HCOOH	7.6%	-1.73 V vs Ag/AgCl, 0.1 M $KHCO_3$, 30 bar	1
Cr	CO	11.8%	-1.49 V vs Ag/AgCl, 0.1 M $KHCO_3$, 30 bar	1
	HCOOH	8.2%	-1.49 V vs Ag/AgCl, 0.1 M $KHCO_3$, 30 bar	1
W	HCOOH	31.9%	-1.61 V vs Ag/AgCl, 0.1 M $KHCO_3$, 30 bar	1
Fe	CO	10.0%	-1.63 V vs Ag/AgCl, 0.1 M $KClO_4$, 30 bar	2
	HCOOH	59.6%	-1.61 V vs Ag/AgCl, 0.1 M $KClO_4$, 30 bar	1
	CH4	2.0%	-1.63 V vs Ag/AgCl, 0.1 M $KHCO_3$, 30 bar	1
Ru	MeOH	30.5%	-0.8 V vs SCE, 0.5 M $NaHCO_3$, *RuOx	3
Co	CO	15.8%	-1.54 V vs Ag/AgCl, 0.1 M $KHCO_3$, 30 bar	1
	HCOOH	21.9%	-1.54 V vs Ag/AgCl, 0.1 M $KHCO_3$, 30 bar	1
	CH4	3.1%	-1.54 V vs Ag/AgCl, 0.1 M $KHCO_3$, 30 bar	1
Rh	CO	61.0%	-1.41 V vs Ag/AgCl, 0.1 M $KHCO_3$, 30 bar	1
	HCOOH	19.5%	-1.41 V vs Ag/AgCl, 0.1 M $KHCO_3$, 30 bar	1
Ir	CO	17.5%	-1.55 V vs Ag/AgCl, 0.1 M $KHCO_3$, 30 bar	1
	HCOOH	22.3%	-1.55 V vs Ag/AgCl, 0.1 M $KHCO_3$, 30 bar	1
Ni	CO	33.5%	-1.59 V vs Ag/AgCl, 0.1 M $KHCO_3$, 30 bar	1
	HCOOH	31.3%	-1.59 V vs Ag/AgCl, 0.1 M $KHCO_3$, 30 bar	1
	CH4	1.78%	-1.8 V vs Ag/AgCl, 0.1 M $KHCO_3$, 60 bar	4
Pd	CO	46.1%	-1.56 V vs Ag/AgCl, 0.1 M $KHCO_3$, 30 bar	1
	HCOOH	44.0%	-1.76 V vs Ag/AgCl, 0.1 M $KHCO_3$, 30 bar	1
Pt	CO	6.1%	-1.48 V vs Ag/AgCl, 0.1 M $KHCO_3$, 30 bar	1
	HCOOH	50.4%	-1.48 V vs Ag/AgCl, 0.1 M $KHCO_3$, 30 bar	1
Cu	CO	47.5%	-1.45 V vs Ag/AgCl, 0.1 M $KHCO_3$, 30 bar	5
	HCOOH	53.7%	-1.64 V vs Ag/AgCl, 0.1 M $KHCO_3$, 30 bar	1
	CH4	56.7%	-1.59 V vs Ag/AgCl, 0.1 M $KHCO_3$, 30 bar	5
	C2H4	25.5%	-1.44 V vs NHE, 0.1M $KHCO_3$	6
Ag	CO	81.5%	-1.37V vs NHE, 0.1M $KHCO_3$	6
	HCOOH	20.5%	-2.2V vs SCE, 0.05 M $KHCO_3$, 0 °C	7
Au	CO	87.1%	-1.14V vs NHE, 0.1M $KHCO_3$	6
	HCOOH	11.8%	-1.30 V vs Ag/AgCl, 0.1 M $KHCO_3$, 30 bar	1
Zn	CO	79.4%	-1.54V vs NHE, 0.1M $KHCO_3$	6
	HCOOH	40.5%	-1.70 V vs Ag/AgCl, 0.1 M $KHCO_3$, 30 bar	1
Cd	CO	3.7%	-2.2V vs SCE, 0.05 M $KHCO_3$, 0 °C	7

	HCOOH	55.9%	-2.2V vs SCE, 0.05 M $KHCO_3$, 0 °C	7
In	CO	14.7%	-2.2V vs SCE, 0.05 M $KHCO_3$, 20 °C	7
	HCOOH	94.9%	-1.55V vs NHE, 0.1M $KHCO_3$	6
Sn	CO	8.0 %	-1.39 V vs Ag/AgCl, 0.1 M $KHCO_3$, 30 bar	1
	HCOOH	92.3%	-1.39 V vs Ag/AgCl, 0.1 M $KHCO_3$, 30 bar	1
Pb	HCOOH	97.4%	-1.63V vs NHE, 0.1M $KHCO_3$	6

Table G.2 shows an overview of the highest efficiencies to CO2RR products found in literature at the different metals studied in this study. To keep this table representative of our study, we only included studies which are performed with similar systems. The studies that are included in this table are in aqueous electrolyte with no unusual cation or anions. If we would include more exotic electrolytes, other products could be included, such as 44% FE towards oxalate on Pb in 0.1M NH_4Cl [8] or 95% FE towards CO on Zn with a CTAB cation[9]. All experiments in this table have been performed in H-cell configuration; with GDE setups sometimes better results can be obtained such as 33% FE toward CO, 35% towards CH_4 and 2.3% for ethanol on Pt at 30 bar pressure [10]. Moreover, we only included pure metals wires and foils in this table. So for example alloys, oxides, carbides and phosphides are not included (there are studies in literature producing for example long chain hydrocarbons on phosphate derived Ni[11]). Moreover, we have only reported products with a reported FE above 1% FE. Very minor products such as methanol and methane have been observed on metals as Ag, Au and Zn [12,13]. Also long chain hydrocarbons have been observed before in very small amounts on many metal catalysts [14].

G.2 Focused screening extra data

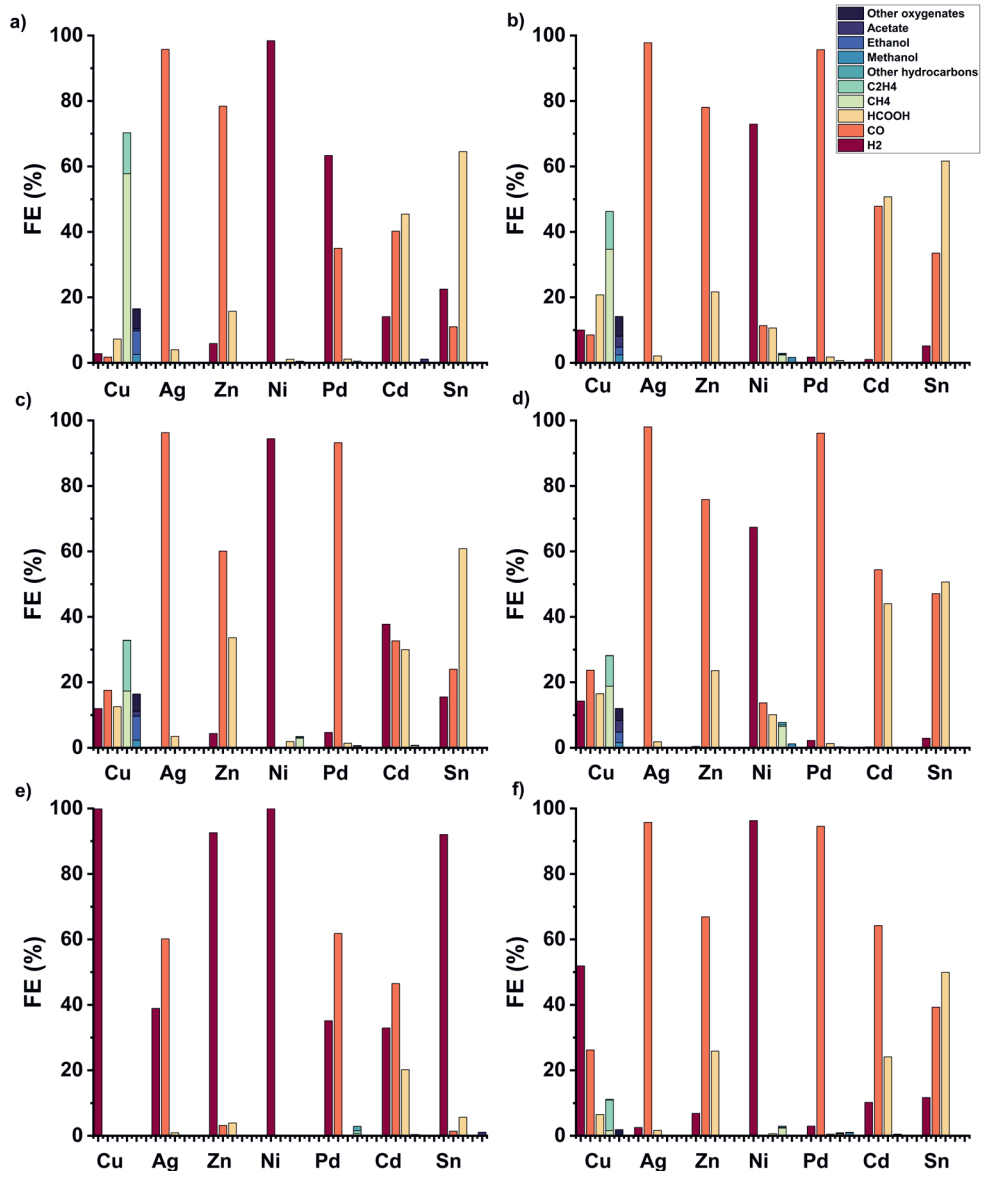

Figure G.1 Faradaic efficiency at six different conditions for Cu, Ag, Zn, Ni, Pd, Cd and Sn at -1.5 V vs SHE in 0.1 M $KHCO_3$ as shown in Figure 1 but categorized per condition a) 25 °C and 1 bar b) 25 °C and 30 bar c) 50 °C and 5 bar d) 50 °C and 30 bar e) 100 °C and 5 bar f) 100 °C and 30 bar

G.3 Broad screening extra data

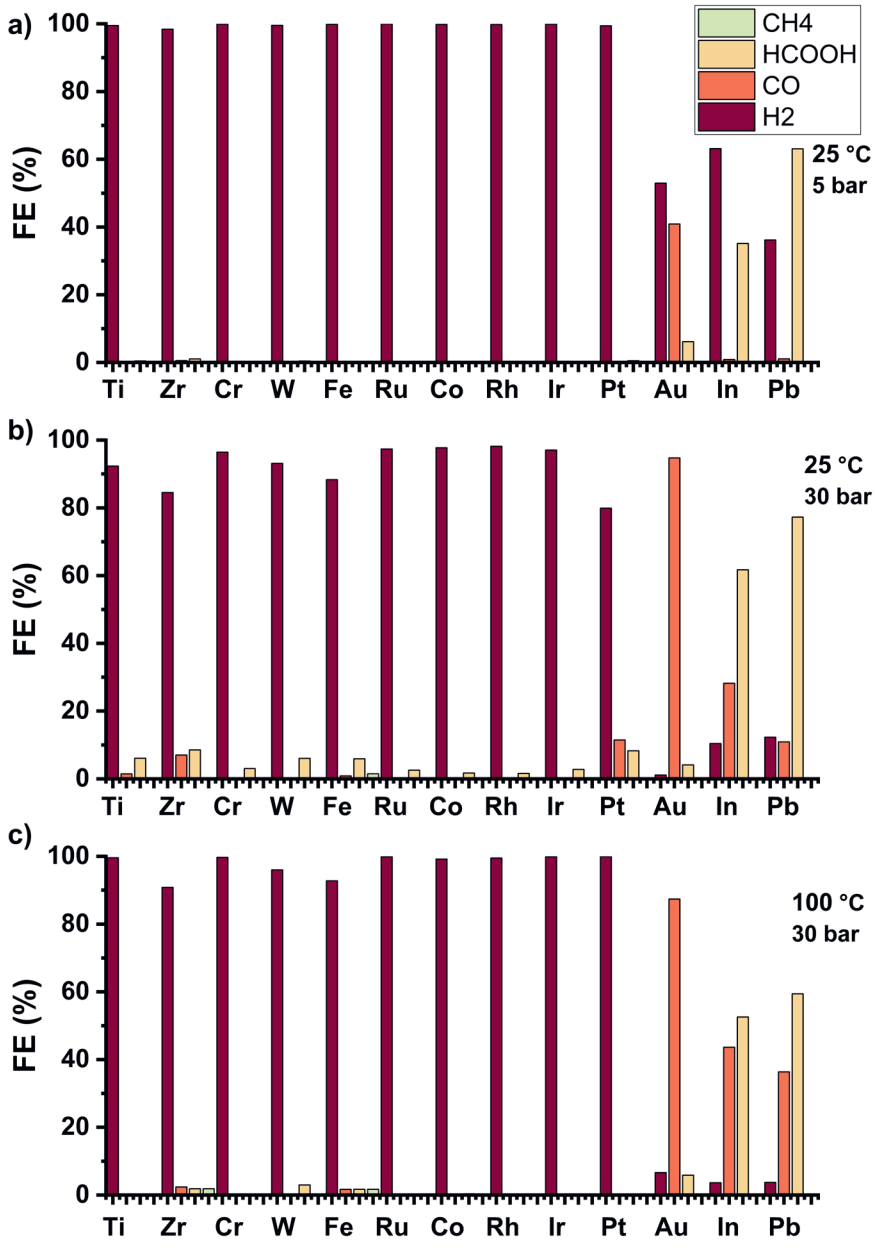

Figure G.2 Faradaic efficiency at the 3 main conditions for a variety of products at -1.5 V vs SHE in 0.1 M $KHCO_3$ as shown in Figure 4 but categorized per condition a) 25 °C and 1 bar b) 25 °C and 30 bar c) 100 °C and 30 bar

G.4 Stability

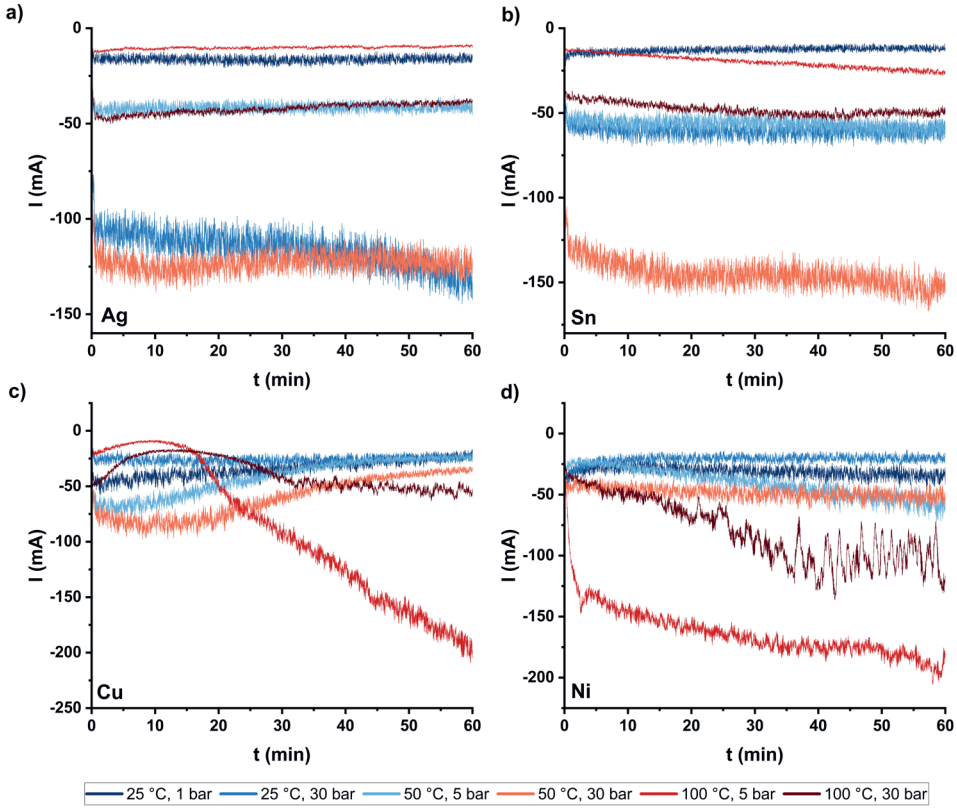

Figure G.3 Current vs time for the different conditions for a) Ag b) Sn c) Cu d) Ni. Higher temperatures lead to more unstable currents, especially on Cu and Ni.

G.5 Comparison to literature

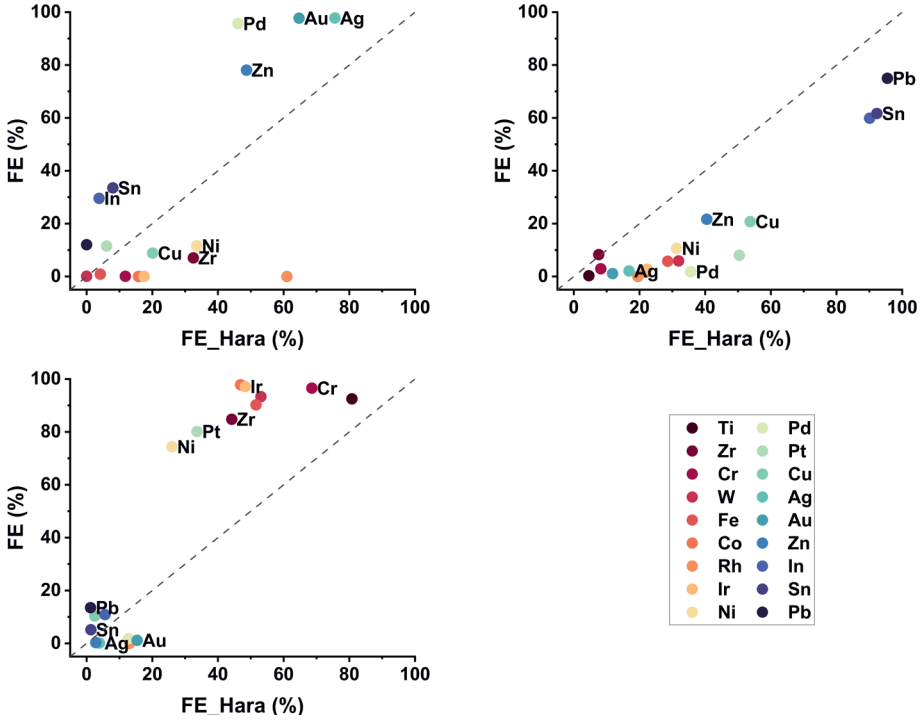

Figure G.4 Comparison of Faradaic efficiency at 30 bar and room temperature between this study and the study of Hara et al.[1] The dotted line shows the same efficiency; above this line, our study has higher efficiencies and below this line, the study of Hara shows higher efficiencies. a) shows the Faradaic efficiency towards CO, b) towards HCOOH and c) towards H_2.

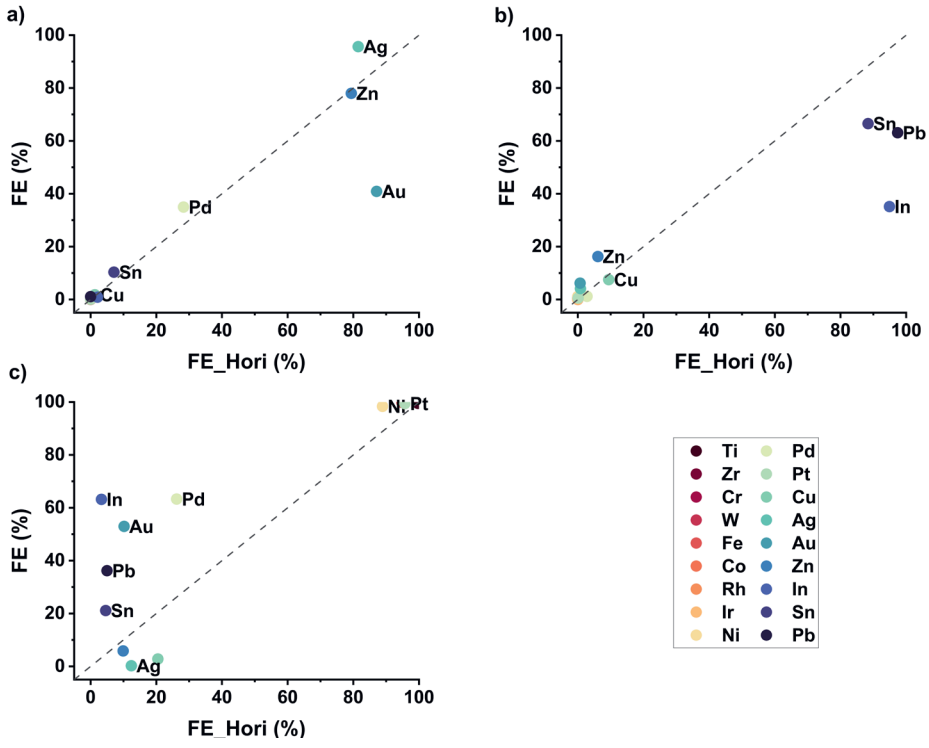

Figure G.5 Comparison of Faradaic efficiency at 1 bar and room temperature between this study and the study of Hori et al.[6] The dotted line shows the same efficiency; above this line, our study shows higher efficiencies, and below this line, the study of Hori shows higher efficiencies. a) shows the Faradaic efficiency towards CO, b) towards HCOOH and c) towards H_2.

G.6 Activity

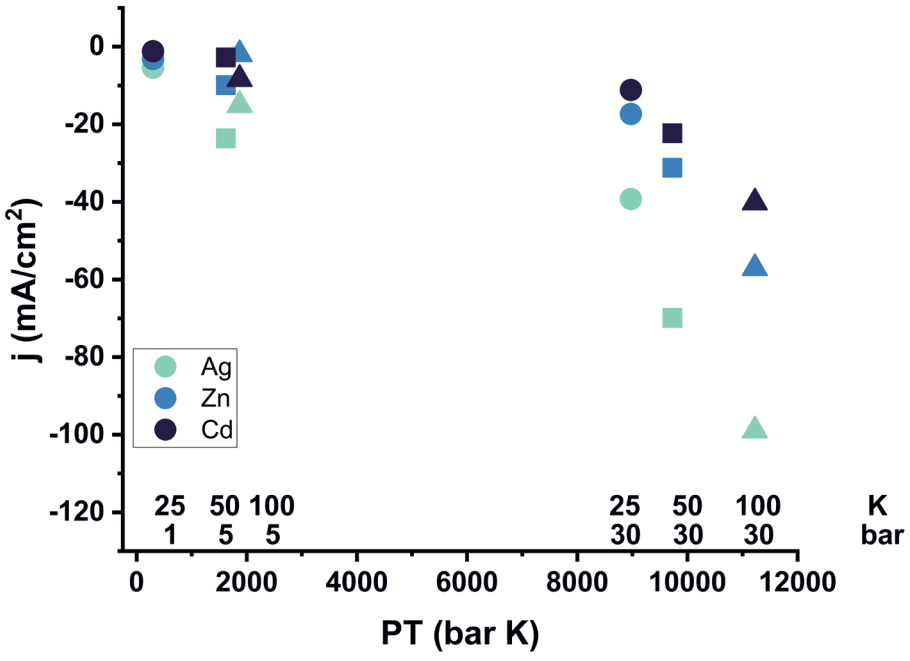

Figure G.6 The partial current density for CO2RR as function of pressure and temperature for Ag, Zn and Cd. Both temperature and pressure increase the CO2RR current density, except when high temperatures are used at low pressures

G.7 Selectivity

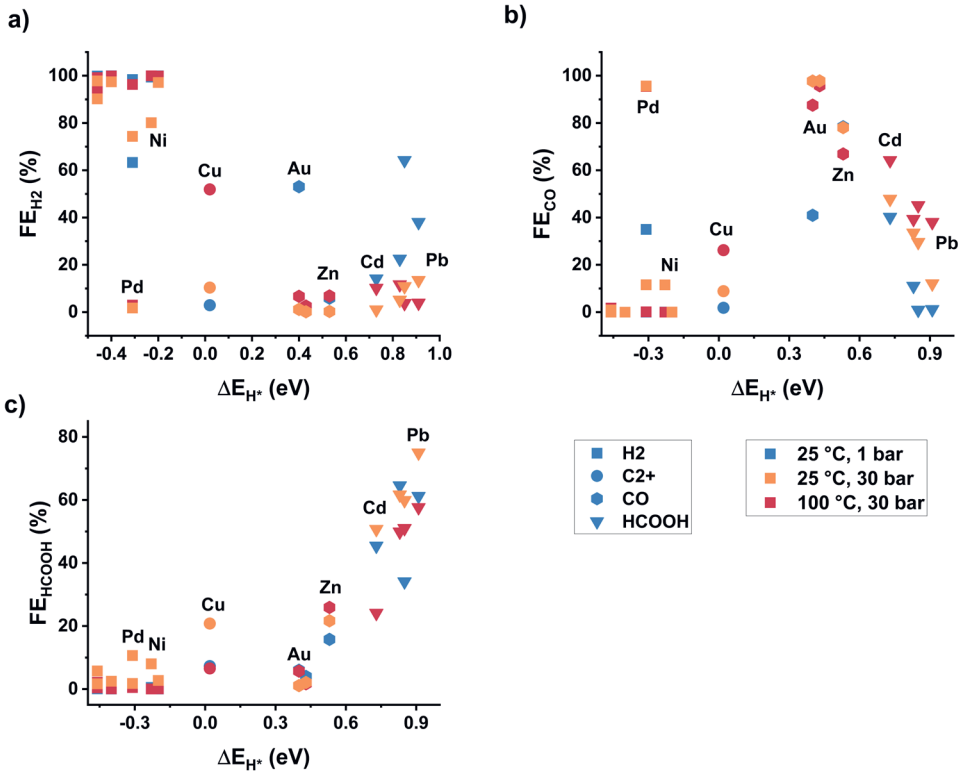

Figure G.7 The Faradaic efficiency at different experimental conditions for all metals tested as function of the binding energy determined by Bagger et al.[15] a) hydrogen b) CO and c) HCOOH. The symbol illustrates to which group the metal is typically classified.

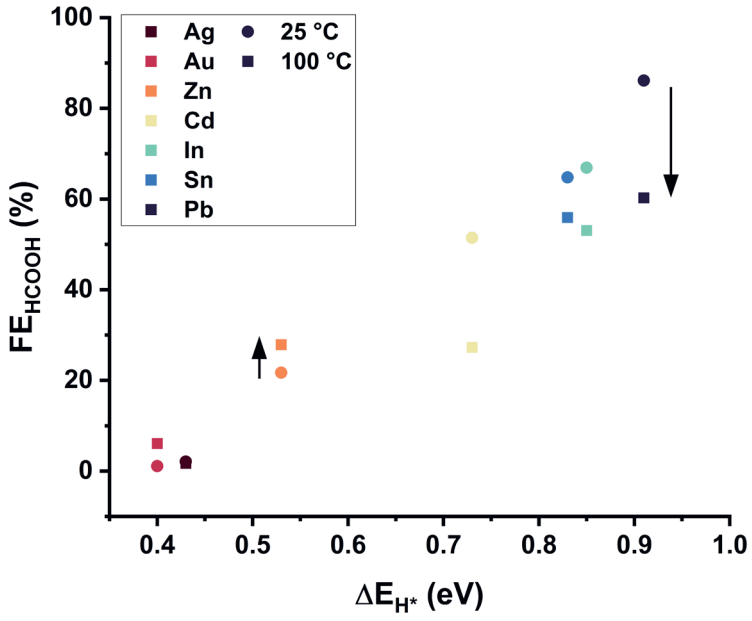

Figure G.8 Trend of formic acid efficiency with increasing temperature at 30 bar plotted vs hydrogen binding energy.

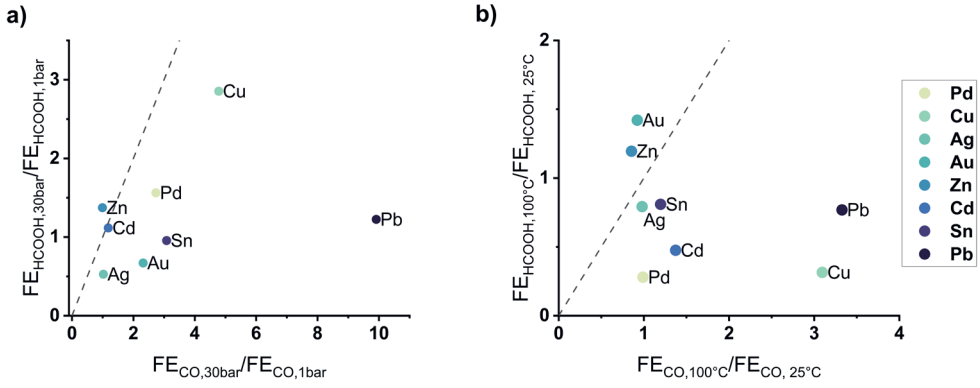

Figure G.9 The ratio between the Faradaic efficiency for HCOOH plotted against the ratio between Faradaic efficiency for CO to illustrate if relatively more CO or HCOOH is produced. The dotted line shows where both CO and HCOOH increase with the same amount; below the line CO increases stronger and above the line HCOOH increases stronger. a) shows the effect of pressure at 25 °C and b shows the effect temperature at 30 bar.

G.8 Hydrocarbon and methanol production

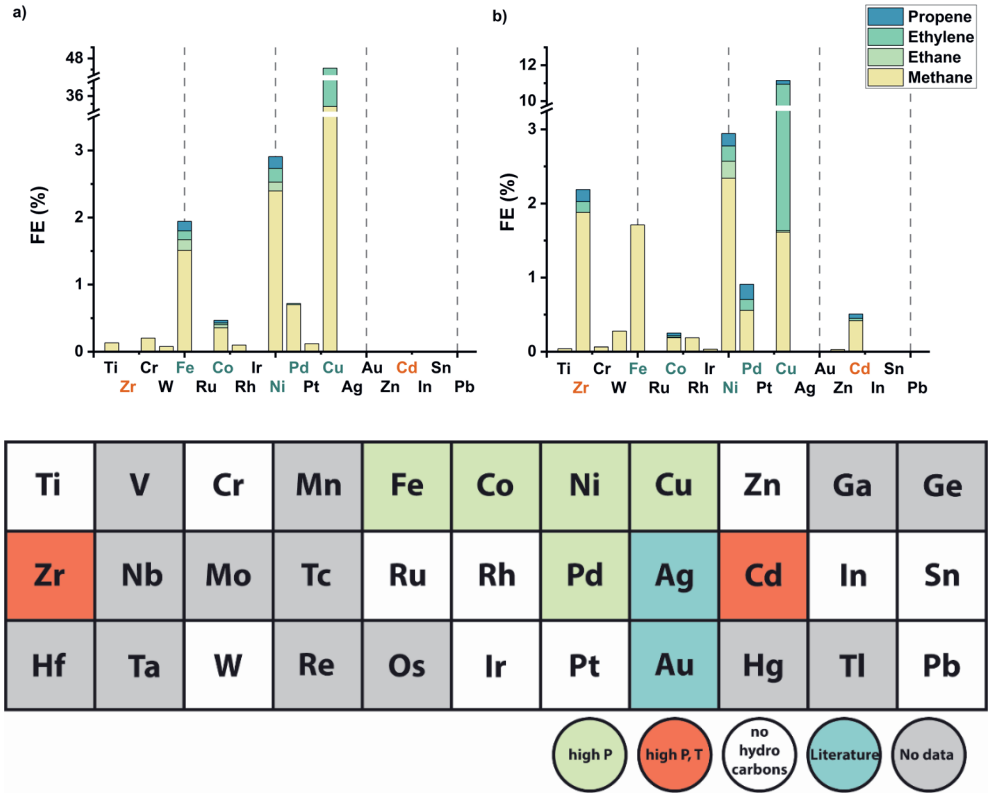

Figure G.10 Hydrocarbon production for all metals studied at a) 30 bar and 25 °C and b) 30 bar and 100 °C. The metals in green can produce longer hydrocarbons already at 25 °C, while the orange metals only produce these at higher temperatures. For the metals in blue hydrocarbons have been found in literature with more than 0.1% FE [14], for the metals in gray no hydrocarbons longer than methane have been observed in this study at – 1.5V vs SHE in 0.1 M $KHCO_3$

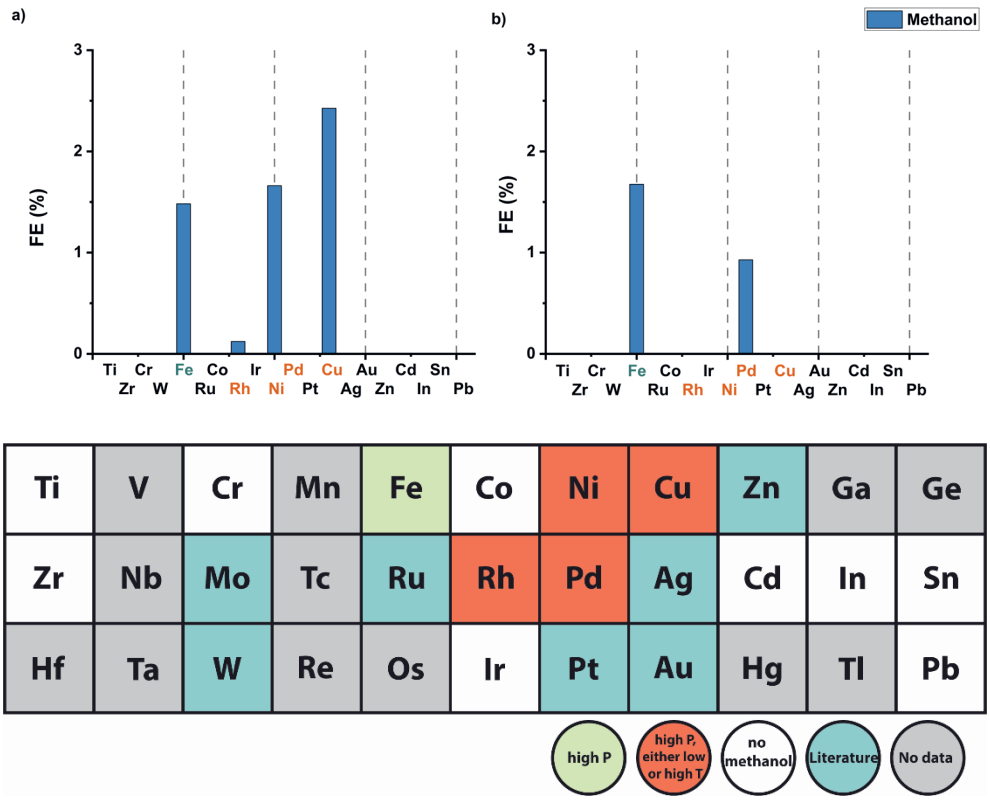

Figure G.11 Methanol production for all metals studied at a) 30 bar and 25 °C and b) 30 bar and 100 °C. The metals in green can produce methanol both at low (25 °C) and high temperature (100 °C), while the orange metals only produce methanol at either high or low temperatures. For the metals in blue methanol has been detected in literature[3,8,13], while in gray no methanol has been detected in this study or in literature.

G.9 How the periodic table in Figure 5 was constructed

For the top figure with the FE of CO2RR vs HER, we looked at the total FE towards CO2RR products and categorized this in 5 different categories. Excellent CO2RR catalysts with efficiencies over 90%, good catalysts with efficiencies between 40 and 90%, intermediate catalysts with efficiencies between 10 and 40%. Poor catalysts with efficiencies lower than 10% and non-active catalysts with efficiencies lower than 1%.

For the bottom figure, we categorized the selectivity towards CO2RR products. If the catalyst was non-active, i.e. less than 1% FE towards CO2RR, we classified it as H_2. Then we look at only the CO2RR products and if the catalyst could produce hydrocarbons over 20% FE (excluding H_2), we categorize it as CH_4. This is to show the unique ability to produce hydrocarbons, where 20% is significant, but also quite the limit without further optimization. The remaining catalysts were categorized in CO or HCOOH depending on their dominant product. However, if the activity towards one of these products was not more than two times larger than the activity towards the other one, we categorized it as mixed products.

References

1. Hara, K., Kudo, A. & Sakata, T. *Journal of Electroanalytical Chemistry* vol. 391 (1995).
2. Hara, K., Kudo, A. & Sakata, T. *Journal of Electroanalytical Chemistry* **386**, 257–260 (1995).
3. Popic, J. P., Avramov, M. L. & Vukovic, N. B. *Journal of Electroanalyticai Chemistry* **421**, 105–110 (1997).
4. Kudo, A., Nakagawa, S., Tsuneta, A. & Sakata, T. *J. Electrochem. Soc* **140**, 1541–1545 (1993).
5. Hara, K., Tsuneto, A., Kudo, A. & Sakata, T. *J Electrochem Soc* **141**, 2097–2103 (1994).
6. Hori, Y., Wakebe, H., Tsukamoto, T. & Koga, O. *Electrochim Acta* **39**, 1833–1839 (1994).
7. Azuma, M., Hashimoto, K., Watanabe, M. & Sakata, T. *Journal of Electroanalytical Chemistry* **294**, 299–303 (1990).
8. Jitaru, M., Lowy, D. A., Toma, M., Toma, B. C. & Oniciu, L. *J Appl Electrochem* **27**, 875–889 (1997).
9. Pan, H., Wang, F., Zhang, Z. & Min, S. *Sustain Energy Fuels* **6**, 2149–2154 (2022).
10. Hara, K., Kudo, A., Sakata, T. & Watanabe, M. *J. Electrochem. Soc.* **42**, L57–L59 (1995).
11. Zhou, Y. *et al. Nat Catal* **5**, 545–554 (2022).
12. Hatsukade, T., Kuhl, K. P., Cave, E. R., Abram, D. N. & Jaramillo, T. F. *Physical Chemistry Chemical Physics* **16**, 13814–13819 (2014).
13. Kuhl, K. P. *et al. J Am Chem Soc* **136**, 14107–14113 (2014).
14. Hwang, S. Y. *et al. Nano Energy* 109881 (2024) doi:10.1016/j.nanoen.2024.109881.
15. Bagger, A., Ju, W., Varela, A. S., Strasser, P. & Rossmeisl, J. *ChemPhysChem* **18**, 3266–3273 (2017).

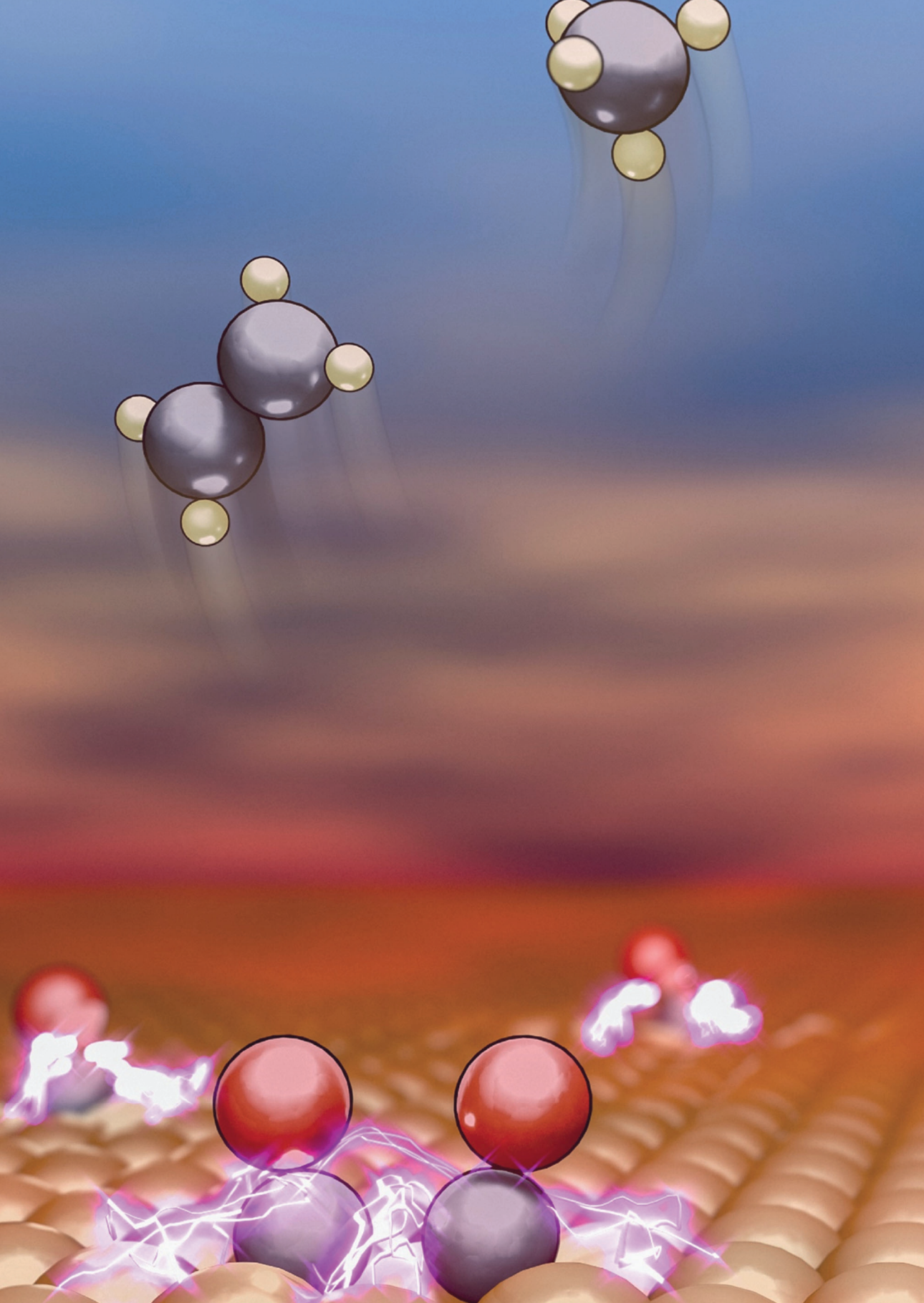

I

Summary
Outlook
& Samenvatting

Summary

One of the largest and most pressing issues of this time is the changing climate due to manmade emissions of greenhouse gasses, most importantly CO_2. To limit the effects of climate change, a rigorous change is needed in the way modern society uses energy and materials. A transition is needed from a world based on fossil fuels to a world based on renewable resources. Electrocatalysis can play a significant role in this transition as it can use renewable electricity to convert molecules as H_2O, CO_2 and N_2 into energy carriers or chemical building blocks such as hydrogen, CO, ethylene and ammonia. Electrochemical CO_2 reduction (CO2RR) can be used to turn CO_2 from a pollutant into a resource by transforming it into valuable chemicals as CO, formic acid or ethylene. Therefore, in recent years the interest in this reaction has grown tremendously. Electrochemical research in general and CO2RR studies specifically are often performed at ambient pressure and temperature and hence conclusions and fundamental insights are drawn at these conditions. However, for practical applications, ambient conditions might not be the most relevant, as industrial electrolyzers typically operate at elevated temperatures, for example due to thermal losses and/or hot feedstocks. Therefore, it is important to study the CO_2 reduction reaction at elevated temperatures and pressures to gain fundamental insights in the effects of these parameters.

Chapter 2 to 5 study the effect of temperature at ambient pressures on Au, Cu, Ag, CuAg alloy and Ni electrodes. Chapter 2 shows that on Au, in a rotating-ring-disk setup, the activity and selectivity of CO2RR increases with temperature. We attribute this to the improved kinetics. We have performed partial pressure experiments to study the effect of temperature and CO_2 solubility independently and show that at high temperatures the reaction is limited by the CO_2 concentration. Moreover, we show that temperature experiments can be used to extract kinetic information such as the transfer coefficient and the apparent activation energy. The latter is influenced by the cation and therefore the magnitude of the temperature effect depends on the electrolyte used.

In Chapter 3, we investigate how reaction temperature affects the electrochemical CO_2 reduction on copper in the temperature range from 18-70 °C. We show that there are two distinct temperature regimes. From 18 up to $\sim$ 48 °C, C2+ products are produced with higher Faradaic Efficiency, while methane and formic acid selectivity decreases, and hydrogen selectivity stays approximately constant. From 48 to 70 °C, it was found that the Hydrogen Evolution Reaction (HER) dominates and the activity of CO2RR decreases. Moreover, the CO2RR products produced in this higher temperature range are mainly the C1 products, namely CO and HCOOH. The observations in the first regime can be explained by an

increase in the CO coverage on the surface as evidenced by in situ Raman spectroscopy, in combination with increased local pH and faster kinetics with temperature. The second regime seems not to be related to any limited CO_2 mass transport, but rather due to changes in the copper surface as shown with lead underpotential deposition and double layer capacitance measurements, although a too high local pH could also be a factor.

Chapter 4 illustrates that the performance of Cu catalysts at elevated temperatures can be improved by alloying, in this case with Ag. By alloying, the hydrogen evolution can be significantly suppressed at elevated temperatures. However, at ambient pressures the optimum in C2+ production with temperature remains, even at the different CuAg alloys. This chapter also demonstrates how intertwined the temperature effect is with other parameters. Temperature influences other parameters, such as the CO_2 solubility, and these should be deconvoluted where possible. In this case we deconvolute the effect of temperature and CO_2 solubility by partial pressure experiments. Moreover, the applied potential significant influences the effect of temperature and both parameters should be studied simultaneously. Lastly, mass transport and temperature also influence each other's effect on the activity and selectivity of CO2RR and therefore studies should combine the study of both parameters.

In Chapter 5, we investigate a nickel-derived catalyst for the electrochemical CO_2 reduction. Ni is an interesting electrocatalyst as it has recently been shown to have the unique ability to produce longer hydrocarbon chains via a chain growth mechanism in low but measurable amounts. However, the effect of the many parameters of this reaction remain to be studied in more detail. Here, we have investigated the effect of temperature, bulk CO_2 concentration, potential, the reactant, cations and anions on the formation of hydrocarbons via a chain growth mechanism on Ni. We show that temperature increases the activity but also the formation of coke, which deactivates the catalyst. The selectivity and thus the chain growth probability is mainly affected by the potential and the electrolyte composition. Remarkably, CO reduction shows lower activity, but higher chain growth probability than CO_2 reduction. Furthermore, we discuss that the rate determining step is most likely a hydrogenation step.

Chapter 6 to 8 discuss the development and application of a high-pressure high-temperature electrochemical cell, which is able to operate up to 140 bar and 200 °C. This setup allows the combined study of temperature and pressure. Moreover, it extends the temperature range that can be studied over 100 °C, even in aqueous electrolyte. Chapter 6 shows, as a the proof of concept of this high pressure cell, the temperature-dependent changes in the cyclic voltammograms of

polycrystalline gold up to 150°C and 50 bar. Moreover, the catalytic performance of CO_2 reduction to CO on a rotating polycrystalline gold disk electrode was investigated under different pressure and temperature. At ambient pressures similar results were reached as in Chapter 2, but at elevated pressures the optimum in CO selectivity with temperature disappeared and CO reaches selectivities around 90%. In these conditions, temperature and pressure can still significantly enhance the activity of CO_2 reduction on gold.

Following the same order as the first chapters, we studied Cu in the high-pressure high-temperature electrochemical cell after studying Au. We show a change in the C-C coupling mechanism above 100 °C at pressures of 24 bar. Where at low temperatures most C-C bonds are formed via the traditional CO dimerization mechanism, at high temperatures the chain growth mechanism takes over and from 125 °C onwards this is the only mechanism making C-C bonds. We also show that temperature can improve the selectivity of the traditional CO dimerization mechanism at temperatures up to 75 °C, and that pressure helps to keep the system stable at these temperatures. Elevated pressures can reduce HER activity and selectivity dramatically, even at pressures of only a few bar. However, it is not pressure itself, but CO_2 pressure that enhances CO_2 reduction and C-C coupling specifically.

Chapter 8 extends the field of electrocatalysts for CO2RR by screening 20 different metals for this reaction at different combinations of pressure and temperature at conditions up to 30 bar and 100 °C in aqueous electrolyte. We show that catalyst which are average at ambient conditions, can reach near 100% efficiency for CO2RR at 30 bar and maintain this at high temperatures, because HER is significantly inhibited at elevated pressures. Both temperature and pressure can increase the CO2RR activity significantly. However, if a catalyst does not perform CO2RR at ambient conditions, increasing pressure and temperature will not turn this into a good CO2RR catalyst and CO2RR selectivity increases to maximum 30%. Nevertheless, some of these poor CO2RR catalysts do show interesting products beyond CO and HCOOH, such as long chain hydrocarbons and methanol. Chapter 6 to 8 give a glimpse of what is possible and thereby open up new promising avenues for future investigations for electrochemical CO2 reduction at high temperatures and high pressure in aqueous electrolytes.

Outlook

This thesis has mainly discussed the effect of temperature on the electrochemical CO_2 reduction. It has also shown the important effect of pressure with the newly developed high-pressure high-temperature electrochemical cell. However, this cell was only completed near the end of my PhD. Therefore, this work is only the start of the understanding of the effect of temperature and many more studies are possible in this unique setup. The next section presents suggestions for future studies as well as some insights that I gained during my PhD, but could not complete into a chapter of this thesis.

O.1 Cu instability

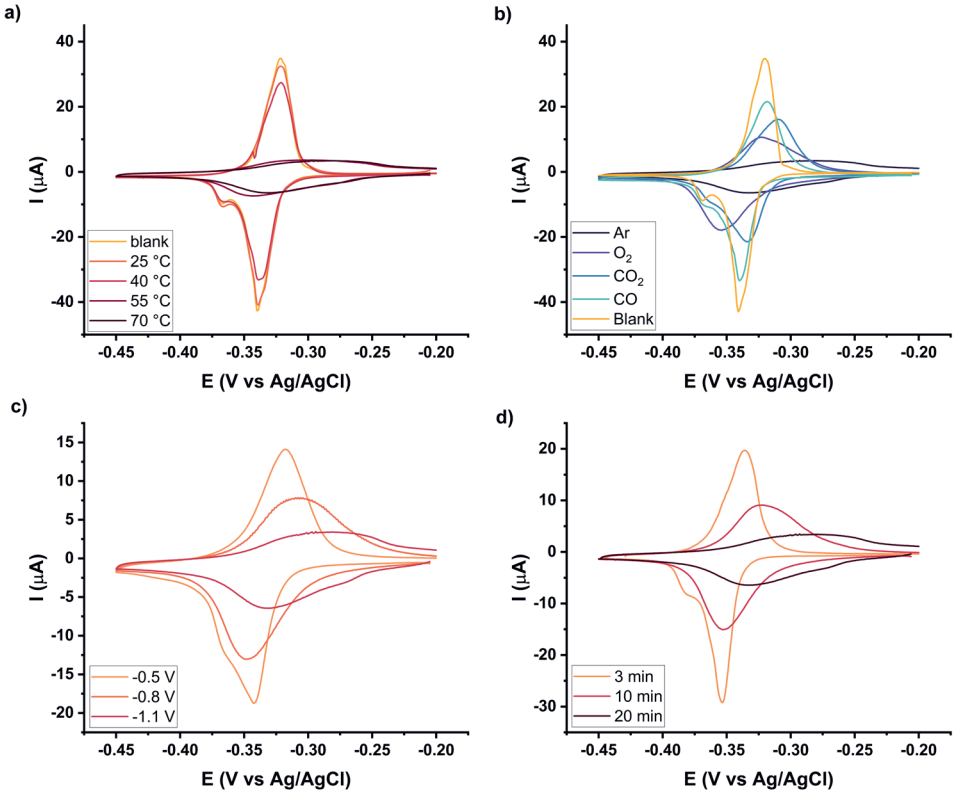

Figure O.1 The Pb UPD CVs under different conditions, all in 0.1 M NaClO4 + 1 mM NaCl + 2 mM PbClO4 pH 3 electrolyte at 5 mV/s. CVs are taken after electrolysis in 0.1 M $KClO_4$ and, if not otherwise specified, at 70 °C in Ar atmosphere at -1.1 V vs RHE for 20 min.

Figures alter one of these parameters a) effect of temperature b) effect of gas composition c) effect of potential of electrolysis and d) effect of time of electrolysis.

In Chapter 3 we showed that the Cu surface is not stable during CO_2 reduction at elevated pressures, as the Pb under-potential (UPD) cyclic voltammogram (CV) changes significantly after electrolysis at these conditions. In a follow-up study, we have looked into this in more detail. The change in the Pb UPD CV of Cu is not caused by CO_2 or bicarbonate because similar behavior is observed in Ar saturated $KClO_4$ electrolyte as shown in Figure O.1a. At room temperatures the Pb UPD CV changes barely and at 40 °C it only changes slightly. However at higher temperatures the CV changes drastically. Figures O.1c and O.1d illustrate that the degree of change not only depends on the temperature but is also time and potential dependent. Moreover, the change in the Pb UPD CV can be suppressed by the gas composition during electrolysis, as shown in Figure O.1b. The change is the largest in an Ar atmosphere, while CO_2, O_2 and especially CO suppress the change in the Cu surface during electrolysis at elevated temperatures. Therefore, our hypothesis is that this change is caused by hydrogen evolution at elevated temperatures. What changes exactly on the Cu surface is still unclear so more research is needed. However, we have indications that the surface changes from mainly Cu(111) to predominantly Cu(110), although it is not the full story and should be confirmed with other techniques.

O.2 Mass transport

In Chapter 4 we showed that mass transport can play an important role in influencing the selectivity towards CO_2 reduction on a Ag catalyst. The similarities between the Ag and the Au catalyst in the H-cell setup indicate that this can be extended to Au and probably other catalysts as well. Previously, Goyal et al.[1] have shown with an RRDE setup that enhanced mass transport indeed influences the selectivity towards CO at the expense of H_2. Faster rotation leads to better mass transport, which lowers the OH^- concentration near the surface. This leads to a lower cation concentration near the surface, resulting in less HER. The activity of the CO2RR towards CO is not influenced by rotation rate and therefore the selectivity increases. However, these experiments have been performed between 800 and 2000 rpm. The experiments in Chapter 4 and Appendix C are performed in an H-cell with a gas flow between 20 and 40 sccm. With ferricyanide experiments we have established that these flowrates translate into rotation rates with an RDE setup of 100-200 rpm. Therefore, we hypothesize that at low rotation rates the effect of mass transport might be opposite to the effect at larger flow rates and HER increases with increasing mass transport. However, this should be studied in more detail and the high-pressure high-temperature cell developed in Chapter 6 is an

ideal setup to do so as this setup allows an RDE setup to be connected to a gas chromatograph. This provides the possibility to study Au at low rotation rates, which is not possible with the RRDE setup employed in Chapter 2, as low rotation rates would lead to too much noise in this setup. Moreover, this also allows to extend the study to other metals such as Ag and Cu, and to study the interdependence of the mass transport and temperature effects on the CO2RR.

O.3 Chain growth mechanism

O.3.1 Chain growth mechanism on Ni

In Chapter 5 we discussed the chain growth mechanism on Ni and in Chapter 7 we showed that this mechanism becomes active on Cu as well at high temperatures and pressures. Moreover, in Chapter 8 we showed that this mechanism is likely to also take place at other metals as Fe, Pd and Cd. However, there is still much unknown about the exact mechanism of the so-called electrochemical Fischer-Tropsch reaction. Therefore, more research is needed to uncover the details of this mechanism. In a preliminary follow-up study of Chapter 5, we have studied the same Ni system under more conditions by changing the electrolyte and reactant. In Chapter 5 we showed that both the activity and chain growth probability differ when CO or CO_2 is used as reactant. In literature, Zhou et al.[2] found that mixing CO and CO_2 would give the highest activity for the chain growth mechanism. However, Figure O.2a and b show that in our system, mixing of CO and CO_2 leads to the mixed results in both activity and chain growth probability. So no optimum is found while mixing both reactants. We also determined the reaction order, which is 0.3 for CO_2 and 1 for CO (between 100 and 70% of CO/CO_2). This indicates that CO is involved in the rate determining step. Experiments changing the buffer concentration

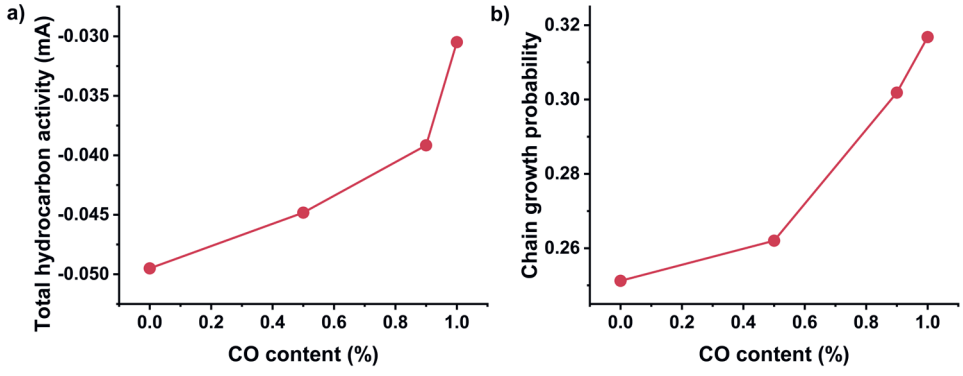

Figure O.2 a) Total hydrocarbon activity and b) chain growth probability during $CO_{(2)}$ reduction with mixed CO CO_2 feeds at -1.175 V vs RHE in 0.1 M pH7 potassium phosphate electrolyte on deposited Ni.

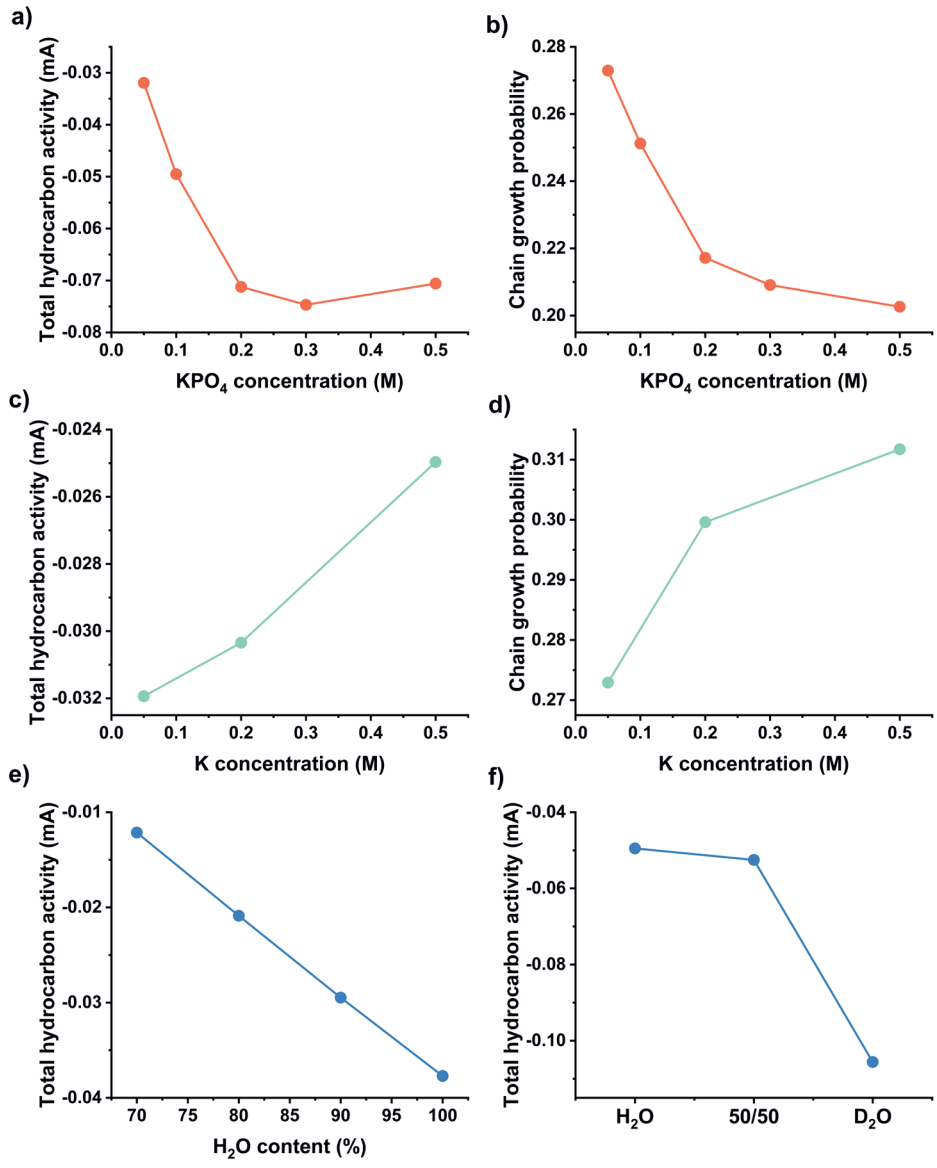

Figure 0.3 a) Total hydrocarbon activity and b) chain growth probability as function of pH7 potassium phosphate concentration at -1.175 V vs RHE on deposited Ni c) Total hydrocarbon activity and d) chain growth probability as function of potassium concentration by adjusting pH 7 0.05 potassium phosphate electrolyte with K_2SO_4. e) total hydrocarbon activity as function of H_2O content adjusted with DMSO in bicarbonate electrolyte and f) total hydrocarbon activity in H_2O, D_2O or mixed electrolyte in phosphate electrolyte

showed that higher phosphate concentrations increase activity and decrease chain growth probability up to 0.2 M after which it plateaus, while cation concentration seems to have the opposite effect, as shown in Figure O.3. The effect of water as proton donor was studied by changing the water content by mixing water with DMSO. This shows that more water leads to a higher activity. However, a kinetic isotope experiment shows a inverse kinetic isotope effect, although mixed H_2O and D_2O experiments show similar results to H_2O. The exact interpretation of the experiments with DMSO and D_2O is still difficult as these different solvents not only change the water concentration but also other parameters. All these preliminary experiments indicate that the rate limiting step is the hydrogenation of CO which is assisted by cations. However, it is still unknown how to exactly interpret the experiments with water to determine its role. Moreover, more experiments are needed to determine if the hydrocarbon chain grows via CH_x coupling, via CO insertion or via a different mechanism. Nickel seems the ideal catalyst to understand this reaction in more detail because of its significant activity, but in a later stage other active catalysts can be studied in more detail as well using the high-pressure high-temperature setup described in Chapter 6.

O.3.2 Chain growth mechanism at elevated temperatures on Cu

Chapter 7 has shown that the C-C coupling mechanism can switch from a CO dimerization or carbonyl coupling mechanism at low temperatures to a chain growth mechanism at high temperatures on Cu. However, some open questions remain. First of all, it would be interesting to study the time dependency in more detail. What happens in the first 30 minutes with the Cu surface and is this related to the initial production of CO? Raman spectroscopy, Pb UPD and SEM experiments can be performed (ex-situ) to gain more insight in the mechanism. For example, if Raman spectroscopy would show coke formation, this would indicate the direct CO dissociation pathway is active. Moreover, experiments changing the electrolyte and CO_2 concentrations as discussed above on Ni could give more insights. An interesting improvement of the setup would be if CO could be used as reactant at elevated pressures, to not only study CO_2 reduction but also CO reduction. Moreover, it would be interesting if a future version of the high-pressure high-temperature electrochemical cell could be coupled to spectroscopy. In that way in-situ spectroscopy could give more insights in the reactions on the surface.

O.4 Further experiments in the high-pressure high-temperature cell

The high-pressure high-temperature setup described in Chapter 6 has shown a lot of potential in Chapter 7 and 8. However, these studies were performed in a short time as the setup was only finished near the end of my PhD. Therefore, we limited these studies to a potassium bicarbonate electrolyte and only a few potentials. This illustrates that a lot of follow-up studies are possible.

First of all, the electrolyte is an important parameter to study as it can significantly influence the CO_2 reduction reaction and more studies are needed to see its effect at elevated pressure and temperature. One could start relatively simple by changing the cation identity from potassium to lithium and cesium or by changing the anion identity from bicarbonate to sulphate or phosphate. Moreover, one could play with the cation and buffer concentrations. Then one could start adding less common salts and molecules to the electrolyte, such as surfactants[3] or organic cations[4], as these have shown to either suppress HER or enhance CO2RR. This all can be done on Cu, to extend the research shown in Chapter 7 and for example see if the chain growth mechanism can be enhanced and optimized on Cu or to suppress HER further at elevated temperatures. However, also the catalysts studied in Chapter 8 can be studied in different electrolytes.

These screened catalysts of Chapter 8 need to be studied in more detail on many different parameters, not only the electrolyte. Due to the large research space, Chapter 8 only studied the metal catalysts at 6 or even 3 combinations of pressure and temperature. However, for the catalyst that are excellent in performing CO2RR such as Ag, Au, Pd, Sn and Pb, another optimum combination of pressure, temperature and potential may exist. This was illustrated by Chapter 6 and 7, where Au and Cu already show very high selectivity for CO2RR and suppression of HER at pressures of a few bar instead of 30 bar in Chapter 8. Therefore, these catalysts should be studied in more detail with smaller temperature and pressure steps and at different potentials as well. It might still be interesting to study some of the inferior CO2RR catalysts (even at elevated temperatures), as they can produce interesting products such as hydrocarbons and methanol. For these catalysts, high pressures seem to be needed, but one could also optimize the temperature and especially the potential and electrolyte.

Besides activity and selectivity, stability is also an important parameter which should be studied in more detail at elevated temperatures. We have shown in Chapter 7 and 8 that Cu, but also other catalysts as Ni and Pd can become unstable at elevated temperatures. Therefore, more research is needed into the causes of these instabilities and strategies have to be developed to enhance the stability. Chapter 4 illustrates that alloying could be a successful strategy in enhancing the

stability at elevated temperatures. Besides stability, alloys could also enhance activity and selectivity. Next to alloying, pulsing could be another possible strategy to increase the stability of the metal catalyst at high temperatures.

Most experiments in this thesis have been performed in an H-cell configuration with simple foil and wire electrocatalysts to keep the studied system as simple as possible and gain fundamental insights. However, it is important to validate these results in other configurations, especially gas diffusion electrodes (GDEs) setups as these are more representative of scaled-up industrial setups.

Lastly, the high-pressure high-temperature setup gives the opportunity to better compare electrocatalysis with thermocatalysis as it allows to go to pressures and temperatures more comparable to thermocatalytic conditions. By combining this with the use of non-aqueous electrolytes and specific substrates for catalysis, one comes closer and closer to the thermocatalytic conditions. On the other hand, thermocatalysis could introduce water and cations to simulate electrocatalytic conditions. By doing this using the same catalyst in both systems, one could build a bridge between thermocatalysis and electrocatalysis and hopefully gain further understanding in the differences and similarities between both and find new ways to control catalytic reaction in the desired way.

References

1. Goyal, A., Marcandalli, G., Mints, V. A. & Koper, M. T. M. *J Am Chem Soc* **142**, 4154–4161 (2020).
2. Zhou, Y. *et al. Nat Catal* **5**, 545–554 (2022).
3. Pan, H., Wang, F., Zhang, Z. & Min, S. *Sustain Energy Fuels* **6**, 2149–2154 (2022).
4. Yang, J. *et al. Angewandte Chemie International Edition* (2024) doi:10.1002/anie.202410145.

Samenvatting

Een van de grootste en meest urgente problemen van deze tijd is het veranderende klimaat als gevolg van door de mens veroorzaakte emissies van broeikasgassen, met name CO_2. Om de effecten van klimaatverandering te beperken, is een rigoureuze verandering nodig in de manier waarop de moderne samenleving energie en materialen gebruikt. Er is een transitie nodig van een wereld gebaseerd op fossiele brandstoffen naar een wereld gebaseerd op hernieuwbare bronnen. Elektrokatalyse kan een belangrijke rol spelen in deze transitie, omdat het hernieuwbare elektriciteit kan gebruiken om moleculen als H_2O, CO_2 en N_2 om te zetten in energiedragers of chemische bouwstenen zoals waterstof, CO, ethyleen en ammoniak. Elektrochemische CO_2 reductie (CO2RR) kan worden gebruikt om CO_2 van een vervuilende stof te veranderen in een grondstof door het om te zetten in waardevolle chemicaliën zoals CO, mierenzuur of ethyleen. Daarom is de interesse in deze reactie de laatste jaren enorm toegenomen. Elektrochemisch onderzoek in het algemeen en CO2RR-studies in het bijzonder worden vaak uitgevoerd bij omgevingsdruk en -temperatuur en daarom worden conclusies en fundamentele inzichten getrokken onder deze omstandigheden. Voor praktische toepassingen zijn omgevingsomstandigheden echter mogelijk niet het meest relevant, aangezien industriële elektrolyzers doorgaans werken bij verhoogde temperaturen, bijvoorbeeld door thermische verliezen en/of hete grondstoffen. Daarom is het belangrijk om de CO_2-reductiereactie bij verhoogde temperaturen en druk te bestuderen om fundamentele inzichten te krijgen in de effecten van deze parameters.

Hoofdstukken 2 tot en met 5 bestuderen het effect van temperatuur bij omgevingsdruk op Au-, Cu-, Ag-, Ni-elektroden en op CuAg-legeringen. Hoofdstuk 2 laat zien dat op Au, in een roterende-ring-schijfopstelling, de activiteit en selectiviteit van CO2RR toeneemt met de temperatuur. We schrijven dit toe aan de verbeterde kinetiek. We hebben experimenten met partiële druk uitgevoerd om het effect van temperatuur en CO_2-oplosbaarheid onafhankelijk van elkaar te bestuderen en laten zien dat bij hoge temperaturen de reactie wordt beperkt door de CO_2-concentratie. Bovendien laten we zien dat temperatuurexperimenten kunnen worden gebruikt om kinetische informatie te bepalen, zoals de overdrachtscoëfficiënt en de schijnbare activeringsenergie. Deze laatste wordt beïnvloed door het kation en daarom hangt de omvang van het temperatuureffect af van de gebruikte elektrolyt.

In Hoofdstuk 3 onderzoeken we hoe de reactietemperatuur de elektrochemische CO_2-reductie op koper beïnvloedt in het temperatuurbereik van 18-70 °C. We laten zien dat er twee verschillende temperatuurregimes zijn. Van 18 tot ∼ 48 °C worden C2+ producten geproduceerd met een hogere Faraday-efficiëntie, terwijl de selectiviteit van methaan en mierenzuur afneemt en de waterstofselectiviteit ongeveer constant blijft. Van 48 tot 70 °C werd vastgesteld dat de waterstofevolutiereactie (HER) domineert en de activiteit van CO2RR afneemt. Bovendien zijn de CO2RR-producten die in dit hogere temperatuurbereik worden geproduceerd voornamelijk de C1-producten, namelijk CO en HCOOH. De observaties in het eerste regime kunnen worden verklaard door een toename van de CO-dekking op het oppervlak, zoals blijkt uit in situ Raman-spectroscopie, in combinatie met een verhoogde lokale pH en snellere kinetiek met temperatuur. Het tweede regime lijkt niet gerelateerd te zijn aan een beperkt CO_2-massatransport, maar eerder aan veranderingen in het koperoppervlak zoals aangetoond met loodonderpotentiaalafzetting en dubbellaagcapaciteitsmetingen, hoewel een te hoge lokale pH ook een factor zou kunnen zijn.

Hoofdstuk 4 illustreert dat de prestaties van Cu-katalysatoren bij verhoogde temperaturen kunnen worden verbeterd door te legeren, in dit geval met Ag. Door te legeren kan de waterstofontwikkeling bij verhoogde temperaturen aanzienlijk worden onderdrukt. Bij omgevingsdruk blijft echter het optimum in C2+-productie met temperatuur, zelfs bij de verschillende CuAg-legeringen. Dit hoofdstuk laat ook zien hoe verweven het temperatuureffect is met andere parameters. Temperatuur beïnvloedt andere parameters, zoals de CO_2-oplosbaarheid, en deze moeten waar mogelijk worden ontward. In dit geval ontwarren we het effect van temperatuur en CO_2-oplosbaarheid door middel van experimenten met partiële druk. Bovendien beïnvloedt de toegepaste potentiaal het effect van temperatuur aanzienlijk en moeten beide parameters tegelijkertijd worden bestudeerd. Ten slotte beïnvloeden massatransport en temperatuur elkaars effect op de activiteit en selectiviteit van CO2RR en daarom zouden studies de studie van beide parameters moeten combineren.

In Hoofdstuk 5 onderzoeken we een van nikkel afgeleide katalysator voor de elektrochemische CO_2-reductie. Ni is een interessante elektrokatalysator omdat onlangs is aangetoond dat het de unieke mogelijkheid heeft om langere koolwaterstofketens te produceren via een ketengroeimechanisme in lage maar meetbare hoeveelheden. Het effect van de vele parameters van deze reactie moet echter nog nader worden bestudeerd. Hier hebben we het effect van

temperatuur, bulk-CO_2-concentratie, potentiaal, de reactant, kationen en anionen op de vorming van koolwaterstoffen via een ketengroeimechanisme op Ni onderzocht. We laten zien dat temperatuur de activiteit verhoogt, maar ook de vorming van coke, die de katalysator deactiveert. De selectiviteit en dus de kans op ketengroei wordt voornamelijk beïnvloed door de potentiaal en de samenstelling van de elektrolyt. Opmerkelijk genoeg vertoont CO-reductie een lagere activiteit, maar een hogere kans op ketengroei dan CO_2-reductie. Verder bespreken we dat de snelheidsbepalende stap hoogstwaarschijnlijk een hydrogeneringsstap is.

Hoofdstuk 6 tot en met 8 bespreken de ontwikkeling en toepassing van een hoge-druk-hoge-temperatuur-elektrochemische cel, die tot 140 bar en 200 °C kan werken. Deze opstelling maakt de gecombineerde studie van temperatuur en druk mogelijk. Bovendien breidt dit het temperatuurbereik dat kan worden bestudeerd uit tot meer dan 100 °C, zelfs in waterige elektrolyt. Hoofdstuk 6 toont, als een proof of concept van deze hoge-drukcel, de temperatuurs-afhankelijke veranderingen in de cyclische voltammogrammen van poly-kristallijn goud tot 150 °C en 50 bar. Verder werd de katalytische prestatie van CO_2-reductie tot CO op een roterende polykristallijne gouden schijfelektrode onderzocht onder verschillende druk en temperatuur. Bij omgevingsdruk werden vergelijkbare resultaten bereikt als in Hoofdstuk 2, maar bij verhoogde druk verdween het optimum in CO-selectiviteit met temperatuur en bereikte CO selectiviteiten rond de 90%. Onder deze omstandigheden kunnen temperatuur en druk de activiteit van CO_2-reductie op goud nog steeds aanzienlijk verbeteren.

In dezelfde volgorde als de eerste hoofdstukken bestudeerden we Cu in de hoge-druk-hoge-temperatuur-elektrochemische cel na bestudering van Au. We tonen een verandering in het C-C-koppelingsmechanisme boven 100 °C bij drukken van 24 bar. Waar bij lage temperaturen de meeste C-C-bindingen worden gevormd via het traditionele CO-dimerisatiemechanisme, neemt bij hoge temperaturen het ketengroeimechanisme het over en vanaf 125 °C is dit het enige mechanisme dat C-C-bindingen maakt. We tonen ook aan dat temperatuur de selectiviteit van het traditionele CO-dimerisatiemechanisme kan verbeteren bij temperaturen tot 75 °C, en dat druk helpt om het systeem stabiel te houden bij deze temperaturen. Verhoogde drukken kunnen de HER-activiteit en selectiviteit drastisch verminderen, zelfs bij drukken van slechts een paar bar. Het is echter niet de druk zelf, maar de CO_2-druk die de CO_2-reductie en C-C-koppeling specifiek verbetert.

Hoofdstuk 8 breidt het veld van elektrokatalysatoren voor CO2RR uit door 20 verschillende metalen te screenen voor deze reactie bij verschillende combinaties van druk en temperatuur bij omstandigheden tot 30 bar en 100 °C in waterige elektrolyt. We laten zien dat katalysatoren die oké zijn bij omgevingsomstandigheden, een efficiëntie van bijna 100% voor CO2RR kunnen bereiken bij 30 bar en dit kunnen behouden bij hoge temperaturen, omdat HER aanzienlijk wordt geremd bij verhoogde druk. Zowel temperatuur als druk kunnen de CO2RR-activiteit aanzienlijk verhogen. Als een katalysator echter geen CO2RR uitvoert bij omgevingsomstandigheden, zullen toenemende druk en temperatuur deze katalysator niet veranderen in een goede CO2RR-katalysator en neemt de CO2RR-selectiviteit toe tot maximaal 30%. Niettemin vertonen sommige van deze slechte CO2RR-katalysatoren interessante producten naast CO en HCOOH, zoals lange koolwaterstoffen en methanol. Hoofdstukken 6 tot en met 8 geven een inkijkje in de mogelijkheden en openen daarmee nieuwe, veelbelovende wegen voor toekomstig onderzoek naar elektrochemische CO_2-reductie bij hoge temperaturen en hoge druk in waterige elektrolyten.

II

List of publications
Curriculum Vitae
& Acknowledgements

List of publications

Chapter 2
R.E. Vos, M.T.M. Koper
The Effect of Temperature on the Cation-Promoted Electrochemical CO_2 Reduction on Gold
ChemElectroChem **9** e202200239 (2022)

Chapter 3
R.E. Vos, K.E. Kolmeijer, T.S. Jacobs, W van der Stam, B.M. Weckhuysen, M.T.M. Koper
How Temperature Affects the Selectivity of the Electrochemical CO_2 Reduction on Copper
ACS Catalysis **13** 8080-8091 (2023)

Chapter 4
R.E. Vos, J.S. Smaak, M.T.M. Koper
The Temperature Dependence of Electrochemical CO_2 Reduction on Ag and CuAg alloys
Journal of Catalysis 115613 (2024)

Chapter 5
R.E. Vos, M.T.M. Koper
Nickel as Electrocatalyst for $CO_{(2)}$ Reduction: Effect of Temperature, Potential, Partial Pressure, and Electrolyte Composition
ACS Catalysis **14** 4432-4440 (2024)

Chapter 6
A.H.M. da Silva, R.E. Vos, R.J.C. Schrama, M.T.M. Koper
Design of a Rotating Disk Electrode setup operating under high pressure and temperature: application to CO2 reduction on gold
Electrochimica Acta 144612 (2024)

Chapter 7
R.E. Vos, D. Schauermann, Pengfei Sun, Selwyn R. Hanselman, M.T.M. Koper
Change in the C-C coupling mechanism during CO_2 electroreduction on Cu at elevated temperature and pressure
In preparation

Chapter 8
R.E. Vos, M.T.M. Koper
Screening of Various Metal Catalysts for Electrochemical CO2 Reduction at Elevated Temperatures and Pressures
In preparation

Other publications

I.E.L. Stephens, et al.
2022 Roadmap on Low Temperature Electrochemical CO_2 reduction
Journal of Physics: Energy **4** 042003 (2022)

A. Shih, et al.
Water Electrolysis
Nature Reviews Methods Primers **2** 84 (2022)

A.H.M. da Silva, Q. Lenne, R.E. Vos, M.T.M. Koper
Competition of CO and Acetaldehyde Adsorption and Reduction on Copper Electrodes and Its Impact on n-Propanol Formation
ACS Catalysis **13** 4339-4347 (2023)

A.H.M. da Silva, G. Karaiskakis, R.E. Vos, M.T.M. Koper
Mechanistic Insights into the Formation of Hydroxyacetone, Acetone, and 1,2-Propanediol from Electrochemical CO2 Reduction on Copper
Journal of the American Chemical Society **145** 15343-15352 (2023)

O. van der Heijden, S. Park, R.E.Vos, J.J.J. Eggebeen, M.T.M. Koper
Tafel Slope Plot as a Tool to Analyze Electrocatalytic Reactions
ACS Energy Letters **9** 1871-1879 (2024)

M.R. Pinto, R.E. Vos, R. Nagao, M.T.M. Koper
Electrolyte Effects on Electrochemical CO_2 Reduction at Sn Metallic Electrode
Journal of Physical Chemistry C, in revision

O. van der Heijden, R.E. Vos, A.H.M da Silva, M.T.M. Koper
Determination of the Temperature Dependent Tafel Slope, Activation Energy and Transfer Coefficients for the Alkaline Oxygen Evolution Reaction on NiFeOOH
In preparation

O. van der Heijden, A.H.M da Silva, R.E. Vos, M.T.M. Koper
Effects of Pressure on the Oxygen Evolution Reaction
In preparation

Curriculum vitae

Rafaël Vos was born on the 28th of November 1995 in Almere, the Netherlands, where he lived the first 18 years of his life. He went to high school at het Oostvaarders College (OVC) from 2008 to 2014 and graduated the gymnasium cum laude with a curriculum of both 'nature and health' and 'nature and technology' extended with economics and French. After high school he moved to Leiden to start his university education.

From 2014 to 2017, Rafaël followed the bachelor Molecular Science and Technology (MST), which is a joint degree of the TU Delft and Leiden University combining Chemistry and Chemical Engineering. He was always interested in sustainability and his first introduction with electrochemistry and with prof. Marc Koper was during an interview for a course in the extracurricular Honours Program. This sparked his interest for electrochemistry and resulted in a bachelor thesis in the CASC research group researching the effect of the carbon substrate on the electrochemical CO_2 reduction on indium protoporphyrins under supervision of Yuvraj Birdja.

After graduating his bachelor summa cum laude, Rafaël started the master Chemistry in Leiden. He chose the 'Energy and Sustainability' specialization and pursued both the Research and Business track. This entailed that besides 60 ECTS of Chemistry courses, which were mainly focused on physical and inorganic chemistry, he also followed business courses such as Finance and Strategy. Rafaël performed his master thesis again in the CASC research group. This time he studied the reduction and adsorption mode of acetylpyridine on Au under supervision of dr. Christoph Bondü. After his master thesis, he carried out a second research internship in the research group of prof. Alexis Bell in Berkeley, USA. Here he researched the electrochemical CO_2 reduction to C2+ products on Cu foils. Besides two research internships, Rafaël also performed a business internship at nlmtd, at that point a small consulting firm focusing on sustainability and specialized in the energy sector. Moreover, Rafaël participated in the Leiden Leadership Programme, an extracurricular programme focusing on self-development via seminars, workshops, group projects and much self-reflection. Due to these extra activities, Rafaël obtained his master cum laude in three years (2017-2020).

For his PhD, Rafaël stayed in Leiden and specifically the CASC research group under supervision of Prof. Marc Koper. He started during the COVID-19 epidemic in 2020 and his research was part of the TRANSCRIPT (Transforming carbon-rich industrial waste gases of metallurgical plants into valuable products) project. This project was cofunded by the Netherlands Organization for Scientific Research

(NWO), Materials Innovation Institute (M2i) and Tata Steel. Besides Rafaël, also one PhD candidate, two postdocs in Leiden and three PhD candidates in Utrecht were part of this project. The project of Rafaël focused on the effect of temperature on the electrochemical CO_2 reduction and he co-developed the high-pressure, high-temperature electrochemical cell. Besides research, Rafaël also supervised several bachelor and master students during their thesis or other internships in the group. Moreover, he supervised bachelor students during their first practical course (Basic Practical Skills) and small lab internships, and assisted during a seminar for chemistry bachelor students.

Furthermore, several courses where followed by Rafaël during his PhD. Besides 'Visualize your Science' (Visualize your science) and 'High Impact Writing' (HRSMC) also several courses from Leiden University were completed (PhD Introductory Meeting, Speed Reading, Manage your Brain, Basic Project Management, Negotiating, Storytelling Lab, Scientific Conduct). Additionally, he presented his work at several national and international conferences and summer schools, both via poster presentations (ECCM graduate school in 2021, HRSMC symposium in 2021, 2022 and 2023, Surfcat summer school in 2022, ISE topical meeting in 2022, NCCC in 2022, Amcel symposium in 2023, ISE 74th Annual Meeting in 2023, the M2I conference from 2020 till 2023) and via oral presentations (NCCC in 2023 in Noordwijkerhout, CHAINS-IUPAC in Den Haag in 2023, M2I conference in Apeldoorn in 2023, NanoGE in Keele in 2023, National Symposium on Electrochemical Conversion in Den Haag in 2024, ISE 75th Annual Conference in Montreal in 2024). Rafaël was also member of the PhD platform of the Holland Research School for Molecular Chemistry (HRSMC) and the PhD representative during the CASC staff meetings.

Acknowledgements

With the end of my PhD also my time at Leiden University comes to an end after a decade long journey. This journey formed me both as a researcher and as a person, and I would like to take this opportunity to express my gratitude to the people who joined me on this journey and contributed to the realization of this thesis, may it be directly or indirectly.

First I would like to thank prof. dr. Marc Koper for his supervision during all these years. We first met in my first year as a bachelor student and during this interview my passion for electrochemistry was ignited. I want to thank Marc for providing me the opportunity to join the Catalysis and Surace Chemistry (CASC) group not once, but three times during all these years. Thank you for the freedom to explore my own ideas, for the impactful advises, for all the feedback on my work, for the opportunities to go on conferences both in the Netherlands and abroad, for providing an excellent work environment and creating such an amazing research group full of wonderful people.

José and Angelo, thank you for arranging things for us and taking great care of us, probably more than we realize. Wen Tian, thank you for approving our orders so fast, taking care of the lab and for all the fun and little chats in the lab.

Yuvraj and Christoph, you got me acquainted with electrochemistry and paved the way for me to pursue a PhD. Thank you for laying the foundations and for your great supervision during my bachelor and master project in the group.

A PhD is not a journey you should do on your own and I'm grateful for all the wonderful people in the CASC research group that joined me on this journey, not only in the lab but also as wonderful friends outside of the university. Sergi, I'm grateful and happy I can call you my good friend. Even though in the lab we did not spend much time together, the more time we spend at the lunch table and outside of university. Thank you for all the laughter, stories, food and good times. Alisson, you have been the closest colleague I worked with. Thank you for all the wonderful scientific discussion we had, for the amazing collaboration and for all the fun, also outside of the lab. With Cássia, Marleen and Francesc, we had a lot of fun times. Thank you for the wonderful dinners, the great parties and your amazing friendship.

I'm thankful to all the other people I closely work with in our project. You were amazing colleagues in and outside of the lab; Xuan, Zhiqin and Quentin. I also want to express my gratitude to our collaborators from Utrecht. Angela, Joyce and Thimo, we had a great time during all the meetings and conferences we were together.

I want to thank Aleksandra for being a great companion, in and outside the CO_2 team. Together with Nicci you livened up our office. Nipon, we started our journey together and I'm thankful for all the time we spend in and outside the lab together. Too bad that our trip didn't take place yet. Onno, we shared a lot of experiences together. At the start as the minority of Dutch people in the lab and I'm happy you were always by my side in the office. We have had great conversations there, both scientific and not at all, such as about football. I could also always count on you if something needed to be organized for the lab. Sunghak, thank you for all the wonderful discussions, for the moments of distraction when we peaked at each other's setup when we were bored and for the wonderful food you made and the recipes you gave me. Mingchuan, I remember the times it was the standard that we were working in the spots next to each other in the lab. Thank you for all the good times and giving us always a reason to laugh.

I would also like to thank my former students, of whom some have turned into colleagues and friends. Kees, Jeroen, Daniel, thank you for your hard work and for your contributes to the scientific work in this thesis. I'm also grateful for the people who taught me at the start of my PhD. Akansha, Giulia, Stefan, thank you for all the nice discussions and teaching me how to work with your setups. I want to thank the other 'old' members of the group for welcome me every time I came back such as Chunmiao, Arthur, Mariana, Kasinath, Xiaoting and Matias. The other people of my generation, with whom I shared the longest journey; Hassan, Zahra, Sheena, thank you for this amazing environment we have created together. The research group kept expanding and I want to thank the other 'new' members of the group; Katinka, Ariba, Greta, Jordy, Arthur for the wonderful times, the more the merrier. I would also like to give a big shoutout to the glass blowers and the technicians at the FMD, especially Robin, for all the equipment you have made for us. Thank you for thinking along, always being there for us and your fantastic work. Without you there would be no science. With such a big research group there are so many people to thank. So I want to thank all the other colleagues, guests and students who have not explicitly been named yet for the great times I shared with you within CASC.

Last, but most importantly, I thank the people who not always understand all the science. My family, especially my parents and sister for their unwavering support. Pap for always making the effort to try to understand the science. Mam for all the support and listening to all my stories about the lab. It makes me sad you could not see the end product, but I'm happy you were there during the entire journey and I'll keep you and your support always with me in my heart. Tysha for being such an amazing sister. And the rest of my family and friends for all the fun times and distractions outside of the lab.